1 of 3

SANDIA REPORT

MELCOR 1.8.2 Assessment:
The DF-4 BWR Damaged Fuel Experiment

Timothy J. Tautges

MELCOR 1.8.2 ASSESSMENT: THE DF-4 BWR DAMAGED FUEL EXPERIMENT

Timothy J. Tautges
Thermal/Hydraulic Analysis Department
Sandia National Laboratories
Albuquerque, NM 87185

Abstract

MELCOR is a fully integrated, engineering-level computer code being developed at Sandia National Laboratories for the USNRC, that models the entire spectrum of severe accident phenomena in a unified framework for both BWRs and PWRs. As a part of an ongoing assessment program, MELCOR has been used to model the ACRR in-pile DF-4 Damaged Fuel experiment. DF-4 provided data for early phase melt progression in BWR fuel assemblies, particularly for phenomena associated with eutectic interactions in the BWR control blade and zircaloy oxidation in the canister and cladding.

MELCOR provided good agreement with experimental data in the key areas of eutectic material behavior and canister and cladding oxidation. Several shortcomings associated with the MELCOR modeling of BWR geometries were found and corrected. Twenty-five sensitivity studies were performed on COR, HS and CVH parameters. These studies showed that the new MELCOR eutectics model played an important role in predicting control blade behavior. These studies revealed slight time step dependence and no machine dependencies. Comparisons made with the results from four best-estimate codes showed that MELCOR did as well as these codes in matching DF-4 experimental data.

Contents

List of Figures

ix

x

List of Tables

Acknowledgements

Chapter 1

Introduction

MELCOR is a fully integrated, engineering-level computer code being developed at Sandia National Laboratories for the U. S. Nuclear Regulatory Commission (US-NRC), that models the progression of severe accidents in light water reactor nuclear power plants [1]. The entire spectrum of severe accident phenomena, including reactor coolant system and containment thermal/hydraulic response, core heatup, degradation and relocation, and fission product release and transport, is treated in MELCOR in a unified framework for both boiling water reactors and pressurized water reactors.

The purpose of the Damaged Fuel, or DF, series of experiments [2],[3],[4],[5] was to investigate core melt progression and to benchmark severe accident codes. The DF-4 experiment was carried out at Sandia National Laboratories in the Annular Core Research Reactor (ACRR) in 1986 [6]. This experiment investigated the behavior of BWR-type fuel materials and configurations in a high-temperature oxidizing environment typical of the conditions during a Loss-Of-Coolant Accident (LOCA). The DF-4 experiment provided information about the physical processes which are important during the early fuel damage phase of a severe accident in a BWR. This experiment provided detailed measurements of experimental conditions in the test bundle, against which MELCOR and other severe accident codes can be assessed.

The primary areas of interest in the DF-4 experiment were the eutectic interaction between the control poison material (B$_4$C) and the stainless steel control blade sheath and tubes, and the oxidation of zircaloy in the cladding and canister. The eutectic interaction was important because it contributed to early control blade failure; this could result in reactivity transients if the control poison were to relocate independently of the fuel.

For this task, an assessment of the MELCOR code was performed using the DF-4 experiment. With the recent addition of eutectic interaction modeling [7], MELCOR is able to model most relevant phenomena in DF-4. These calculations were performed as post-test analyses, with both test data and the results of other code analyses available for comparison. Sensitivity studies were performed on the core (COR) package, control volume hydrodynamics (CVH) package and heat structures (HS) package parameters, and the results of the base case calculation are compared with results from other codes modeling DF-4. The version of MELCOR used to model

1

DF-4 was version 1.8NX of the code. All modifications resulting from this assessment task have been implemented in the production version of the code.

The remainder of this report is structured as follows. The experimental setup of DF-4 is described in Chapter 2. The base case MELCOR model for DF-4, which represents the best approximation of experimental conditions, is described in Chapter 3. The results calculated with MELCOR using the base case input model are discussed in Chapter 4. A number of sensitivity studies were done on MELCOR parameters in the COR, CVH and HS packages, on the input problem nodalization, and on the time steps used to model DF-4. These studies are discussed in Chapter 5. The MELCOR base case results are compared with results from four other severe accident codes in Chapter 6. Several code problems were identified as part of this work; these problems and the corrections made to MELCOR to fix them are described in Chapter 7. This work is summarized and final conclusions are given in Chapter 8. The MELCOR input deck used for the base case calculation is given in Appendix A.

Chapter 2

Facility and Test Description

The DF-4 experiment [5] was part of a series of Damaged Fuel experiments conducted at Sandia National Labs between 1984 and 1986 [2],[3],[4],[5], using the ACRR at Sandia to provide the nuclear heating which drove the bundle damage progression. The DF experiments involved the nuclear heating of a representative fuel bundle to the point of core material melting, oxidation and relocation.

2.1 Facility Description

The DF-4 experiment represented a typical BWR D-Lattice core geometry. The fuel bundle in DF-4 consisted of fuel rods, a canister or channel box, and a control blade sheath surrounding five steel-clad B_4C control rods. These components were surrounded by several layers of thermal insulation. A radial cross section of the DF-4 fuel bundle is shown in Figure 2.1.1. Each of these components is described in the following sections, and general core component parameters are given in Table 2.1.1 (for more details of the experimental facility, see [5]).

2.1.1 Stainless Steel/B_4C Control Blade

Located at the center of the DF-4 test bundle was the control blade, consisting of five stainless steel tubes filled with B_4C powder (70% theoretical density), surrounded by a stainless steel sheath. Dimensions for the control blade tubes and sheath are typical of a General Electric D-Lattice design (see Figure 2.1.1 and Table 2.1.1).

2.1.2 Channel Box

The control blade was completely surrounded by a zircaloy-4 channel box or canister. This arrangement was opposite that of a normal BWR fuel assembly, where the channel box surrounds the fuel rods and not the control blade. This arrangement still allowed separate steam flow regions for the fuel rods and control blade, as occurs in normal BWR cores. The thickness of the canister walls and the gap thickness between the sheath and the inside canister wall were typical of the GE D-Lattice design. The control blade was displaced to one end inside the canister (see Figure 2.1.1) to

3

CONTAINMENT BOUNDARY
(stainless steel)

ZrO₂ FIBER INSULATOR
(ZIRCAR - FBC, density=1.1 g/cc)

GAP - HELIUM (101 kPa)

HELIUM (83 kPa)

FULLY DENSE ZrO₂ TUBE
(OD=127 mm, wall=4.76 mm)

PRESSURE BOUNDARY
(stainless steel)
(OD=177.8 mm, wall=6.35 mm)

ZIRCALOY CHANNEL BOX
(wall 2.5 mm)

ZIRCALOY CLADDING
(OD=9.63 mm, wall=0.61 mm)

UO₂ FUEL
(density=10.9 g/cc)

CONTROL BLADE
SHEATH - stainless steel
- wall 1.42 mm
TUBE - stainless steel
- od=4.75 mm
- wall=0.66 mm
ABSORBER - B₄C powder
(density=1.7 g/cc)

Figure 2.1.1. Radial cross section of the DF-4 test bundle (from [6]).

4

(127 mm)

LINE OF SIGHT TUBE

ACRR POOL
SURFACE 10 m

INLET STEAM LINES

UPPER SUPPORT GRID

UPPER FUEL PLENUM
SPRING - 67.2 mm

ALUMINA SPACERS - 47.75 mm

ACTIVE CORE
HEIGHT - 508 mm

TEST BUNDLE REGION
(ONE FUEL ROD SHOWN)

INCONEL NEUTRON FILTER

UO$_2$ FUEL PELLETS
FISSILE LENGTH - 505 mm

ACRR
MIDPLANE

ZrO$_2$ FIBER INSULATOR
(ZIRCAR - FBC)

ACRR CENTRAL CAVITY
LOADING TUBE

FULLY DENSE ZrO$_2$
CERAMIC TUBE

ALUMINA SPACERS - 38.1 mm

CONTAINMENT BOUNDARY

INLET STEAM LOWER
PLENUM REGION AND
LOWER SUPPORT GRID

PRESSURE BOUNDARY

(229 mm)

Figure 2.1.2. Axial cross section of the DF-4 test bundle (from [6]).

5

Table 2.1.1. Important parameters for the DF-4 experiment [6]. Core material masses are for active fuel region only.

Parameter	Value
Dimensions:	
Fuel pellet diameter	8.26 mm
Cladding thickness	0.61 mm
Fuel rod OD	9.63 mm
Channel box thickness	2.5 mm
Fuel rod pitch	
(square & triangular)	12.7 mm
Masses:	
Fuel	4.13 kg
Zircaloy (clad)	0.79 kg
Zircaloy (canister)	1.08 kg
Stainless steel	0.57 kg
Boron carbide	0.04 kg

represent the tip region of a typical BWR control blade. Various canister dimensions are given in Table 2.1.1.

2.1.3 Fuel Rods

Seven fuel rods were situated on each side of the canister in the DF-4 test bundle, for a total of 14 rods. The rods on each side of the canister were arranged in two rows, with the inner row in a square 1.3 cm (0.5 in.) pitch and the outer row in a triangular 1.3 cm (0.5 in.) pitch (see Figure 2.1.1). This allowed increased radiation view factors between the outer row of fuel rods and the canister while decreasing the overall size of the test bundle.

The fuel rods consisted of 10% enriched UO_2, clad by zircaloy-4. The fuel rods were more prototypic of PWR rods (which were more readily available), but their pitch and the distance to the channel box outer wall were typical of BWR fuel assemblies. The active fuel region was 50.5 cm long. The end regions consisted of Al_2O_3 spacers and zircaloy-4 end caps, with an Inconel spring on the upper end to hold the fuel pellets in place. The fuel rods were backfilled with helium gas to approximately atmospheric pressure. An axial cross section of the DF-4 test bundle is shown in Figure 2.1.2.

2.1.4 Test Section Insulation and Radial Boundary

The active test bundle, consisting of fuel rods, a control blade and a canister, was surrounded by four layers of insulation. These layers served as thermal and material boundaries for the test bundle.

The first layer of insulation, closest to the fuel rods, consisted of a porous zirconia (ZrO_2) material conformed to the general shape of the active test bundle. This material formed the primary thermal barrier to the test bundle, and had an outer diameter of 12.2 cm. The second layer consisted of dense ZrO_2, which acted as a barrier to any molten core material penetrating the inner porous zirconia layer. Porous zirconia formed the third layer, with an outer diameter of about 17 cm. The fourth layer of insulation was a 6 mm thick stainless steel wall, which formed the pressure boundary to the test bundle.

2.1.5 Other DF-4 Experiment Components

There were several components outside the DF-4 test bundle that were important to the execution of the experiment. These components are described individually.

Steam Supply System

The steam line system was used to provide steam to the test bundle. Two inlet steam lines entered the test bundle from the top, and ran down between the dense zirconia tube and the stainless steel pressure boundary. These lines emptied into a lower plenum below the test bundle, from which the steam could flow into the fuel (channel) and control blade (bypass) regions.

The stainless steel plate separating the inlet plenum and the channel and bypass regions of the test bundle (see Figure 2.1.2) contained orifices, one each to the channel and bypass regions, such that 80% of the flow entered the channel region (40% to each side of the canister) and 20% entered the bypass region. This flow split was maintained throughout the experiment by a large pressure drop across the orifices, so that the flow was not influenced by downstream pressure.

Test Bundle Instrumentation

The primary instrumentation in the test bundle consisted of temperature thermocouples. These thermocouples were located at four axial levels in the active fuel region, and were physically attached to the fuel rod clad, control blade sheath and canister walls. Two types of thermocouples were used in the DF-4 experiment. The first type (designated "type S") was a platinum-rhodium (Pt/Rh) thermocouple, welded directly to the instrumented component. This type had good response time, but failed at the substrate melting temperature (which was 1700K for the stainless steel control blade and 2200K for the zircaloy cladding). "Type C" thermocouples were fabricated from tungsten-rhenium (W/Re), and were sheathed in a ceramic zirconia tube. This sheath touched the component being instrumented. Because of the sheath and also because of the horizontal placement of these thermocouples (see Figure 2.1.3 and

7

[5]), the temperature indicated by these thermocouples lagged the actual component temperatures by several hundred degrees K. However, these instruments survived component melting because of the zirconia sheath.

The axial locations of both types of thermocouples are shown in Figure 2.1.3. Type S thermocouples are indicated with a black dot on the component instrumented, while type C thermocouples are indicated with a sheath assembly that touches the instrumented component. Distances in Figure 2.1.3 are measured from the bottom of the active fuel region (see Figure 3.1.2 for the relative axial positioning within the assembly). Also shown are the alphanumeric indicators for each thermocouple. The notation used for these alphanumeric indicators is explained in Figure 2.1.4.

Hydrogen Recombiner

The system used to measure hydrogen production in DF-4, referred to as the hydrogen recombiner, was designed specially for this experiment. It measured the heat liberated from a chemical reaction between CuO and H_2, and from that inferred the mass of H_2 flowing through the recombiner. A measure of the integral amount of hydrogen produced during DF-4 was provided by subsequent PIE's (Post Irradiation Examinations) performed by the experimenters [6].

Visual Diagnostic System

The upper portion of the test bundle was kept clear of structure and components to allow visual observation of experiment progression. Steam exiting from the test bundle was diverted to an outlet line using an opposing steam flow [5]. Video pictures were taken through an optical port in the top of the experiment package. This visual record provided further data on the timing of major experimental phenomena, such as control blade failure.
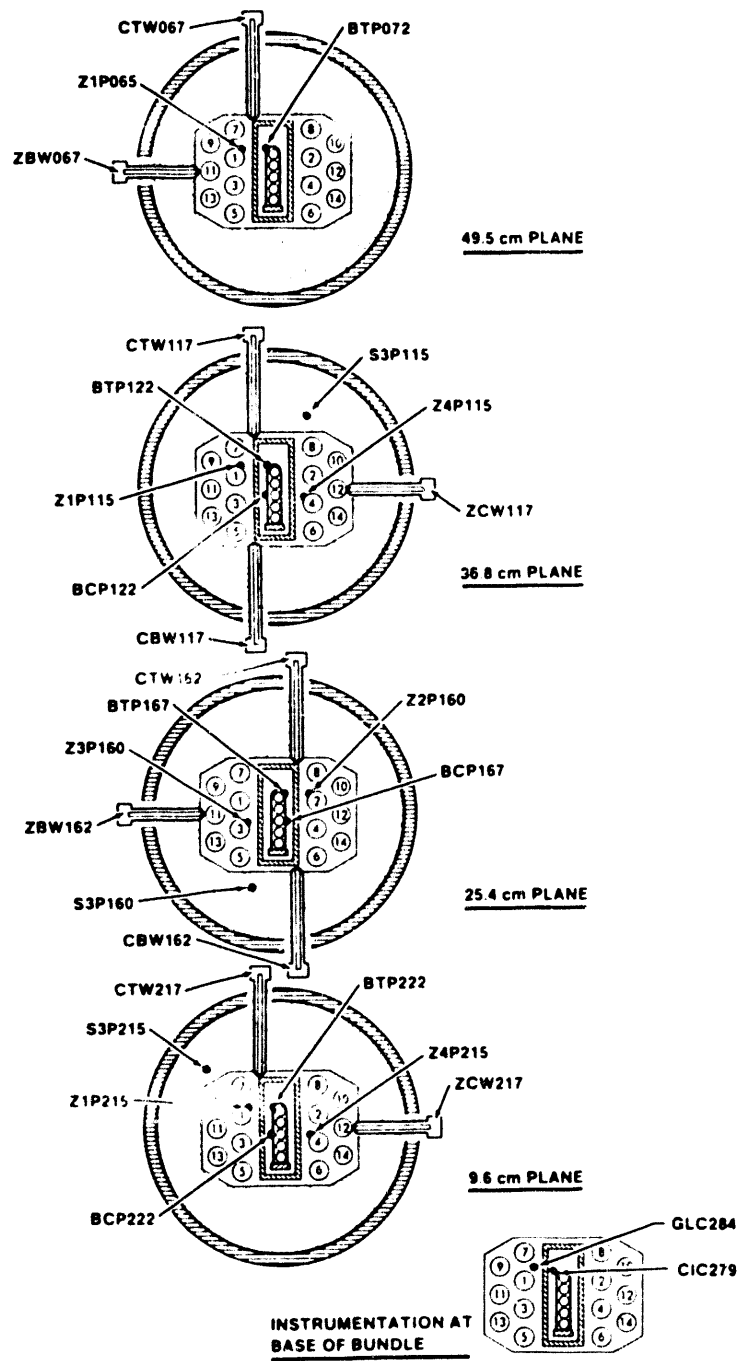
Figure 2.1.3. Radial locations of bundle thermocouples (from [6]).

9

```
                                        ┌
                                        │ Z:   "Zircaloy" cladding of fuel rod
         ┌──────────────────────────────│ B:   Stainless steel control "blade"
         │                               │ C:   "Channel box"
         │                               └

         │    ┌──────────────────────────┌
         │    │                          │ 1,2,3,4: fuel rod number  ⎫ *
         ↓    ↓                          │ B,C     : fuel rod 11 or 12⎭
         Z 3 P 1 6 0                     │ T,B     : "top" or "bottom" of channel box**
                                         └

         ↑──
         │
         │  ↑────────────────────────────┌
         │                               │ axial distance in tenths of inches from ***
         │                               │ the lower surface of the upper fuel
         │                               │ grid
         │                               └

         │
         │                               ┌
         │                               │ P:  "Pt/Rh" thermocouple (Type S)
         └───────────────────────────────│
                                         │ W:  "W/Re" thermocouple (Type C)
                                         └
```
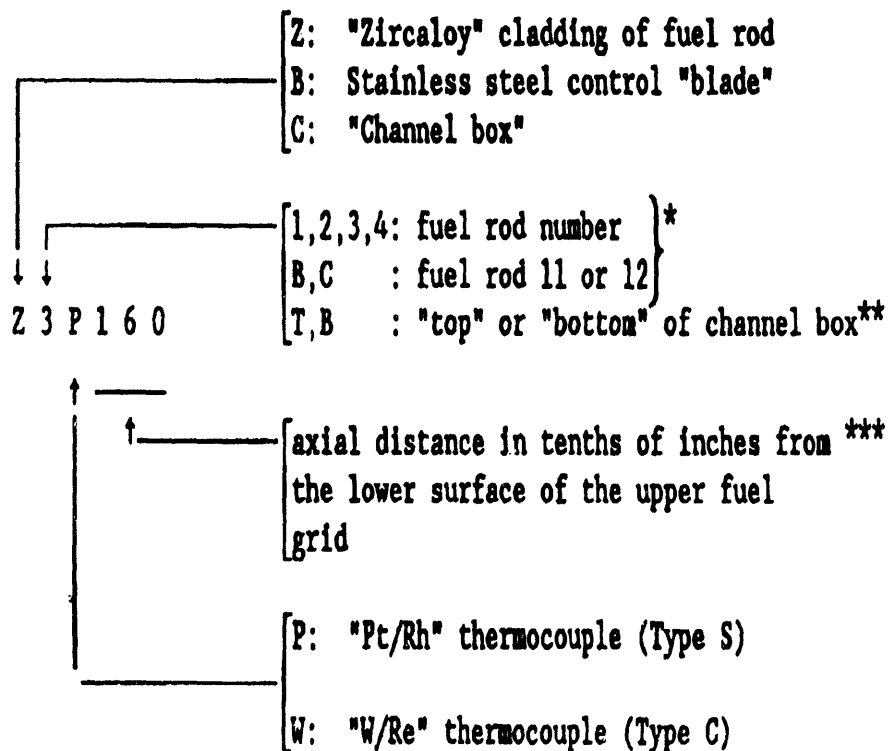
* - this notation used only if the leading prefix is "Z" for zircaloy fuel rod cladding

** - this notation used when the leading prefix is "C" for channel box

*** - this datum is located 26 inches (660 mm) above the bottom of the fuel rod fissile
       length.

Figure 2.1.4. Mnemonic indicators for bundle thermocouple locations (from [6]).

2.2 Test Description

The DF-4 test consisted of three primary phases: the startup phase (0-2200 seconds), the hydrogen calibration phase (2200-6000 seconds), and the fuel damage phase (6000-8100 seconds). The purposes of the first two phases were to bring the test bundle to the proper thermal initial conditions, and to calibrate the hydrogen recombiner system. These two phases were not modeled by MELCOR and therefore are not described in this report. The results of these two phases are represented by the MELCOR input model in the initial conditions of the test bundle. The remaining phase and its "subphases" can be represented best by a plot of the ACRR reactor power versus time, shown in Figure 2.2.1, and the inlet steam mass flow rate, shown in Figure 2.2.2. (Note that during the entire test, the inlet steam was partitioned such that 80% went to the fuel rods outside the channel box and 20% was diverted to the control blade inside the channel box.)

The fuel damage phase extended over the period of 6000-8100 seconds. Although five separate subphases were defined [5], the most important of the subphases were the oxidation pre-transient subphase (7200-7500 seconds) and the oxidation transient subphase (7500-8000) seconds. It was during these subphases that most of the test bundle damage occurred. During the other subphases, the test bundle components underwent nuclear heating and reached approximate temperature equilibrium.
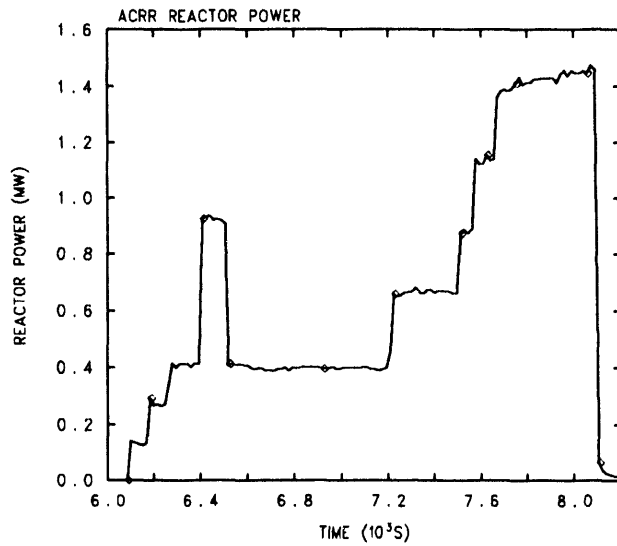
Figure 2.2.1. Measured reactor power in the ACRR during the fuel damage phase of the DF-4 experiment.

11

STEAM INLET MASS FLOW RATE
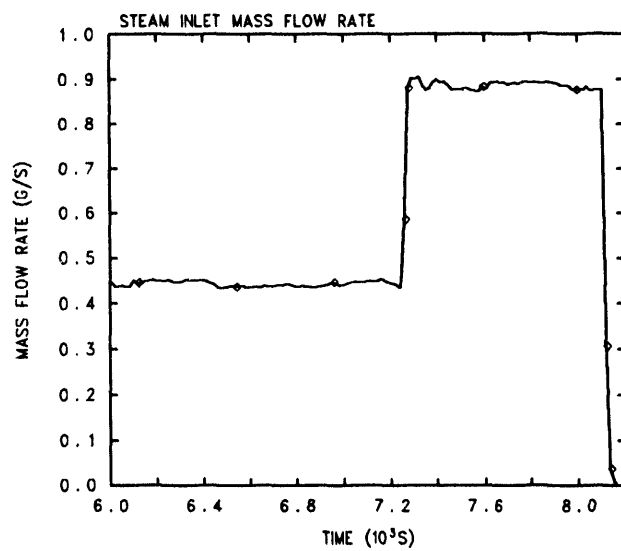
Figure 2.2.2. Total inlet steam flow rate during the fuel damage phase of the DF-4 experiment.

12

Chapter 3

MELCOR Input Model

The input model used to represent the DF-4 experiment for the base case calculation is described in this chapter. The base case model did not use all the MELCOR default input options, but rather used input which resulted in best agreement with experimental data. This base case was derived from a number of sensitivity studies, some of which are described in Chapter 5.

The part of the MELCOR base case model describing geometric and mass input is described first, followed by a discussion of initial and boundary conditions used in the base case calculation. A listing of the base case MELCOR input is included in Appendix A, for reference.

3.1   Geometry

The DF-4 base case input model represented only those parts of the DF-4 experiment that were considered significant to the results of the experiment. The parts of the experiment modeled included the active test bundle (fuel rods, canister, control blade), the lower or inlet plenum, and the test bundle insulation. Any experimental conditions outside these boundaries were modeled in MELCOR as boundary conditions.

3.1.1   CVH/FL Package Models

The base case MELCOR model consisted of four fluid flow control volumes and four flow path junctions. The arrangement of the control volumes and flow paths is shown in Figure 3.1.1. The two control volumes numbered CV101 and CV102 corresponded to the core channel and bypass volumes, respectively. The channel volume included the inlet plenum, while the bypass volume started at the bottom of the fuel rods. A time-specified control volume, CV100, was used to provide the inlet mass flow to the channel and bypass volumes. A sensitivity study on the number of control volumes in the test bundle region is described in Section 5.7.

The flow paths connecting the inlet volume to the channel and bypass volumes were numbered FL101 and FL102, respectively. The flow areas in these flow paths were determined by the cross-sectional flow areas of the channel and bypass regions,

13

Table 3.1.1. View factors used in MELCOR DF-4 base case model, compared to analytical values given in [8].

View Factor	MELCOR Value	Analytical Value
$F_{\text{can-clad}}$	0.550	0.5836
$F_{\text{blade-can}}$	0.9999	0.9999
$F_{\text{cell-cell(radial)}}$	0.10	0.0818
$F_{\text{cell-cell(axial)}}$	0.50	N/A

respectively, in the test bundle. Since the channel and bypass control volumes included the entire axial extent of the test bundle, the lengths of both inlet flow paths were set to half the distance between the lower plenum and the end of the test bundle. The outlet flow paths, FL201 and FL202, were similar to the inlet flow paths, and started at the middle of the test bundle.

3.1.2 COR Package Model

The core package model used for the base case calculation consisted of one radial ring and fourteen axial levels, for a total of fourteen core cells. Nine of these cells represented active fuel cells, and were numbered cells 104-112. The remaining five cells represented the inlet plenum (cell 101), the core plate region (cell 102), the lower and upper spacer regions (cells 103 and 113, respectively) and the upper spring region (cell 114). The core nodalization used in the DF-4 input model is shown in Figure 3.1.2. A core nodalization study is described in Section 5.7.

The materials used for the active fuel, clad, canister, control blade sheath and tube, and control poison materials corresponded exactly to the materials used in the experiment. Since the MELCOR code does not allow assignment of fuel material on a cell-by-cell basis, the spacer material in the DF-4 fuel rods was specified to be UO_2, like the active fuel (the actual material used was Al_2O_3). Likewise, the Inconel spring in the upper-most core cell was approximated as stainless steel in the other structure component. Zero peaking factors were used in the spacer regions (core cells 103 and 113), resulting in no power generation in those regions (peaking factor input is described in Section 3.2).

The radiation view factors used in the base case MELCOR model are listed in Table 3.1.1, along with the values calculated analytically for the DF-4 experiment [8]. A sensitivity study on the radiation view factors is discussed in section 5.1.4.

The minimum component mass and the minimum mass used for temperature control in sensitivity coefficient array 1502 were set to 10^{-5} and 10^{-4} kg, respectively. These are the component masses below which component mass and energy are discarded and below which a component is not subject to maximum temperature change criteria, respectively. These parameters were reduced to take into account the reduced component masses in this experiment compared to those found in full-scale reactor core models. A sensitivity study on these parameters is described in Section 5.1.6.
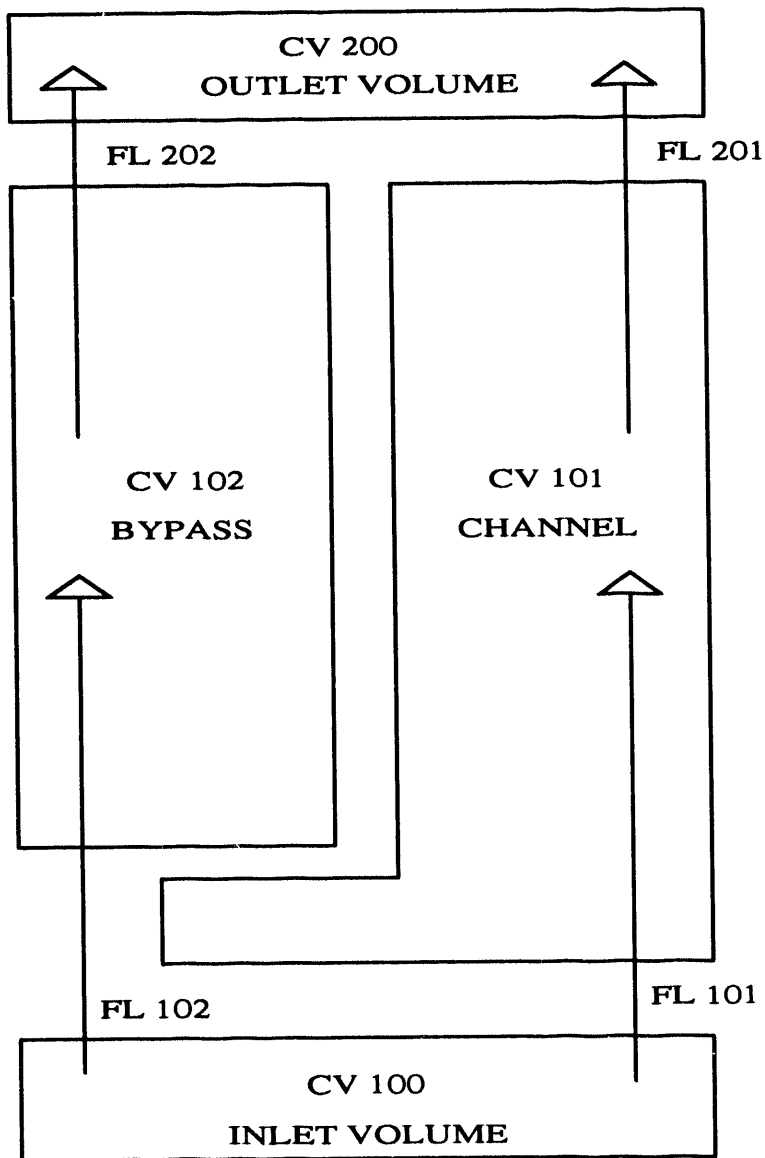
Figure 3.1.1. Control volume and flow path arrangement in the MELCOR DF-4 base case input model.
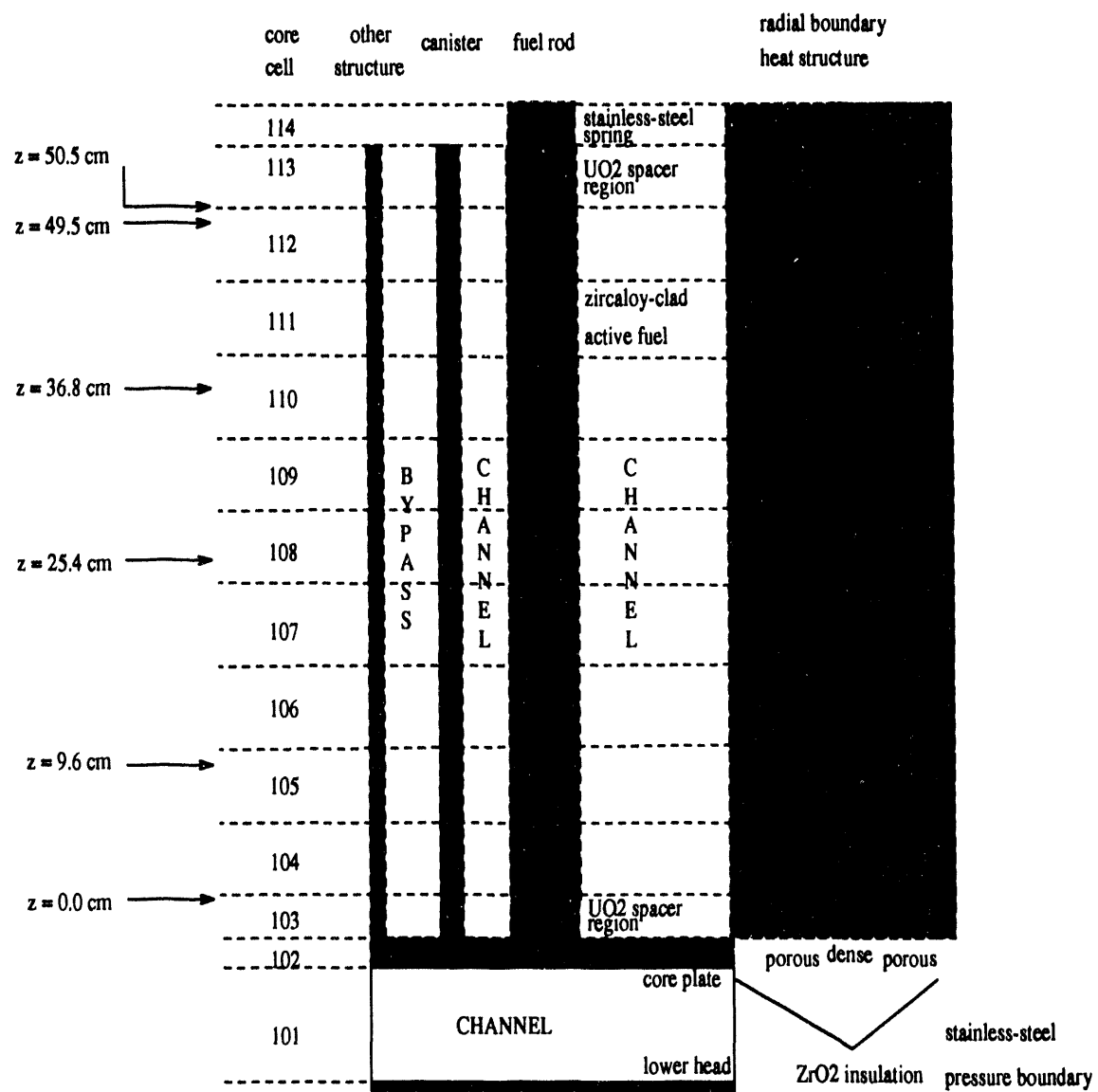
Figure 3.1.2. Core and heat structures nodalization in the MELCOR DF-4 base case input model (upper boundary heat structure not shown).

Table 3.1.2. Core radial boundary heat structures parameters.

Layer	Material	Thickness	Number of temperature nodes
1	ZrO_2 (porous)	2.43 cm	11
2	ZrO_2 (dense)	0.48 cm	10
3	ZrO_2 (porous)	1.91 cm	10
4	Stainless steel	0.64 cm	5

The minimum thicknesses for ZrO_2 and stainless steel oxide required to hold up molten material, in SC1131, were set to one tenth the clad and other structure thicknesses, respectively. A sensitivity study on these parameters is discussed in Section 5.1.8.

The sensitivity coefficients in SC1501 were adjusted such that all of the input canister mass and area were allocated to the "canister-b" component (that part of the canister that is adjacent to the control blade). This took into account the geometry in the DF-4 test bundle, where most of the canister surface area was adjacent to the fuel rods (see Figure 2.1.1). A sensitivity study on this parameter is discussed in Section 5.1.5.

The temperature used to model the eutectic interaction between B_4C and stainless steel was changed in SC1011 fιom 1520K to 1570K. A sensitivity study on this parameter is described in Section 5.4.2. The B_4C-stainless steel eutectic interaction temperature was an important factor for this experiment in predicting the timing of control blade failure and relocation.

The properties of zircaloy were changed to the values given by the MATPRO material properties package [9]. In particular, the melting temperature of zircaloy was changed from 2098K to 2200K. Other MELCOR assessments have shown the MATPRO value to be superior [10], [11]. A sensitivity study on these properties is discussed in Section 5.1.2.

The density of the control poison material, B_4C, was adjusted using MP package input. The density used in the MELCOR base case model was 1700.0 kg/m^3, and accounted for the 70% packing density for B_4C given in [5].

3.1.3 Heat Structures Model

The base case MELCOR model for DF-4 contained fifteen heat structures. Fourteen of these were radial boundary heat structures, one for each core axial level, required by the COR package. The last heat structure was the upper axial boundary heat structure. The radial heat structures consisted of four material layers; from the inside out, they were: porous zirconia, dense zirconia, porous zirconia, and stainless steel. The thickness of these layers and the number of nodes used to model them are given in Table 3.1.2 (all heat structure nodes are equally spaced). The materials that made up the radial heat structures in the MELCOR base case model are shown in Figure 3.1.2.

17

The porous zirconia material (ZrO_2, 77% porosity) used in the radial boundary heat structure was input to the MP package as a new material. Its density was 23% of the MELCOR-default value for ZrO_2. The specific enthalpy and specific heat tables were not changed, since these quantities are scaled by mass. The thermal conductivity for this material was represented by an empirical correlation given in [8]:

$$k_{effective} = 0.11498 + 0.795289 \cdot 10^{-4}T + 0.155981 \cdot 10^{-6}T^2 \text{ W/(m-K)}. \quad (3.1)$$

This correlation took into account the augmentation of heat transfer at high temperatures by radiation and the penetration of the porous ZrO_2 by steam. The expression in Equation (3.1) is compared to the thermal conductivity for ZrO_2 (taken from the MELCOR default material properties database and scaled by a factor of 0.23 to take into account the reduced density) in Figure 3.2.1. The increasing slope of the correlation curve with increasing temperature shows that radiation heat transfer is taken into account at higher temperatures. A sensitivity study on the thermal conductivity used for porous ZrO_2 is discussed in Section 5.5.3.

The material properties for the dense zirconia layer were the default MELCOR values for ZrO_2.

All heat structures in the DF-4 MELCOR input model used the "equiv-band", or equivalent band, radiation model, with emissivities of 0.7. A sensitivity study on the HS package radiation model option is described in Section 5.6.1, and a sensitivity study on the emissivities used for all heat structures surfaces is described in Section 5.6.2.

The inner boundaries of the radial boundary heat structures were specified to communicate with fluid temperatures calculated by the COR package rather than bulk control volume temperatures[1]. This capability was added as a result of this project (see Section 7 for a complete description of the Defect Investigation Reports (DIRs) resulting from this project).

The boundary conditions used on either side of the fifteen heat structures are discussed in Section 3.2.

3.2 Test Bundle Initial and Boundary Conditions

Although the DF-4 experiment had a duration of over 8000 seconds, the first 6000 seconds were used to calibrate instrumentation and establish bundle initial conditions. Therefore the MELCOR analyses had a starting time of 6000 seconds, with the initial conditions specified to match bundle conditions at that time. Also, the test bundle was a small part of the overall DF-4 experiment, which included hydrogen recombiners, a steam condenser, and other equipment. Since the test bundle was of primary interest, the operation of the other experimental components was specified in

---

[1]Fluid temperatures calculated by the COR package dT/dz model have a finer resolution than control volume bulk temperatures, which apply over many core cells

18

Table 3.2.1. Initial conditions for the MELCOR base case input model for the DF-4 experiment.

Property	Value
Initial Core Component Temperatures	480K
Channel & Bypass Volume Temperatures	480K
Channel & Bypass Volume Pressures	0.716 MPa

the base case model using boundary conditions such as wall temperatures and steam inlet conditions.

The initial temperatures and pressures for the base case input model are listed in Table 3.2.1. The initial temperatures of the core radial boundary heat structures were determined by MELCOR using a steady state initialization option and an outer surface temperature of 473K. These conditions were approximations of the actual experimental conditions at 6000 seconds (actual conditions are found in [5]). The greatest approximation was in initial core component temperatures. A constant temperature of 480K was assumed for core components at time 6000 seconds, while Figures 4.1.1– 4.1.8 show that the actual temperatures were between 460–510K. A sensitivity study on these temperatures is described in Section 5.1.3.

The ACRR power history during the DF-4 experiment is shown in Figure 2.2.1. The fission power experienced by the DF-4 test bundle was not measured in the experiment directly, but was inferred using a power coupling relationship derived in [5]. The spatially-dependent power coupling factor was represented by a chopped sinusoidal relation [5]

$$f(x) = 1.3 + 0.4 sin[\pi(\frac{x}{\lambda}) - 0.2] \text{ W/(gm MW)},$$ (3.2)

where λ is the length of the active fuel zone (50.5 cm) and x is the distance from the bottom of the active fuel, in centimeters. Equation (3.2) was integrated over the axial extent of each cell and multiplied by the cell fuel mass to get the axial peaking factors and the overall bundle power used in the base case model. These normalized peaking factors are compared with Equation (3.2) and the experimental data in Figure 3.2.2. The core axial level peaking factors used in the MELCOR analyses are also given in Table 3.2.2, along with cell elevations. A sensitivity study on total bundle power is discussed in Section 5.5.5.

The inlet steam temperature was set in the MELCOR base case input model using a time-specified inlet volume. The inlet steam temperature used in MELCOR corresponded to the measured inlet steam temperature in Figure 3.2.3. A sensitivity study on the inlet steam temperature is discussed in Section 5.5.2. The mass flow rate of steam into the test bundle is shown in Figure 2.2.2. This data was used to calculate time-specified velocities in flow paths FL101 and FL102, such that 80% of the flow went through FL101 and 20% went through FL102. A sensitivity study on the inlet steam flow rate is discussed in Section 5.5.1.

19

Table 3.2.2. Starting elevations and power peaking factors for core cells in the MELCOR DF-4 base case input model. Axial levels in the active fuel regions are 5.6 cm in height.

Cell	Starting elevation (cm)	Peaking Factor	Cell	Starting elevation (cm)	Peaking Factor
101	-10.8	0.00	108	22.4	1.09
102	-7.6	0.00	109	28.1	1.09
103	-7.5	0.00	110	33.7	1.06
104	0.0	0.83	111	39.3	1.01
105	5.6	0.92	112	44.9	0.93
106	11.2	1.00	113	50.5	0.00
107	16.8	1.06	114	55.7	0.00

During the initial phases of the DF-4 experiment, the stainless steel pressure boundary was heated to a temperature sufficient to preclude steam condensation inside the test bundle. The MELCOR input model specified a constant temperature of 473K on the outside surfaces of the radial boundary heat structures. During the fuel damage phase of the experiment, these surfaces actually increased in temperature. The temperature used in MELCOR is compared to these time-dependent surface temperatures for several axial levels in Figure 3.2.4. A sensitivity study which varied the surface temperatures on these heat structures is discussed in Section 5.5.4.

The pressure in the test bundle was set to a constant value of 715.7 kPa, or about 104 psi, using a time-specified outlet volume.
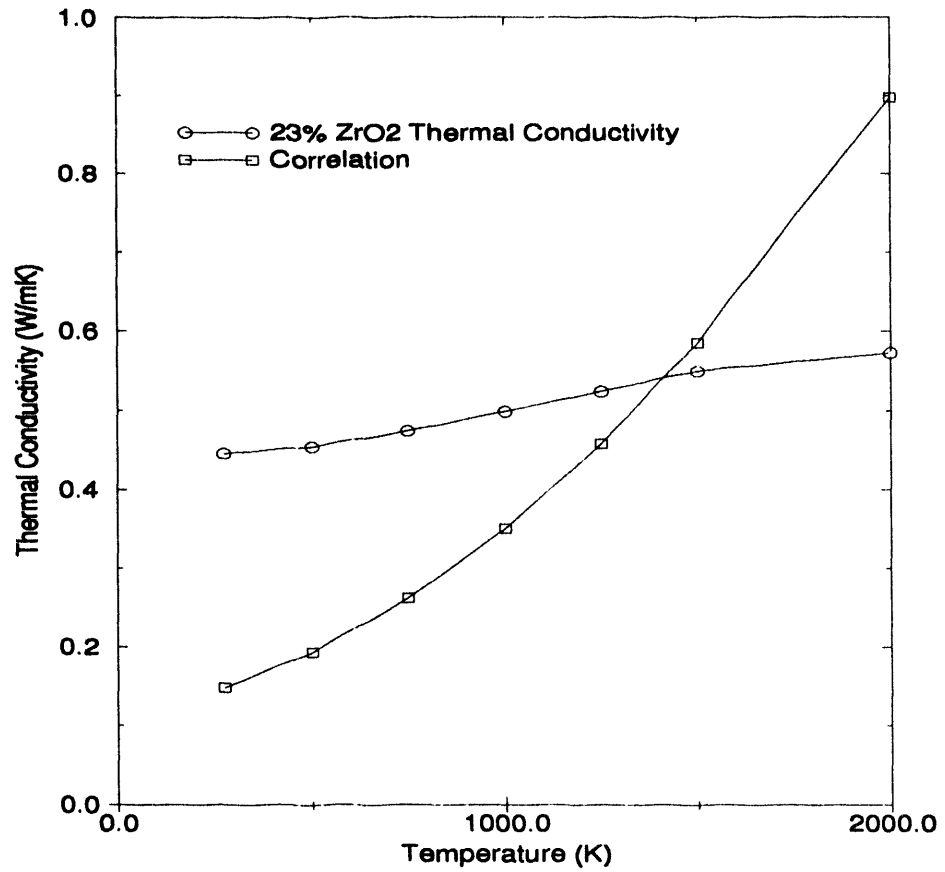
Figure 3.2.1. Empirical thermal conductivity correlation for porous ZrO_2 (from [8]) compared to 23% of MELCOR thermal conductivity for this material.
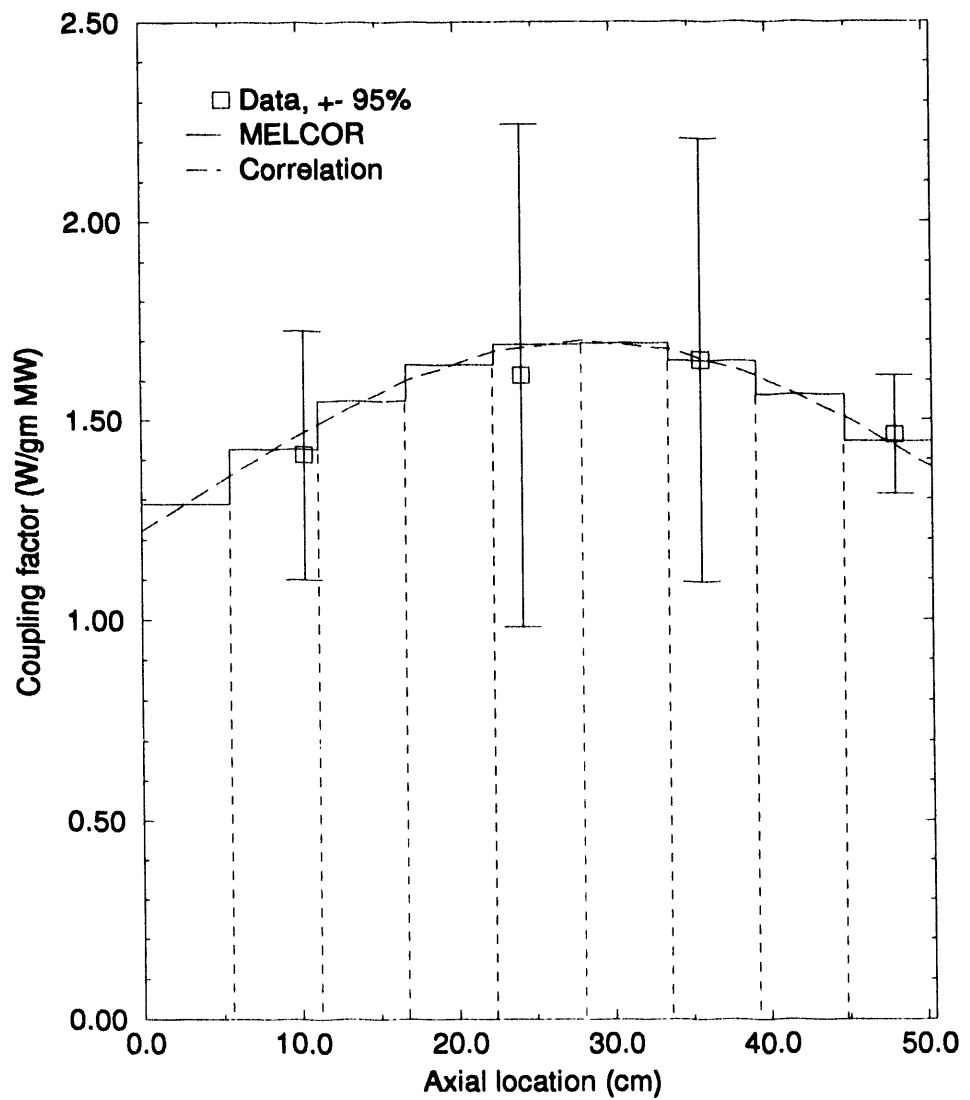
Figure 3.2.2. Cell fission power coupling factors used in MELCOR, compared to data and the correlation derived from those data. Error bars on data values show the 95% confidence limits.
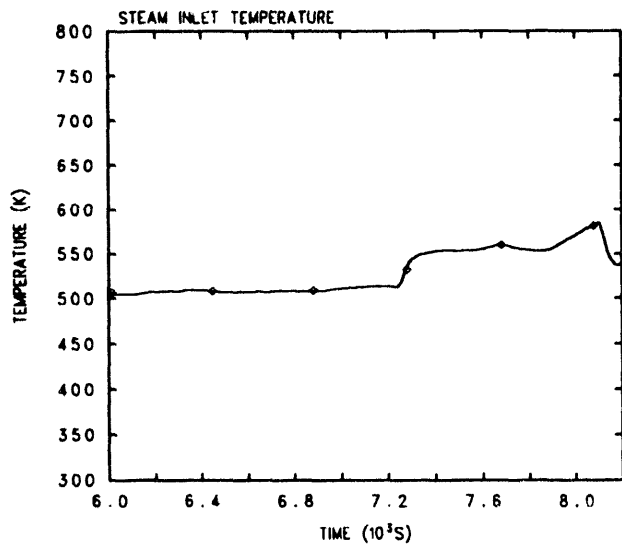
Figure 3.2.3. Steam inlet temperature used in MELCOR.
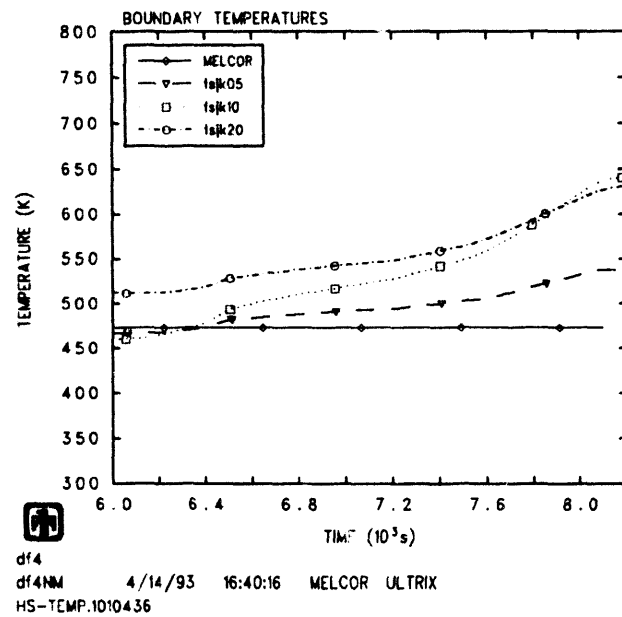
Figure 3.2.4. Constant heat structure outside surface temperature used in MELCOR compared to measured temperatures at several axial levels. TSJK05 is at the top of the bundle and TSJK20 is at the bottom.

23

Chapter 4

MELCOR Base Case Calculation Results

The results of the MELCOR base case calculation are discussed in this chapter. Note that the base case input model did not use all default MELCOR input options and sensitivity coefficients, but rather used those that either resulted in better agreement with experimental data or that reflected the state of knowledge about either experimental conditions or model accuracy. The base case model was the result of many MELCOR sensitivity studies, some of which are described in the next chapter.

The component temperature results are discussed first, since these quantities were measured directly by the experiment instrumentation. Failure and relocation phenomena are then discussed, and the final core state is analyzed and compared with PIE (Post Irradiation Examination) data. The hydrogen generation behavior in DF-4 is discus― 1 last.

Temperature and relocation phenomena are discussed starting at the top of the test bundle and progressing downward, since this was the direction of fuel damage progression in the DF-4 experiment. The control blade behavior is discussed first, because that was the component that began melting first.

4.1 Temperature Response

4.1.1 Control Blade

The control blade was instrumented with one Pt/Rh thermocouple at the 49.5 cm plane, and two Pt/Rh thermocouples at each of the 36.8, 25.4 and 9.6 cm planes (see Figure 2.1.3).

49.5 cm Plane

The control blade temperature response calculated by MELCOR is compared to the measured temperature at the 49.5 cm plane in Figure 4.1.1. The general agreement with experimental data was good until about 6900 seconds, when the calculated temperature increased to about 200K more than the experimental value.

24

The temperature remained high until melting and failure of the control blade at this level.

The control blade reached the eutectic temperature of the B_4C-stainless steel mixture at about 7470 seconds. The materials interactions model in MELCOR held the mixture at a constant temperature while the liquifaction of B_4C and stainless steel took place.[1] After all the B_4C was dissolved, the control blade temperature rose to the stainless steel melting temperature of 1700K, and the blade was held at this temperature while the stainless steel melted. The control blade at this level was completely consumed after all its stainless steel had melted, at about 7600 seconds. After this point, MELCOR set the temperature of this component to zero.

Other codes modeling the DF-4 experiment also over-predicted temperatures in the upper-most axial level (see Chapter 6). This effect was also observed in the cladding temperature response predicted by MELCOR and other codes (see Figure 4.1.5 and Chapter 6). This would suggest that the power coupling relationship in Equation 3.2 was inaccurate at the upper-most axial level.

36.8 cm Plane

The control blade temperature response at the 36.8 cm plane calculated by MELCOR is compared to the measured temperature in Figure 4.1.2. The temperature response for this plane was similar to the response at the 49.5 cm plane. The control blade temperature at the 36.8 cm plane rose to the B_4C-stainless steel eutectic reaction temperature, where it leveled off while the B_4C was consumed by the eutectic reaction. After the depletion of the B_4C, the temperature rose to the stainless steel melting temperature of 1700K, where it remained while the steel melted. The control blade was calculated to fail shortly thereafter.

The calculated temperature response at this plane was close to the measured temperature response, with the largest difference occurring between 6400 and 7000 seconds. This difference could possibly be attributed to the fact that the MELCOR temperature for the control blade was a bulk temperature, while that measured by the thermocouple was a surface temperature. The calculated temperature differed from the measured temperature by approximately 100K between 6500 and 6900 seconds. In other phases, calculated temperatures were within 10K of the measured results.

25.4 cm Plane

The control blade temperature response calculated by MELCOR is compared to the measured temperature at the 25.4 cm plane in Figure 4.1.3. This plot is similar to that for the 36.8 cm plane until approximately 7400 seconds. The arrival of molten material from higher axial levels is indicated by the sudden increase in temperature, from 1350K to 1500K, at 7480 seconds. More melt arrived shortly thereafter, bringing the control blade to the eutectic interaction temperature at 7560 seconds. The timing of the overall melt arrival agreed well with experimental data.

---

[1]Note that in the base case input model, the eutectic reaction temperature was set to 1570K, which was 50K larger than the default value (see Sections 3.1.2 and 5.4.2).

OTHER STRUC TEMPS, 49.5 CM
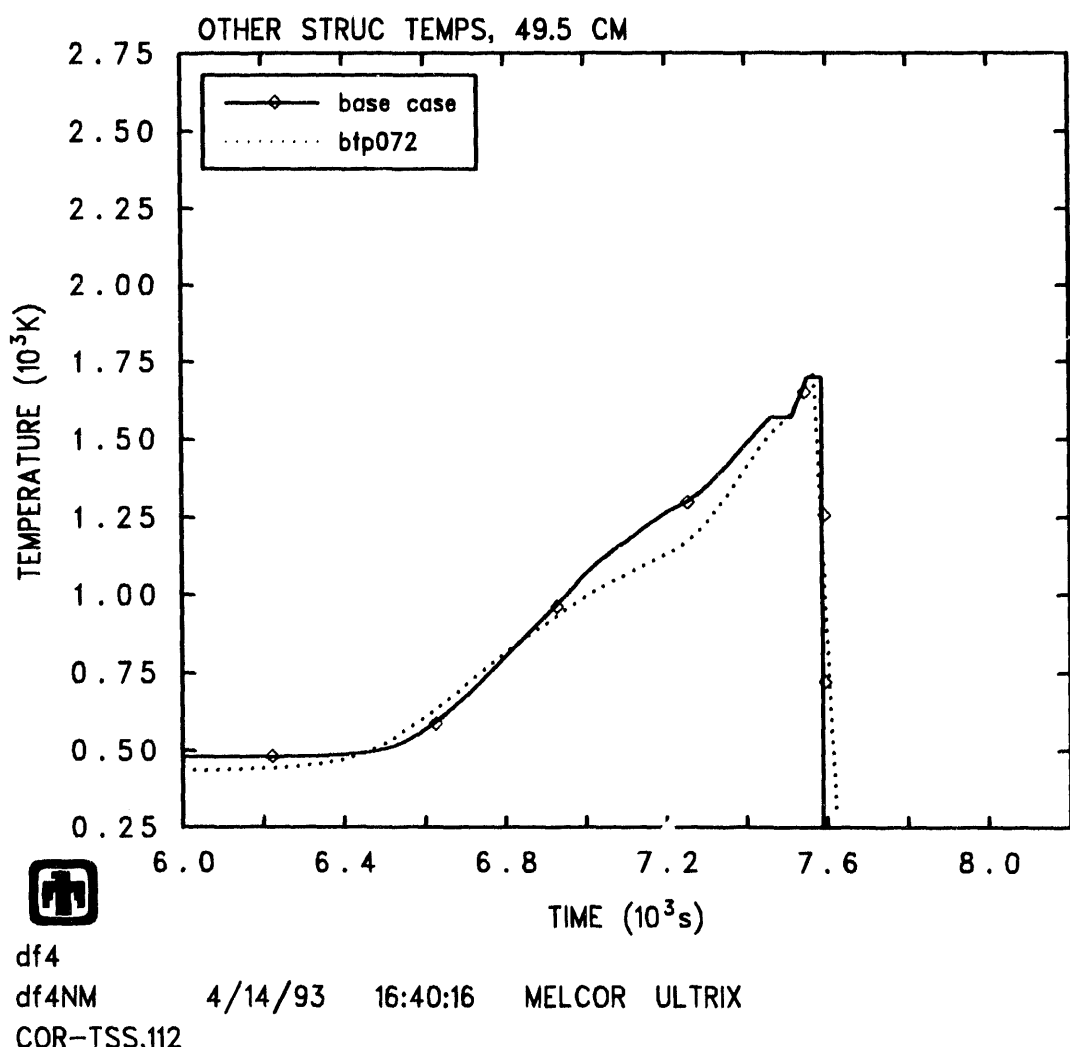
Figure 4.1.1. Measured vs. calculated control blade temperatures at the 49.5 cm level.
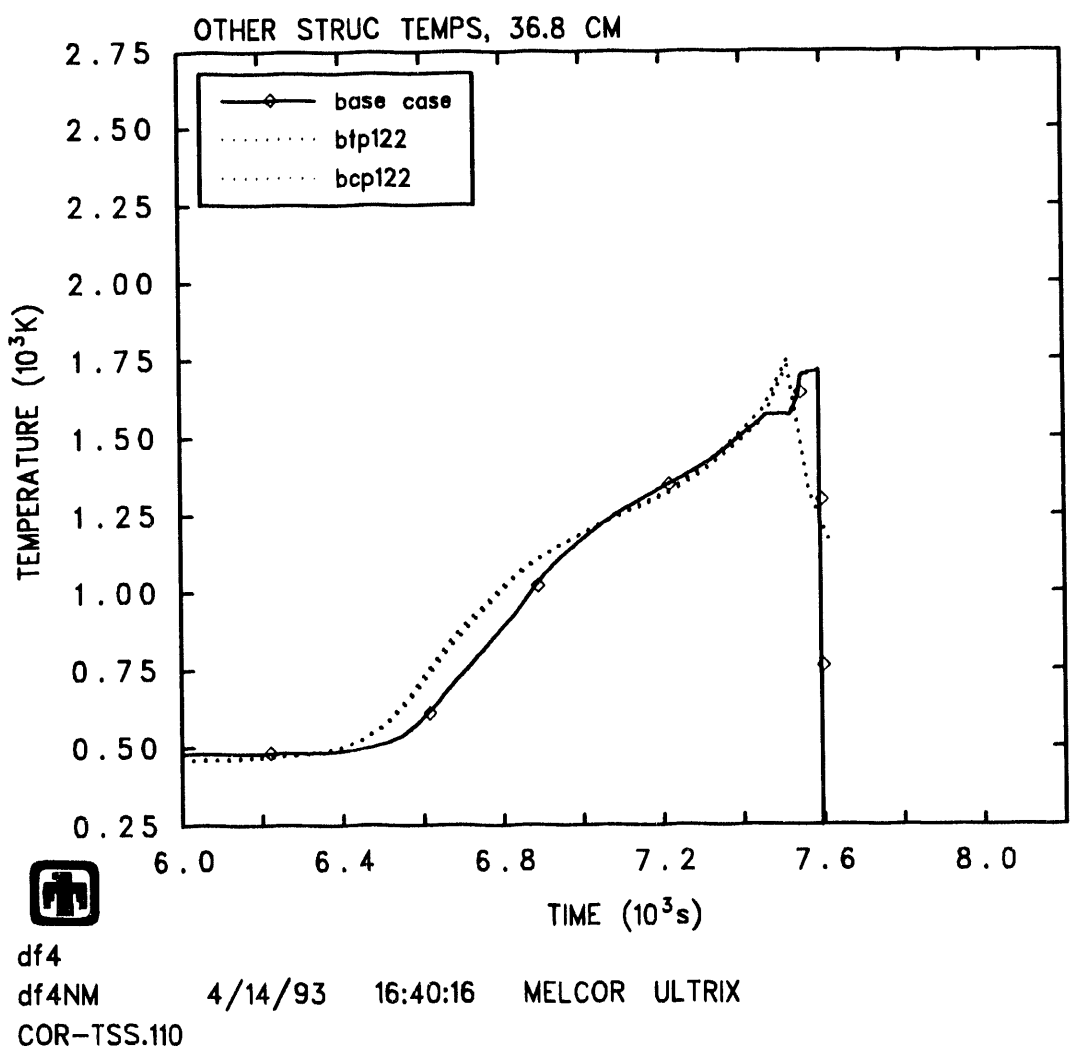
Figure 4.1.2. Measured vs. calculated control blade temperatures at the 36.8 cm level.

The eutectic interaction at this level took place much quicker than it did at the 36.8 cm plane because of the arrival of more relocating melt from higher axial levels. The blade reached the stainless steel melting temperature of 1700K at approximately 7650 seconds, and failed shortly afterwards. Although the experimental data showed increasing temperatures beyond the MELCOR-calculated failure time, these data were not reliable because the substrate material for the thermocouple at this location had already melted (as indicated by temperatures in excess of the stainless steel melting temperature). The fact that the MELCOR-calculated temperature of this component arrived at the stainless steel melting temperature at the same time as the measured temperature shows that the failure timing at this level was predicted accurately.

9.6 cm Plane

The control blade temperature response calculated by MELCOR is compared to the measured temperature at the 9.6 cm plane in Figure 4.1.4. This shows that the temperature at the 9.6 cm plane was under-predicted by approximately 100K before the arrival of melt material at 7000 seconds. The first arrival of molten material was approximately 100 seconds later than measured in the experiment. However, the calculated temperature rose more rapidly to the eutectic interaction temperature, whereas the measured temperature rose to this point in more continuous increments. The calculated versus measured failure times for the control blade at this level (i.e. the time at which the control blade reached the stainless steel melting point) differed by less than 50 seconds. Thus, although the temperature response was different due to discrete relocation events, the overall failure timing was predicted well at this level.

4.1.2 Cladding

The cladding was instrumented with one Pt/Rh thermocouple at the 49.5 cm plane, and two Pt/Rh thermocouples at each of the 36.8, 25.4 and 9.6 cm planes (see Figure 2.1.3). In addition, single W/Re thermocouples were used at each axial level to instrument the cladding.

The cladding temperatures measured by W/Re thermocouples are shown with the Pt/Rh data in Figures 4.1.5— 4.1.8. These figures show that the temperatures registered by these thermocouples were approximately 300K below the temperatures registered by the type P thermocouples, until the latter thermocouples failed at elevated temperatures. This temperature lag was due to the poor conductivity of the ZrO_2 sheath that protected the W/Re thermocouples from molten materials. Figures 4.1.5— 4.1.8 also show that the W/Re thermocouples lagged the Pt/Rh thermocouples in time by approximately 25 seconds.

49.5 cm Plane

The cladding temperature response calculated by MELCOR is compared to the measured temperature at the 49.5 cm plane in Figure 4.1.5. The general shape of the

OTHER STRUC TEMPS, 25.4 CM

Legend:
- base case
- btp167
- bcp167

Y-axis: TEMPERATURE (10^3K) — 0.25, 0.50, 0.75, 1.00, 1.25, 1.50, 1.75, 2.00, 2.25, 2.50, 2.75

X-axis: TIME (10^3s) — 6.0, 6.4, 6.8, 7.2, 7.6, 8.0

df4
df4NM   4/14/93   16:40:16   MELCOR   ULTRIX
COR-TSS.108
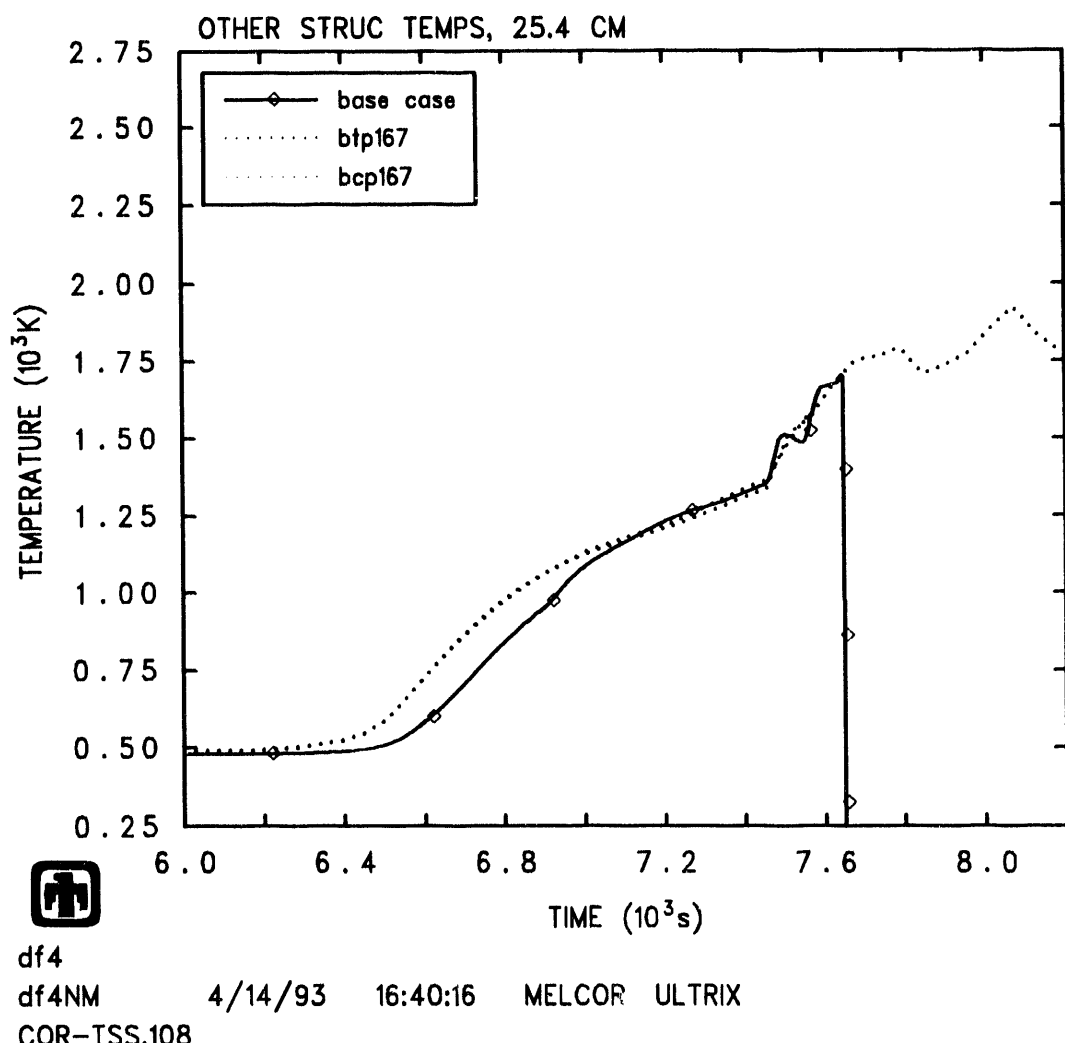
Figure 4.1.3. Measured vs. calculated control blade temperatures at the 25.4 cm level.
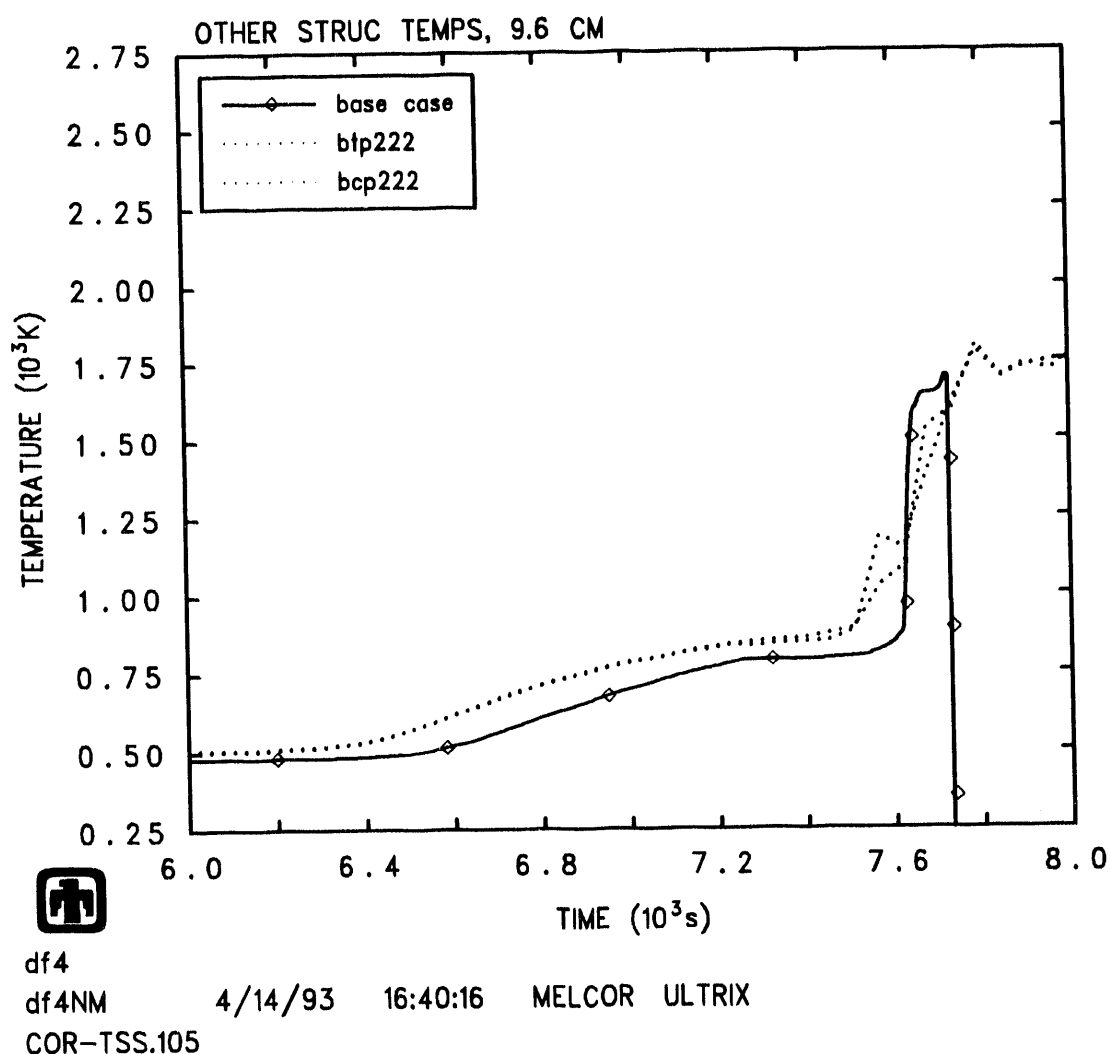
Figure 4.1.4. Measured vs. calculated control blade temperatures at the 9.6 cm level.

temperature response was correct; however the MELCOR results show consistently higher temperatures at this plane starting at 6500 seconds. The calculated temperatures diverged from data by about 250K by 7200 seconds, then drew closer until the beginning of rapid oxidation at 7550 seconds. A similar effect was observed in the control blade temperature response, and could be attributed to the inaccuracy of the power coupling factor used to calculate bundle peaking factors (this conclusion is reinforced by the results of other codes' DF-4 analyses, which showed the same behavior - see Section 6.1 and Figure 6.1.5). Rapid oxidation at this level began when the clad temperature reached a temperature of 1750K. This occurred at the 49.5 cm plane at 7550 seconds. The clad at this level quickly reached the zircaloy melting temperature, and was completely molten or oxidized by 7625 seconds.

36.8 cm Plane

The cladding temperature response calculated by MELCOR is compared to the measured temperature at the 36.8 cm plane in Figure 4.1.6. The temperature response at this level closely matched the measured temperature response for all but the final period of oxidation. At this point, the temperatures diverged by approximately 50K. Autocatalytic oxidation was calculated to begin at the measured time of rapid oxidation. The clad at this level remained at a temperature close to the zircaloy melting temperature until about 7650 seconds, at which time the cladding component failed.

25.4 cm Plane

The cladding temperature response calculated by MELCOR is compared to the measured temperature at the 25.4 cm plane in Figure 4.1.7. The temperature response at this level matched the measured temperature response for most of the time, diverging by approximately 100K just before the start of rapid oxidation. Figure 4.1.7 shows that the calculated start of rapid oxidation occurred at about the measured oxidation time of 7610 seconds. The clad at this level remained close to the melting temperature of zircaloy until failure at 7700 seconds.

9.6 cm Plane

The cladding temperature response calculated by MELCOR is compared to the measured temperature at the 9.6 cm plane in Figure 4.1.8. The calculated temperature at this plane was approximately 50K lower than that measured. This was consistent with the temperature results for the control blade, which were also lower than measured (see Figure 4.1.4). The arrival of debris at this level is indicated by the sudden increases in temperature after 7600 seconds, which was very close to the measured debris arrival time. This was consistent with the results for the canister (see Figure 4.1.10).
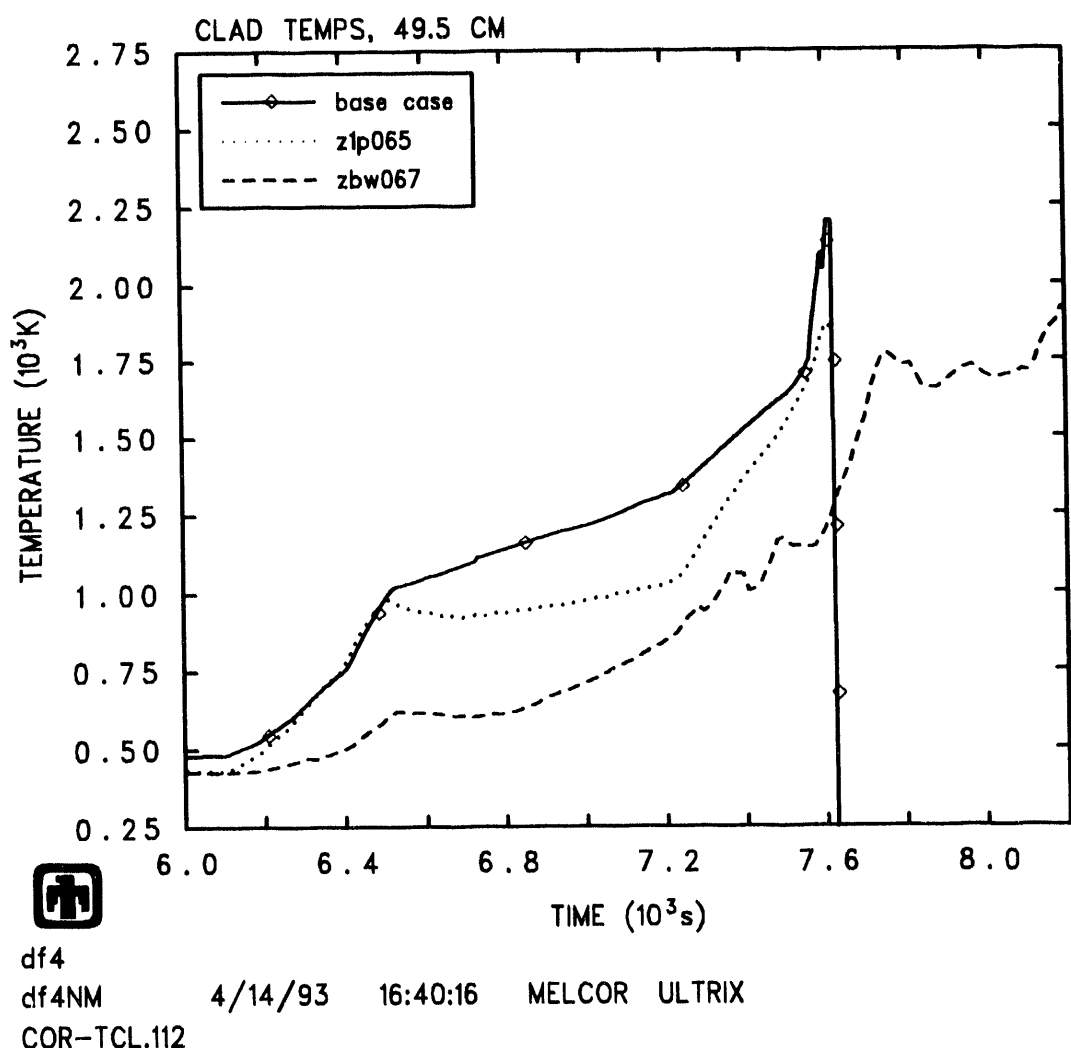
Figure 4.1.5. Measured vs. calculated fuel rod cladding temperatures at the 49.5 cm level.

CLAD TEMPS, 36.8 CM

Legend:
- base case
- z1p115
- z4p115
- zcw117

x-axis: TIME (10³s)
y-axis: TEMPERATURE (10³K)

df4
df4NM   4/14/93   16:40:16   MELCOR   ULTRIX
COR-TCL.110
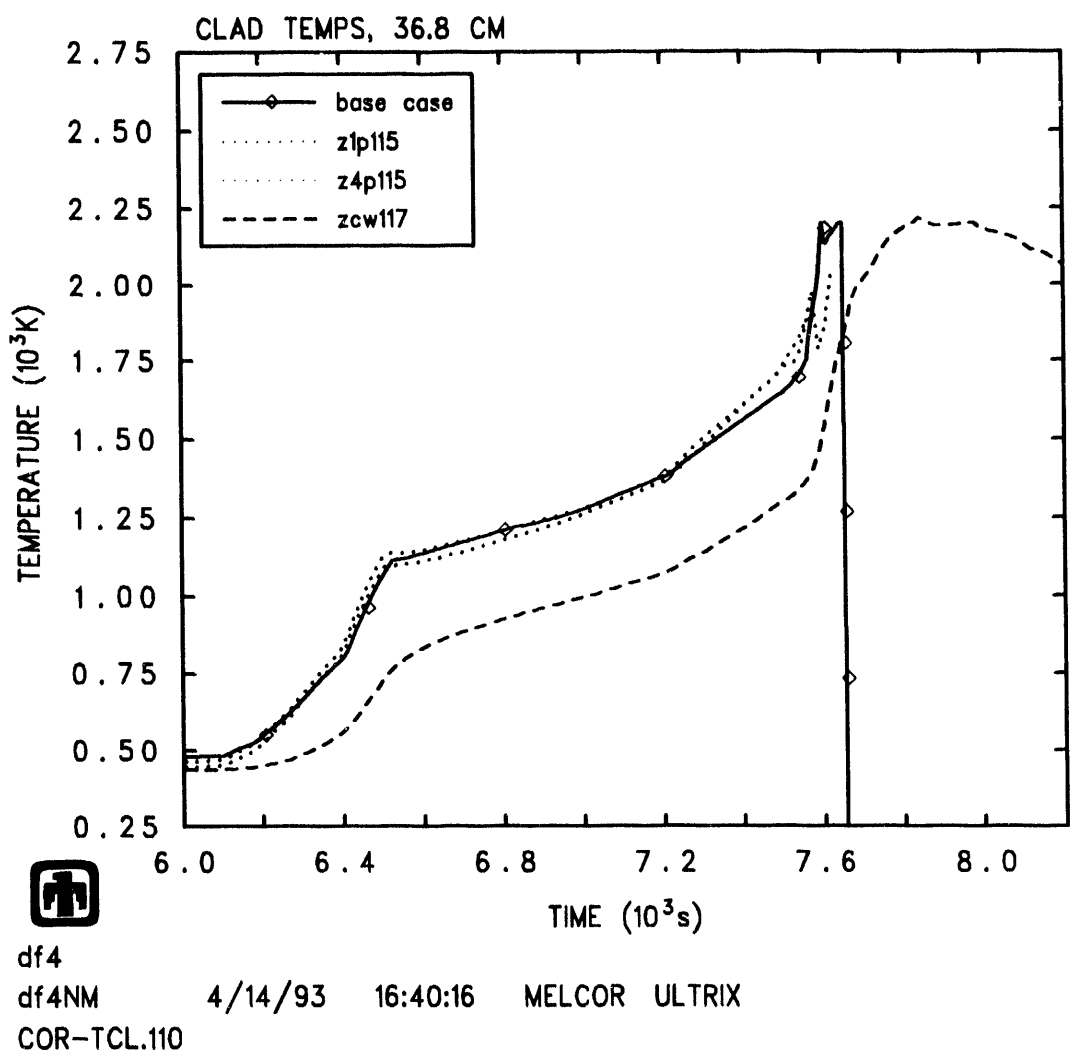
Figure 4.1.6. Measured vs. calculated fuel rod cladding temperatures at the 36.8 cm level.

CLAD TEMPS, 25.4 CM

Legend:
- base case
- z2p160
- z3p160
- zbw162

TEMPERATURE (10^3K)

TIME (10^3s)

df4
df4NM   4/14/93   16:40:16   MELCOR   ULTRIX
COR-TCL.108
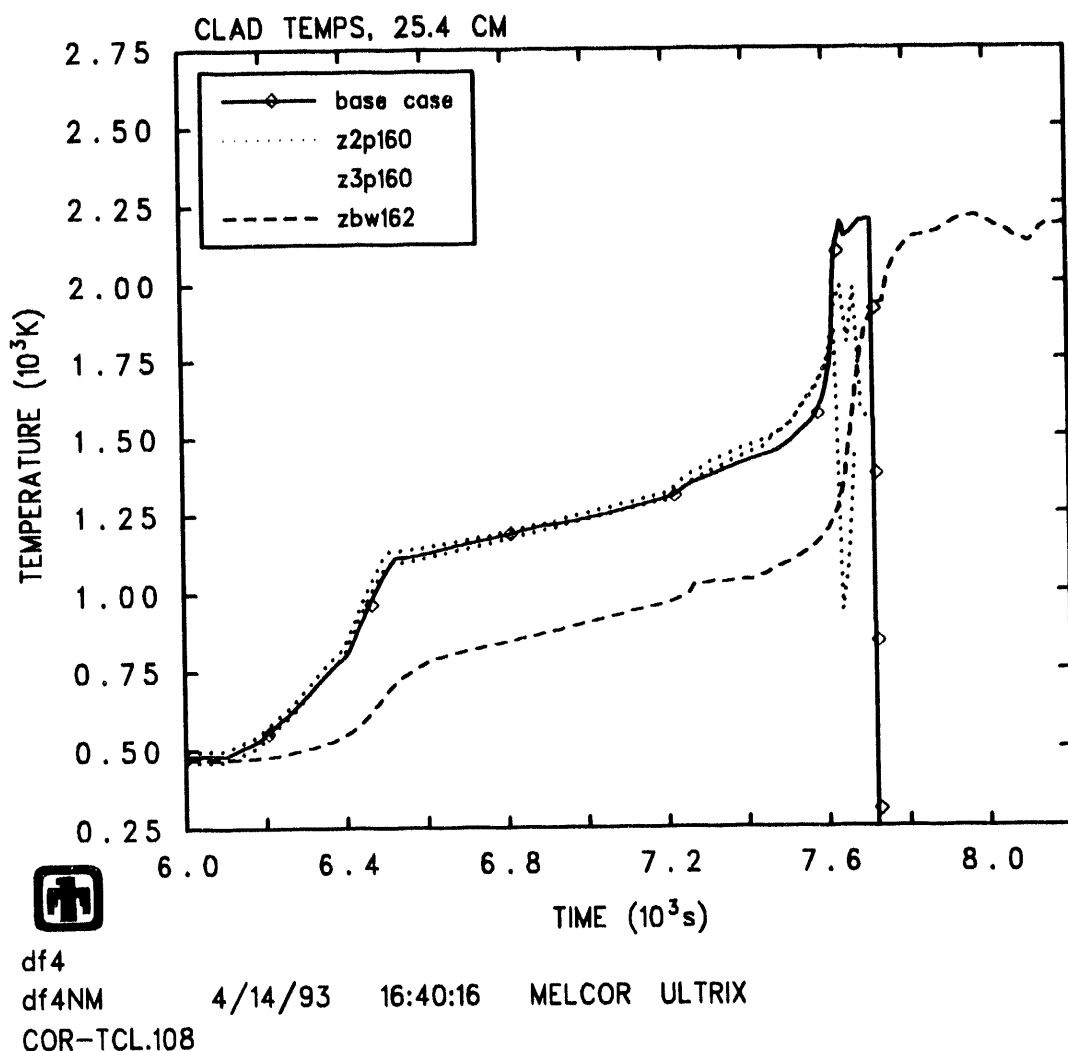
Figure 4.1.7. Measured vs. calculated fuel rod cladding temperatures at the 25.4 cm level.

CLAD TEMPS, 9.6 CM

Legend:
- base case
- z1p215
- z4p215
- zcw217

Y-axis: TEMPERATURE (10^3K)
X-axis: TIME (10^3s)

df4
df4NM   4/14/93   16:40:16   MELCOR   ULTRIX
COR-TCL.105
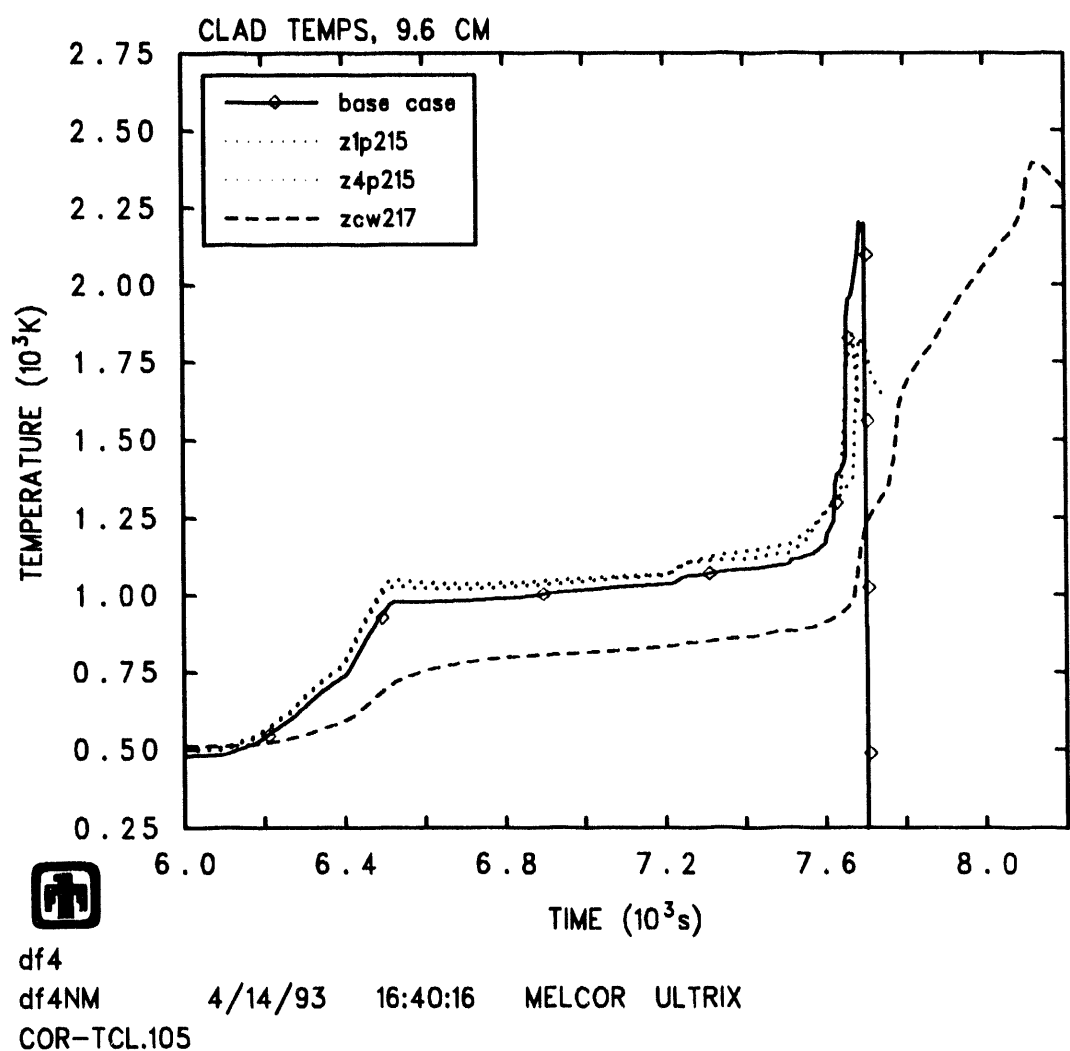
Figure 4.1.8. Measured vs. calculated fuel rod cladding temperatures at the 9.6 cm level.

4.1.3 Canister

The canister in the DF-4 experiment was instrumented with one W/Re thermocouple at the 49.5 cm and 9.6 cm planes, and two W/Re thermocouples at each of the 36.8 and 25.4 cm planes (see Figure 2.1.3). These types of thermocouples showed temperature and time lags of 300K and 25 seconds, respectively, in the canister temperatures.

49.5 and 36.8 cm Planes

The calculated temperature response of the canister-b component [2] at the 49.5 and 36.8 cm planes is shown in Figure 4.1.9. The response of the W/Re thermocouples at these planes is also shown. The calculated temperatures for the 49.5 cm plane were more than 500K greater than the measured temperatures, after applying the 300K correction for the type C thermocouples. This was the same behavior shown by the cladding and control blade temperatures at this plane. The calculated onset of rapid oxidation, indicated by a sudden increase in the heatup rate, was within the 25 second time lag correction of the measured onset of rapid oxidation shown for the 49.5 cm plane in Figure 4.1.9.

The calculated temperature behavior at the 36.8 cm plane shown in Figure 4.1.9 was close to the corrected measured temperatures, and the onset of rapid oxidation was also predicted accurately.

Both the 36.8 and 49.5 cm planes showed a decrease in temperature approximately 75 seconds after rapid oxidation began. This was due to the relocation of the fuel rod material from these levels, which removed the heating source for the canister component. The canister components at these planes then fell to the temperature of the steam flowing at those levels. The measured temperatures did not show this effect, possibly because of the temperature and time lags of these thermocouples.

25.4 and 9.6 cm Planes

The temperature response of the canister-b component in the 25.4 and 9.6 cm planes is shown in Figure 4.1.10. The response of the W/Re thermocouples at these planes is also shown. The temperature response and onset of rapid oxidation at the 25.4 cm plane corresponded to the measured canister temperature and oxidation timing at that plane, after correcting for the time and temperature lags. The calculated temperatures in the later parts of the oxidation subphase were lower than those measured. This was due to the fact that MELCOR does not allow fuel material in the particulate debris component to generate fission power (note that this is only a problem for in-pile experiments and ATWS-type accident scenarios, where core melt progression is driven by fission power rather than decay heat). Since there was still significant reactor power being applied after fuel began relocating, there was probably a significant amount of fission power generated in the fuel debris. The calculated

---

[2]Note that in the MELCOR base case input model all canister mass was allocated to the canister-b component, or that part of the canister that is adjacent to the control blade.

CANISTER TEMPS, 36.8 & 49.5 CM

df4
df4NM   4/14/93   16:40:16   MELCOR   ULTRIX
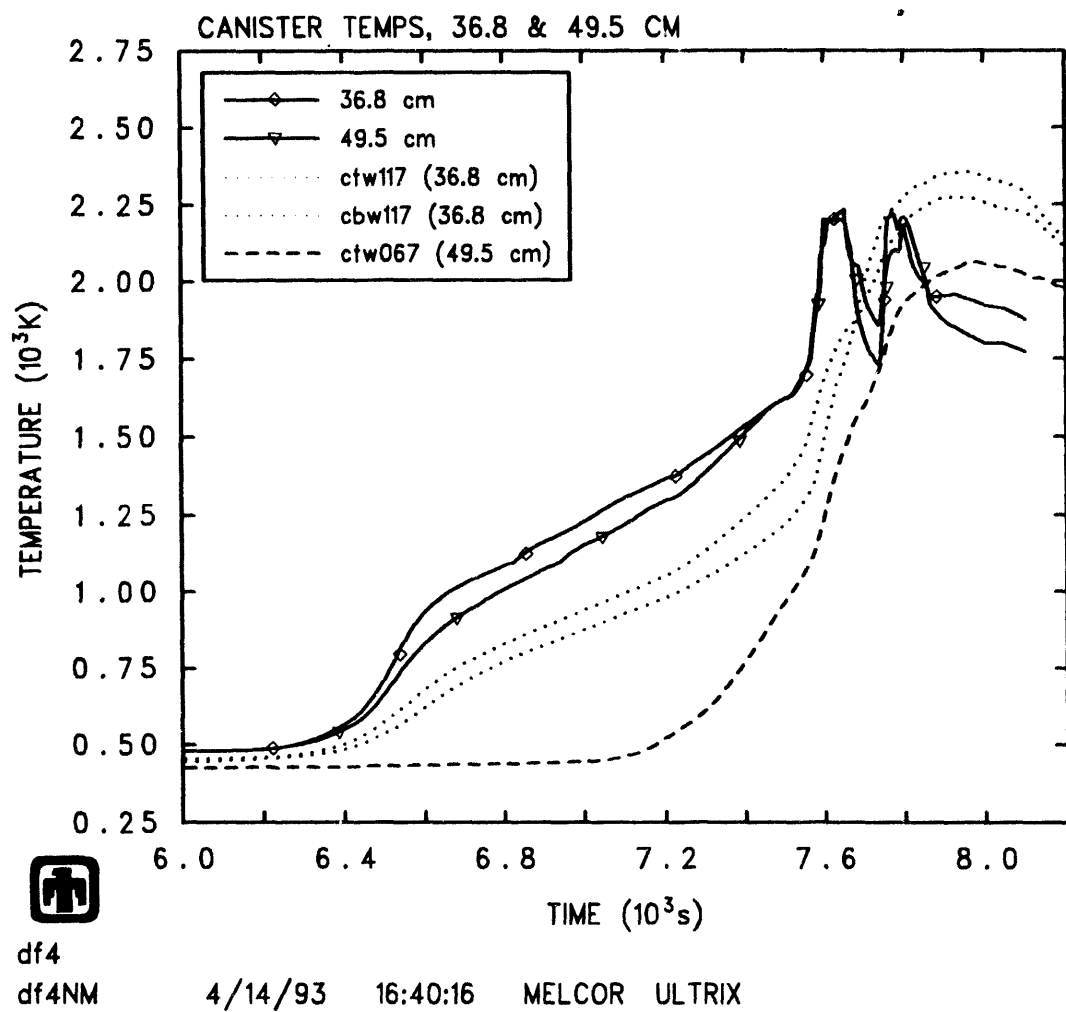
Figure 4.1.9. Measured vs. calculated canister temperatures at the 49.5 and 36.8 cm levels.

temperatures in the 25.4 cm plane did not show the decrease in temperature experienced in higher planes. The fuel material at this plane did not relocate downward, as the fuel at higher planes did.

The calculated temperature behavior at the 9.6 cm plane shows the arrival of relocating melt about 100 seconds early, the same time difference shown in the cladding and control blade temperatures in Figures 4.1.8 and 4.1.4, respectively. The temperatures at this plane in the later part of the oxidation subphase were higher than those at the 25.4 cm plane, due to the higher amounts of debris at this level.

4.1.4   Component Temperature Response Overview

The temperatures across the test bundle in the cladding and control blade components are shown in Figures 4.1.11 and 4.1.12, respectively. In the cladding component, the experimental data indicated that the upper two levels (36.8 and 49.5 cm) began oxidizing at about the same time. This is consistent with MELCOR calculations which showed that oxidation started at cell 111, which was centered at 42.5 cm. The oxidation front propagated down to the 25.4 cm plane in approximately 75 seconds, and to the 9.6 cm plane in approximately 175 seconds. The steady increase in temperature at the 25.4 cm plane indicates that oxidation began as a result of the propagation of the oxidation front down the fuel rod, while the large increase in temperature at the 9.6 cm plane was probably the result of debris relocating to that level.

In Figure 4.1.12, the thermal signature left by the melt candling down the control blade can be seen. The material in the upper two planes, at 36.8 and 49.5 cm, started melting at about the same time. Shortly afterwards, melt arrived at the 25.4 cm plane. This plane was not heated to the eutectic interaction temperature of 1570K until the stainless steel started melting at the 36.8 and 49.5 cm planes and this melt arrived at the 25.4 cm plane (shown by the second steep increase in control blade temperature). Slow candling was shown by the relatively late temperature increase at the 9.6 cm plane.

The temperatures of the fuel, cladding, canister-b and other structure components at the 36.8 cm plane are shown together in Figure 4.1.13. This figure indicates that at elevated temperatures, all components were very close in temperature. This was the result of the test bundle equilibration sub-phase of the experiment (between 6500 and 7200 seconds), where the bundle power was held constant to allow all components to equilibrate in temperature. Rapid oxidation began in the cladding component, but quickly propagated to the canister-b component. The other structure component also showed a temperature rise at about the same time, which brought the blade to the stainless steel melting temperature, resulting in total melting and failure of the control blade. Note that the eutectic interaction in the control blade started before oxidation, as indicated by the flat spot in the control blade temperatures in Figure 4.1.13 before the steep increase in cladding and canister temperatures.

Component temperatures at the 25.4 cm plane, shown in Figure 4.1.14, behaved in a similar manner as those at 36.8 cm. The one exception is the increase in other structure temperature caused by the candling of molten eutectic down the control

38

CANISTER TEMPS, 9.6 & 25.4 CM

Legend:
- 9.6 cm
- 25.4 cm
- ctw217 (9.6 cm)
- ctw162 (25.4 cm)
- cbw162 (25.4 cm)

TEMPERATURE (10^3K)

TIME (10^3s)

df4
df4NM   4/14/93   16:40:16   MELCOR   ULTRIX
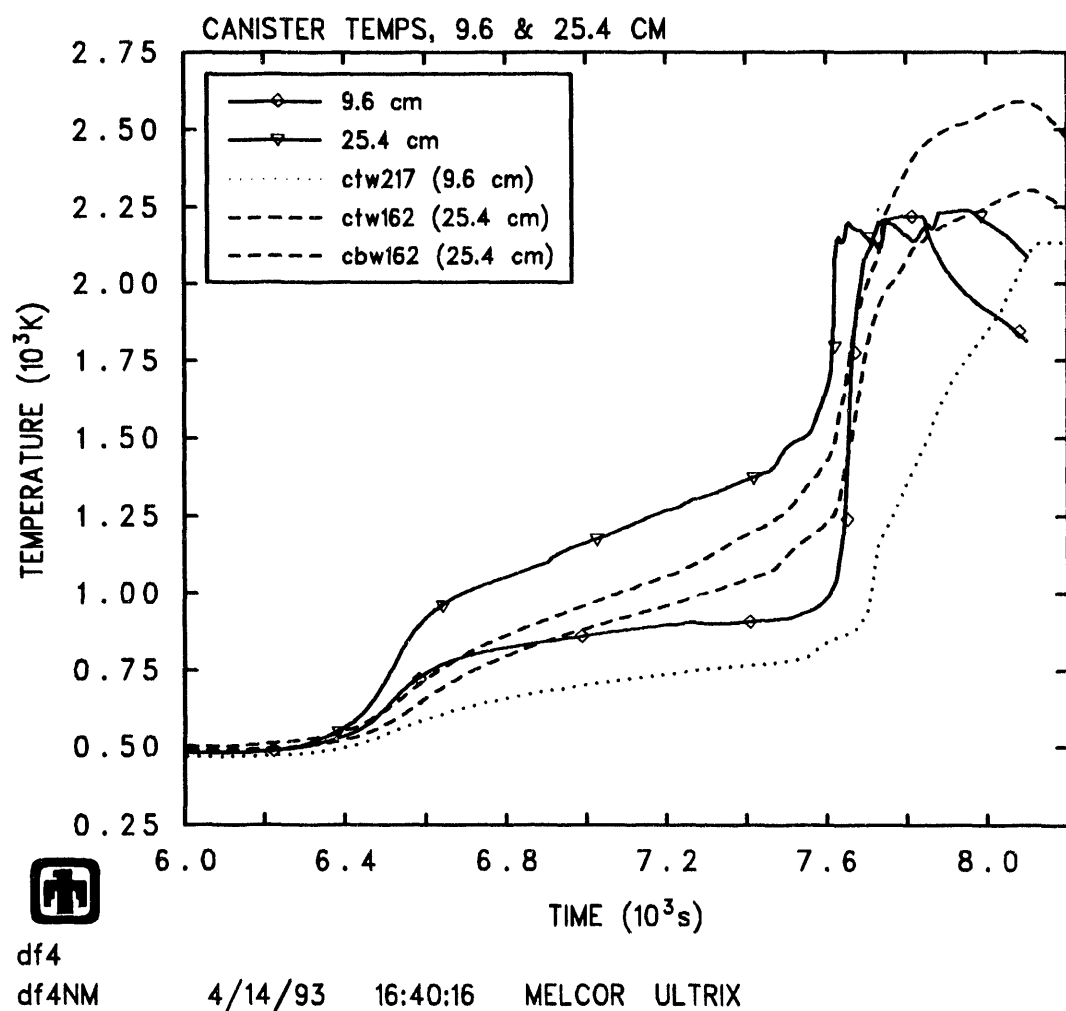
Figure 4.1.10. Measured vs. calculated canister temperatures at the 25.4 and 9.6 cm levels.

blade. This caused the control blade temperature to exceed the cladding and canister temperature by a small amount, until the arrival of the oxidation front.

4.2 Melting and Relocation

The discussion of the temperature response in the last section gives some indication of the melting and relocation of bundle materials. In this section a more detailed discussion of melting and relocation is given. The initial state of the fuel bundle is given first, in the format that is used to discuss core degradation and relocation. The damage progression is then discussed, starting at the beginning of the oxidation at 7500 seconds and proceeding to the later stages of bundle damage.

4.2.1 Initial State

The initial material distribution in the test bundle is shown in Figure 4.2.1. Shown are volume fraction plots, where the shaded areas represent the fraction of total volume in each core cell occupied by the designated components and materials at each level. Each major component is represented in a different frame, with the fuel and cladding components on the upper left of the figure, the particulate debris on the upper right, the canister-b component on the lower left, and the other structure component on the lower right. Each plot shows the locations of intact and conglomerate debris materials for the designated component, with the shading used for each material shown at the right of the figure.

The UO$_2$ in the uppermost and lower-most axial cells in Figure 4.2.1 represents spacer material (the actual material used in the spacers was Al$_2$O$_3$), and was not allocated fission power in the base case MELCOR model. Note that the core plate was represented by stainless steel in the other structure component, and that there were no core components in the lower plenum cell. In the following subsections, levels are referred to by their *starting* elevations. For reference, the starting elevations of all axial levels are given in Table 3.2.2. Each axial level in the active fuel region was 5.6 cm in height.

4.2.2 Early Oxidation Subphase (7450–7625 seconds)

The start of significant test bundle damage in the DF-4 experiment was at approximately 7450 seconds. The core material states between 7450 and 7625 seconds, in 50 second increments, are shown in Figures 4.2.2— 4.2.6.

At 7450 seconds, Figure 4.2.2 shows the early stages of cladding and canister oxidation between 25 and 50 cm. At 7500 seconds, B$_4$C (CRP in Figure 4.2.3) had started relocating from axial level 11 (39.3 cm elevation). Note that the measured temperatures at the 36.8 and 49.5 cm planes in Figures 4.1.1 and 4.1.2 were below the melting point of stainless steel (1700K) at 7500 seconds. This shows the beginning of the eutectic interaction between the B$_4$C and stainless steel. The eutectic interaction products became molten and candled down approximately 10 cm, to axial levels 8 and

40
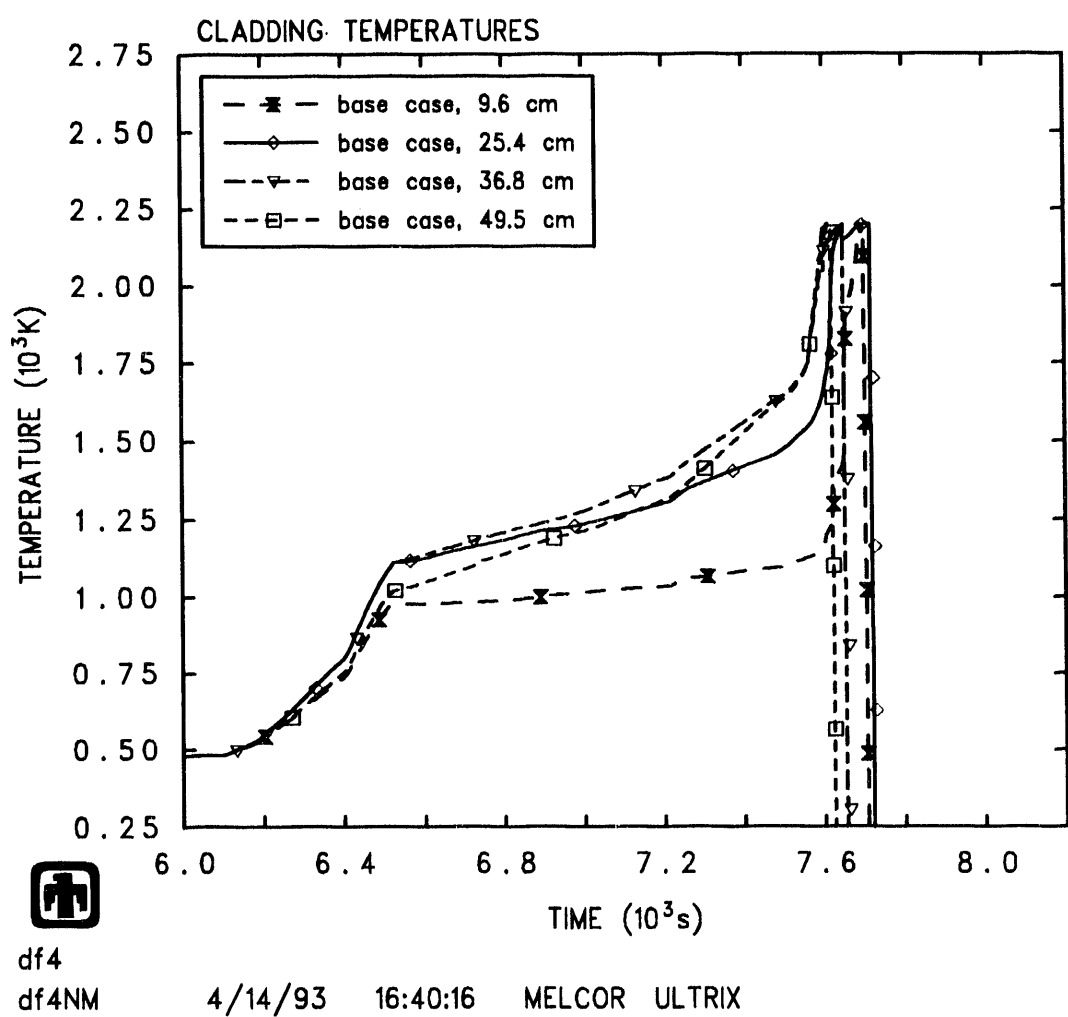
Figure 4.1.11. Cladding temperatures at the four measured axial planes, for the base case input model.

41

OTHER STRUCTURE TEMPERATURES

Legend:
- — ✱ — base case, 9.6 cm
- ——◇—— base case, 25.4 cm
- — ▽ — base case, 36.8 cm
- — ▣ — base case, 49.5 cm

TEMPERATURE (10^3K)

TIME (10^3s)

df4
df4NM   4/14/93   16:40:16   MELCOR   ULTRIX
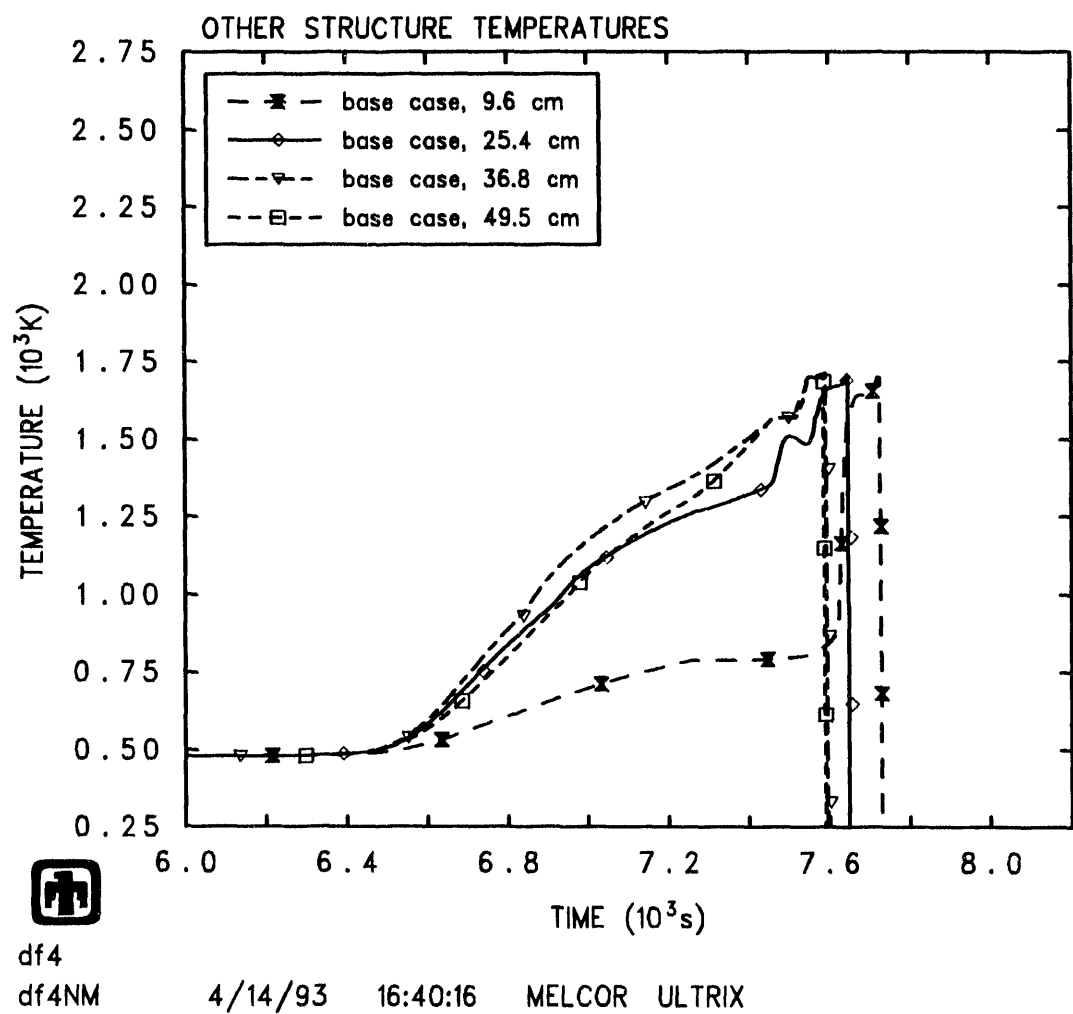
Figure 4.1.12. Control blade temperatures at the four measured axial planes, for the base case input model.

COMPONENT TEMPERATURES, 36.8 CM PLANE
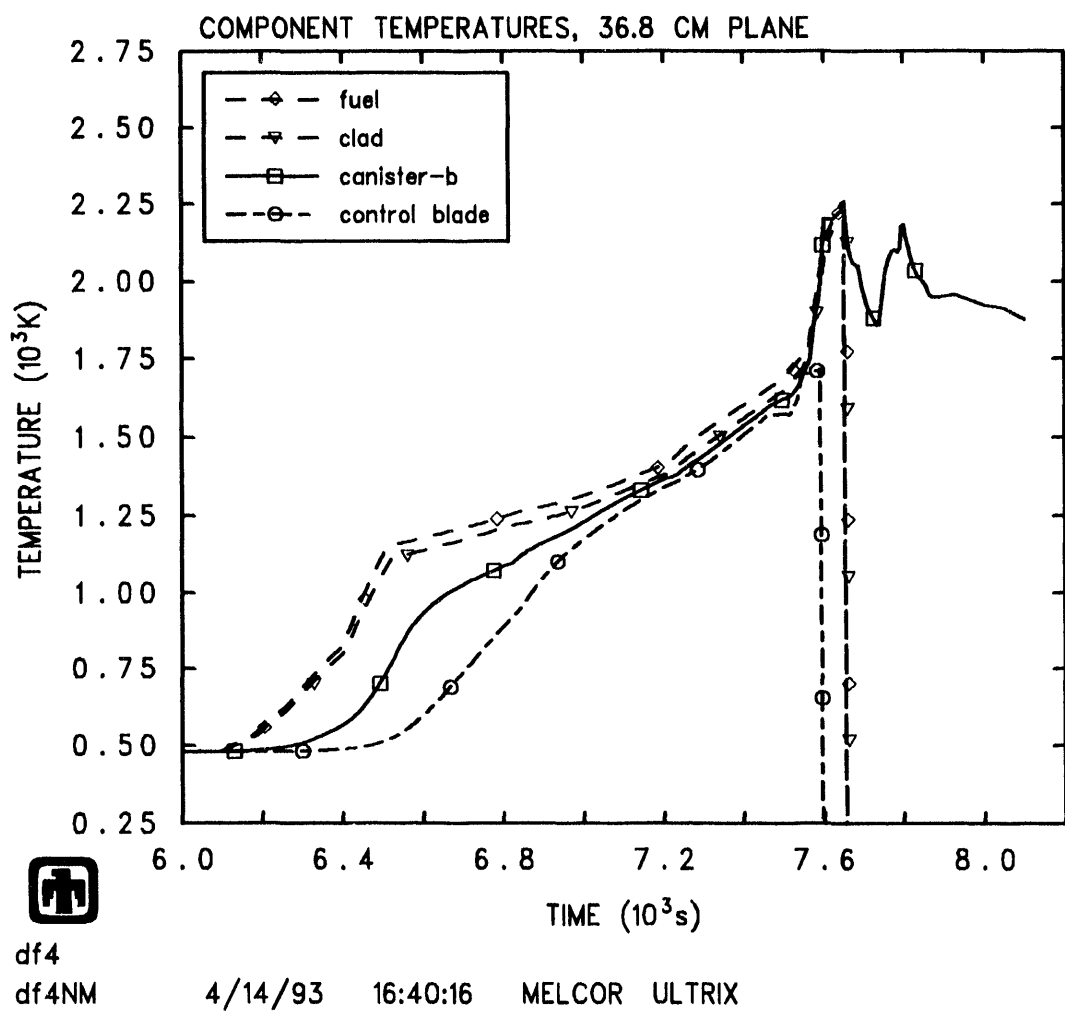
Figure 4.1.13. Component temperatures for the fuel, cladding, canister-b and other structure (control blade) components, at the 36.8 cm plane, for the base case input model.
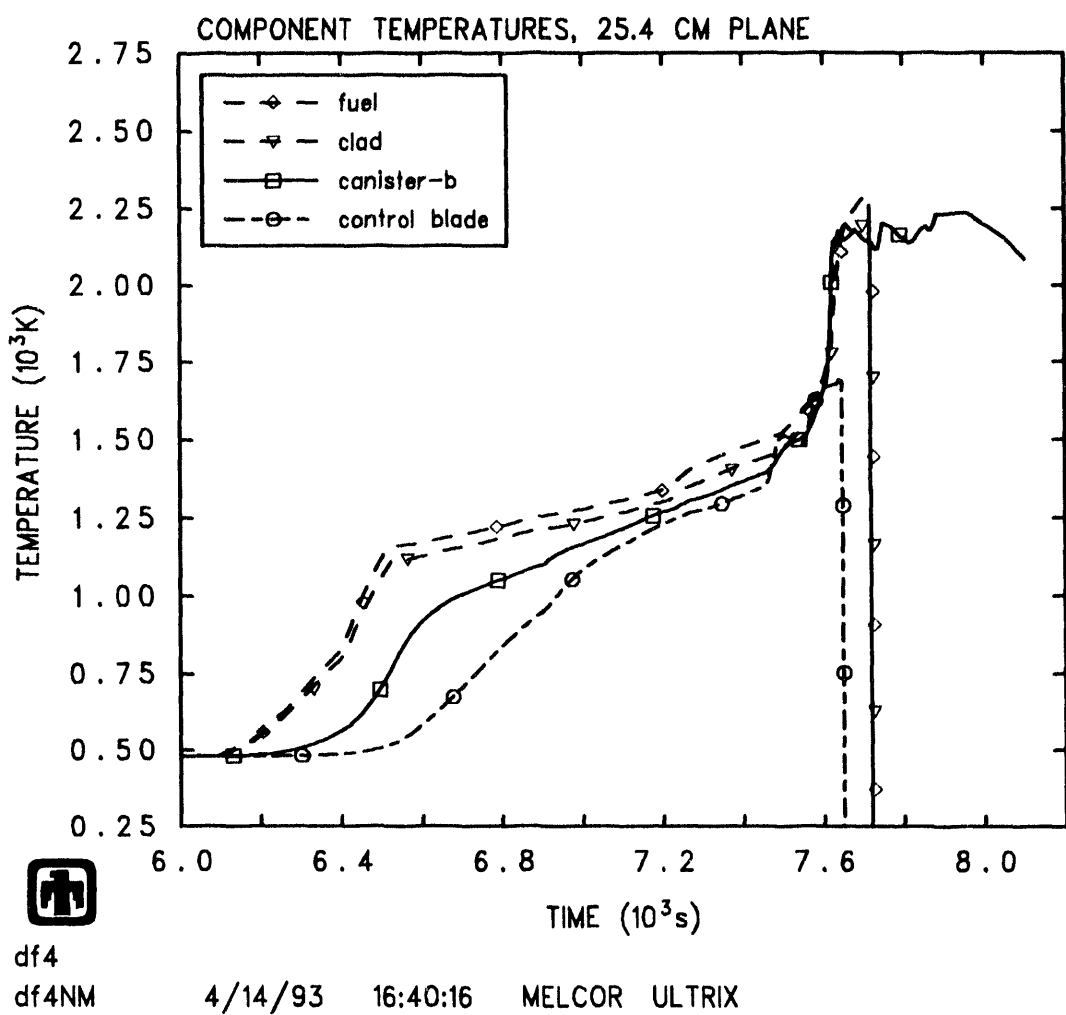
Figure 4.1.14. Component temperatures for the fuel, cladding, canister-b and other structure (control blade) components, at the 25.4 cm plane, for the base case input model.

DF-4 Fuel & Clad (t=6000.0s)

DF-4 Particulate Debris (t=6000.0s)

Elevation (10⁻¹m)

Fraction of Total Cell Volume X 10⁻¹

DF-4 Canister-B (t=6000.0s)

DF-4 Other Structure (t=6000.0s)

Elevation (10⁻¹m)

Fraction of Total Cell Volume X 10⁻¹

Intact:

UO₂

Zr

SS

ZrO₂

SSOX

CRP

INC

Cong Debris:

UO₂ in Deb

Zr in Deb

SS in Deb

ZrO₂ in Deb

SSOx in Deb

CRP in Deb

INC in Deb
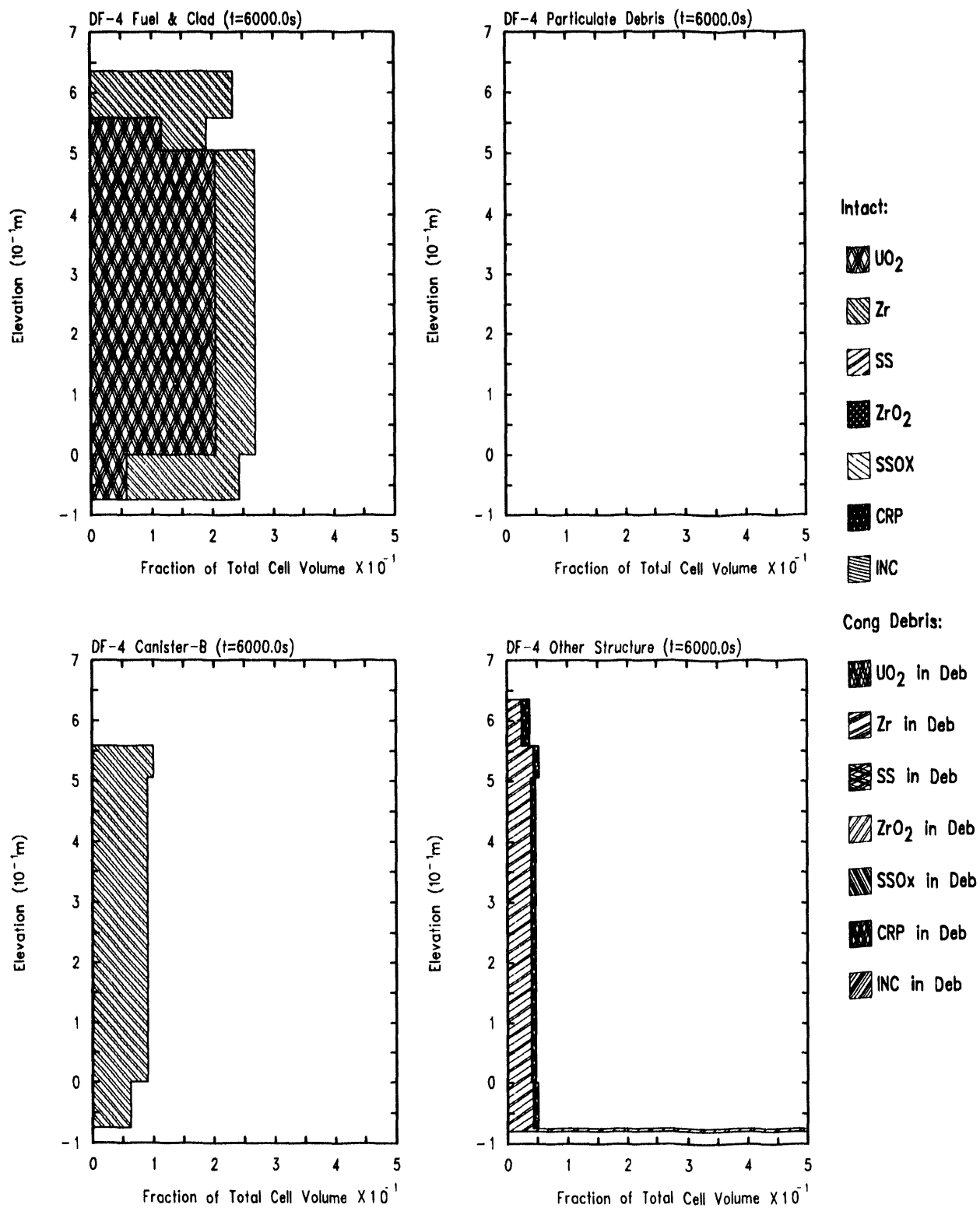
Figure 4.2.1. Initial locations (at 6000 seconds) of fuel and clad (upper left), particulate debris (upper right), canister-b (lower left) and other structure (lower right) component materials in DF-4.
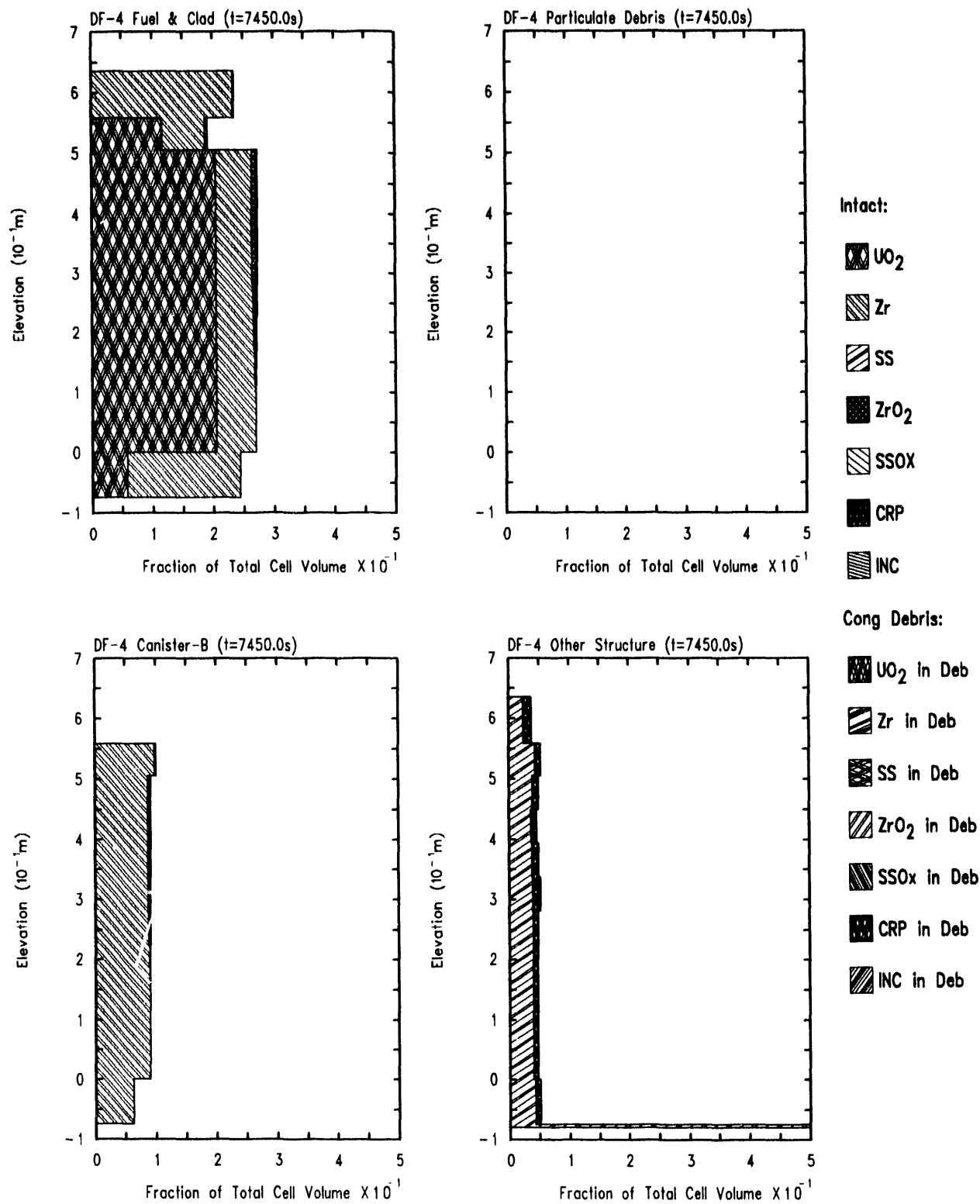
Figure 4.2.2. Locations of fuel and clad (upper left), particulate debris (upper right), canister-b (lower left) and other structure (lower right) component materials in DF-4 at 7450 seconds.

DF-4 Fuel & Clad (t=7500.0s)

DF-4 Particulate Debris (t=7500.0s)

DF-4 Canister-B (t=7500.0s)

DF-4 Other Structure (t=7500.0s)

Elevation $(10^{-1}m)$

Fraction of Total Cell Volume X10^{-1}

Intact:

UO$_2$

Zr

SS

ZrO$_2$

SSOX

CRP

INC

Cong Debris:

UO$_2$ in Deb

Zr in Deb

SS in Deb

ZrO$_2$ in Deb

SSOx in Deb

CRP in Deb

INC in Deb
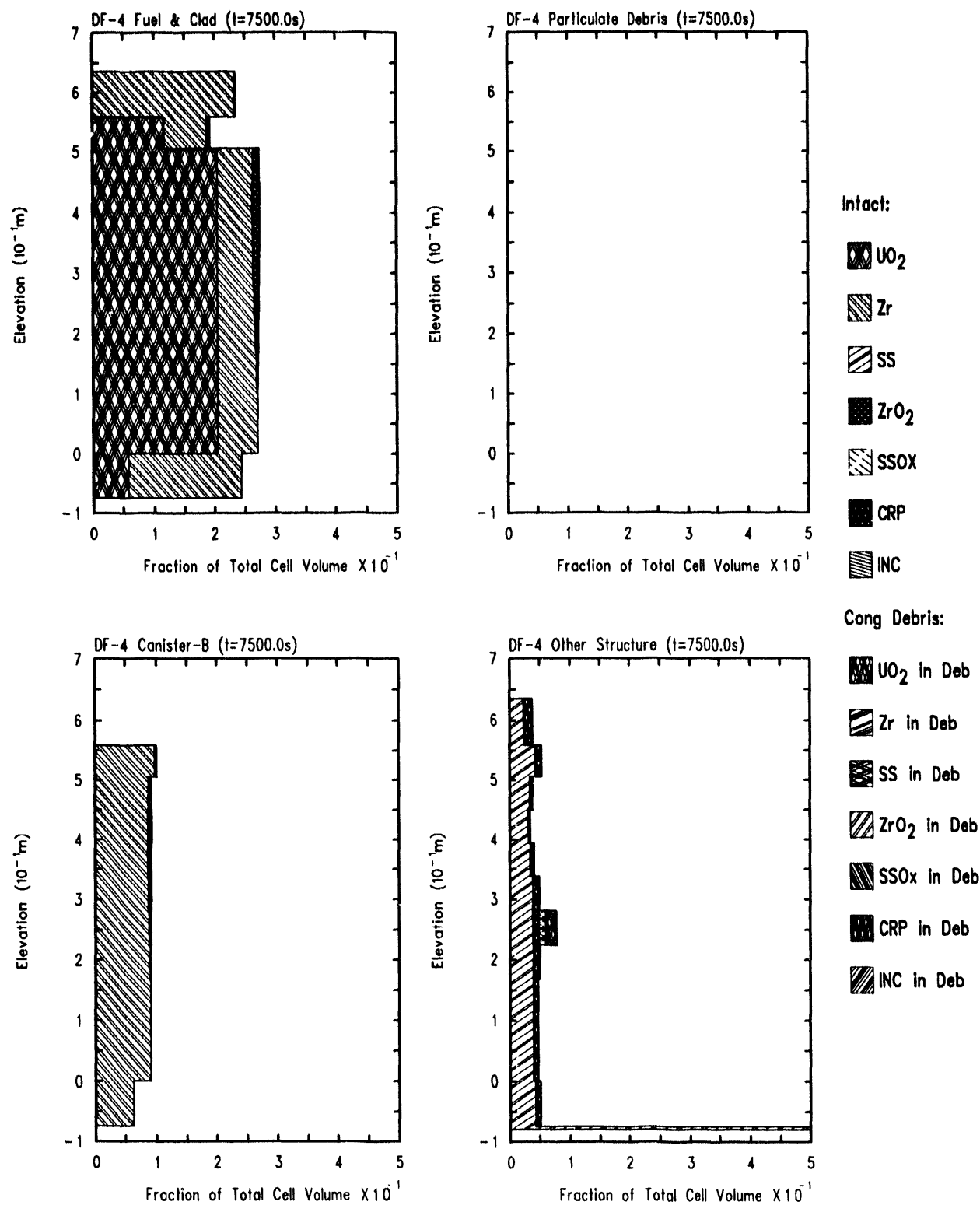
Figure 4.2.3. Locations of fuel and clad (upper left), particulate debris (upper right), canister-b (lower left) and other structure (lower right) component materials in DF-4 at 7500 seconds.
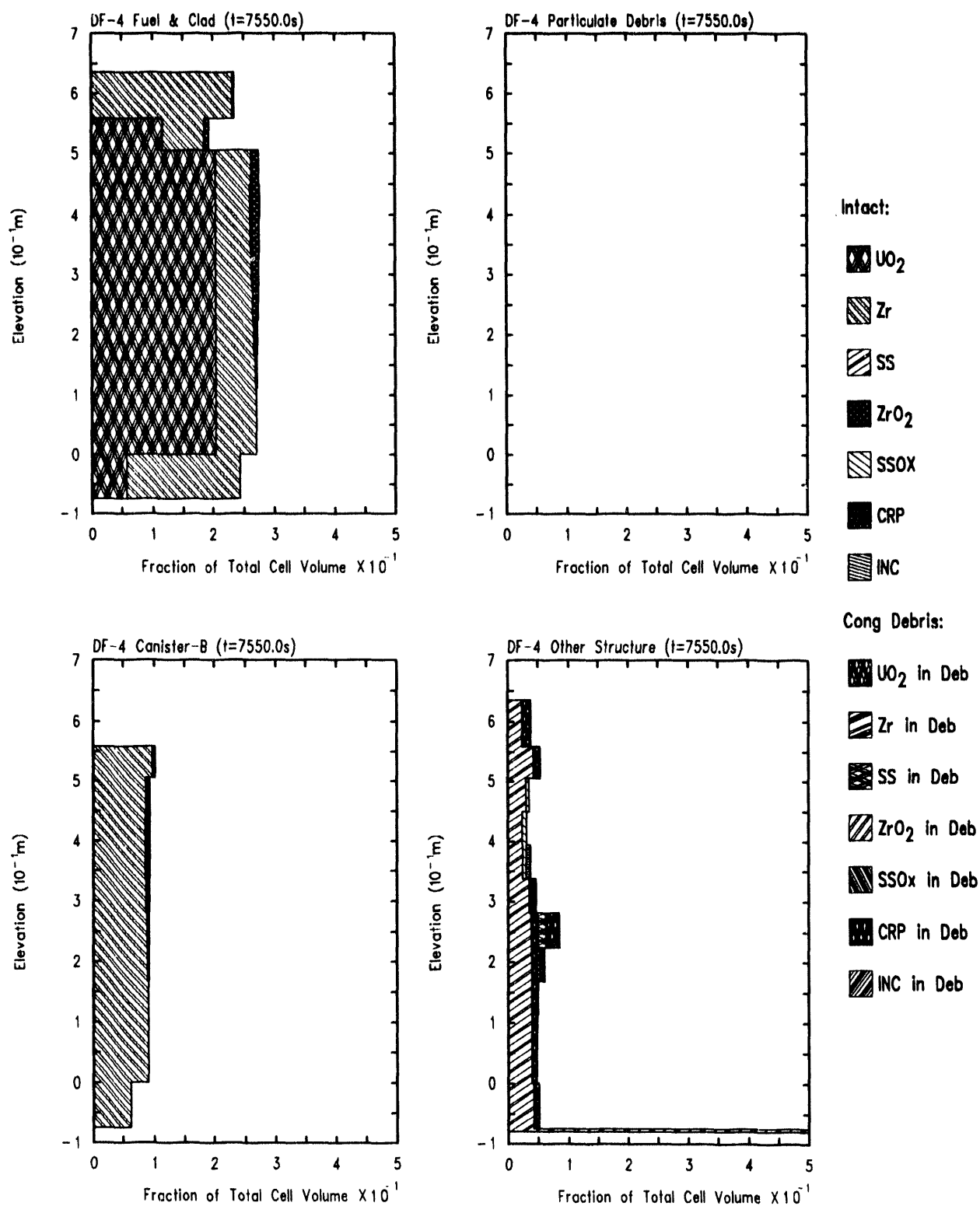
Figure 4.2.4. Locations of fuel and clad (upper left), particulate debris (upper right), canister-b (lower left) and other structure (lower right) component materials in DF-4 at 7550 seconds.

48
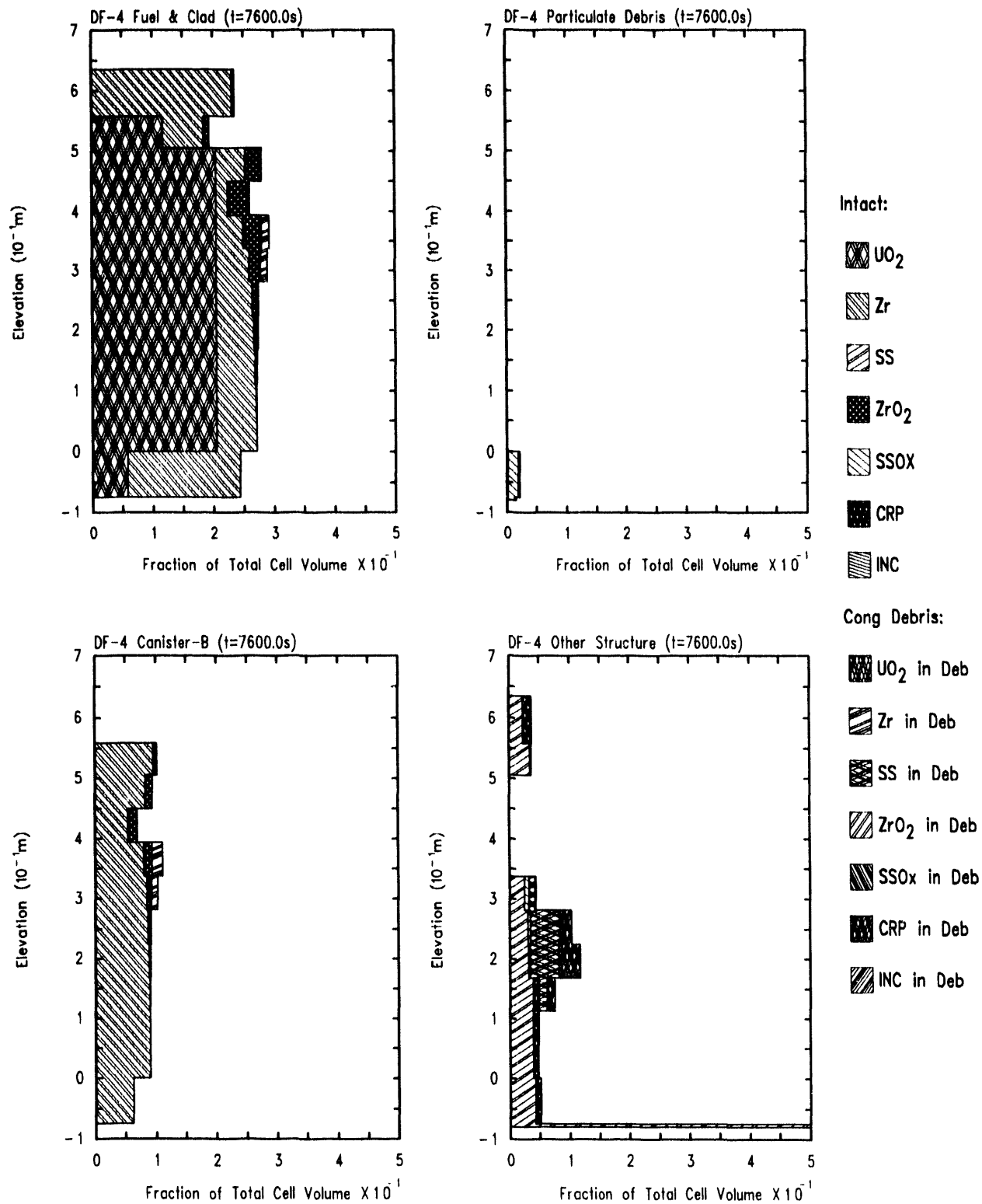
Figure 4.2.5. Locations of fuel and clad (upper left), particulate debris (upper right), canister-b (lower left) and other structure (lower right) component materials in DF-4 at 7600 seconds.
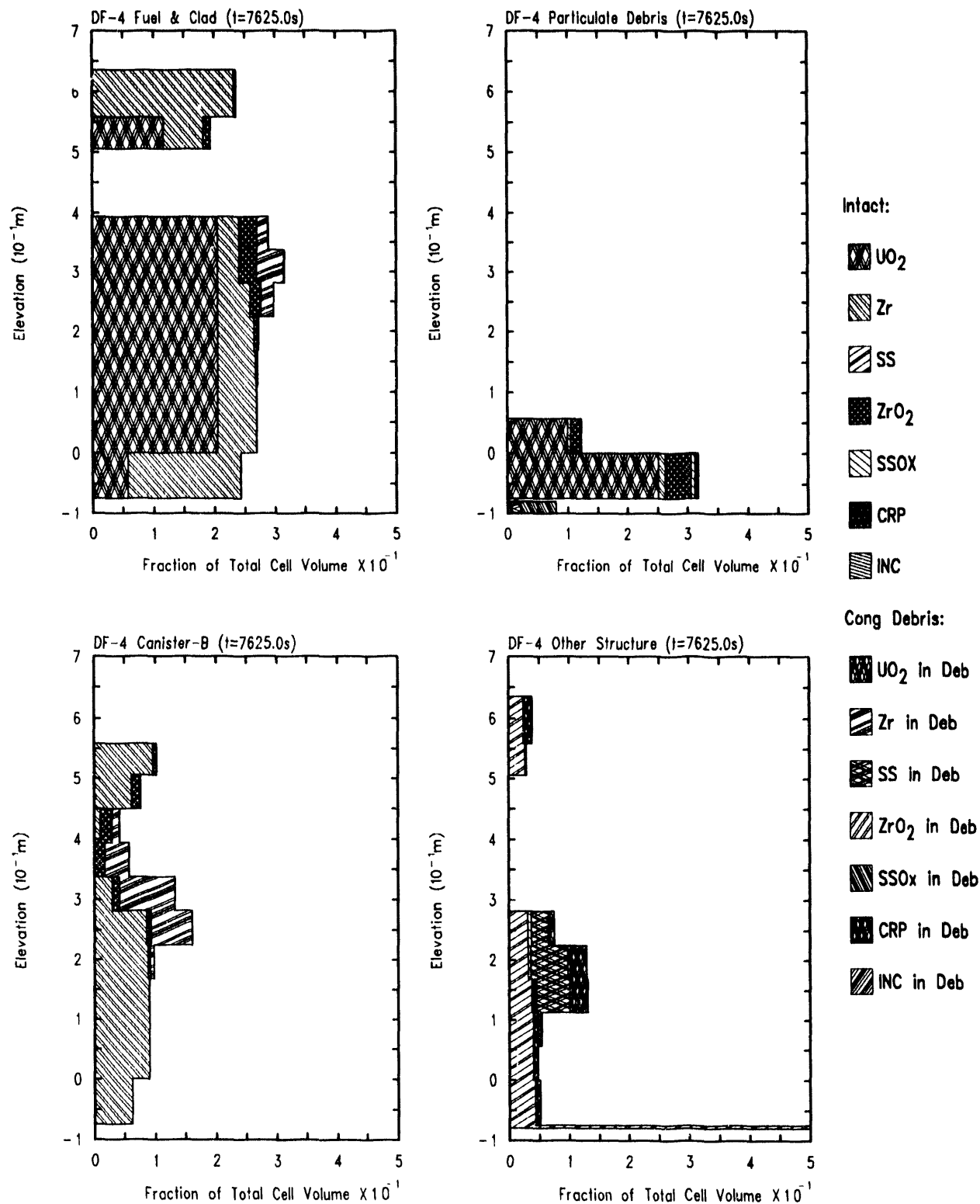
Figure 4.2.6. Locations of fuel and clad (upper left), particulate debris (upper right), canister-b (lower left) and other structure (lower right) component materials in DF-4 at 7625 seconds.

9 (elevations 22.4 and 28.1 cm, respectively). At 7500 seconds the B_4C was almost entirely depleted from axial level 11 (elevation 39.3 cm), but the eutectic reaction had not depleted noticeable amounts of B_4C from any other axial levels. The canister and clad components were continuing to oxidize slowly at this time.

The relocation of B_4C had speeded up by 7550 seconds, as shown in Figure 4.2.4. All of the B_4C had relocated from axial levels 10, 11 and 12 (elevations 33.7, 39.3 and 44.9 cm, respectively) by this time. This shows the migration of the eutectic reaction front both up and down from the origination point in level 11.

Note that the B_4C and stainless steel did not candle very far down the control blade before refreezing. This was in contrast to the early arrival of melt measured on the control blade at the 9.6 cm plane, shown in Figure 4.1.4. This may indicate a different candling heat transfer coefficient for the control blade materials than that used in the MELCOR base case input model. A sensitivity study on this parameter is discussed in Section 5.1.7.

Figure 4.2.6 shows that by 7625 seconds the first fuel relocation had taken place. Note that the fuel had completely relocated from axial level 11. This was due to the onset of rapid oxidation in that cell, which quickly depleted the cladding, leaving no support for the fuel pellets in that cell. The resulting debris relocated down to the core plate at axial level 2 (elevation -7.6 cm), which supported debris. Part of the cladding had also candled, again going only two or three levels before refreezing. The onset of rapid oxidation in the cladding drove the canister component to rapid oxidation as well. The largest amount of canister oxidation had taken place at axial level 11, but had also spread in both directions, like the eutectic reaction front in the control blade at earlier times. Candling of molten zircaloy in the canister component showed the same behavior as shown for B_4C in the blade, where refreezing took place only two or three axial levels below the melting level. The rapid oxidation in the canister in turn drove the stainless steel in the control blade to melting and relocation, candling down a maximum of three or four axial levels.

Figures 4.2.2— 4.2.6 show two important features of these MELCOR calculations. First, although the control rod poison material began to relocate before the fuel material, it did not candle far before refreezing onto the control blade. This behavior was highly dependent on the candling heat transfer coefficient (see Section 5.1.7). Second, large scale melting and relocation seemed to be driven by fuel rod heatup and oxidation, and took place level by level instead of component by component. That is, all materials in a cell tended to relocate together before large scale relocation took place in other cells. This is also important for reactivity control. Note that the eutectic interaction front traveled faster than the oxidation front. The issue of fuel and poison separation for this problem is therefore highly dependent on the candling of control blade materials.

4.2.3   Later Oxidation Subphase (7650–7700 seconds)

The progression of melting and relocation in the test bundle at 25 second intervals is shown in Figures 4.2.6— 4.2.9. The behavior of the fuel and cladding was similar to earlier times, where the fuel material in axial levels relocated level by level,

accompanied by a small amount of zircaloy candling.

The behavior of the canister and control blade was also similar. Melting and relocation progressed on a level by level basis, with B_4C and other materials candling only two or three cells down before refreezing. Note that the control blade melting and relocation led that of the fuel and clad, but the control poison material did not relocate as far as the fuel did. Thus, the fuel and control rod poison leap-frogged each other, but remained relatively close. This conclusion is based upon the behavior of the core plate, which remained intact during this phase of the experiment, and on the candling heat transfer coefficients.

There are two more interesting features to note in Figure 4.2.9. First is the existence of stainless steel oxide in the particulate debris component at axial level three (elevation -7.5 cm). This material originated in the other structure component at axial level 13 (elevation 50.5 cm), the level containing the upper spacer region of the fuel. This was the result of the stainless steel at this level melting and having no material in cells below on which to candle. In this situation, MELCOR put the candling material into the particulate debris component. Second, the canister at axial levels seven (elevation 16.8 cm) and above had significant amounts of zircaloy in the conglomerate debris, but little ZrO_2. This indicates that the zircaloy was not oxidizing very quickly in the canister at these levels. This was probably due to the oxide layer that had formed on the canister, above the conglomerate debris layer. It may also have been due to steam starvation as a result of debris oxidation farther down in the debris bed.

4.2.4 Final State

The final calculated state of the test bundle is shown in Figure 4.2.10, at 8100 seconds. This was the time when the ACRR was shut down (see Figure 2.2.1). This can be compared to photos resulting from the PIE, shown in Figures 4.2.11— 4.2.14 [5], for the 95 mm, 133 mm, 238 mm and 308 mm axial levels.

At 95 mm (9.5 cm), the PIE showed that most of the refrozen zircaloy inside the test bundle was left unoxidized, with some oxidation taking place in the outer portions of the bundle. There were also large amounts of stainless steel refrozen at the 95 mm level and below, due to the early candling of control blade eutectic mixture. The calculated state at this level in Figure 4.2.10 shows large portions of zircaloy remaining in the canister-b conglomerate debris and some in the particulate debris component. This material would correspond to the refrozen material shown in Figure 4.2.11. Figure 4.2.10 shows small amounts of control blade conglomerate debris but no intact material at this level; this is in contrast to the void filling the former position of the control blade showed in the PIE photo in Figure 4.2.11. There is more UO_2 and zircaloy at this level than shown by the PIE, indicating again that the control blade material was calculated by MELCOR to candle only a short distance in the test bundle before refreezing, rather than flowing all the way to the bottom of the bundle as it did in the experiment. This indicates that the default values for candling heat transfer coefficients for control blade materials (which were used in the MELCOR base case model) do not represent the materials in DF-4 very well. The

52
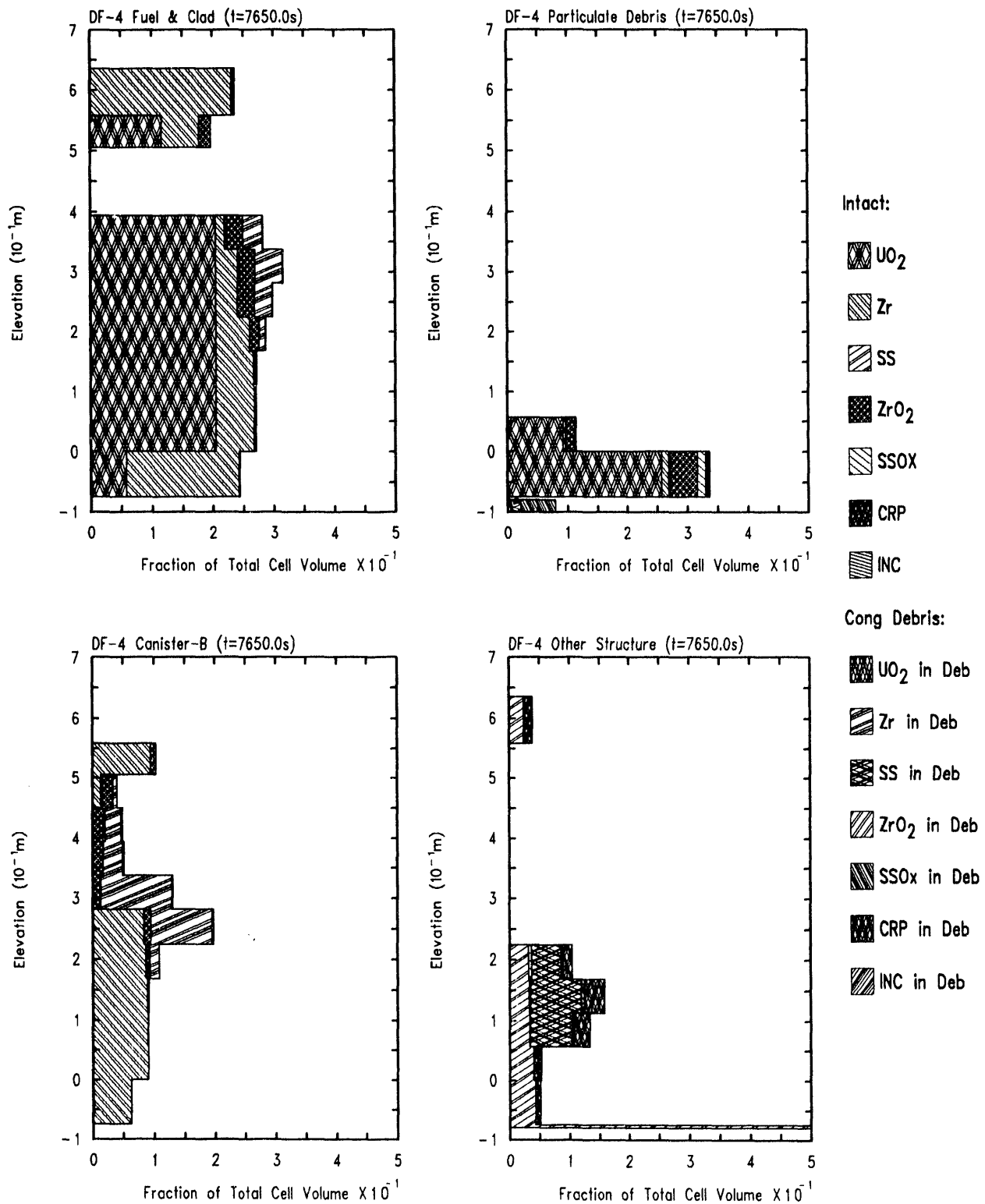
Figure 4.2.7. Locations of fuel and clad (upper left), particulate debris (upper right), canister-b (lower left) and other structure (lower right) component materials in DF-4 at 7650 seconds.

53
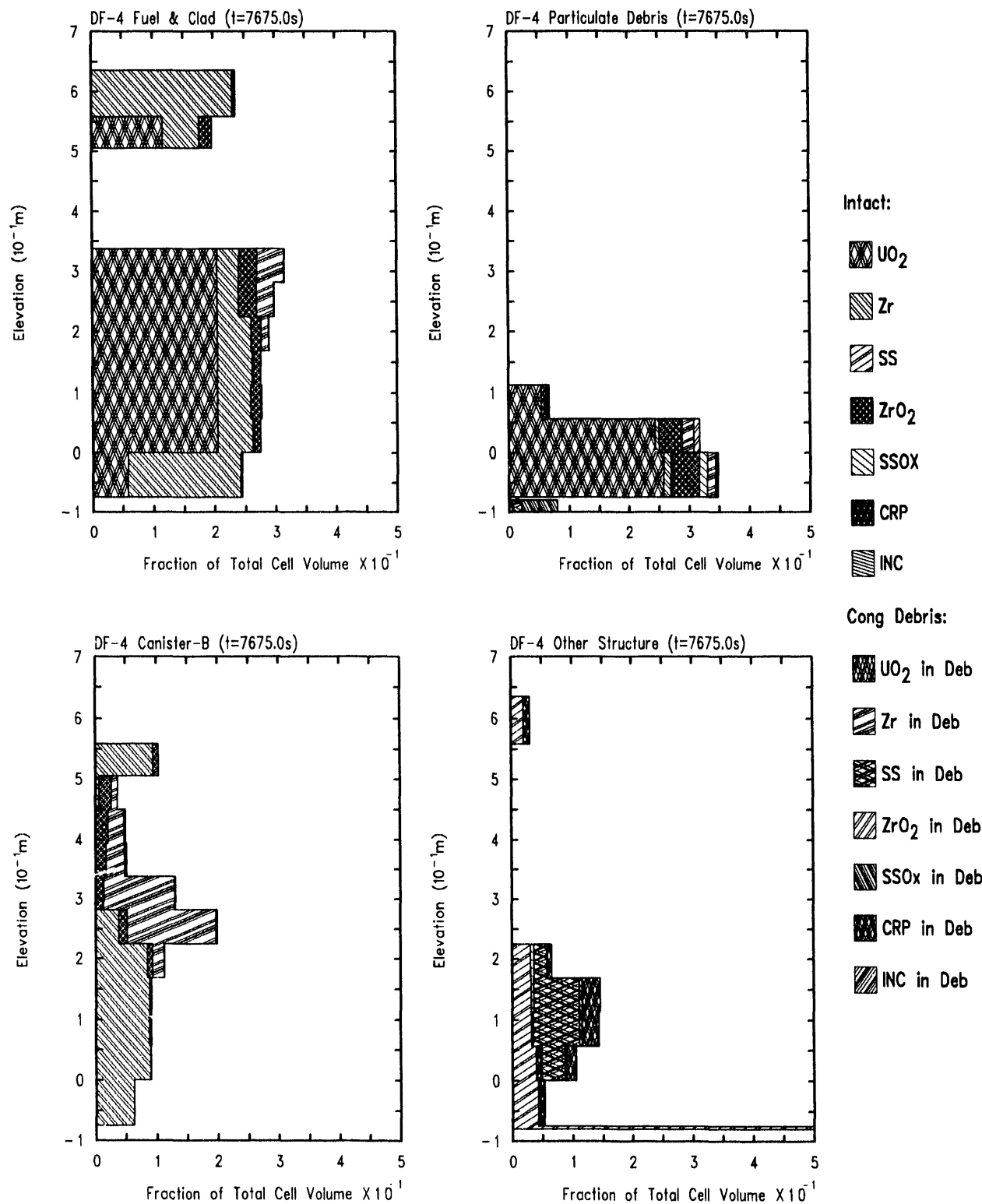
Figure 4.2.8. Locations of fuel and clad (upper left), particulate debris (upper right), canister-b (lower left) and other structure (lower right) component materials in DF-4 at 7675 seconds.
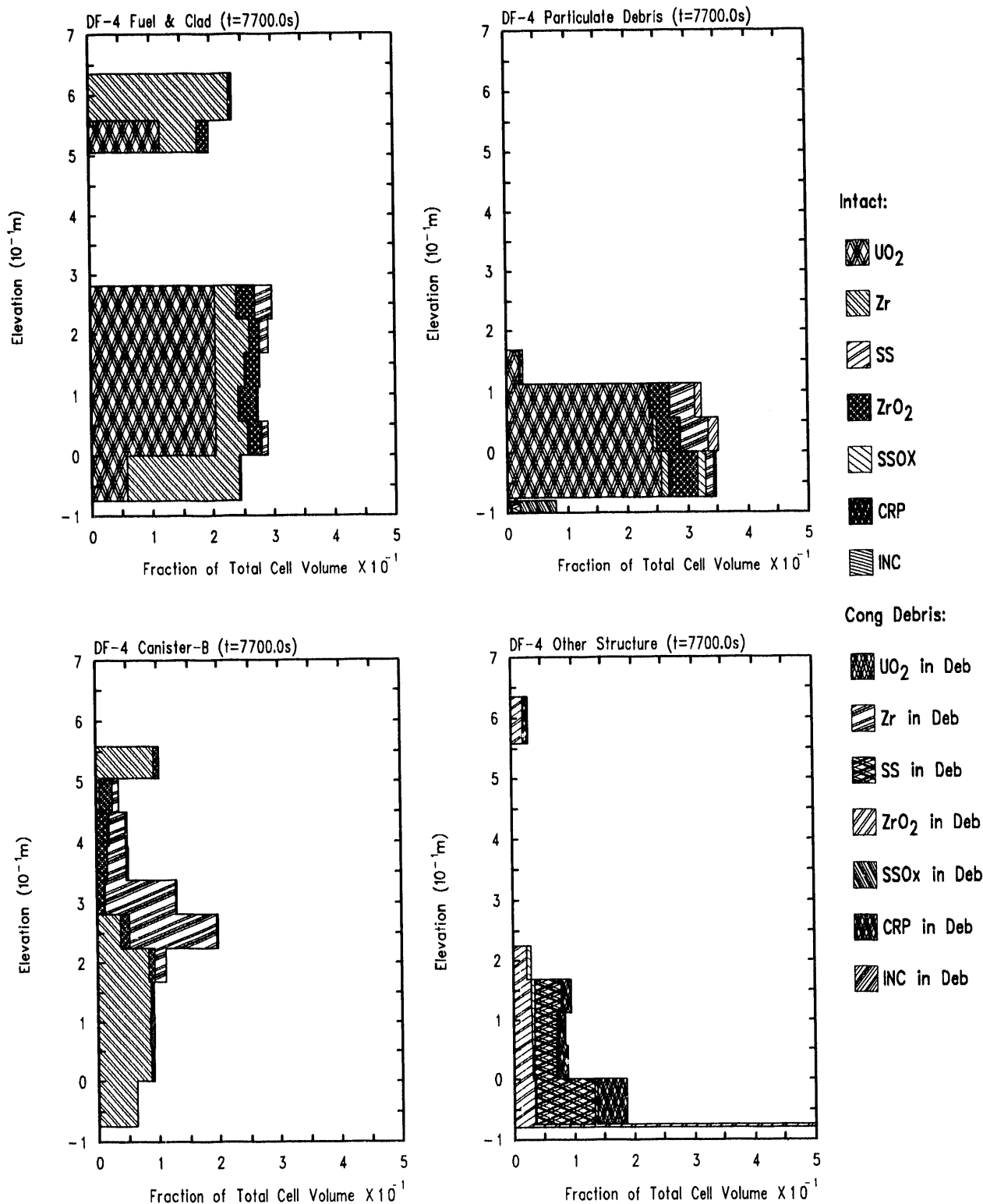
Figure 4.2.9. Locations of fuel and clad (upper left), particulate debris (upper right), canister-b (lower left) and other structure (lower right) component materials in DF-4 at 7700 seconds.

control blade candling heat transfer coefficient defaults in MELCOR did not capture the rivulet-type candling shown by the video record of DF-4.

The debris at 133 mm (13.3 cm) was very porous, as shown in Figure 4.2.12. This indicates the upper extent of debris in the test bundle. (In the next axial level shown in the PIE photos, the test bundle was largely void; this photo is not shown here.) MELCOR calculated the canister and control blade debris to end at approximately this level, neglecting the fuel debris.

Figure 4.2.13 shows some remnants of the canister and some material refrozen inside the canister area at 238 mm (23.8 cm). The channel area between the remaining fuel rods was largely void. Figure 4.2.10 shows ZrO_2 remaining in the canister component at this level, corresponding to canister remnants. There were also substantial amounts of refrozen conglomerate debris on the canister at this level. This agrees well with the PIE results.

The PIE photo in Figure 4.2.14 for the 308 mm (30.8 cm) level shows some canister material remaining, and less debris material refrozen inside the canister.

At all levels, the PIE showed that the fuel rod pellets were mostly left standing. This was in contrast to the calculated state, where MELCOR relocated the fuel pellets after all the cladding had melted or oxidized. The stacking of fuel pellets has been observed in other core melt progression experiments, e.g. the CORA experiments [12]. There were various postulated reasons for this stacking, two of which were the internal Ti electrical heating elements inside the CORA fuel rods and the use of fresh instead of irradiated fuel in most of these experiments. However, there are no clear conclusions as to how the fuel pellets would behave during a real nuclear power plant accident. Therefore, we make no recommendations concerning the adjustment of fuel relocation parameters, except to say that these parameters should be investigated in a sensitivity study. A sensitivity study on core relocation parameters is reported in Section 5.1.8.

In summary, the distribution of debris materials in the test bundle was predicted by MELCOR with mixed success in comparison with the final state revealed during the PIE. The stainless steel was predicted to end up in the lower portions of the test bundle and there were large amounts of unoxidized zircaloy predicted in the debris, both in good agreement with PIE data. However, no fuel pellet stacking was predicted by MELCOR, resulting in a debris bed whose surface was higher than that observed in the PIE.

4.3 Hydrogen Production

The hydrogen production in DF-4 was measured using the hydrogen recombiner system designed specifically for this experiment. The measured total hydrogen production is compared to the calculated hydrogen production in Figure 4.3.1. Also shown is the total hydrogen production indicated by the hydrogen recombiner tubes, and an extrapolated production curve based on the final range of values for hydrogen production given by the PIE [6].

The calculated hydrogen production began much earlier than the measured production, building up to about 5 grams of hydrogen by 7550 seconds. The start of rapid
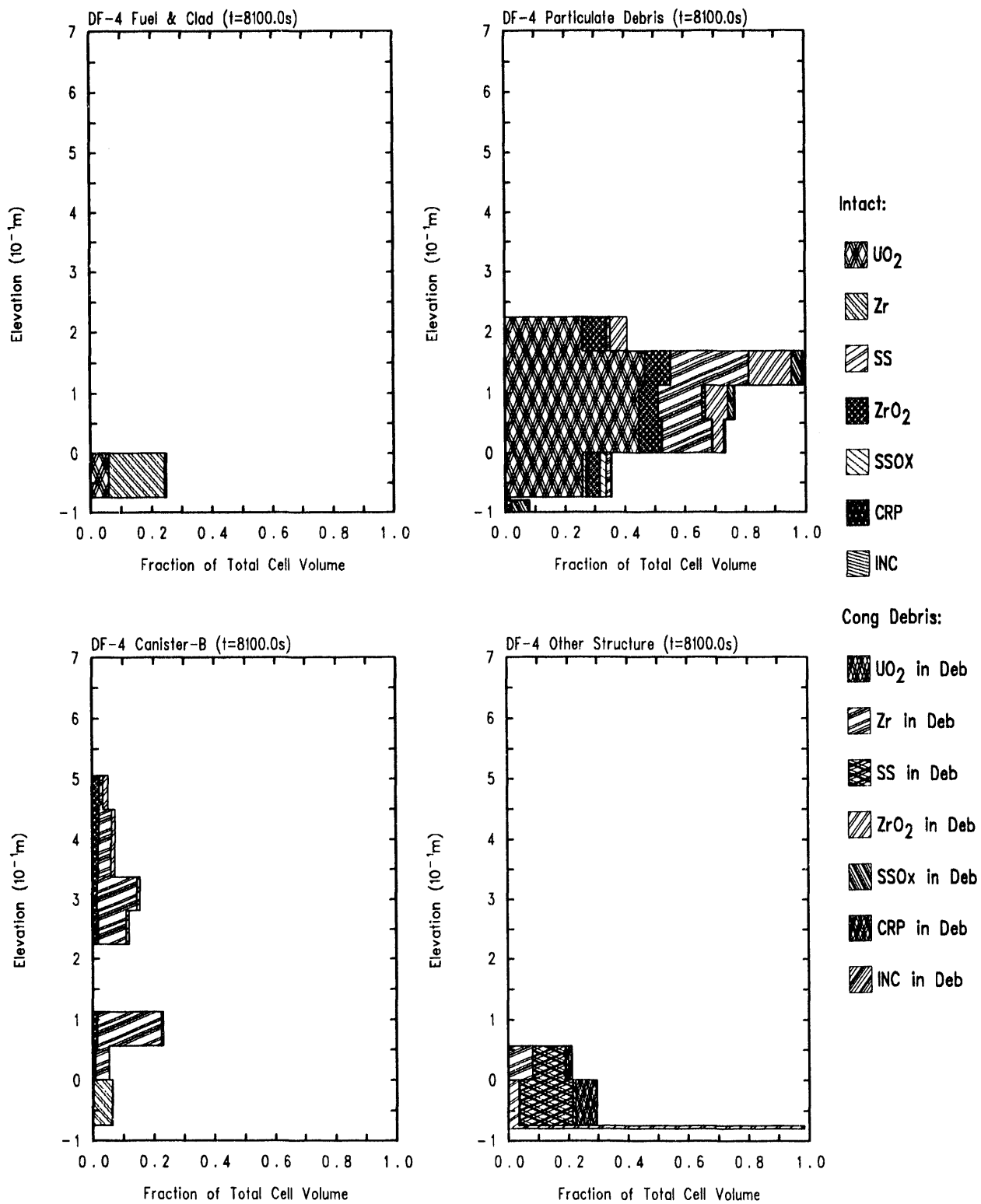
Figure 4.2.10. Locations of fuel and clad (upper left), particulate debris (upper right), canister-b (lower left) and other structure (lower right) component materials in DF-4 at 8100 seconds.

Figure 4.2.11. PIE photo showing final state of the DF-4 test bundle at the 95 mm axial level [5].
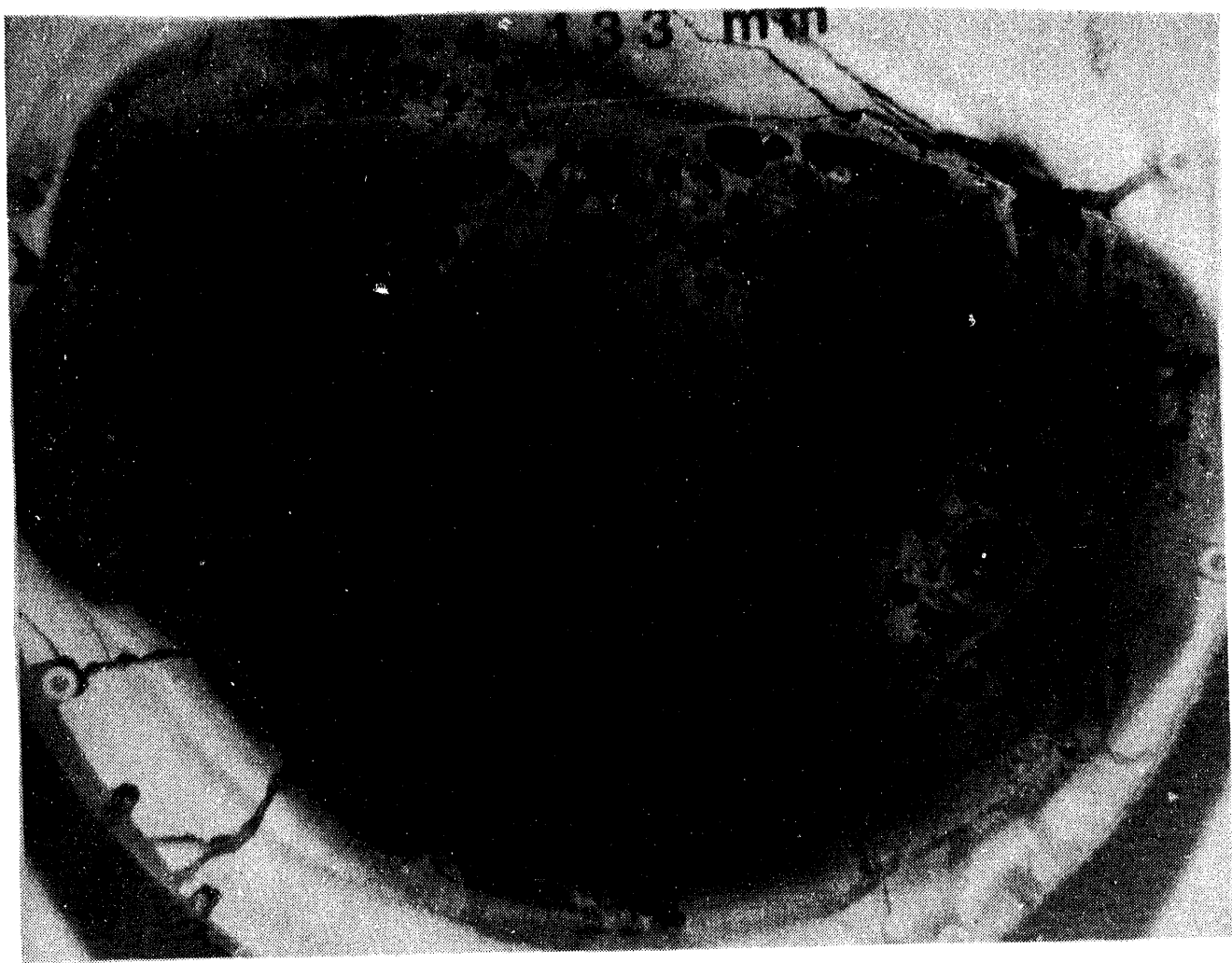
Figure 4.2.12. PIE photo showing final state of the DF-4 test bundle at the 133 mm axial level [5].
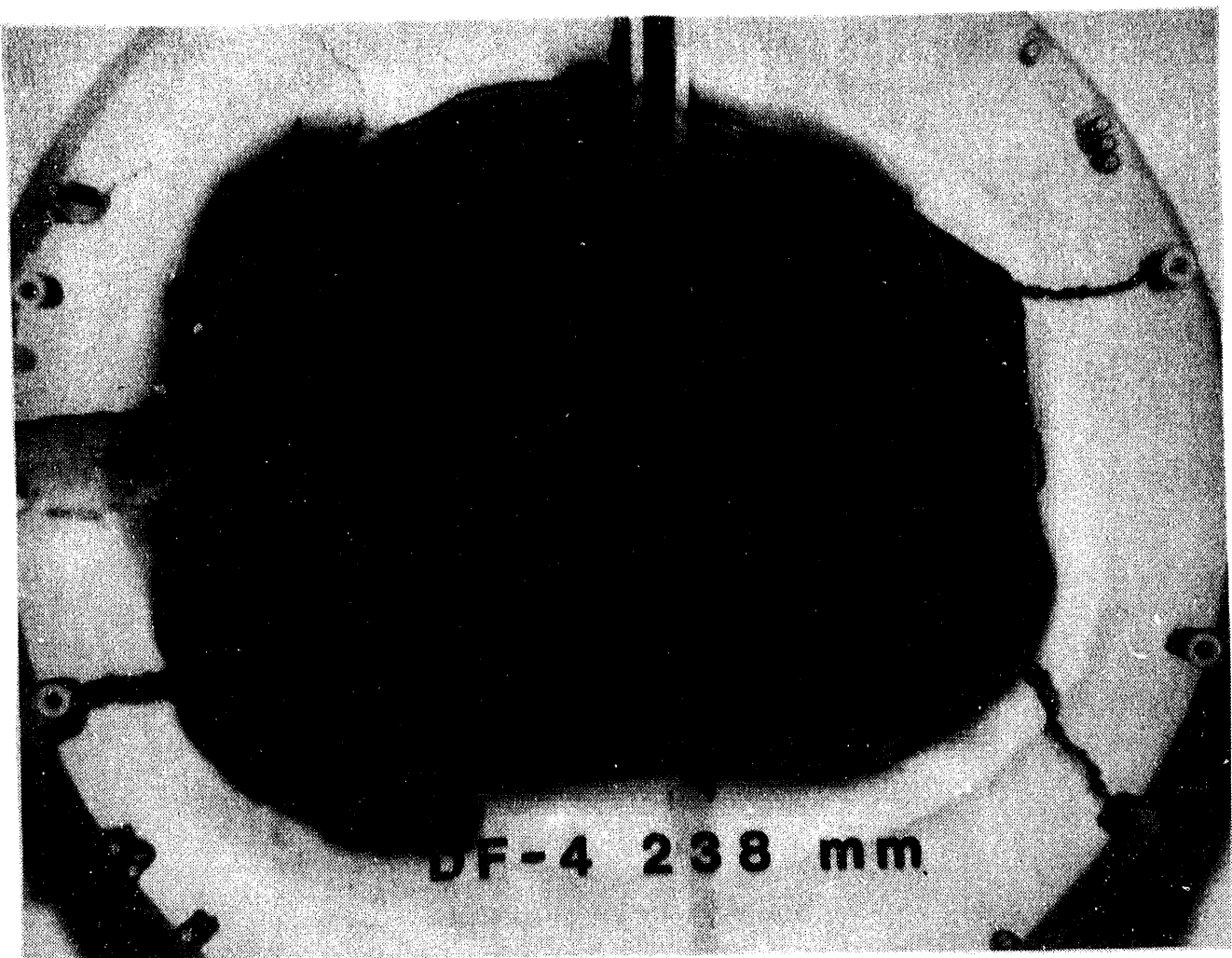
Figure 4.2.13. PIE photo showing final state of the DF-4 test bundle at the 238 mm axial level [5].
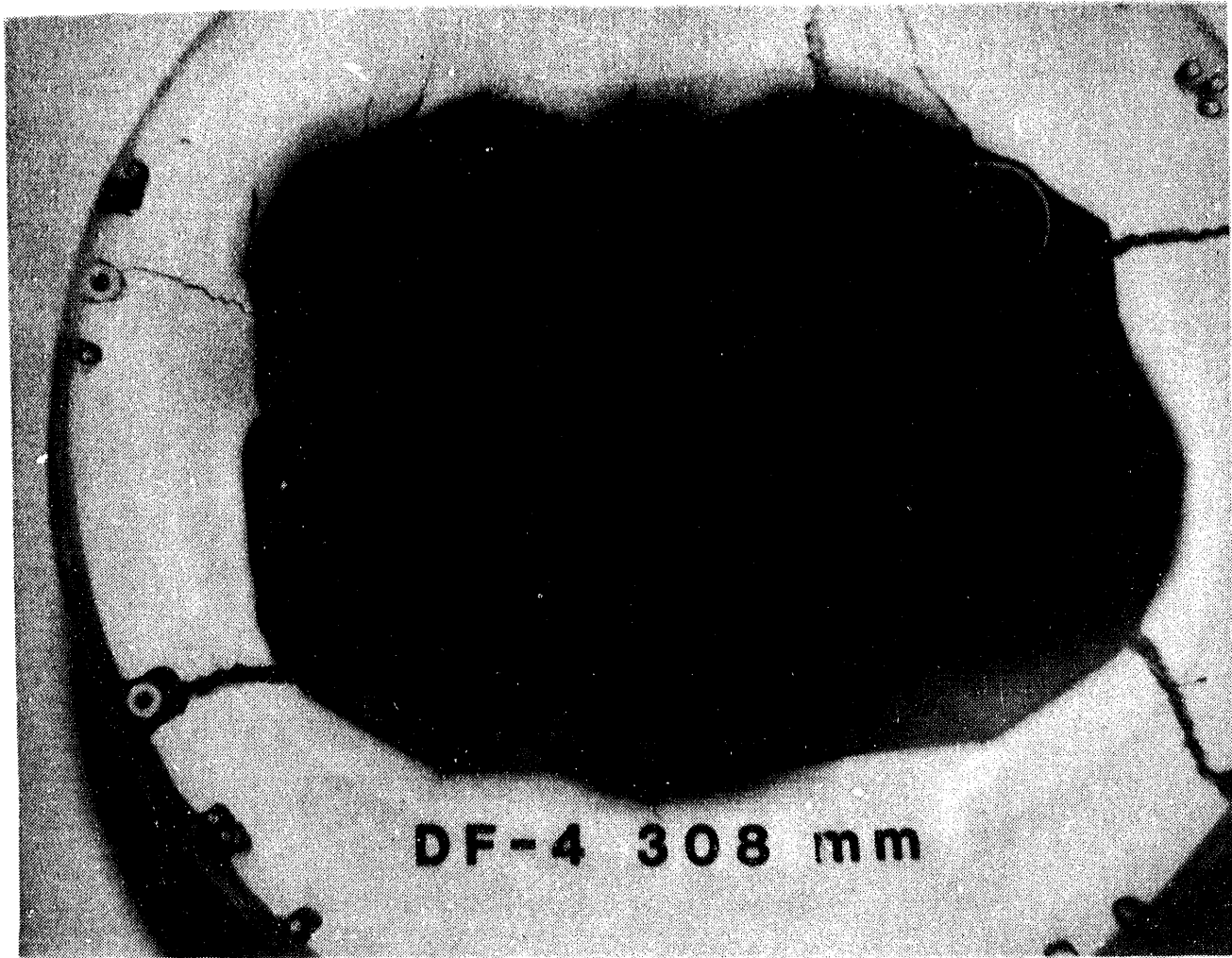
Figure 4.2.14. PIE photo showing final state of the DF-4 test bundle at the 308 mm axial level [5].

hydrogen production was very close to that measured in the experiment, but the production rate was initially higher than measured. The bulk of the calculated hydrogen production also took place early, compared to the measured hydrogen production. These results indicate that MELCOR may have over-predicted oxidation during the melting stage and under-predicted oxidation after debris had been formed. The same results for hydrogen production were also noted in the MELCOR model of the CORA-13 experiment [13]. The total hydrogen production calculated by MELCOR was 36.4 grams, which was well within the range of 33–40 grams given by the DF-4 PIE [6].

The measured and calculated hydrogen production rates are shown in Figure 4.3.2. The maximum possible hydrogen production rate (corresponding to steam-starved conditions), based on an inlet steam flow of 0.88 grams/second, would be 0.098 grams/second. After the onset of rapid oxidation at about 7550 seconds, the production rate rose quickly to the steam-starved conditions. The calculated rate dropped along with the measured rate after the remainder of the core had relocated, but peaked again between 7800 and 8000 seconds. This was due to the uncovery of more unoxidized zircaloy by the eutectic dissolution of the canister. Note that the measured hydrogen production rate in Figure 4.3.1 started tailing off at about 7800 seconds. This indicates that the measured hydrogen production given by the recombiner tubes was not accurate after this time, since the measured production rate shown in Figure 4.3.2 could not have resulted in the total hydrogen produced indicated by the PIE. Therefore, the peak in the hydrogen production rate predicted by MELCOR after 7800 seconds may have occurred during the experiment, despite the contradicting hydrogen recombiner data. This conclusion is reinforced by the hydrogen production rate calculated by the APRIL code, as described in Chapter 6.
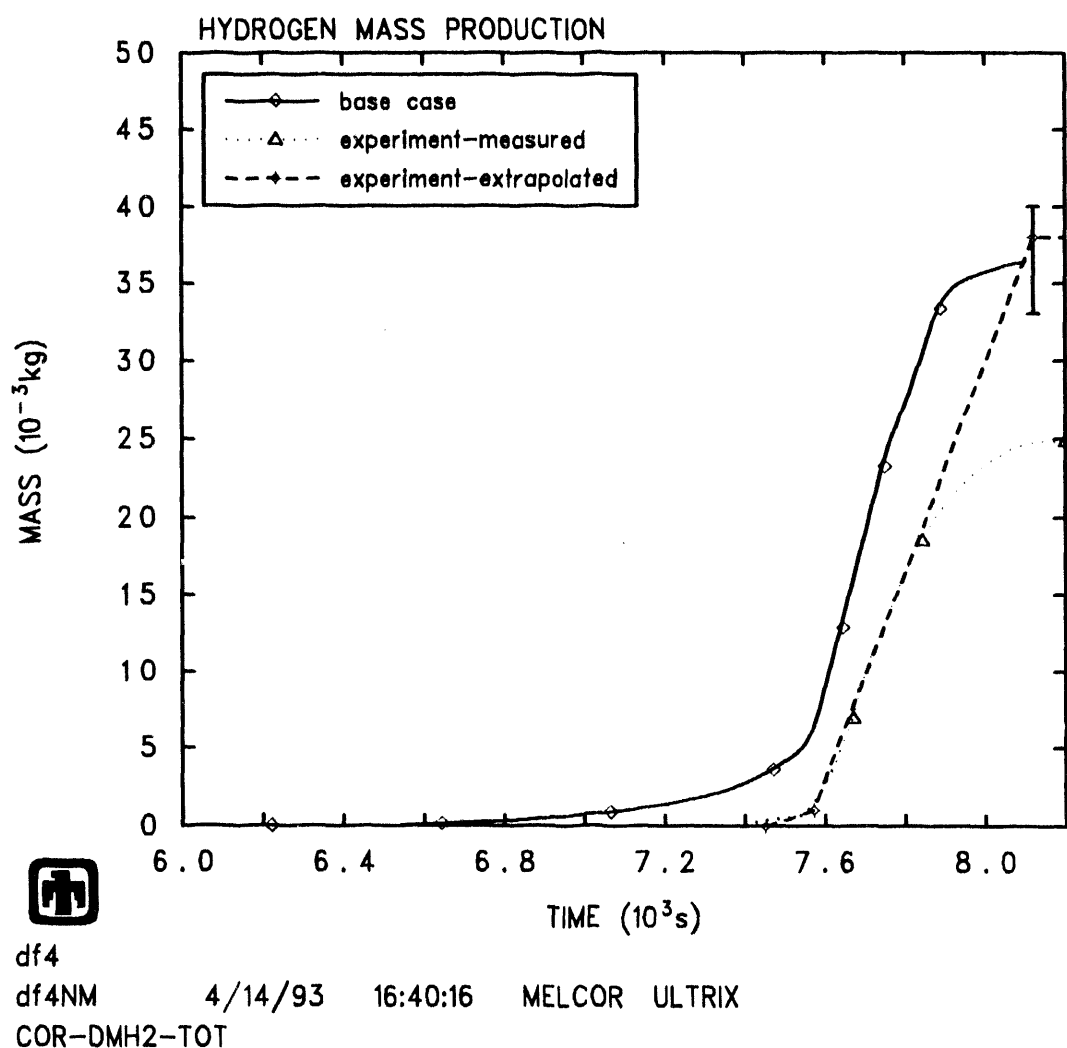
Figure 4.3.1. Calculated and measured integral hydrogen production in the DF-4 experiment. The final amount of the extrapolated production was given by the PIE.

HYDROGEN MASS PRODUCTION RATE

base case

--⊟-- experiment

df4

df4NM   4/14/93   16:40:16   MELCOR ULTRIX

CFVALU.801
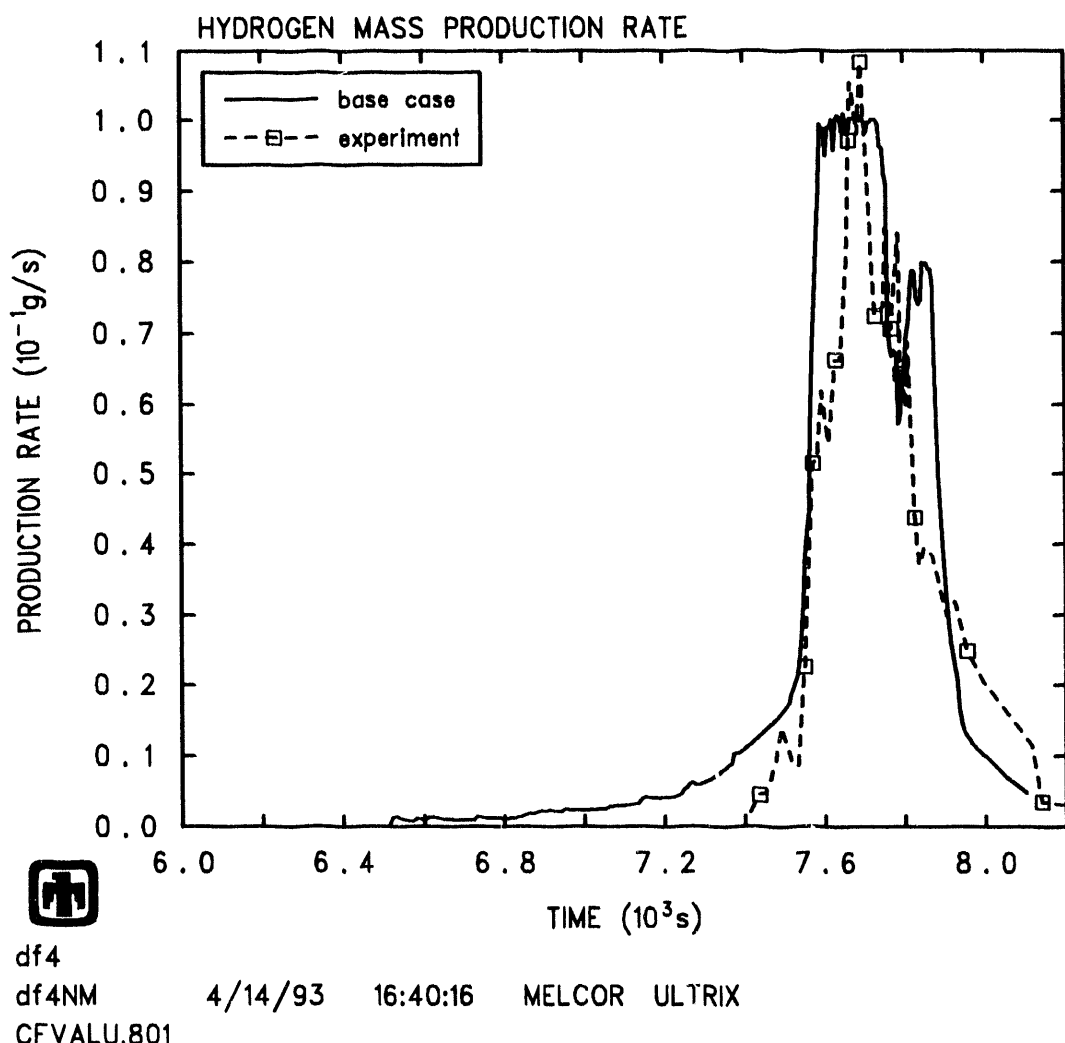
Figure 4.3.2. Calculated and measured hydrogen production rate in the DF-4 experiment.

Chapter 5

Sensitivity Studies

A number of sensitivity studies were done to investigate the influence on results of varying all of the non-default options and some of the other input options that were used. Many of the non-default options used in the DF-4 base case model were the result of preliminary versions of these sensitivity studies. The focus of most of the sensitivity studies was the core package in MELCOR, because of the emphasis the DF-4 assessment placed on this package.

The studies reported in this chapter are grouped into eight main areas. These areas are: general core package input options, core package debris, oxidation and eutectic modeling, thermal/hydraulic initial and boundary conditions, heat structures package studies, COR and CVH nodalization for DF ' nd time step and machine dependency studies.

5.1 General Core Package Studies

Nine sensitivity studies on general MELCOR core package input options are reported in this section. The options studied are: convective heat transfer coefficients in the core package, core material properties, core component initial temperatures, core component view factors, canister mass and area partition, minimum component mass, candling heat transfer coefficients, minimum oxide shell thickness and boundary heat structure fluid temperature option. The studies are described in the order given.

5.1.1 Convective Heat Transfer Coefficients

For this sensitivity study, all the convective heat transfer coefficients in the COR package were increased and decreased by 50%. This was done using sensitivity coefficient arrays 1212, 1214, 1221, 1222, 1231, and 1232.

The hydrogen production for the two variations is compared to that of the base case and to experimental values in Figure 5.1.1. Both increasing and decreasing the convective heat transfer coefficients decreased the amount of hydrogen generated during the experiment. The difference in production took place mostly after 7700 seconds, which was after most relocation had taken place. This suggests that decreased

production in the debris state had the most influence on final results. This conclusion is reinforced by comparing the cladding and control blade temperatures to base case and measured results. Figures 5.1.2 and 5.1.3 show that temperatures in the cladding and control blade, respectively, were not affected very much by variations in convective heat transfer coefficients. The largest variation was in the control blade during the test bundle equilibration subphase (6400–7200 seconds), when the control blade was being heated up as a result of heat transfer through the canister. The higher the heat transfer coefficient, the hotter the control blade was and the earlier blade failure occurred. The behavior observed here is similar to that observed in the LOFT LP-FP-2 MELCOR assessment [11], which also indicated nonmonotonic dependence of hydrogen production on core convective heat transfer.

5.1.2 Core Package Material Properties

Properties from the MATPRO materials properties package [9] were used in the base case model (the MATPRO package is used in the CONTAIN [14], MELPROG [15] and SCDAP/RELAP5 [16] codes). For this study, the material properties for zircaloy were changed back to the MELCOR default values. The most significant change made for this study was the decrease in zircaloy melting temperature from the MATPRO value of 2200K to the MELCOR default value of 2098K. Material properties were adjusted using a combination of MP and TF package inputs.

The temperature response of all core components was almost identical, up to the point of zircaloy melting. Figure 5.1.4 shows that the cladding temperature in both calculations at the 36.8 cm plane was identical for this study, and the component failed at nearly the same time. Figure 5.1.5 shows that, when the MELCOR-default zircaloy melting temperature was used, the hydrogen production was decreased from 36.4 grams to 28 grams. The lower zircaloy melting temperature caused the cladding to melt and relocate downward, out of the oxidizing regions. This reduced the total mass of hydrogen produced from cladding oxidation.

5.1.3 Core Component Initial Temperatures

In the DF-4 MELCOR base case model, all core components were assumed to have initial temperatures of 480K. The core component temperatures at the beginning of the DF-4 experiment (at 6000 seconds) were actually in the range of 420–510K (see Figure 3.2.4). For this sensitivity study, the temperatures of the fuel, cladding, canister and other structure components were set to the instrumented initial temperatures (the fuel component temperature was set equal to the cladding component temperature). Initial component temperatures were set on record CORijj03.

After the first few hundred seconds, the component temperatures calculated for this study were identical to the base case temperatures. All other quantities calculated by MELCOR for this study were also the same as the base case values.

HYDROGEN MASS PRODUCTION
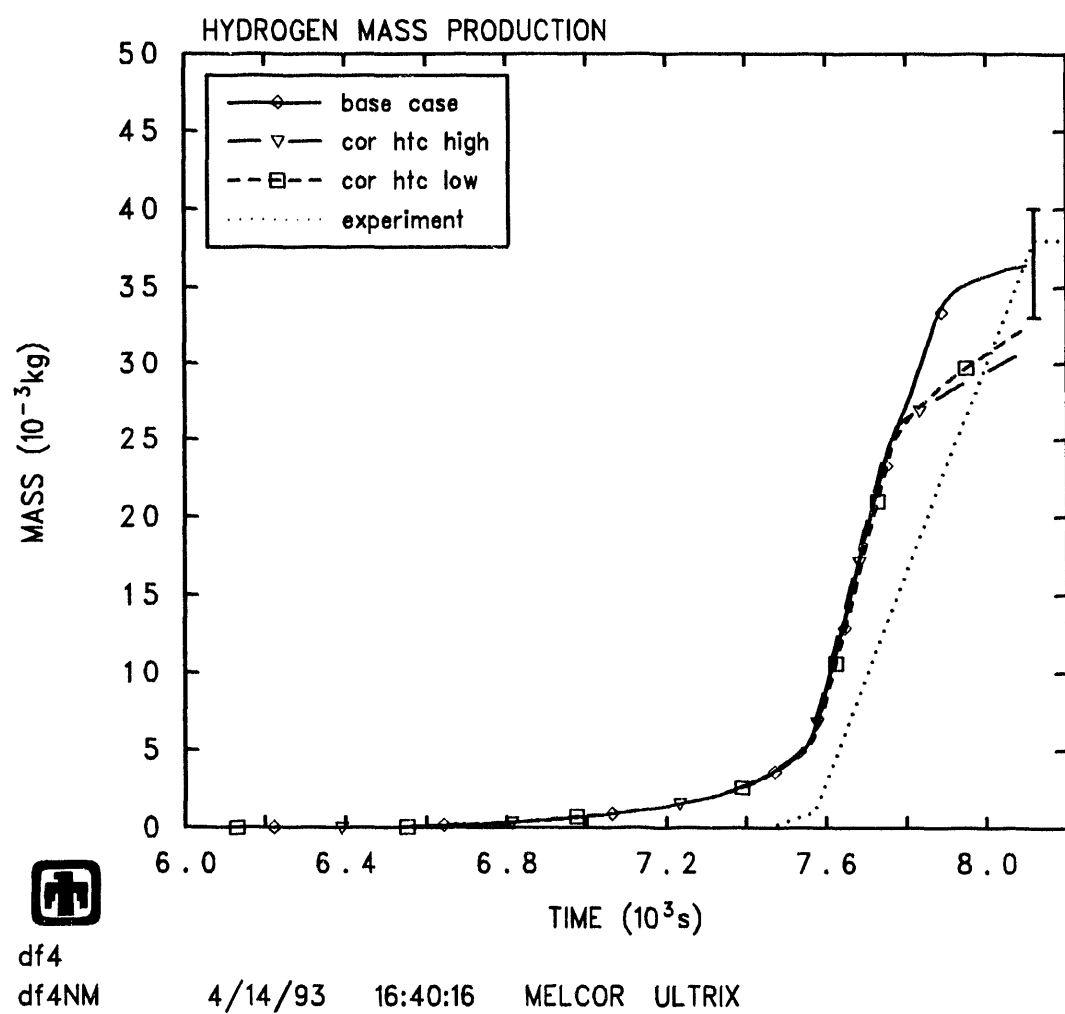
Figure 5.1.1. Hydrogen production for variations on the core convective heat transfer coefficients, compared to base case and measured values.

67
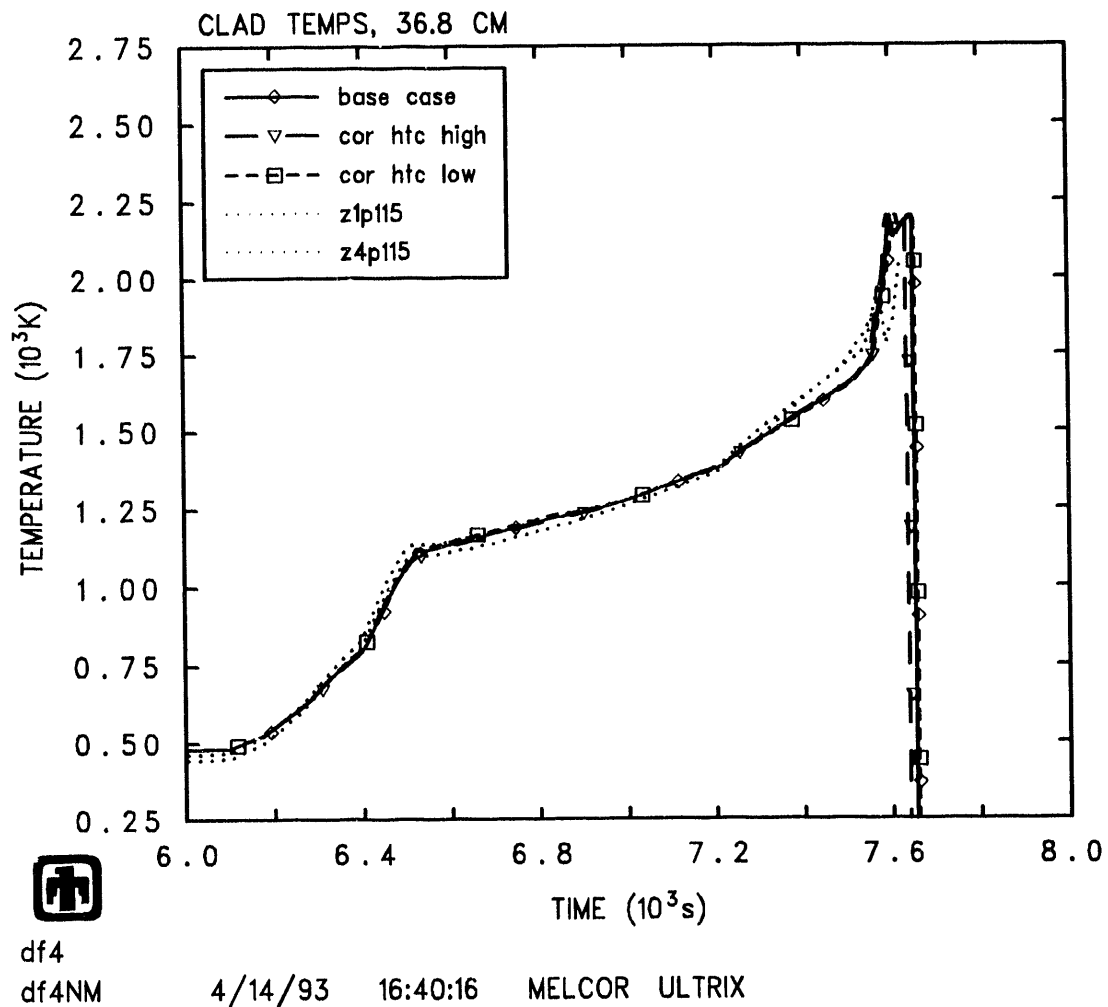
Figure 5.1.2. Cladding temperatures at the 36.8 cm plane for variations on the core convective heat transfer coefficients, compared to base case and measured values.
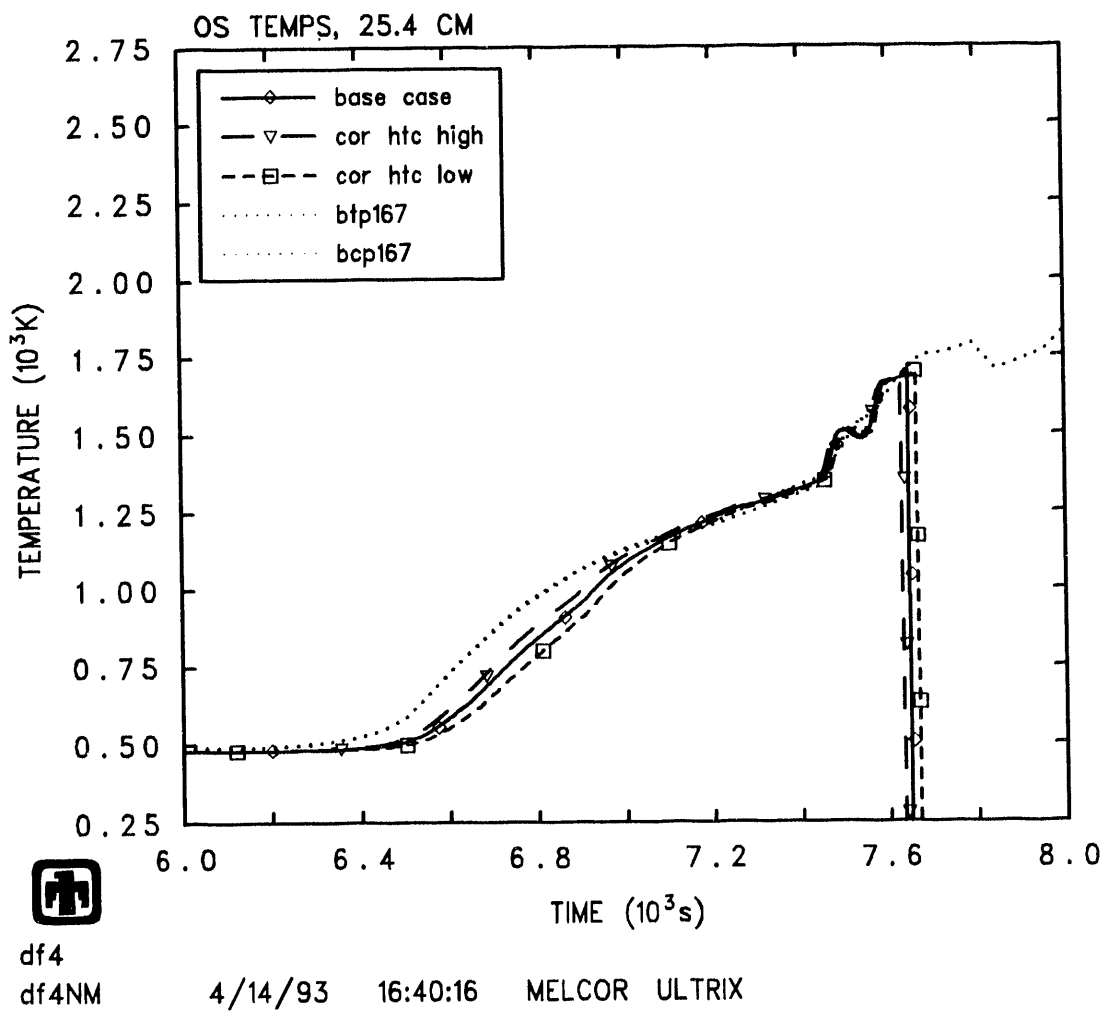
Figure 5.1.3. Control blade temperatures at the 25.4 cm plane for variations on the core convective heat transfer coefficients, compared to base case and measured values.

CLAD TEMPS, 36.8 CM

TEMPERATURE (10^3K)

2.75
2.50
2.25
2.00
1.75
1.50
1.25
1.00
0.75
0.50
0.25

base case
matpro
z1p115
z4p115

6.0   6.4   6.8   7.2   7.6   8.0

TIME (10^3s)

df4
df4NM   4/14/93   16:40:16   MELCOR   ULTRIX
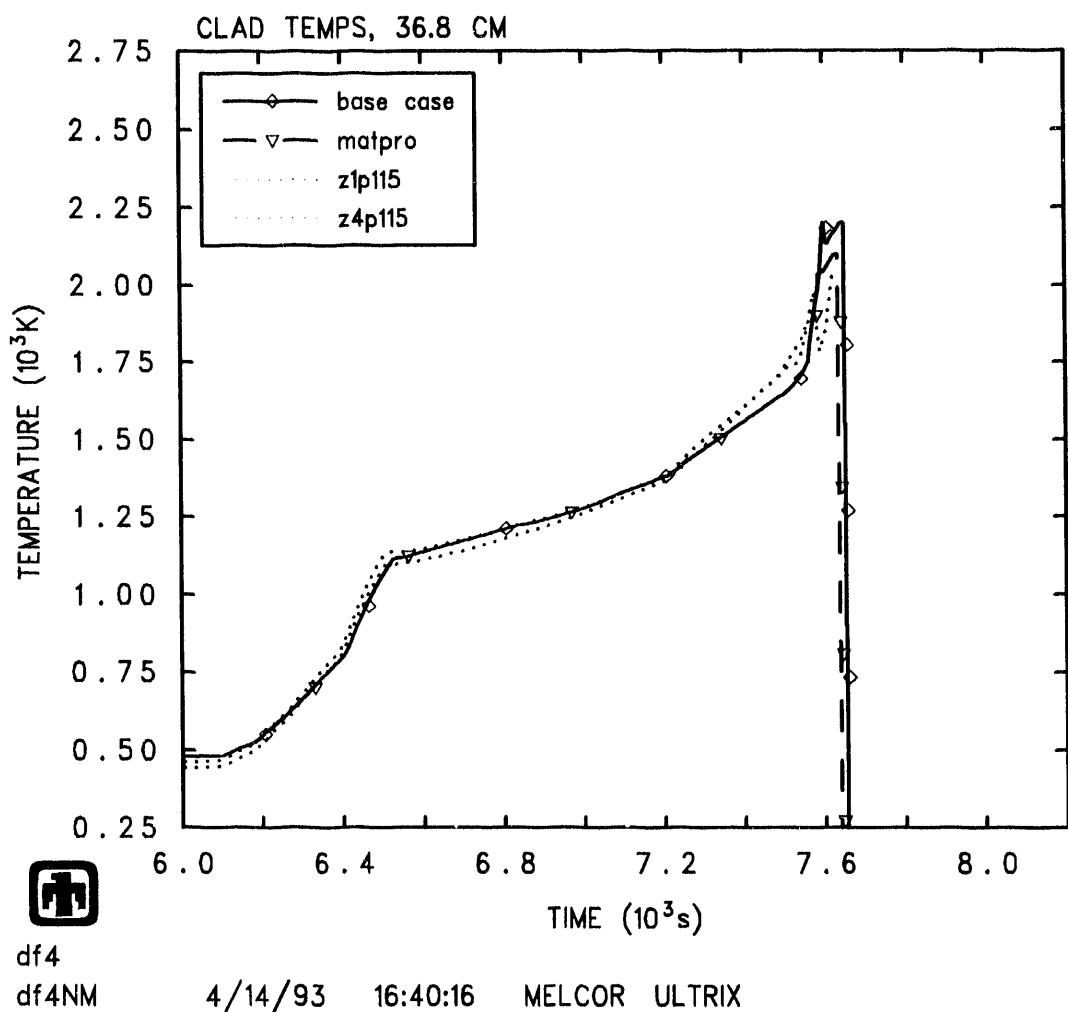
Figure 5.1.4. Cladding temperatures at the 36.8 cm plane for the MATPRO sensitivity study, compared to base case and measured values.
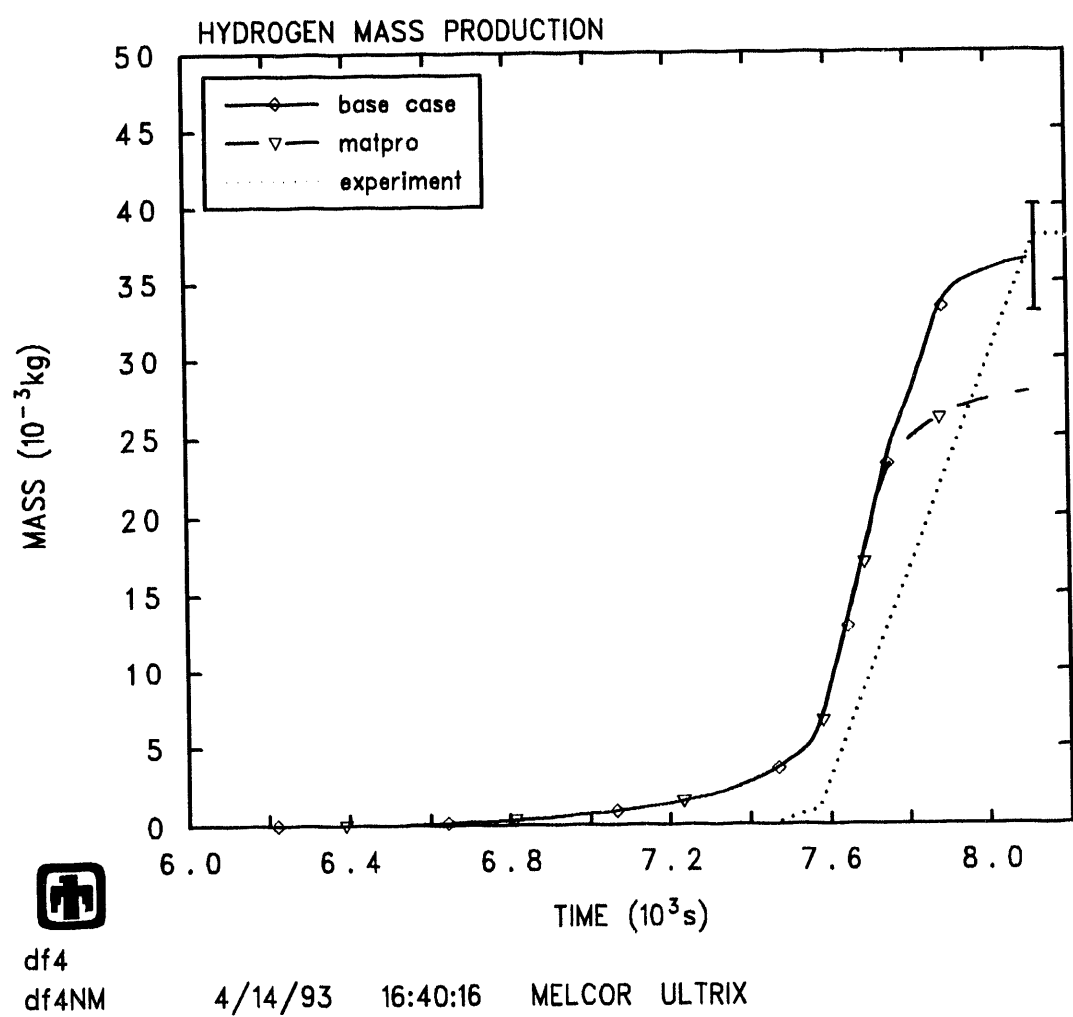
Figure 5.1.5. Hydrogen production for the MATPRO sensitivity study, compared to base case and measured values.

71

5.1.4 Core Component View Factors

The core component view factors used in the MELCOR model for DF-4 were very important in determining heat losses to the insulating shroud outside the test bundle. The test bundle for DF-4 was designed to have high radiation heat transfer between the fuel rods and the canister, which was an important factor in heating up the control blade and starting the B_4C-stainless steel eutectic reaction. The view factors used in the DF-4 base case model were derived from analytical view factor calculations, and are given in Table 3.1.1. Three cases were run for this study, two cases with core package view factors that were 50% and 150% of the base case view factors, and a case using the MELCOR default core component view factors. View factors are input on record COR00003, and have default values of 0.25.

The cladding temperatures at the 25.4 cm plane calculated for this study are shown in Figure 5.1.6. This shows that indeed the radiation view factors did have some influence on the temperature results. Increasing and decreasing the view factors had the expected effect on the cladding; increasing view factors to 150% of the base case values increased the radiation heat transfer from the fuel rods, which lowered the fuel rod temperatures and delayed cladding failure. Decreasing view factors to 50% of the base case values had the opposite effect. The cladding temperature was unchanged below a temperature of 1200K.

Although at first it seems like the default view factors case should have behaved like the 50% case (since most view factors in the DF-4 MELCOR base case model were greater than the default MELCOR values), in reality it behaved like the 150% view factors case. This is because the cell-cell (radial) view factor in the 150% case was closer to the default value than that of the 50% case. Increasing this view factor decreased the cladding temperatures and delayed cladding failure. This effect offset the decrease in the canister-other structure view factor, which resulted in less heat transfer to the control blade.

The control blade temperatures at the 36.8 cm plane showed slightly different behavior in the heatup stage of the experiment. Figure 5.1.7 shows that increasing and decreasing the view factors decreased and increased control blade temperatures at this plane, respectively. The changes were only evident at temperatures above 1200K, similar to the cladding temperature results. Using the default view factors lowered the control blade temperature. This was not surprising, since the canister-other structure view factor was lowered from the base case value of 0.9999 to the default value of 0.25. This resulted in less heat transfer to the control blade and later control blade failure.

The hydrogen production for this study is shown in Figure 5.1.8. Decreasing view factors and thereby increasing cladding temperatures tended to increase early production of hydrogen, while increasing view factors and decreasing cladding temperatures had the opposite effect. Although the timing of hydrogen production was affected, the total amount produced was the same for both cases, and was approximately 3 grams less than that produced in the base case calculation. These data may indicate some tradeoff between the oxidation of zircaloy in the cladding component versus the oxidation of zircaloy in the particulate debris component. The default view fac-

tor case behaved in a similar manner as the 150% case, as it did with the cladding temperatures.

In general, there was a fair amount of sensitivity of final results to view factors, mostly in the timing of failure and of hydrogen production but also in the total amount of hydrogen produced. Note that the influence of view factors on core degradation modeling would probably be greater in the absence of continued nuclear heating, since nuclear heating in DF-4 tended to drive core degradation no matter what the radiation heat transfer was. In any case, the COR component view factors should always reflect the geometry being modeled.

5.1.5   Canister Mass and Area Partition

The COR package in MELCOR allocates canister mass to two components, designated canister and canister-b. The canister-b component is that part of the canister which is adjacent to the control blade, while the canister component is adjacent to other canisters. The separation of the canister mass into these two components affects the heat transfer to the control blade and to the radial boundary in the DF-4 model.

In the MELCOR base case model, all canister zircaloy was allocated to the canister-b component. This was done to more closely match the geometry of the DF-4 test bundle (see Figure 2.1.1), where the majority of the canister area was adjacent to the control blade. In this sensitivity study, the canister mass and area were split evenly between the canister and canister-b components (this is the default configuration in MELCOR). The canister area partition between canister and canister-b components is controlled by sensitivity coefficient 1501.

The temperature response of the cladding at the 36.8 cm plane is compared with that of the base case in Figure 5.1.9. This shows that the default partition of canister mass resulted in earlier failure of the cladding. Figure 5.1.10 shows the same results for the control blade at the 25.4 cm plane. The reason for this could be that allocating less canister mass to the canister-b component provided less of a heat sink between the fuel rods and the control blade, resulting in earlier control blade and cladding heatup and failure.

The overall hydrogen production for this study was almost identical to the base case value, but was generated slightly earlier in the problem. This was consistent with the temperature behavior.

The final material distributions for the canister and canister-b components for this sensitivity study calculation are shown in Figure 5.1.11. These component distribution plots can be compared with the final base case canister-b component material distribution shown in Figure 4.2.10. This figure indicates that using the default partition of canister mass resulted in slightly less total canister mass remaining in the middle of the test bundle and slightly more refrozen zircaloy at the bottom of the test bundle at the end of the problem. This suggests that the canister and canister-b components melted faster in this sensitivity study calculation, and relocated to the bottom of the core.

This study indicates that there were slight differences in final material locations due to the allocation of all canister mass to the canister-b component, while the
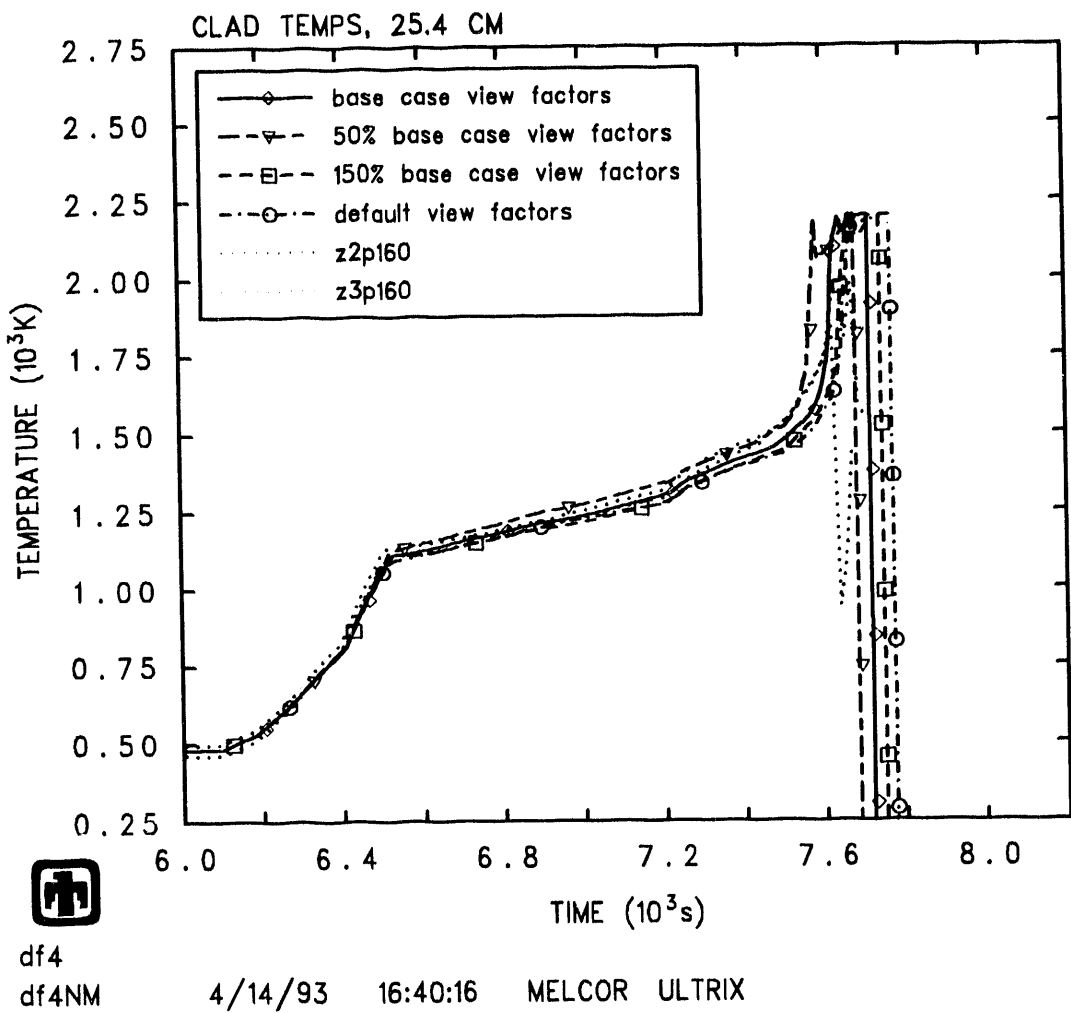
Figure 5.1.6. Cladding temperatures at the 25.4 cm plane for the radiation view factor sensitivity study, compared to base case and measured values.
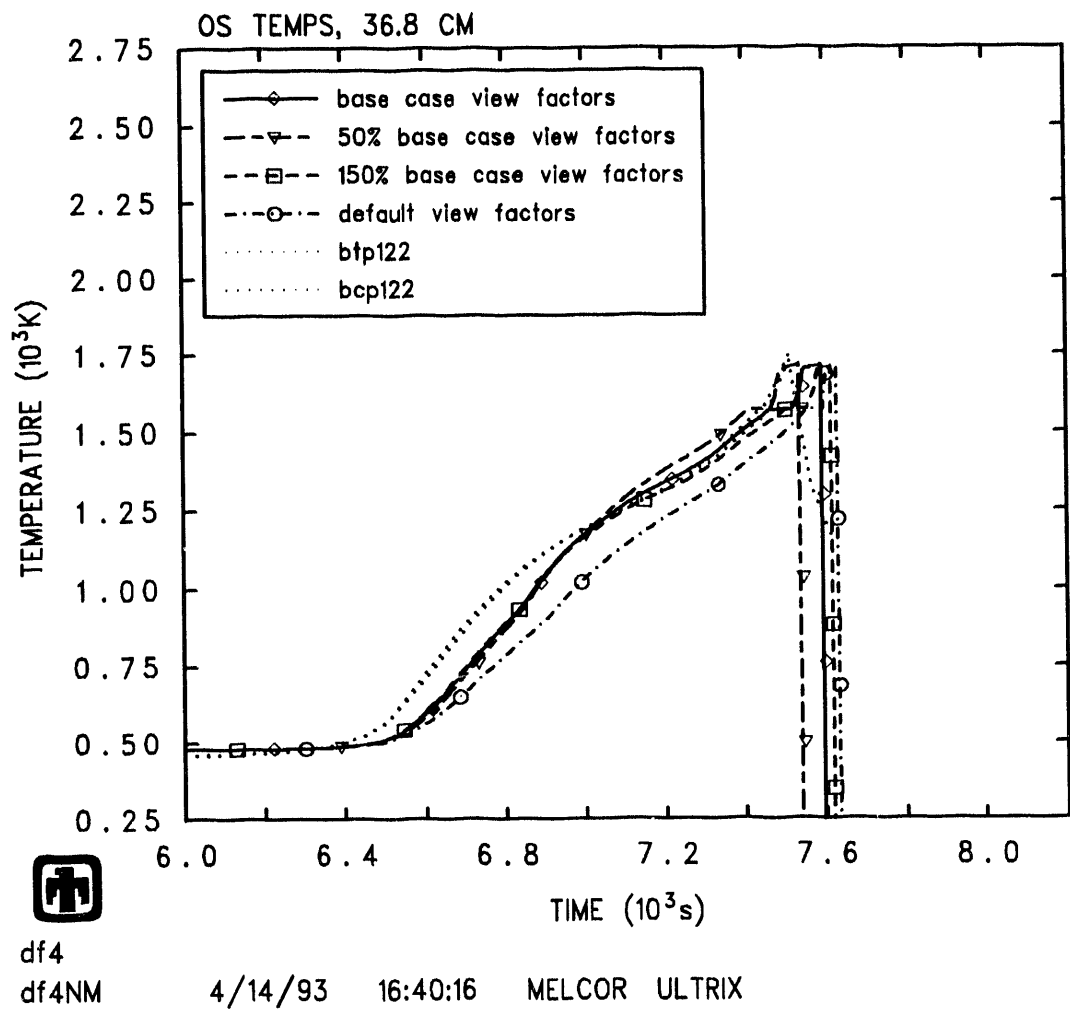
Figure 5.1.7. Control blade temperatures at the 36.8 cm plane for the radiation view factor sensitivity study, compared to base case and measured values.
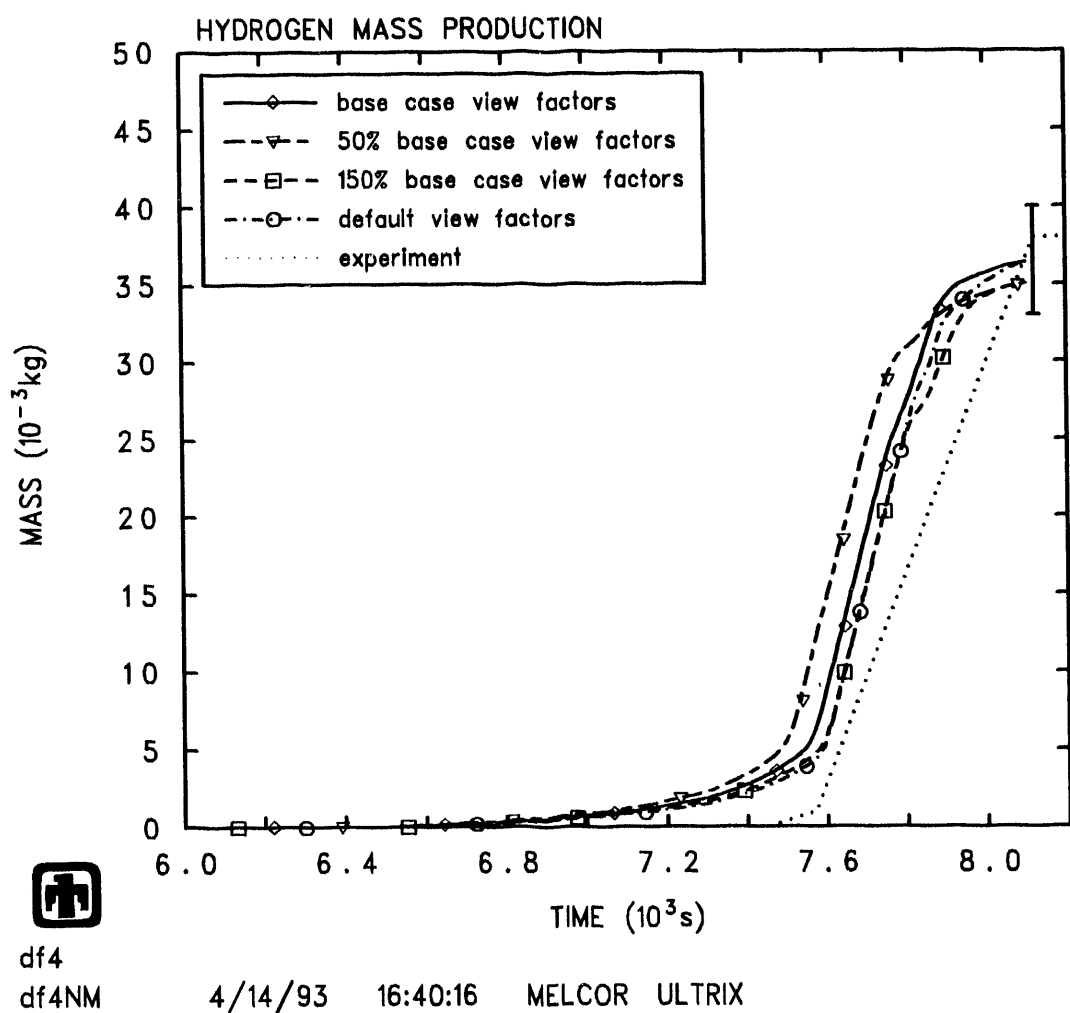
Figure 5.1.8. Hydrogen production for the radiation view factor sensitivity study, compared to base case and measured values.

temperature and failure timing of the cladding and control blade components showed some sensitivity to where the canister mass was allocated. We suggest allocating canister mass in a manner which best represents the experimental or plant geometry.

5.1.6 Minimum Component Mass

The COR package allows the user to set the minimum significant mass for any component in sensitivity coefficient array 1502. When a component falls below this value its mass and energy are discarded. SC1502 also contains an element for the minimum component mass which is used for time step control. The default values for these coefficients are 10^{-3} kg and 10.0 kg, respectively (these values are based on typical PWR and BWR cores). In the MELCOR base case model, these limits were set to 10^{-5} and 10^{-4} kg, respectively. These are compared with the minimum single-cell initial component mass in the DF-4 model of 4.4 grams, for the control rod poison (B_4C) component. In this sensitivity study, the minimum component mass and the minimum mass for temperature control sensitivity coefficients were changed to the default MELCOR values.

The hydrogen production for this case is compared with the base case and measured results in Figure 5.1.12. There was a slight increase in hydrogen production at the end of the problem when the minimum component mass parameters were set to their default values. The temperature results for the cladding and control blade were almost identical to the base case results. The minimum component mass parameters in the COR package did not affect the COR package or the system time step.

Although in this case there were no obvious effects, we nevertheless recommend that the values of these parameters reflect the component masses in the input problem.

5.1.7 Candling Heat Transfer Coefficient

The COR package in MELCOR treats candling using an effective heat transfer coefficient between the candling and substrate materials. This coefficient is supposed to account for the fraction of component area that is actually covered by the candling material. In this way, the COR package can model either "rivulet" or "film" candling. The default candling heat transfer coefficients were not chosen to model either of these options, but were based on other considerations [17].

The discussion of relocation behavior in Section 4.2 indicates that control blade materials in the MELCOR base case calculation candled a shorter distance before refreezing than was indicated by experimental data. In this sensitivity study, the candling heat transfer coefficients for all materials were reduced to 10% and 1% of the default values for all materials in an attempt to more closely match experimental relocation behavior (the default value for candling heat transfer coefficients in MELCOR is 1000 W/m^{2}K). These values are input on record COR00005.

The largest change as a result of reducing the candling heat transfer coefficients in the COR package was expected in the control blade temperatures in the lower half of the test bundle, where most of the candling took place. The cladding and control blade temperatures at that plane are compared to base case and measured results
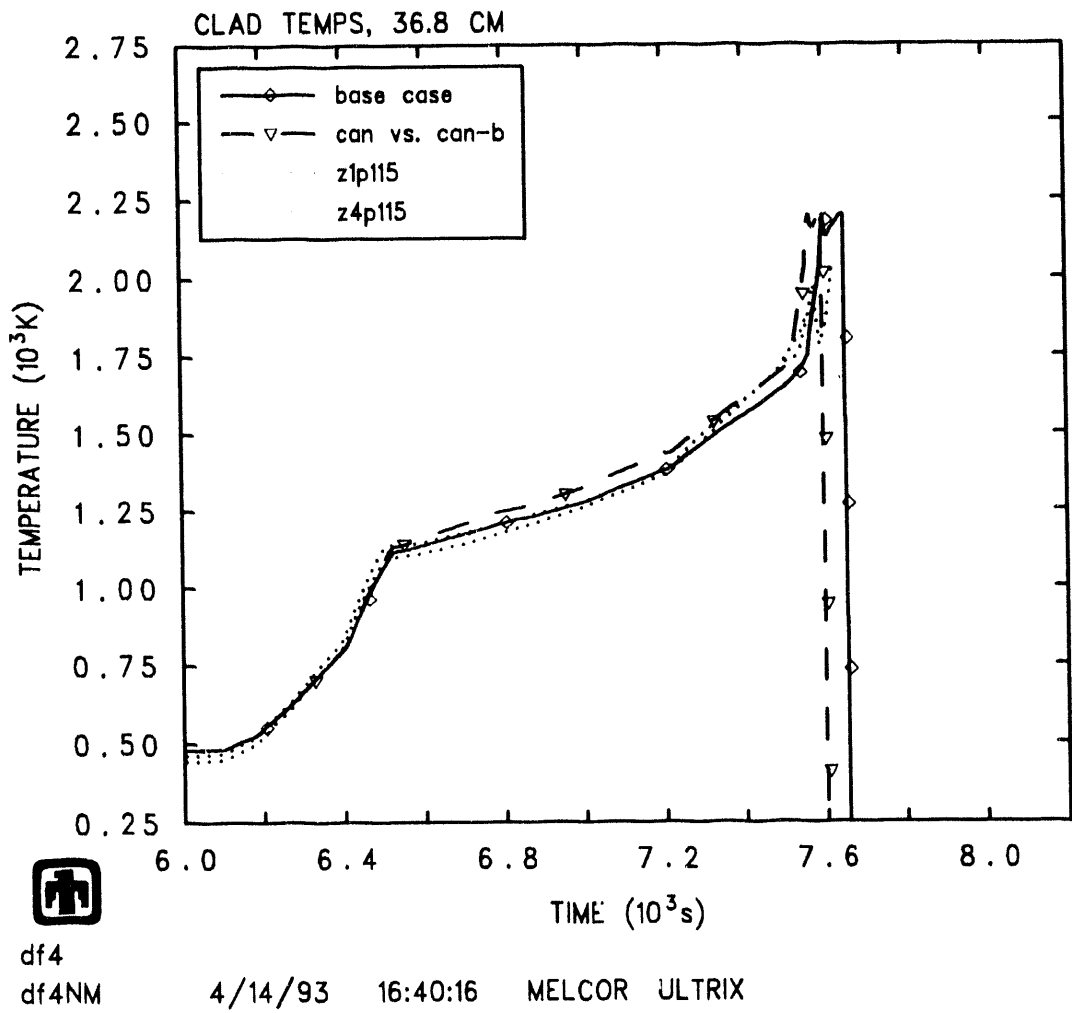
Figure 5.1.9. Cladding temperature response at the 36.8 cm plane for the canister mass and area partition sensitivity study calculation, compared to base case and measured values.
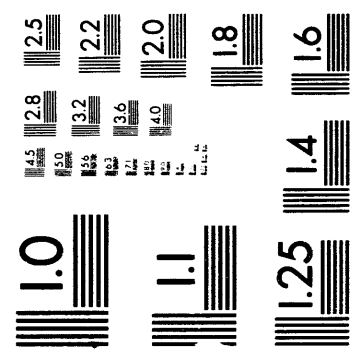
2 of 3
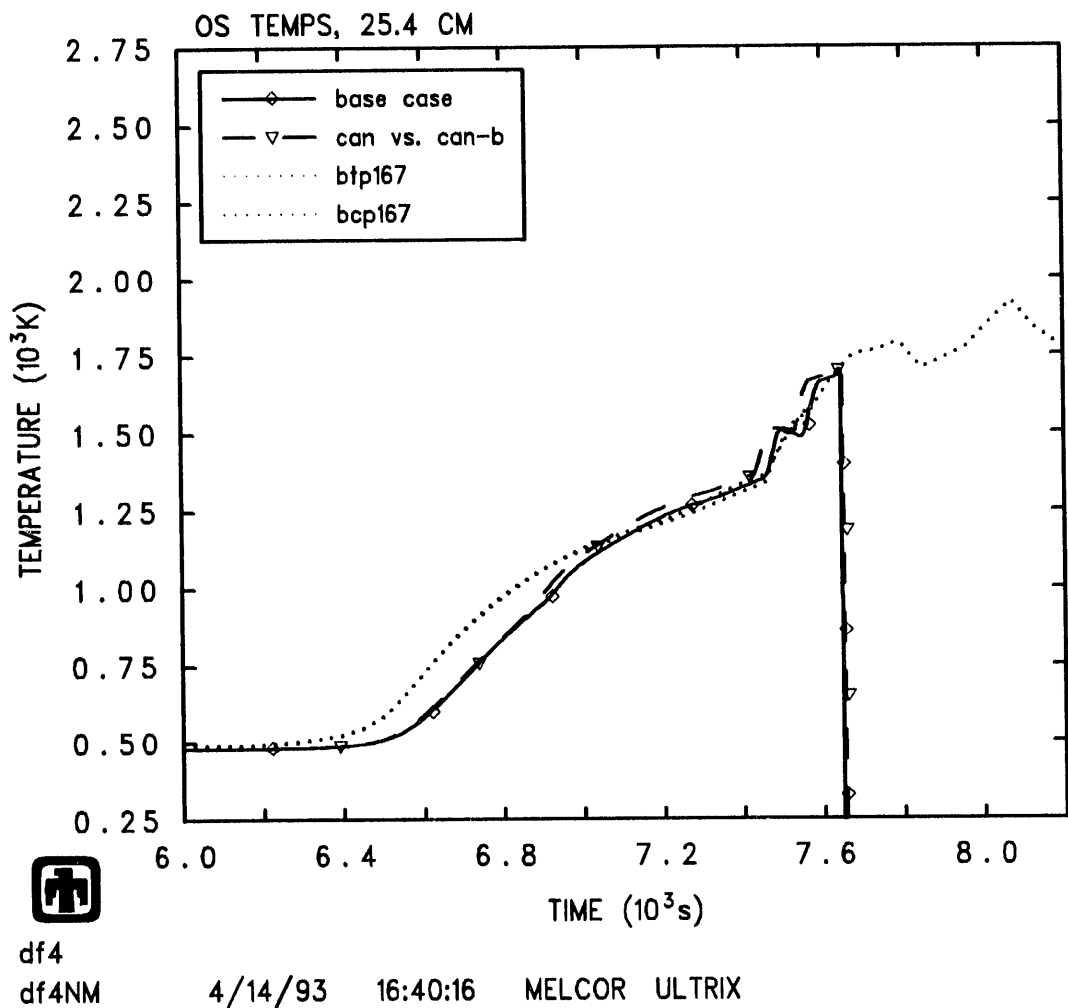
Figure 5.1.10. Control blade temperature response at the 25.4 cm plane for the canister mass and area partition sensitivity study calculation, compared to base case and measured values.

DF-4 Canister-B (t=8100.0s)

Elevation (10⁻¹m)

Fraction of Total Cell Volume X 10⁻¹

Intact:

UO₂

Zr

SS

ZrO₂

SSOX

CRP

INC

Cong Debris:

UO₂ in Deb

Zr in Deb

SS in Deb

ZrO₂ in Deb

SSOx in Deb

CRP in Deb

INC in Deb

DF-4 Canister (t=8100.0s)

Elevation (10⁻¹m)

Fraction of Total Cell Volume X 10⁻¹
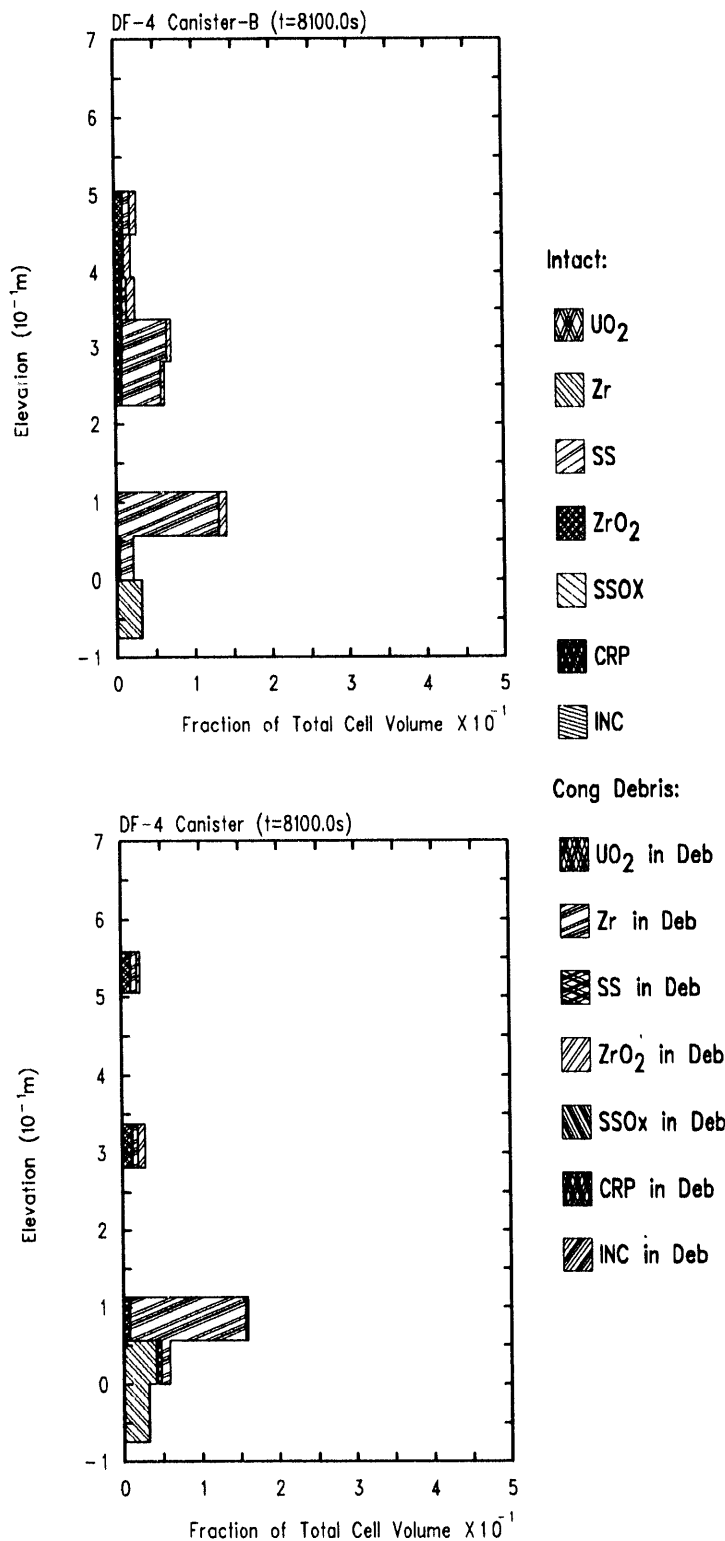
Figure 5.1.11. Canister component (top) and canister-b component (bottom) material distributions at 8100 seconds for the canister mass and area partition sensitivity study calculation (base case canister-b component material distributions are shown in Figure 4.2.10).

HYDROGEN MASS PRODUCTION
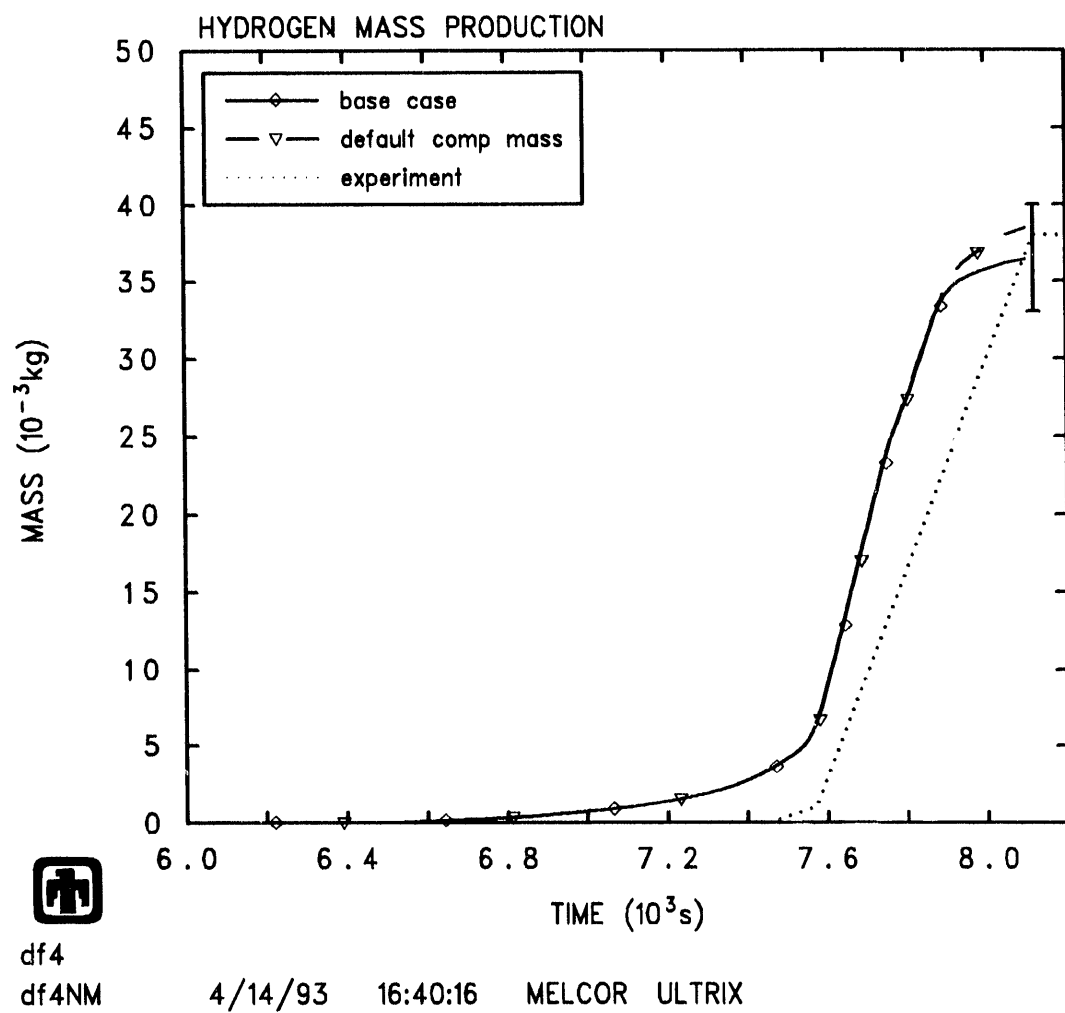
Figure 5.1.12. Hydrogen production for the minimum component mass sensitivity study, compared to base case and measured values.

81

in Figures 5.1.13 and 5.1.14, respectively. For the cladding, the early temperature rise due to the arrival of melt was slightly greater for the 1% case, but otherwise the temperatures were very close. This is not surprising, given that most of the material relocating into this region was solid debris that did not candle.

The results for the control blade were much different. Candling played a significant role in the relocation of control blade material. Decreasing the candling heat transfer coefficient resulted in much better agreement with experimental results in the timing of melt arrival at the base of the control blade. The blockage formed by core materials prevented the control blade at this plane from failing, and allowed this component to heat up beyond the stainless steel melting temperature.

The cladding and control blade temperatures at the 25.4 cm plane are shown in Figures 5.1.15 and 5.1.16, respectively. The cladding heatup at about 7600 seconds was slightly delayed for the 1% case. In the base case model a great deal of material refroze at this plane. Reducing the candling heat transfer coefficient forced this material to candle past the 25.4 cm plane, resulting in less heatup. This effect is more obvious in the control blade, where candling played a stronger role in relocation. The heatup due to melt arrival was delayed slightly for the 10% case and more significantly for the 1% case. Note that failure of the control blade at this plane was not delayed by more than 20 seconds even for the 1% case.

At the 36.8 cm and 49.5 cm planes, the temperature behavior was almost identical for all cases, because very little material candled and refroze in these planes.

The hydrogen production for the 10% and 1% cases is compared to base case and measured results in Figure 5.1.17. Decreasing the candling heat transfer coefficient slightly decreased the overall hydrogen production. This was the result of refreezing much lower in the test bundle, which decreased the amount of zircaloy heated to autocatalytic oxidation temperatures in the active regions of the core.

The material locations at 7600 seconds for the 1% case are shown in Figure 5.1.18. This figure can be compared to the base case values at 7600 seconds, shown in Figure 4.2.5. Figure 5.1.18 shows much more control blade (other structure) material at the bottom of the test bundle. This is in better agreement with the PIE and the video record of DF-4, which showed the control blade material to candle much farther down in the test bundle. The fuel and cladding component plot shows that axial level 11 (at 40 cm) had not failed at 7600 seconds; this agrees with the slightly delayed cladding temperature shown in Figure 5.1.15.

In conclusion, reducing the candling heat transfer coefficient improved agreement with measured response in the timing of melt arrival at the base of the bundle and in the final distribution of control blade materials. However, it also made the temperature response in the 25.4 cm plane a bit worse compared to the measured response. The MELCOR user is advised to study the effect of varying the candling heat transfer coefficients in the COR package.

5.1.8 Minimum Oxide Shell Thickness

The relocation of core materials after they become molten is controlled by parameters in three MELCOR input records. The minimum oxide shell thickness required
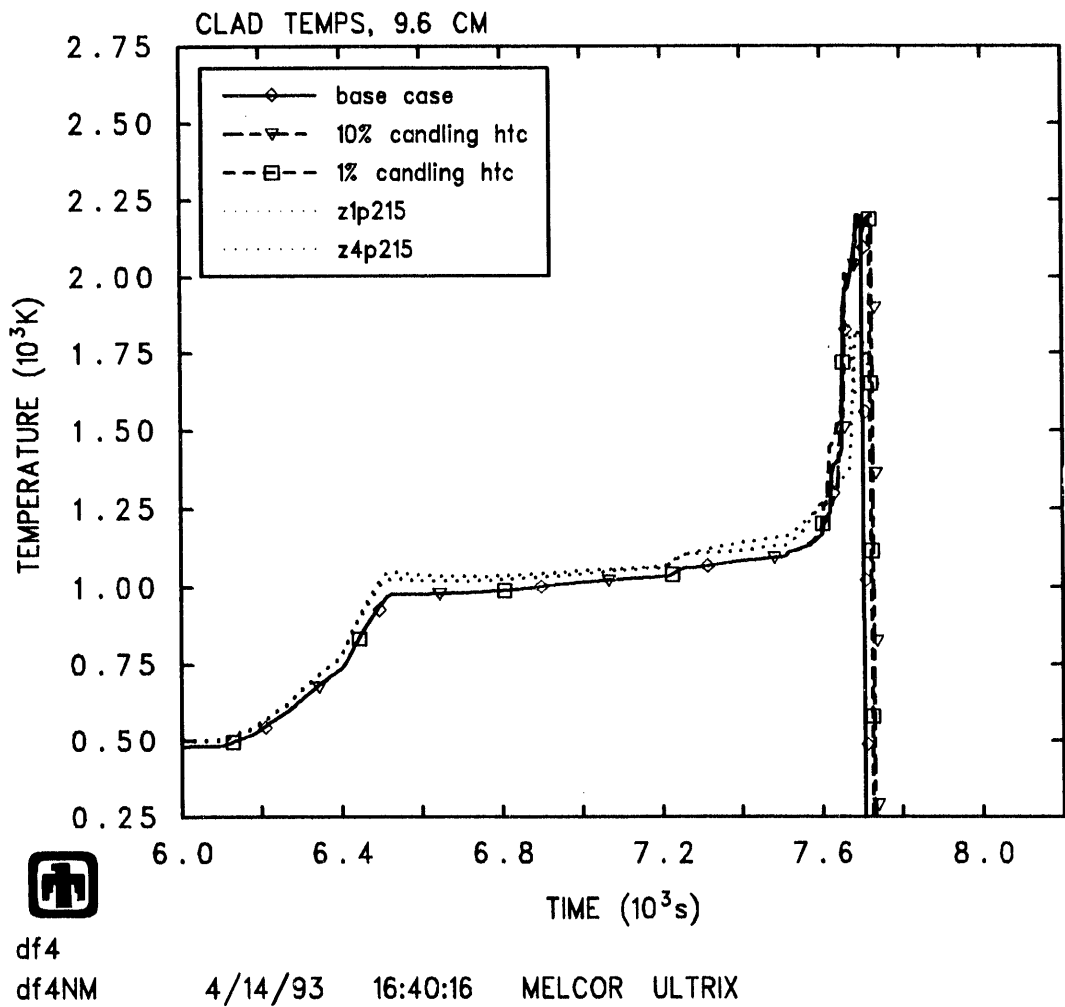
Figure 5.1.13. Cladding temperature response at the 9.6 cm plane for the candling heat transfer coefficient sensitivity study, compared to base case and measured values.
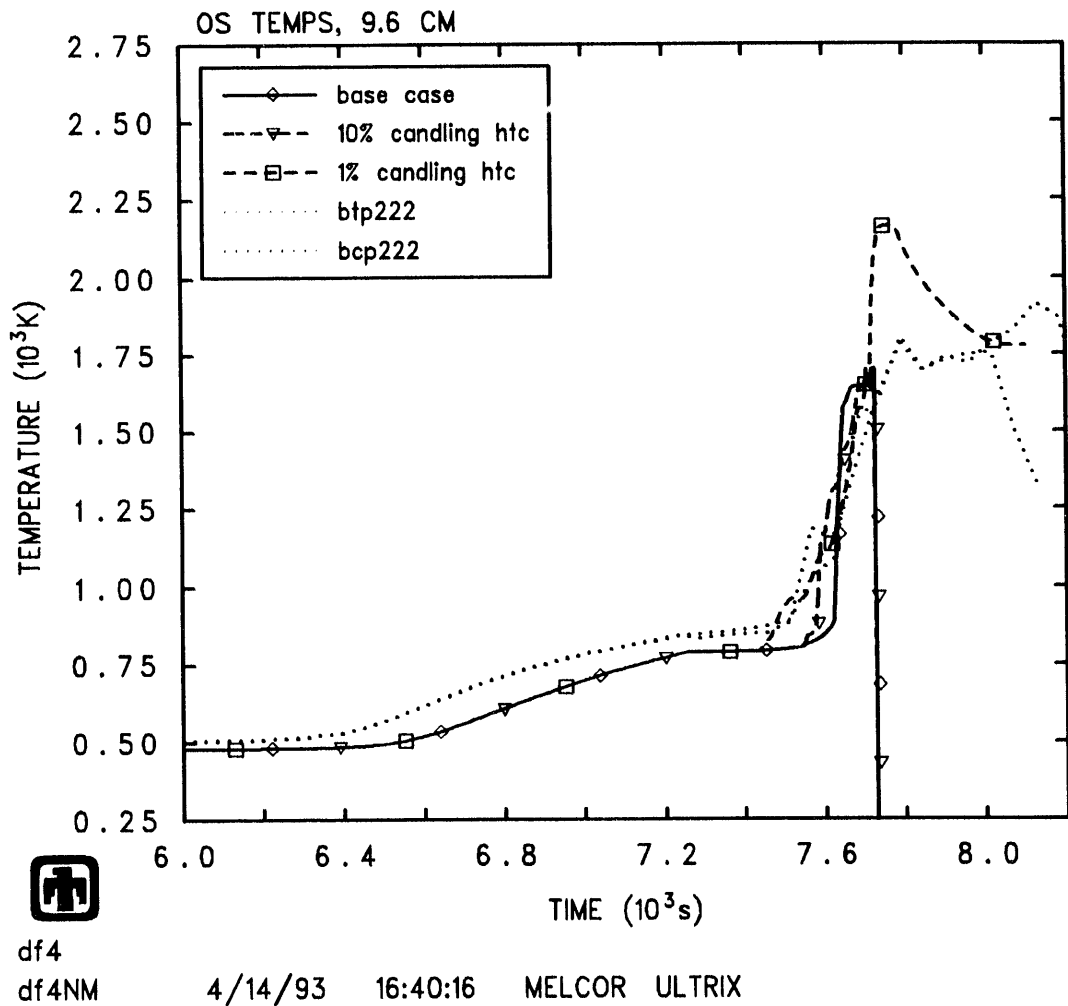
Figure 5.1.14. Control blade temperature response at the 9.6 cm plane for the candling heat transfer coefficient sensitivity study, compared to base case and measured values.
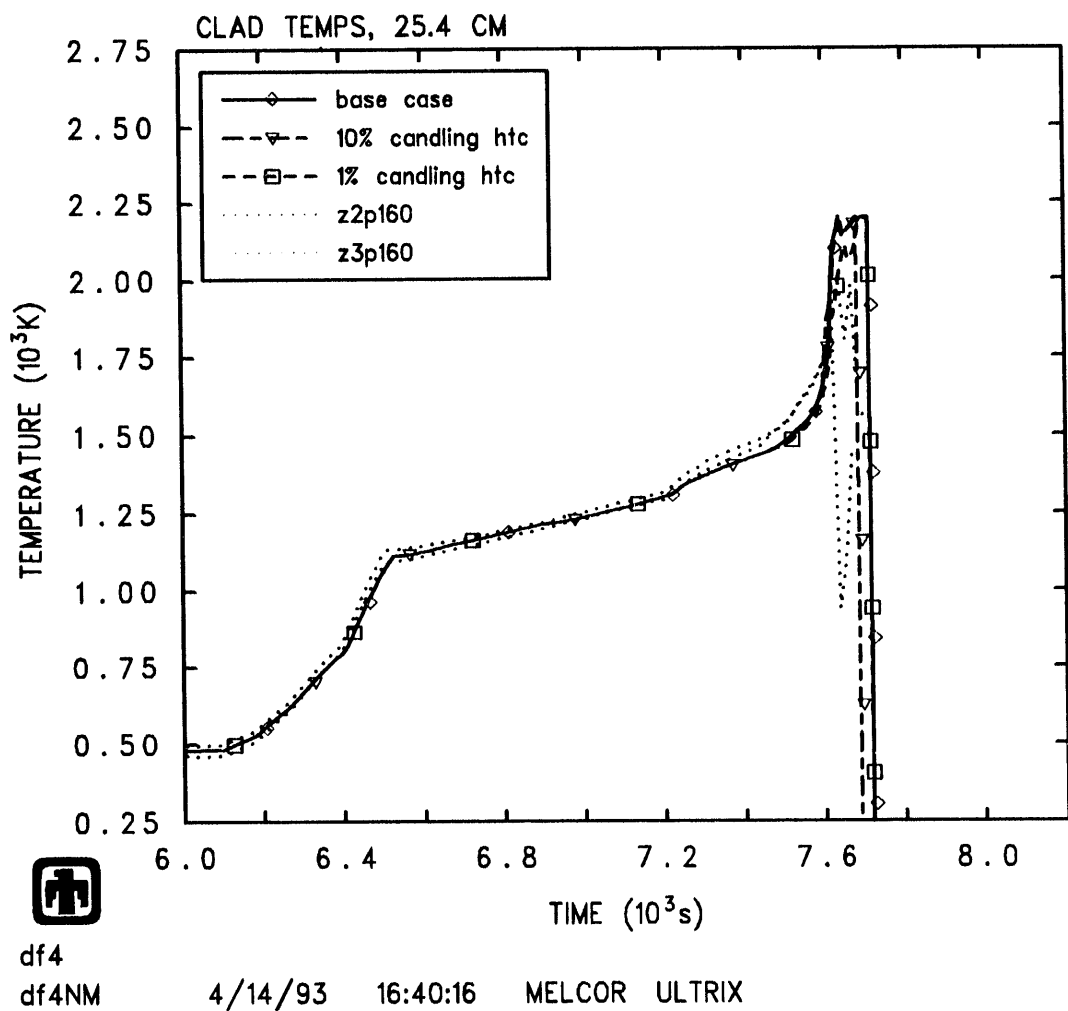
Figure 5.1.15. Cladding temperature response at the 25.4 cm plane for the candling heat transfer coefficient sensitivity study, compared to base case and measured values.
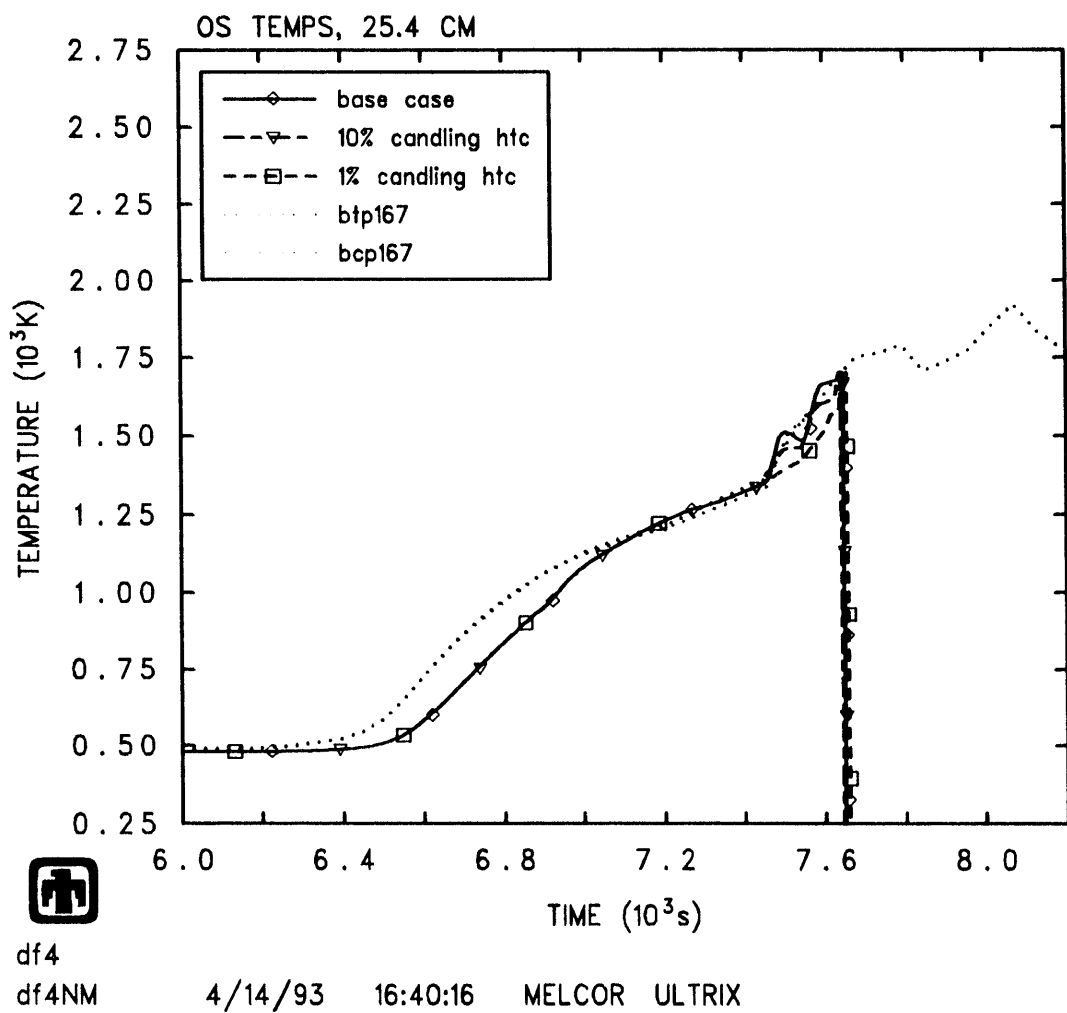
Figure 5.1.16. Control blade temperature response at the 25.4 cm plane for the candling heat transfer coefficient sensitivity study, compared to base case and measured values.
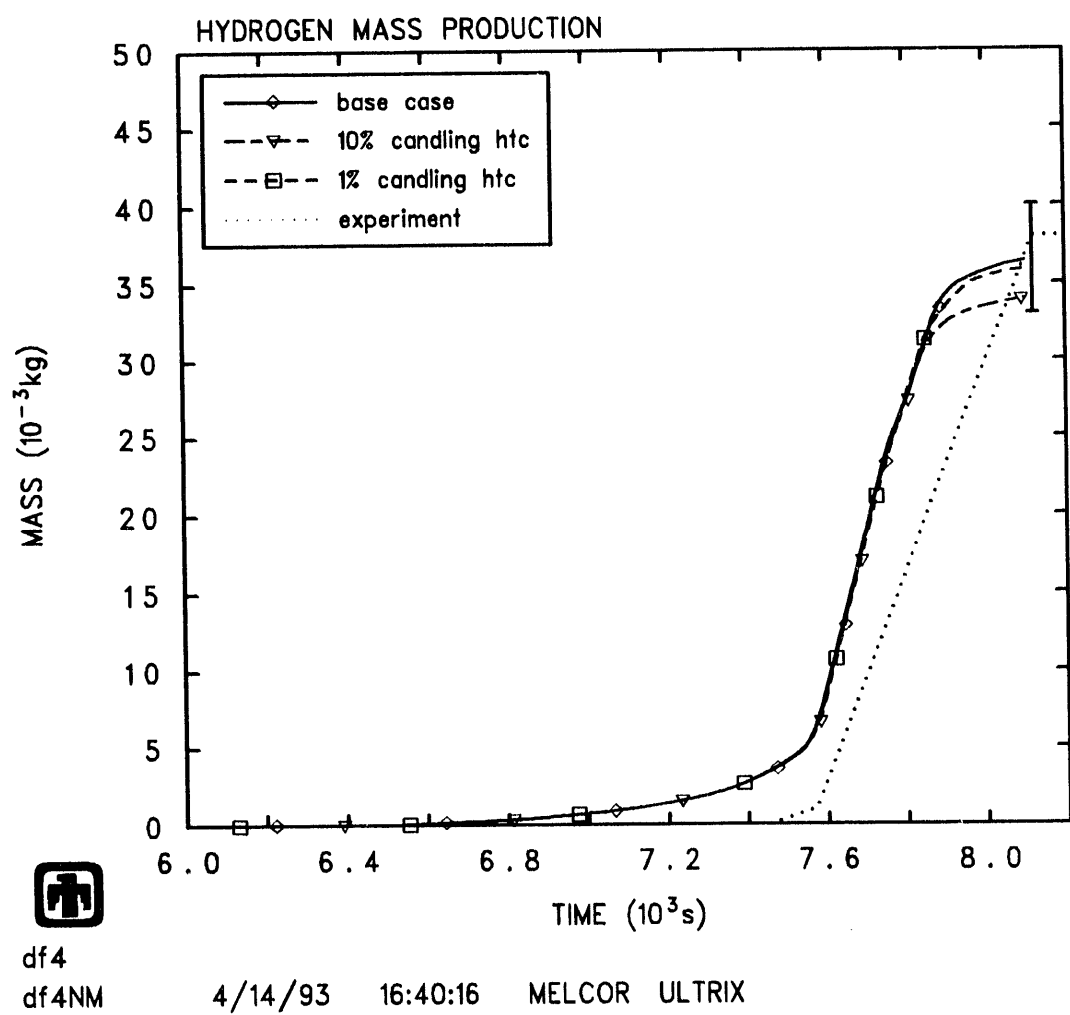
Figure 5.1.17. Hydrogen production for the candling heat transfer coefficient sensitivity study, compared to base case and measured values.
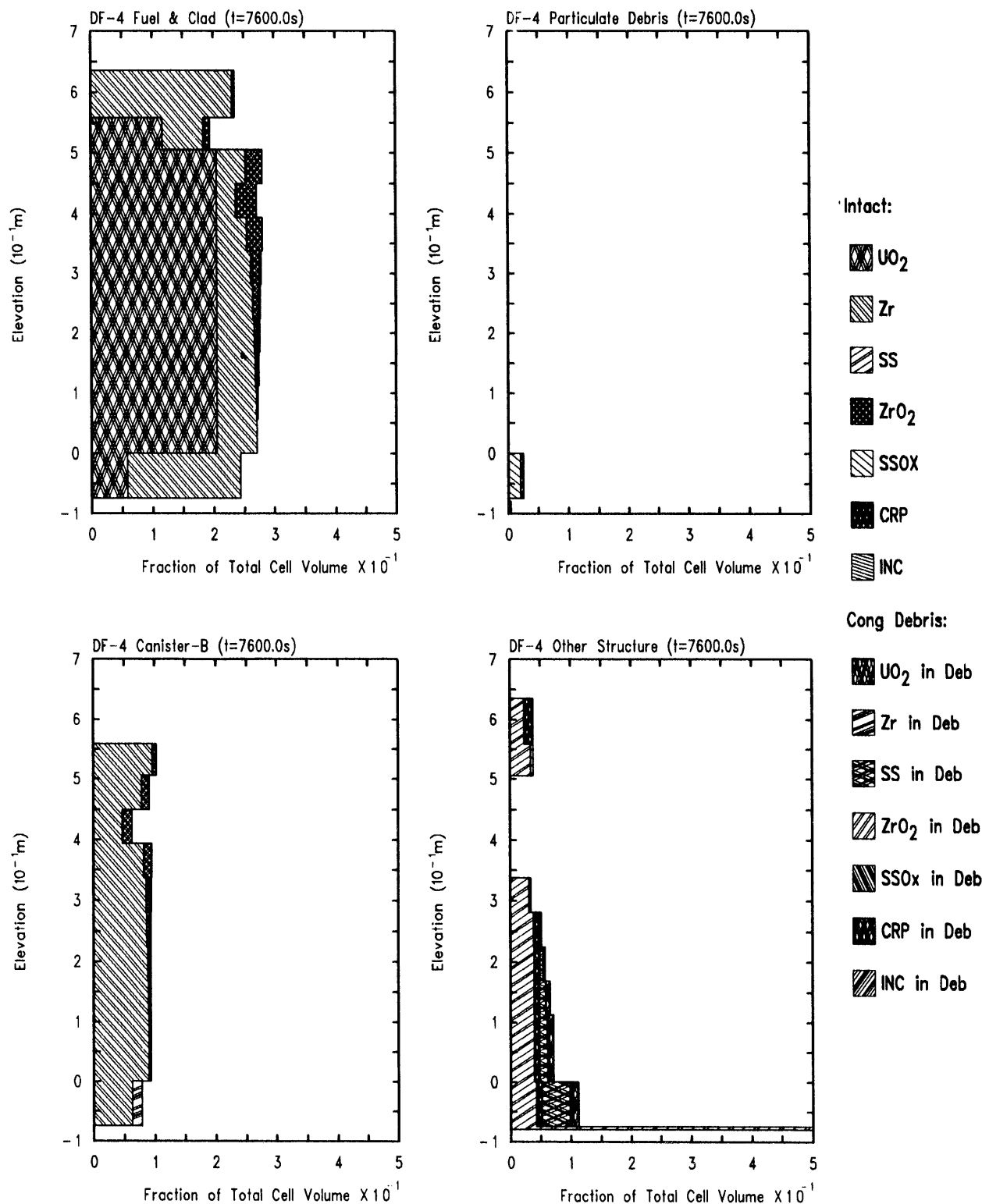
Figure 5.1.18. Component material distributions at 7600 seconds for the 1% case of the candling heat transfer coefficient sensitivity study.

to hold up molten material for both zirconium oxide and stainless steel oxide is controlled using sensitivity coefficient array 1131. When materials melt and candle, they are allowed to take along other materials in the same core cell. This is called "secondary material transport," and is intended to model the dissolution of intact material by the candling material (this model is disabled when the eutectics model is active). The transport of secondary materials with the primary candling materials is controlled by parameters input on record COR00007. Finally, the critical minimum thickness of unoxidized zircaloy in the cladding and canister components and of unoxidized stainless steel in the other structure component are input on record COR00008; the zircaloy parameter determines the minimum thickness of unoxidized zircaloy necessary to hold up fuel and cladding materials, while the stainless steel parameter determines the minimum stainless steel thickness required to hold up other structure materials.

In the DF-4 base case input model, the minimum oxide shell thickness needed to hold up molten material at that level was specified to be approximately one tenth the thickness of the oxidizing component. For zircaloy, this parameter was specified as 61μm, and for stainless steel it was specified as 142μm. The default value for both of these parameters is 1 mm. Also, the default values for the secondary material transport parameters were used. Both critical minimum unoxidized material thicknesses were left at their default values of 0.0001 m (0.1 mm).

Two cases were originally designed, each with two changes to the base case. First, the minimum oxide shell thicknesses for both ZrO_2 and stainless steel oxide were set to 10μm and 1μm. Second, in the same way as was done in the LOFT assessment [11], the transport of secondary materials was disabled in both cases using record COR00007 input. Both of these cases (using 10μm and 1μm for minimum oxide shell thicknesses and no secondary material transport) resulted in almost no difference in temperature behavior throughout the test bundle, for both the cladding and other structure components, and insignificant differences in total hydrogen production.

After further investigation, it was decided to run two more cases for this sensitivity study, each of which had three changes to the base case. The first two changes were identical to those in the previous paragraph. In addition, the debris formation parameters in record COR00008 were adjusted such that no unoxidized zircaloy and stainless steel was required to hold up the associated components. It was later determined that changing the secondary material transport parameters had no effect on the results, since the secondary transport model in MELCOR is disabled when the eutectics model is active.

For the latter two sensitivity study calculations, the changes to component temperatures were also relatively minor. For example, the cladding temperatures at the 36.8 cm plane are shown in Figure 5.1.19. The only difference with base case temperatures in this case was that the cladding component at the 36.8 cm plane did not fail. This was due to the oxide layer preventing the conversion of fuel, cladding and oxides at that axial level to debris after all intact zircaloy was depleted. The control blade temperatures at the 36.8 cm plane are shown in Figure 5.1.20, and the hydrogen production is shown in Figure 5.1.21. There was little change in the control blade temperatures and the overall hydrogen production.

The final material locations for the 1μm case are shown in Figure 5.1.22 (the 10μm case was almost identical). This should be compared to Figure 4.2.10 for the base case. The adjustment of debris formation parameters strongly affected the final material locations, as expected. All of the control blade relocated, due to the dissolution of control blade materials by B$_4$C, while the fuel component was intact at all levels, held up by a layer of ZrO$_2$.

The fuel pellet stacking that resulted from the adjustment to the parameters described in this section was more realistic when compared to the final debris state in DF-4. However, these adjustments also resulted in the full oxide layer remaining in place of the intact cladding. This is in contrast to DF-4, where much of the oxidized cladding was dissolved by candling zircaloy. When modeling experiments that exhibit fuel pellet stacking, these parameters should probably be adjusted to allow MELCOR to leave fuel pellets stacked.

5.1.9 Heat Structure Boundary Fluid Temperature Option

The COR package dT/dz model calculates the rise in control volume atmosphere temperature as the atmosphere vapor travels through core cells. This model provides a finer resolution of core atmosphere temperatures than the CVH package is able to provide. These dT/dz temperatures are used to calculate heat transfer between the fluid and the core components and radial boundary heat structures. The default temperature used to calculate heat transfer with the radial boundary heat structures is the bulk CVH atmosphere temperature (the control volume bulk pool temperatures are used below the liquid level in each core control volume). For this project, an option was implemented in the HS and COR packages to use local dT/dz temperatures instead of bulk CVH atmosphere temperatures to calculate heat transfer to the radial boundary heat structures. This option was implemented in the release version of MELCOR and was used for all radial boundary heat structures in the DF-4 base case model. In this sensitivity study, the default MELCOR option was specified for all radial boundary heat structures so that CVH bulk atmosphere temperatures were used to calculate heat transfer with radial heat structures. This option is specified on the HSCCCCC004 record.

The control volume bulk atmosphere temperature for this case is compared with base case results in Figure 5.1.23. Using the default option in all cells had the effect of raising control volume bulk atmosphere temperatures. This was the result of the artificial heatup of the heat structure surfaces in the lower core cells by bulk CVH atmosphere temperatures which were higher than the dT/dz temperatures in those lower core cells. The resulting cladding and control blade temperatures at the 36.8 cm plane are shown in Figures 5.1.24 and 5.1.25, respectively. Raising the CVH bulk atmosphere temperature increased the cladding and control blade temperatures, and resulted in earlier component failure. The hydrogen production for both cases
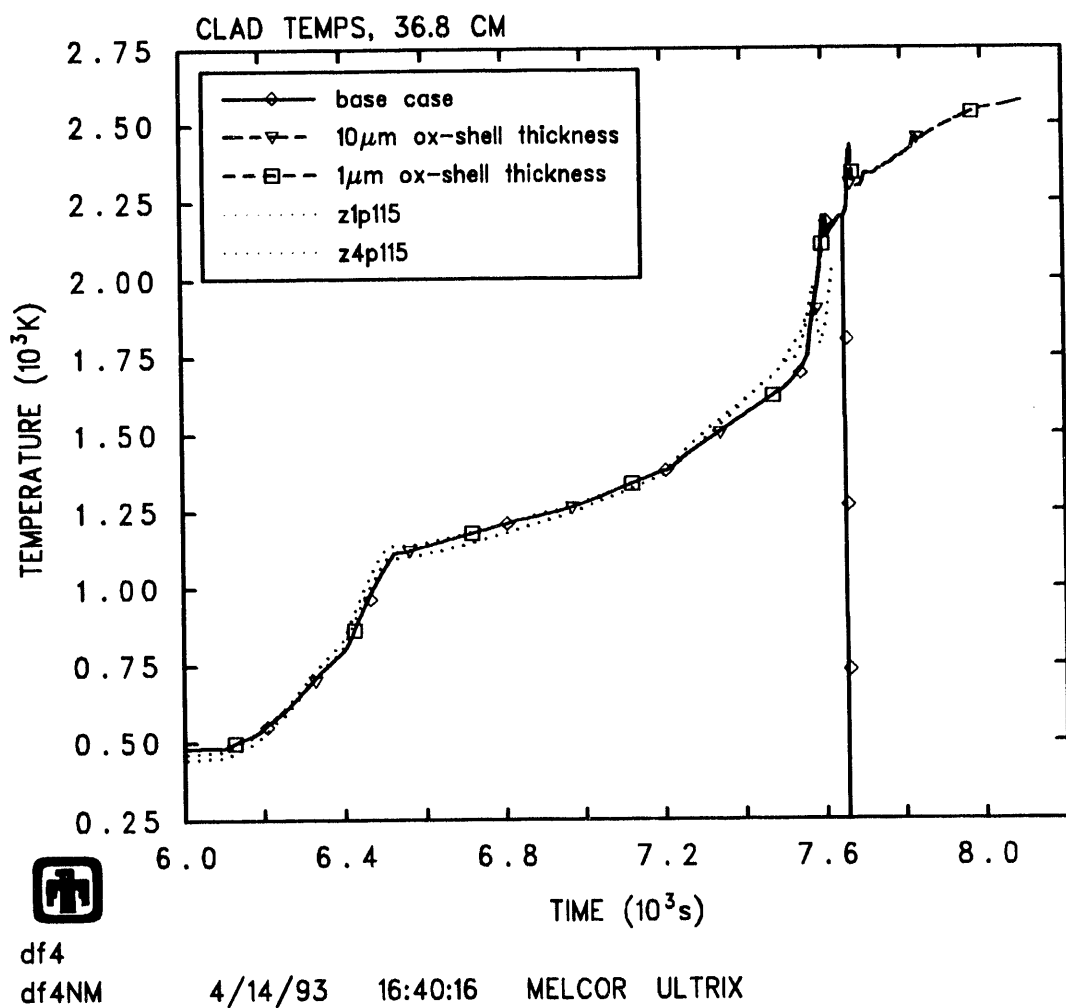
Figure 5.1.19. Cladding temperatures at the 36.8 cm plane for the minimum oxide shell thickness sensitivity study, compared to base case and measured values.
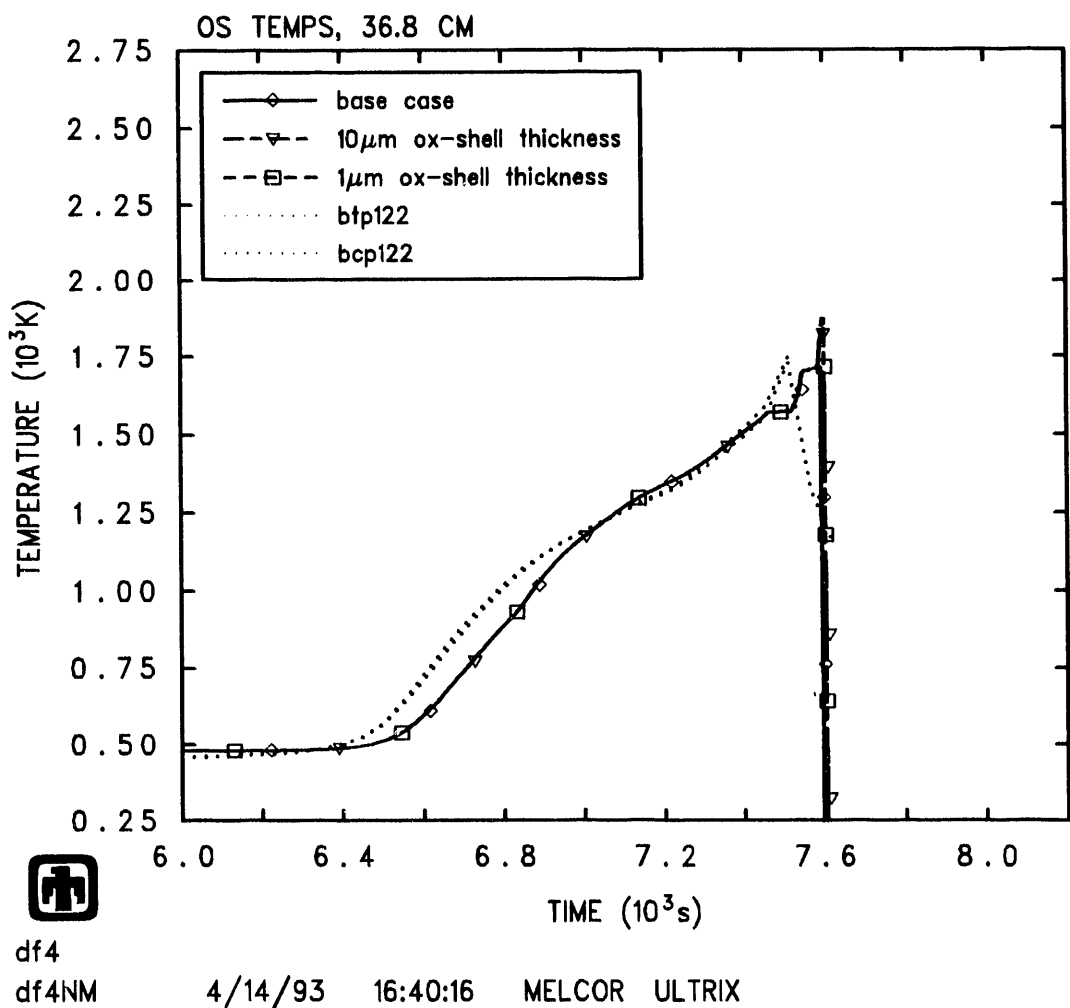
Figure 5.1.20. Control blade temperatures at the 36.8 cm plane for the minimum oxide shell thickness sensitivity study, compared to base case and measured values.

HYDROGEN MASS PRODUCTION

50

45

40

35

30

25

20

15

10

5

0

MASS (10^{-3}kg)

base case
10μm ox-shell thickness
1μm ox-shell thickness
experiment

6.0   6.4   6.8   7.2   7.6   8.0

TIME (10^{3}s)

df4
df4NM   4/14/93   16:40:16   MELCOR   ULTRIX
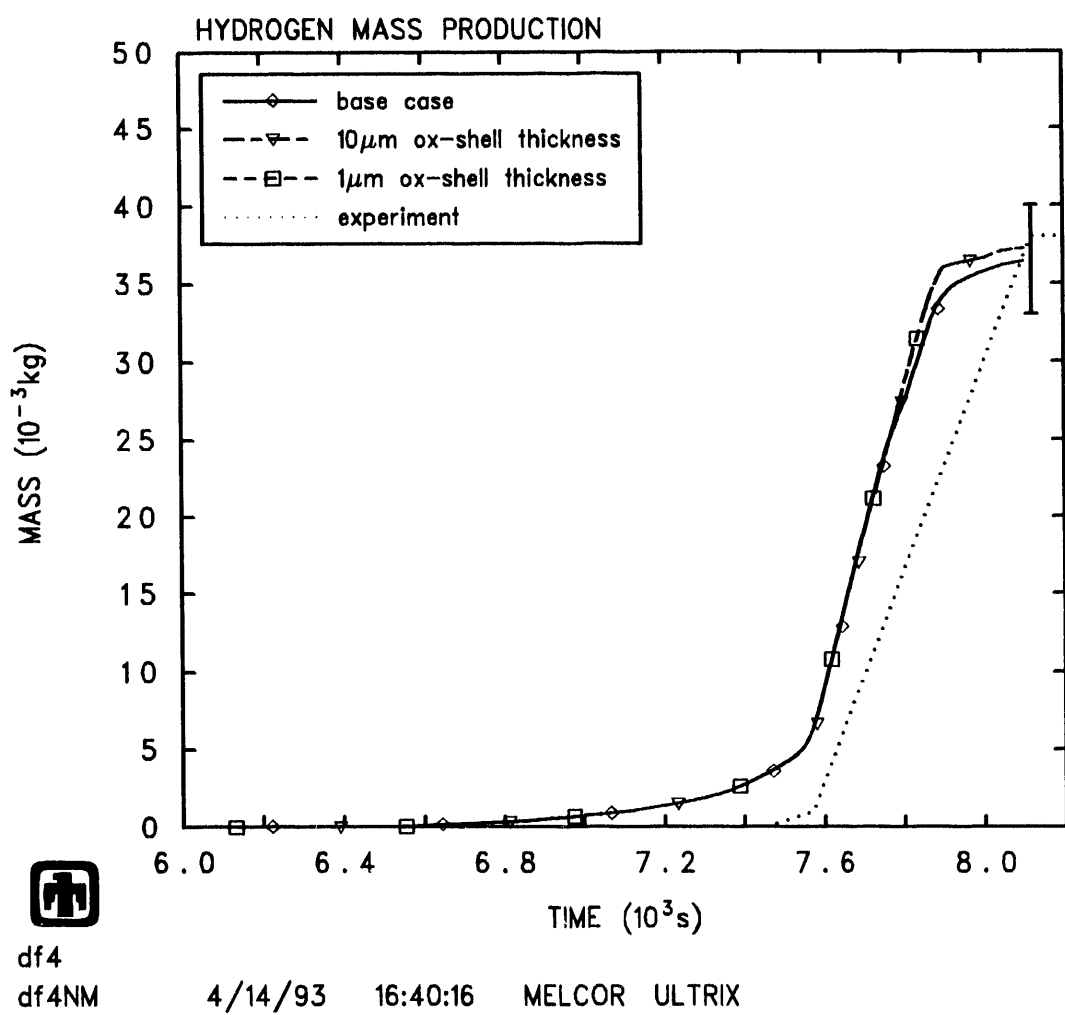
Figure 5.1.21. Hydrogen production for the minimum oxide shell thickness sensitivity study, compared to base case and measured values.

93
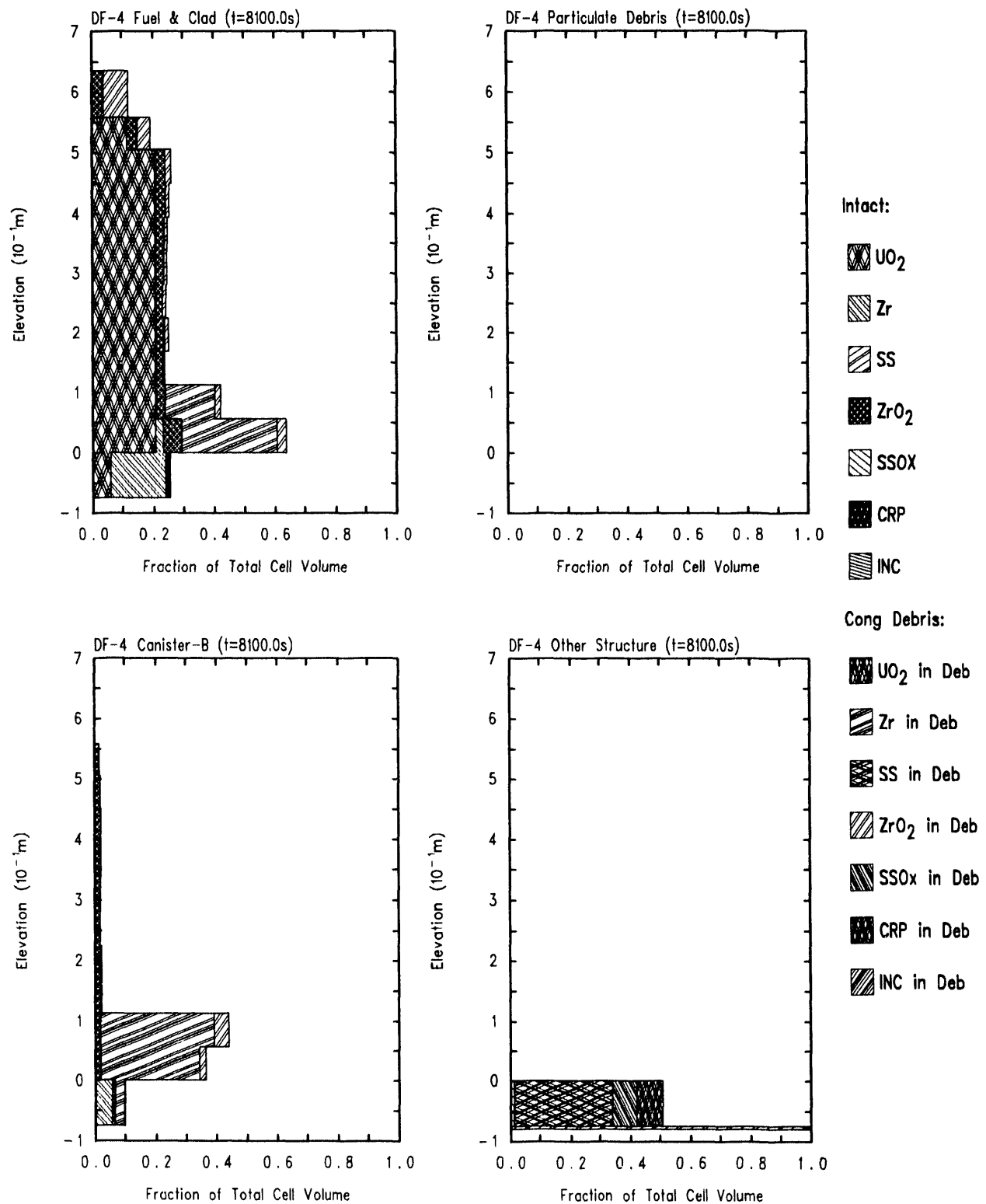
Figure 5.1.22. Component material distributions at 8100 seconds for the 1μm case of the minimum oxide shell thickness sensitivity study.

is shown in Figure 5.1.26. The early component failure decreased the time available for the oxidation of intact core components, which resulted in less overall hydrogen production. The hydrogen production in the sensitivity study case was moved forward in time as well, due to the increased cladding temperatures.

The effect of the new boundary heat structure fluid temperature option was to lower core component temperatures and delay component failure. Using this option more accurately models the heat transfer with radial boundary heat structures. It is therefore recommended that this new option be used in future MELCOR modeling efforts.

5.2 Debris Behavior Studies

Two sensitivity studies were performed to study the effects of varying debris behavior parameters in MELCOR. These studies concerned the debris porosity and the particulate debris diameter specified in COR package input.

5.2.1 Debris Porosity

The debris porosity is specified for each axial level in the COR package on record CORZjj01. The intact material porosity is also specified on this record. For this sensitivity study, the debris porosity was increased and decreased from its base case value of 0.50, resulting in porosities of 0.30 and 0.70. The intact porosity was also increased from the base case value of 0.0 to 0.25 for both cases. There are no default values for intact or debris porosities. Increasing the porosity of a component had the effect of increasing the volume occupied by that component, and raising the upper surface of the debris pile in the bottom of the test bundle.

Decreasing the debris porosity had a relatively large effect on the amount of hydrogen produced. This was especially true for the DF-4 experiment, where more than 50% of the hydrogen was produced as a result of debris oxidation. Figure 5.2.1 shows that decreasing the debris porosity decreased the amount of hydrogen produced by about 10 grams, or 26%. Increasing the porosity increased the hydrogen produced by 12%. Changing the debris porosity changed the amount of debris surface area exposed to the control volume atmosphere. It also affected how much cladding was exposed to the atmosphere, since the debris porosity determined the height of debris stacked in the bottom of the test bundle.

The final state of the particulate debris component in the test bundle for the small debris porosity case (porosity = 0.30) is shown in Figure 5.2.2, while the final state of the particulate debris component for the large debris porosity case (porosity = 0.70) is shown in Figure 5.2.3 (these can be compared with the final state of components in the base case, shown in Figure 4.2.10). These figures show that decreasing the debris porosity resulted in more debris at lower axial levels. This increased debris concentration led to earlier cladding failure at those levels (see Figure 5.2.4). The temperature response for the control blade, however, shows that decreasing the debris porosity delayed slightly the arrival of melt at the 9.6 cm plane (see Figure 5.2.5).
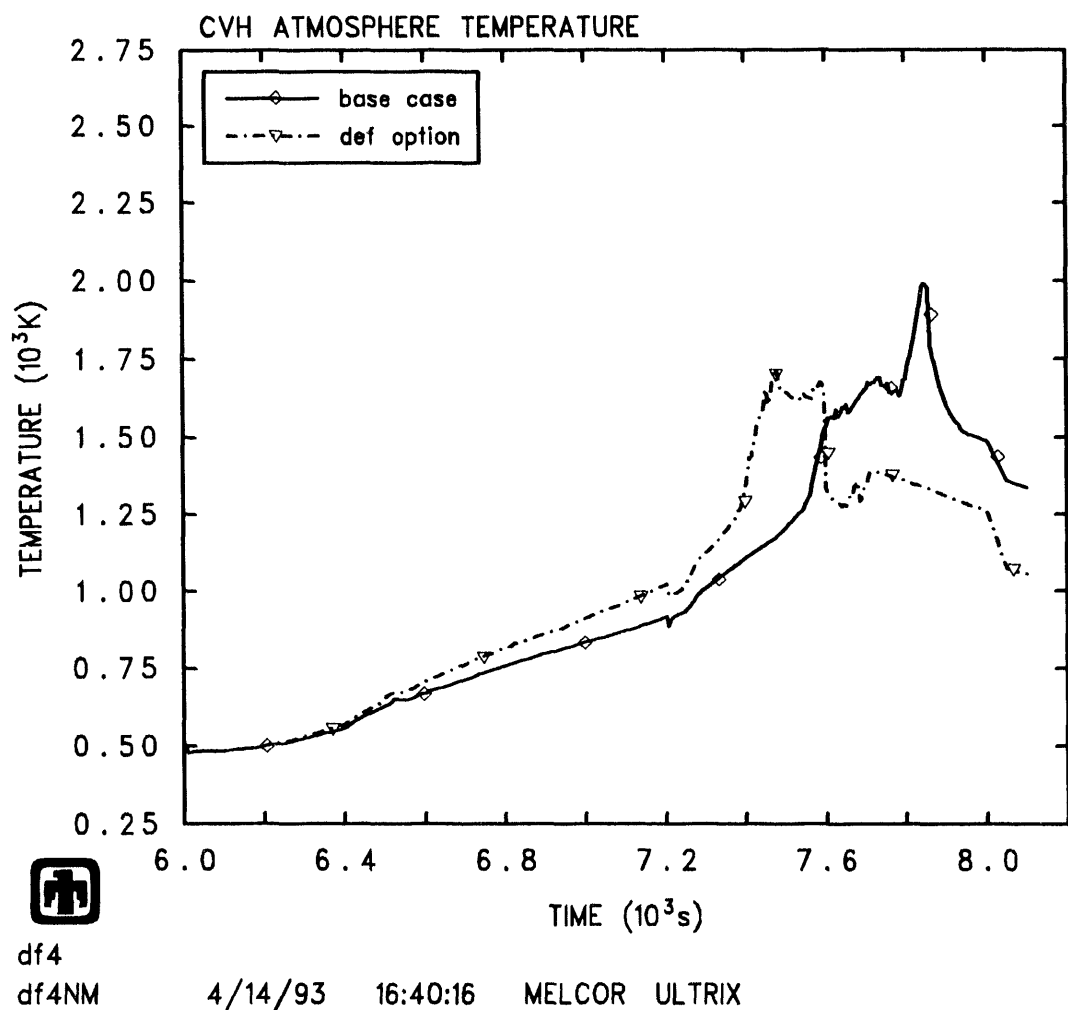
Figure 5.1.23. CVH bulk atmosphere temperature for the default boundary fluid temperature option sensitivity study, compared to base case values.
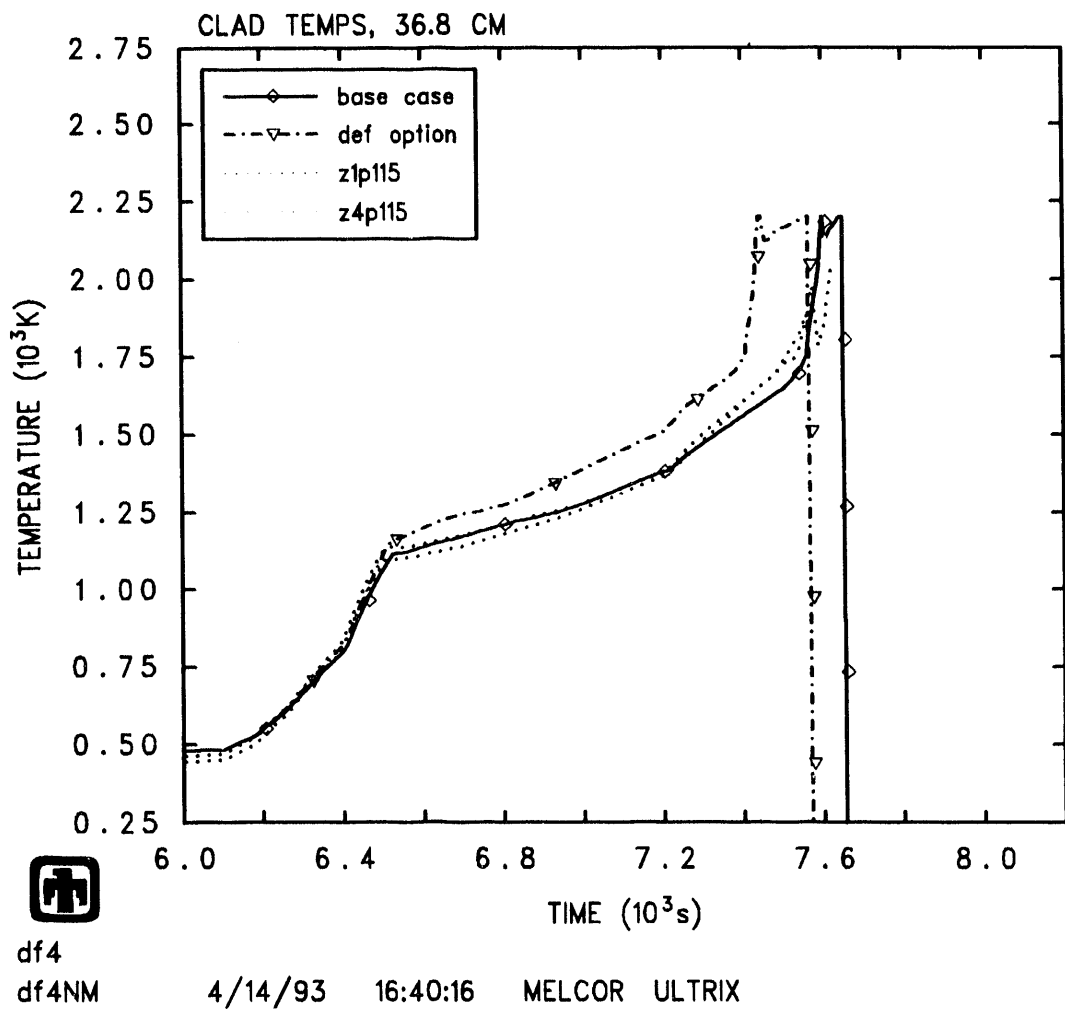
Figure 5.1.24. Cladding temperatures at the 36.8 cm plane for the default boundary fluid temperature option sensitivity study, compared to base case and measured values.
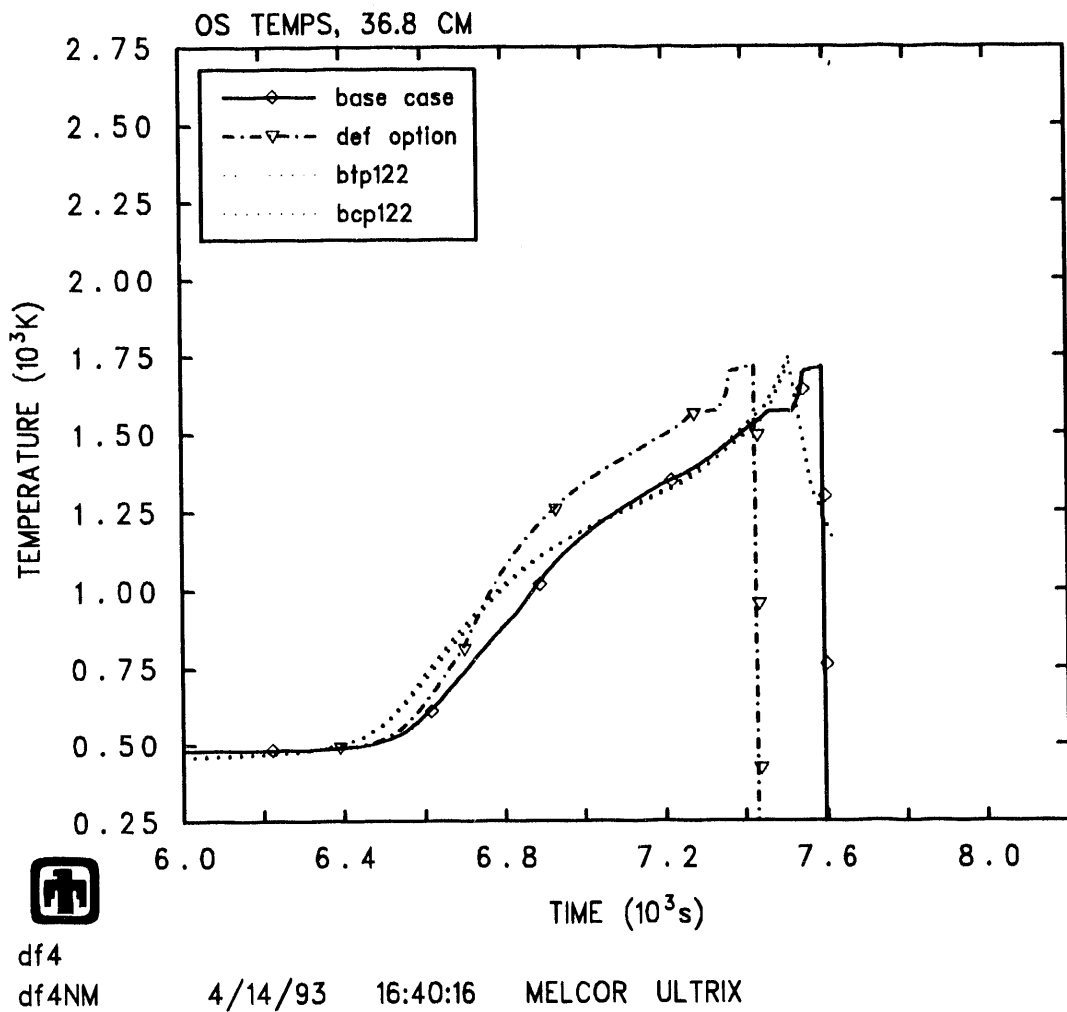
Figure 5.1.25. Control blade temperatures at the 36.8 cm plane for the default boundary fluid temperature option sensitivity study, compared to base case and measured values.
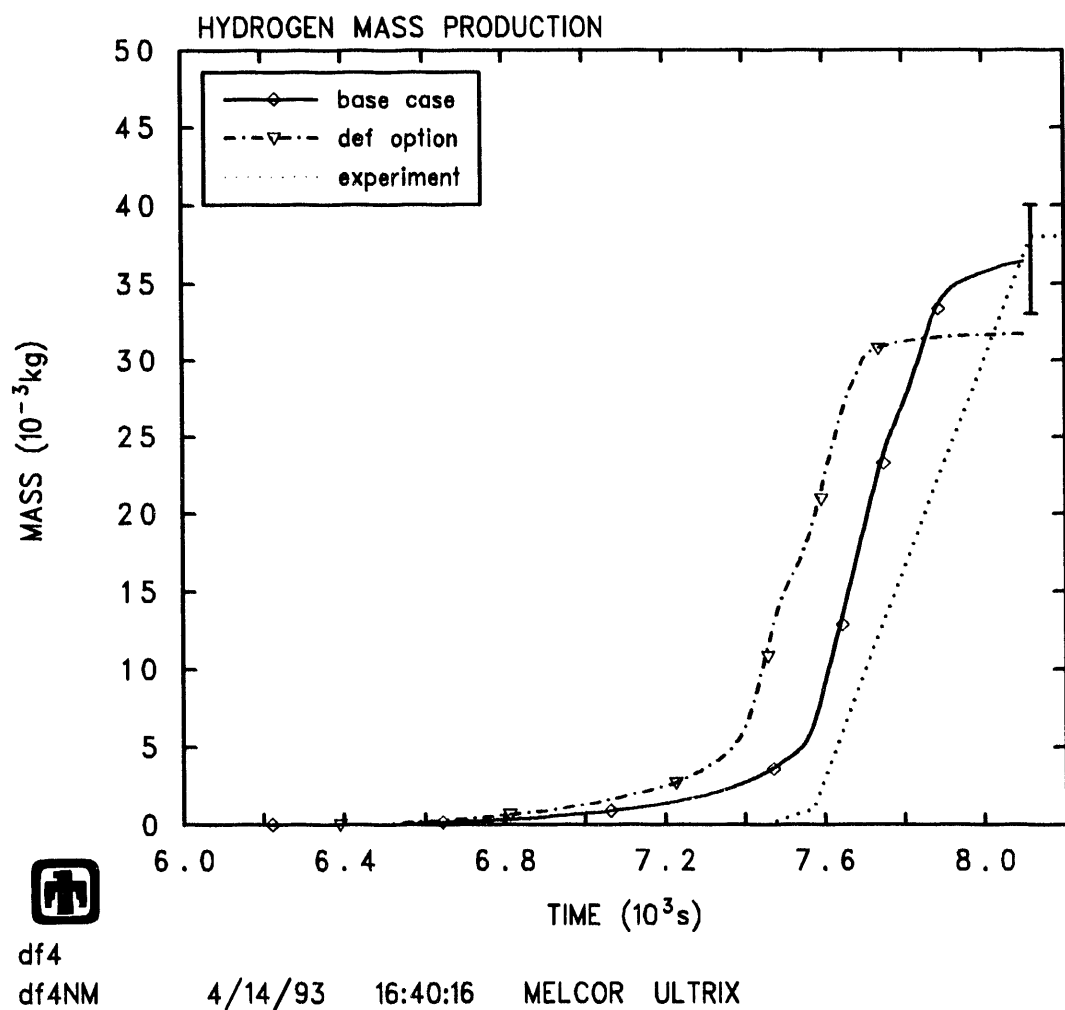
Figure 5.1.26. Hydrogen production for the default boundary fluid temperature option sensitivity study, compared to base case and measured values.

This was due to the delayed heatup of the control blade further up the bundle, where there was less debris stacked up outside the canister wall.

This study shows that the hydrogen production was sensitive to the debris porosity, and to a lesser extent temperatures in the lower portions of the bundle were affected as well. The volume occupied by debris was also strongly affected. The debris porosity could be more important in problems where the debris resided in the lower plenum. The debris porosity would determine the amount of decay heat emitted by the debris in the lower plenum (because it affects the mass of debris in a given volume) and would affect the debris surface area in contact with the pool. The timing of lower head failure would depend on both of these effects.

5.2.2 Debris Diameter

The diameter of particulate debris determines the debris surface areas used for heat transfer and oxidation (this parameter is input on record CORijj04). In the MELCOR base case model for DF-4, the debris diameter was set to 8.26 mm, which was the diameter of fuel pellets in the test bundle. In this sensitivity study, the debris diameter was increased and decreased by a factor of two.

The hydrogen production for the two cases is compared to the base case and measured results in Figure 5.2.6. This shows that reducing the debris diameter resulted in a substantial increase in hydrogen production. This result is not surprising, given that decreasing the debris diameter increased the debris surface area available for oxidation, and a large amount of debris oxidation occurred in DF-4. Increasing the debris diameter had the opposite effect, for the same reason.

The temperature responses of the cladding and control blade components for the 9.6 cm plane are shown in Figures 5.2.7 and 5.2.8, respectively. Changing the debris diameter resulted in no change in cladding and control blade temperature behavior.

In summary, the component temperatures were not sensitive to changes in debris diameter, but hydrogen production was quite sensitive to this parameter. The value used for this parameter should reflect the expected debris geometry and composition.

5.3 Oxidation Studies

Two studies were performed to investigate the oxidation modeling in the MELCOR core package. The two studies concern B_4C oxidation and the transition temperature between slow and fast oxidation reaction rates.

5.3.1 B_4C Oxidation Model

The B_4C oxidation model in the MELCOR core package is turned off by default because of difficulties encountered with the model [17]. The model was left off in the base case MELCOR model for DF-4. For this sensitivity study, this model was turned on by activating a flag on the CORTST01 input record.

HYDROGEN MASS PRODUCTION

MASS (10^{-3}kg)

TIME (10^3s)

Legend:
- base case
- small porosity
- large porosity
- experiment

df4
df4NM   4/14/93   16:40:16   MELCOR ULTRIX
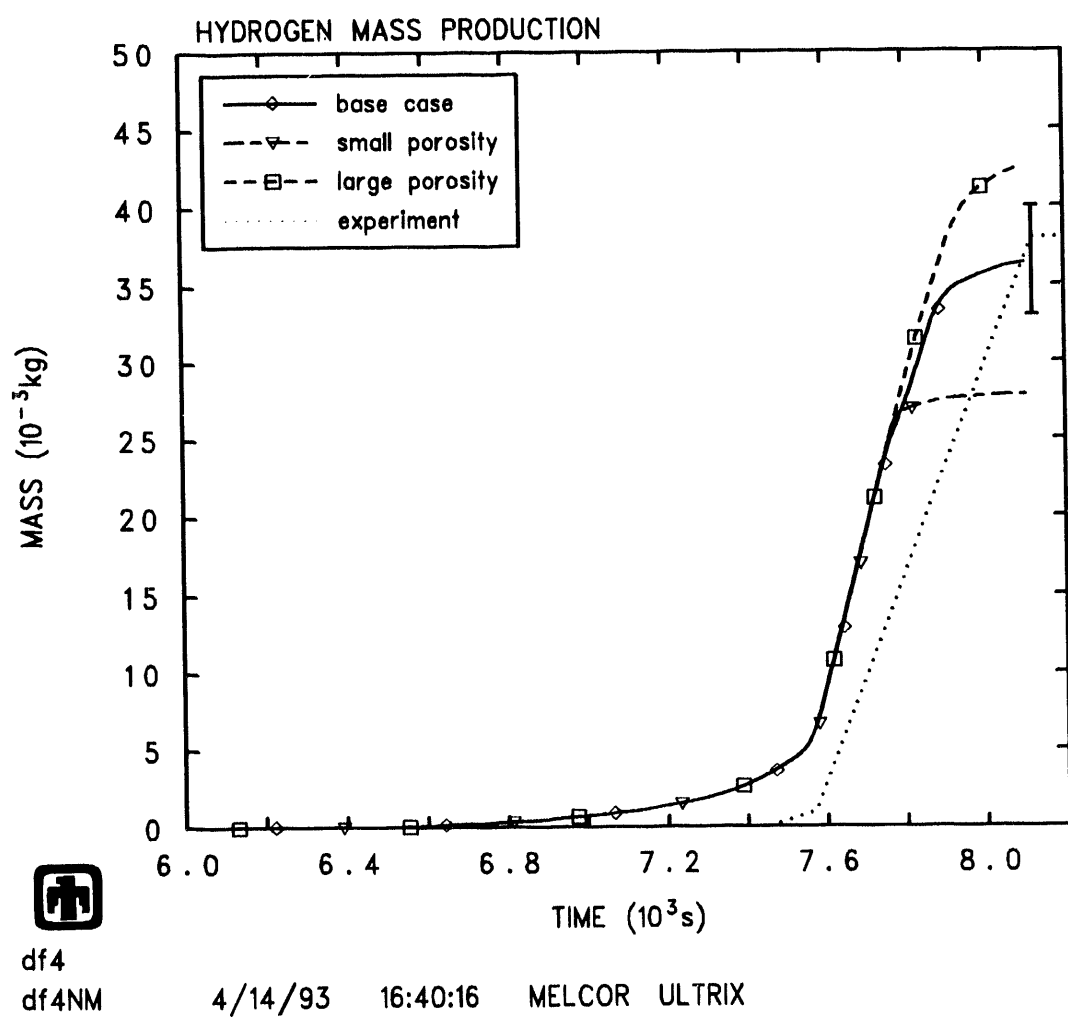
Figure 5.2.1. Hydrogen production for the debris porosity sensitivity study, compared to base case and measured values.
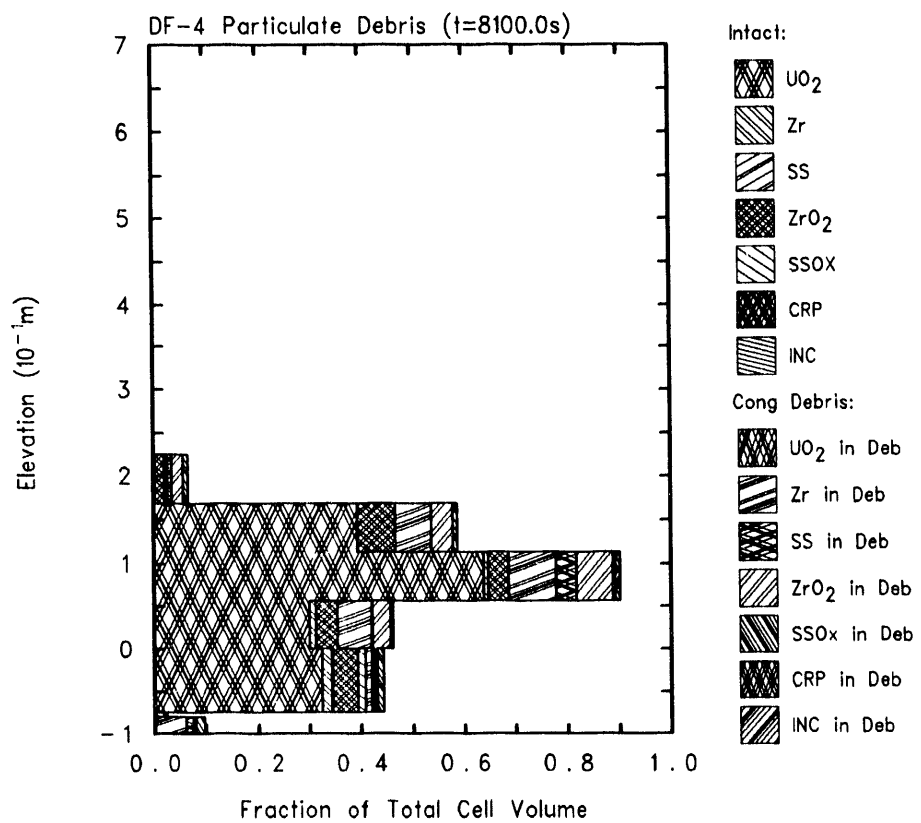
Figure 5.2.2. Particulate debris component material locations at 8100 seconds for the "small" case of the debris porosity sensitivity study.
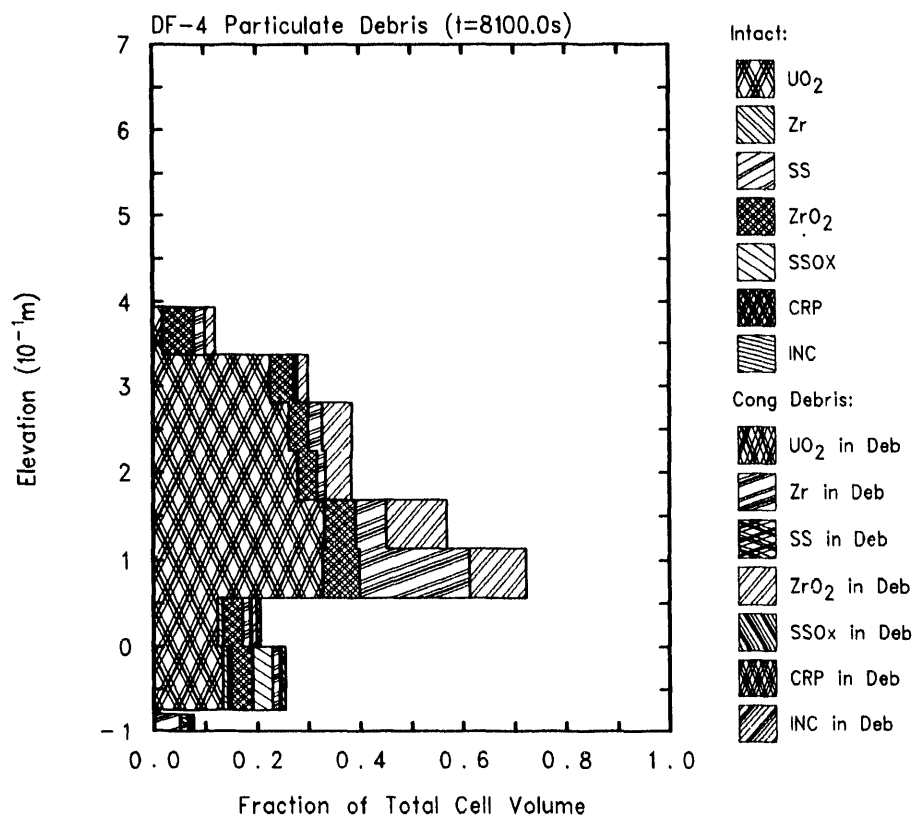
Figure 5.2.3. Particulate debris component material locations at 8100 seconds for the "large" case of the debris porosity sensitivity study.

CLAD TEMPS, 9.6 CM

2.75

2.50

2.25

2.00

1.75

1.50

1.25

1.00

0.75

0.50

0.25

TEMPERATURE (10³K)

base case
small porosity
large porosity
z1p215
z4p215

6.0   6.4   6.8   7.2   7.6   8.0

TIME (10³s)

df4
df4NM   4/14/93   16:40:16   MELCOR   ULTRIX
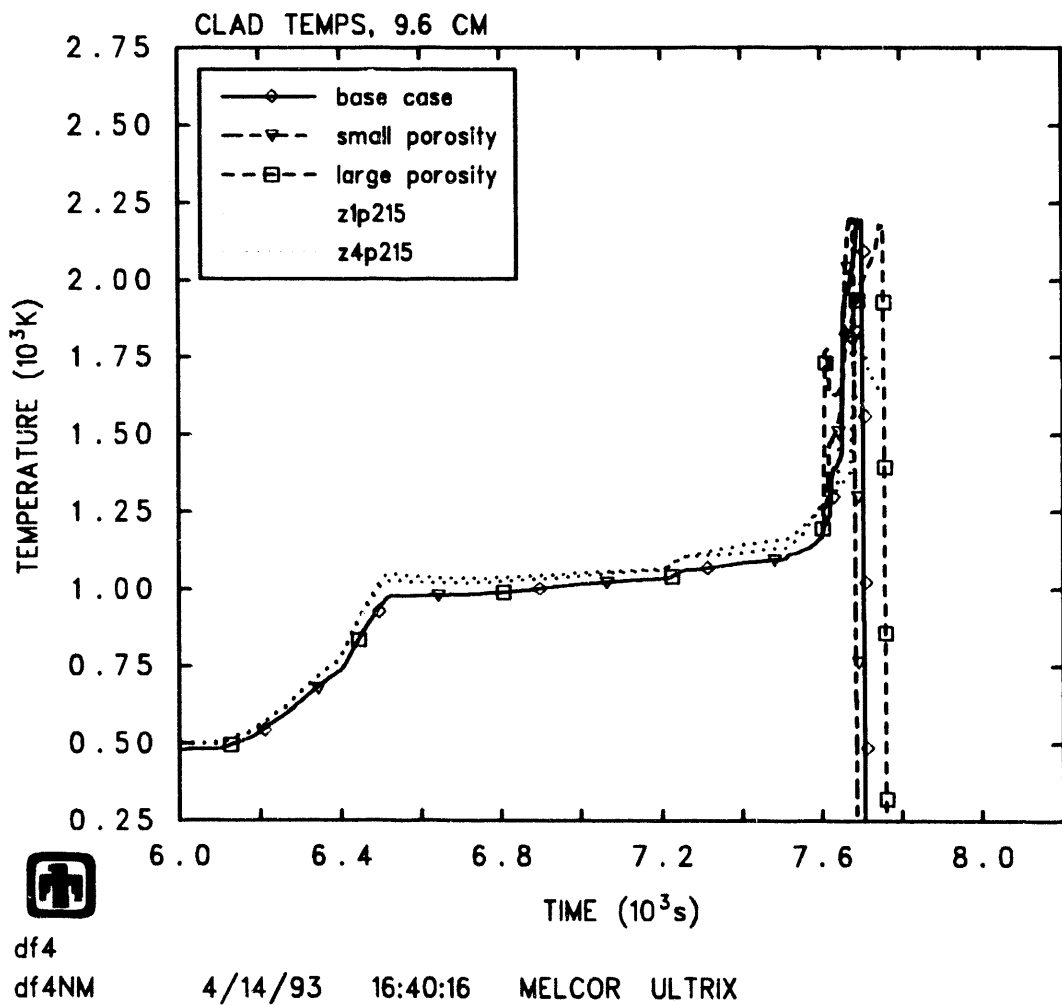
Figure 5.2.4. Cladding temperature response at the 9.6 cm plane for the debris porosity sensitivity study, compared to base case and measured values.
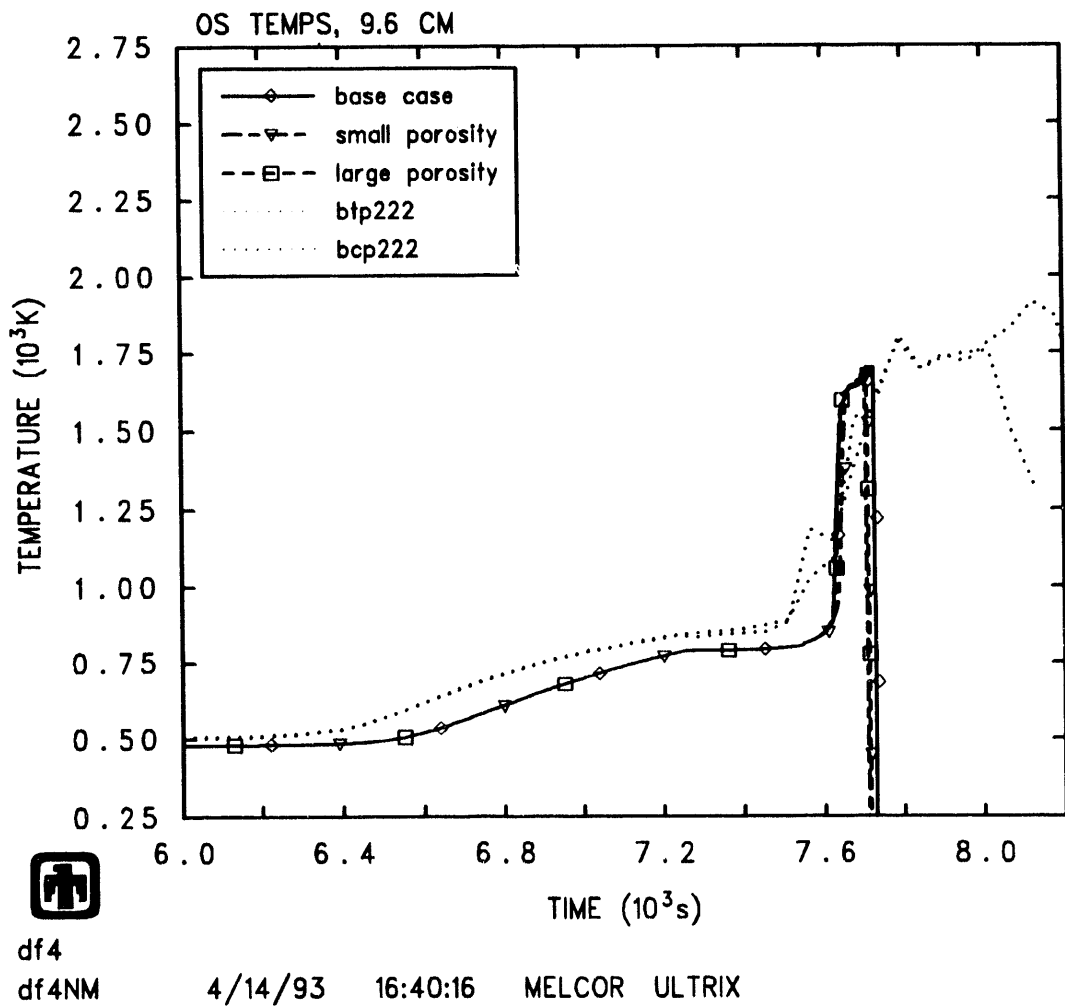
Figure 5.2.5. Control blade temperature response at the 9.6 cm plane for the debris porosity sensitivity study, compared to base case and measured values.
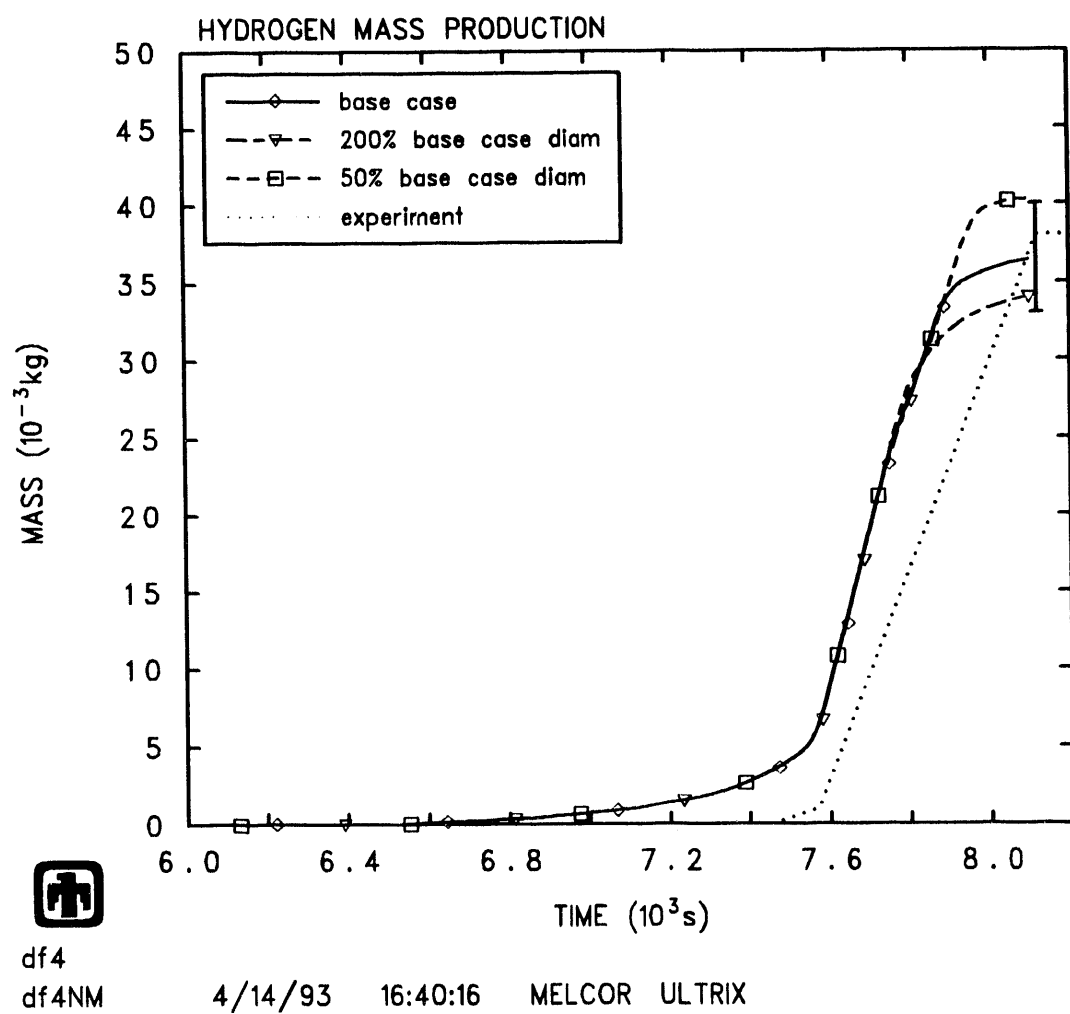
Figure 5.2.6. Hydrogen production for the debris diameter sensitivity study, compared to base case and measured values.
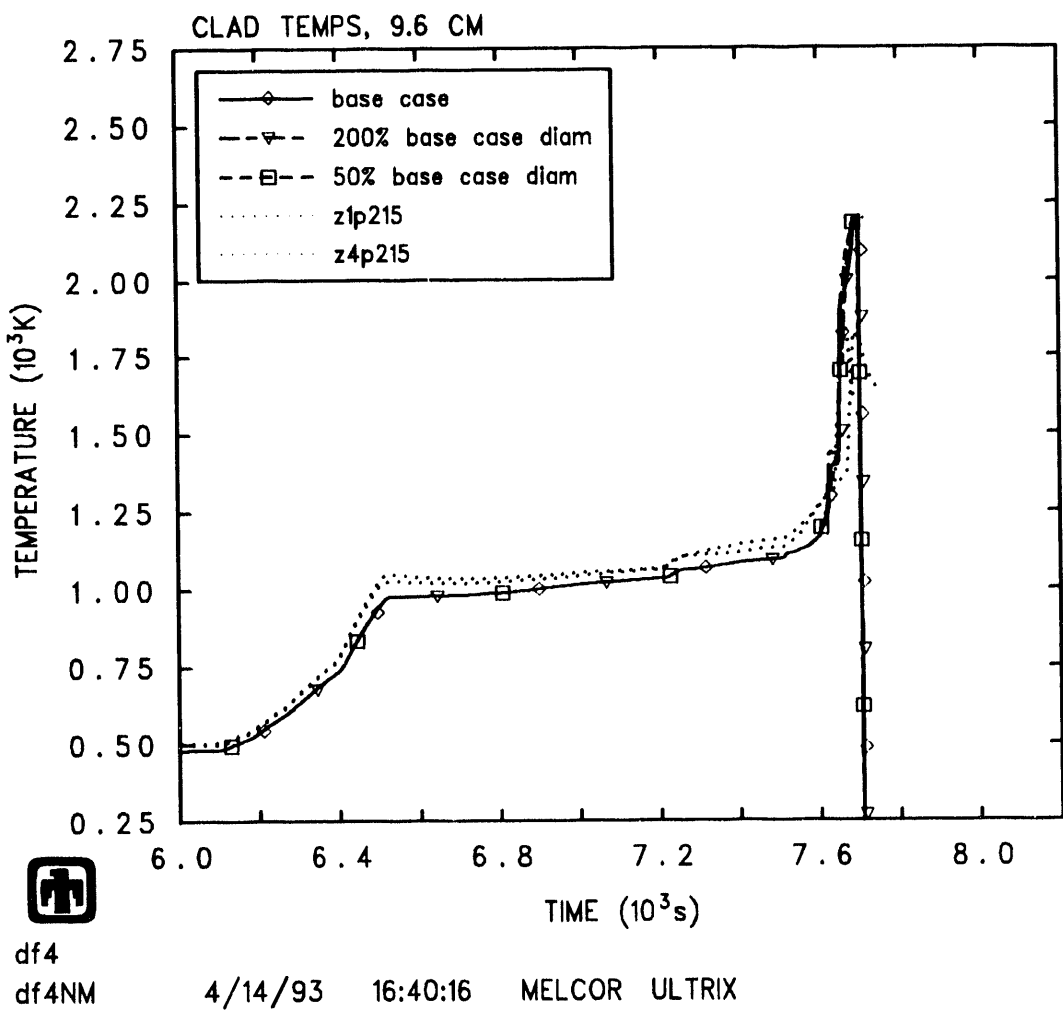
Figure 5.2.7. Cladding temperature response at the 9.6 cm plane for the debris diameter sensitivity study, compared to base case and measured values.
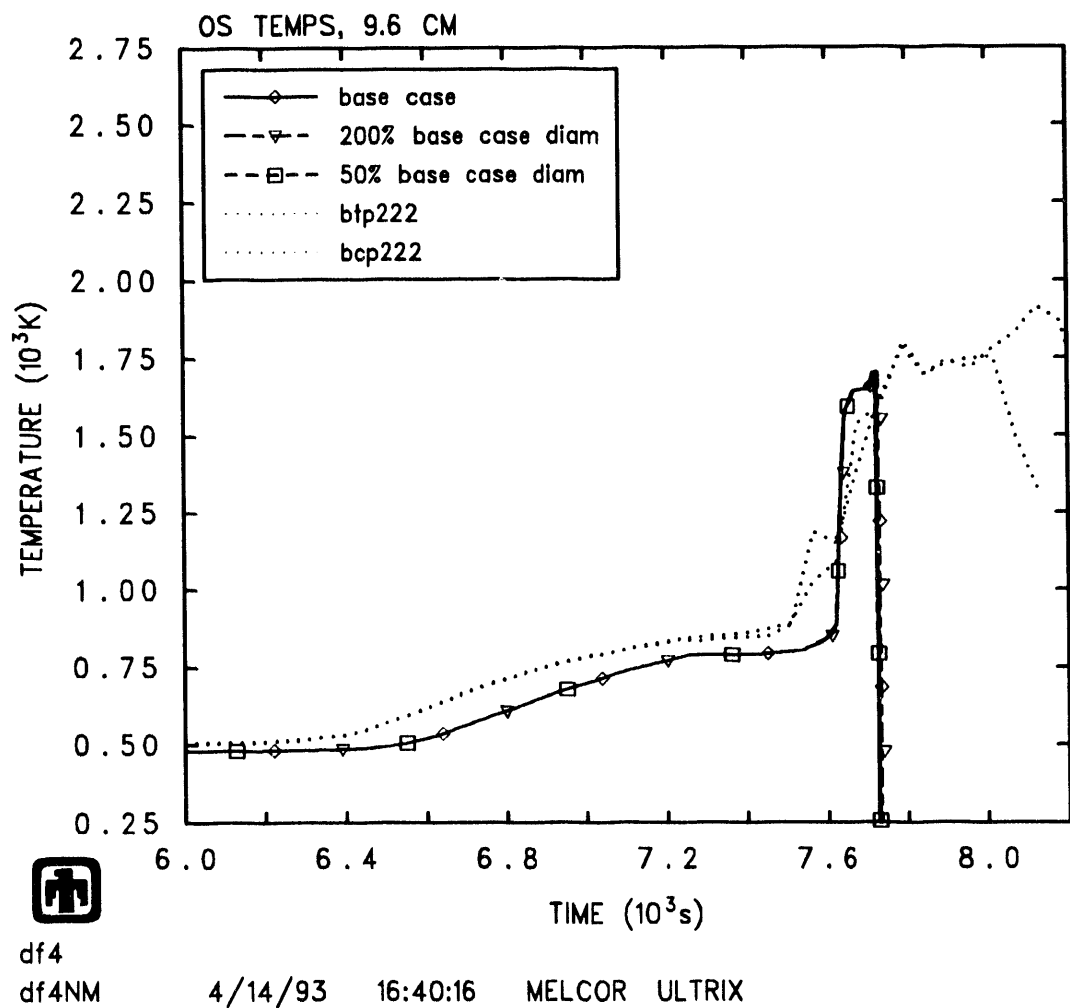
Figure 5.2.8. Control blade temperature response at the 9.6 cm plane for the debris diameter sensitivity study, compared to base case and measured values.

In the MELCOR implementation of B_4C oxidation, the poison material did not begin oxidizing until the other structure component reached the stainless steel melting temperature. In effect this modeled breach of the stainless steel tubes which held the B_4C. The results from this sensitivity study, though, show that the B_4C model was never exercised, even when the model was enabled. This is because, with the new eutectic model enabled, all of the B_4C was consumed in the eutectic reaction with stainless steel before the other structure component could reach the stainless steel melting temperature (this assumes there was enough stainless steel available to totally consume the available B_4C in a eutectic reaction). The B_4C oxidation model does not calculate oxidation for B_4C in the liquid state. This situation would probably exist in any realistic BWR input model, which would have the eutectic model active. So, in conclusion, without the capability of oxidizing B_4C in a eutectic mixture, the B_4C oxidation model is of little use to the MELCOR user for modeling BWR cores.

5.3.2 Oxidation Reaction Rate Transition Temperature

Oxidation is modeled in MELCOR using a parabolic rate equation. For the zircaloy-H_2O reaction, the rate constant is calculated using the Urbanic-Heidrich correlation [18]:

$$K(T) = 29.6 exp\left(\frac{-16820.0}{T}\right) \text{ for T} < \text{T}_{trans}, \tag{5.1}$$

$$= 87.9 exp\left(\frac{-16610.0}{T}\right) \text{ for T} \geq \text{T}_{trans}. \tag{5.2}$$

The transition temperature, T_{trans}, has a default value of 1853K, and is adjustable using sensitivity coefficient 1001 in the COR package. In this sensitivity study, values of 1550K, 1650K and the default value of 1853K were compared with the DF-4 base case which used a transition temperature of 1750K.

The cladding and control blade temperatures for the 36.8 cm plane for these three cases are compared to base case and measured results in Figures 5.3.1 and 5.3.2, respectively. The trends in these figures are consistent with the adjustments to the oxidation transition temperature. That is, when the oxidation transition temperature was decreased, rapid oxidation started earlier and resulted in earlier component failure.

The hydrogen production for these three cases in this study is compared to the base case and measured results in Figure 5.3.3. The hydrogen production for each case was also consistent with the trends in transition temperatures, where the lower transition temperature cases resulted in earlier and more hydrogen production. It is interesting to note that the 1853K case showed much less hydrogen production. This can be understood by looking at Figure 5.3.1, which shows that in this case the clad reached its melting temperature much sooner after starting rapid oxidation than the other cases, which means it had less time to produce hydrogen at the increased rate.

The oxidation reaction rate transition temperature used in the base case model, 1750K, resulted in the best overall agreement with experimental data, in terms of temperatures, failure timing and overall hydrogen production. The results showed

sensitivity to this parameter, and it is recommended that this parameter be investigated as a part of any MELCOR modeling effort. (Both the LOFT LP-FP-2 [11] and the CORA-13 [13] assessments adjusted this parameter in the base case models.)

5.4 Eutectic Model Studies

The materials interaction (eutectic) model in the core package was a recent addition to the MELCOR code [7]. This model represents the interaction between certain materials in BWR and PWR reactor cores which results in liquid mixtures forming well below their normal individual melting temperatures. This phenomenon was of concern because it could result in control poison escaping the core before significant fuel relocation, possibly resulting in a reactivity transient. Two studies were done to test the eutectic model in MELCOR. These studies concerned the use of the eutectic model and the eutectic temperature of the B_4C-stainless steel reaction.

5.4.1 Deactivate Eutectic Model

The base case MELCOR model for DF-4 used the new MELCOR 1.8.2 eutectic model, which is activated using input record COR00006. In this sensitivity study, the eutectic model was reset to its default state, where it is inactive.

The largest difference in results due to the eutectic model was evident in the relocation behavior of the B_4C between 7500–7600 seconds. The distribution of control blade materials in the other structure component at 7550 seconds for the deactivated eutectic model calculation is shown in Figure 5.4.1. This figure can be compared to the other structure component material distribution plot in Figure 4.2.4. Figure 4.2.4 shows that the eutectic model calculated eutectic interaction and relocation of B_4C from core cells 109–112 (see Table 3.2.2). According to the base case model, at 7550 seconds there was no B_4C material left in cells 110–112 (between 34 cm and 50.5 cm). The case with the eutectic model deactivated showed no significant relocation of B_4C from any level at 7550 seconds. The material distribution for the deactivated eutectic model case at 7600 seconds is shown in Figure 5.4.2, for comparison to the base case results in Figure 4.2.5. At this time, the other structure component had failed in cells 109–112 in both calculations. After failure of the substrate material (stainless steel), in the case with no eutectics interaction, the B_4C was converted to particulate debris and was relocated to the bottom of the core in a manner similar to the way UO_2 relocated. This shows the value of using the eutectic model in MELCOR; it is clear from both the temperature measurements and the video record of the DF-4 experiment that the control blade material melted and relocated at a temperature lower than the stainless steel melting temperature, and that it relocated (candled) in the liquid phase.

The final bundle state for this sensitivity study is shown in Figure 5.4.3. This figure can be compared with the base case results, shown in Figure 4.2.10. In the case with no eutectic modeling, more of the fuel and canister components survived intact, instead of being converted to particulate debris. This shows less dissolution of these

110
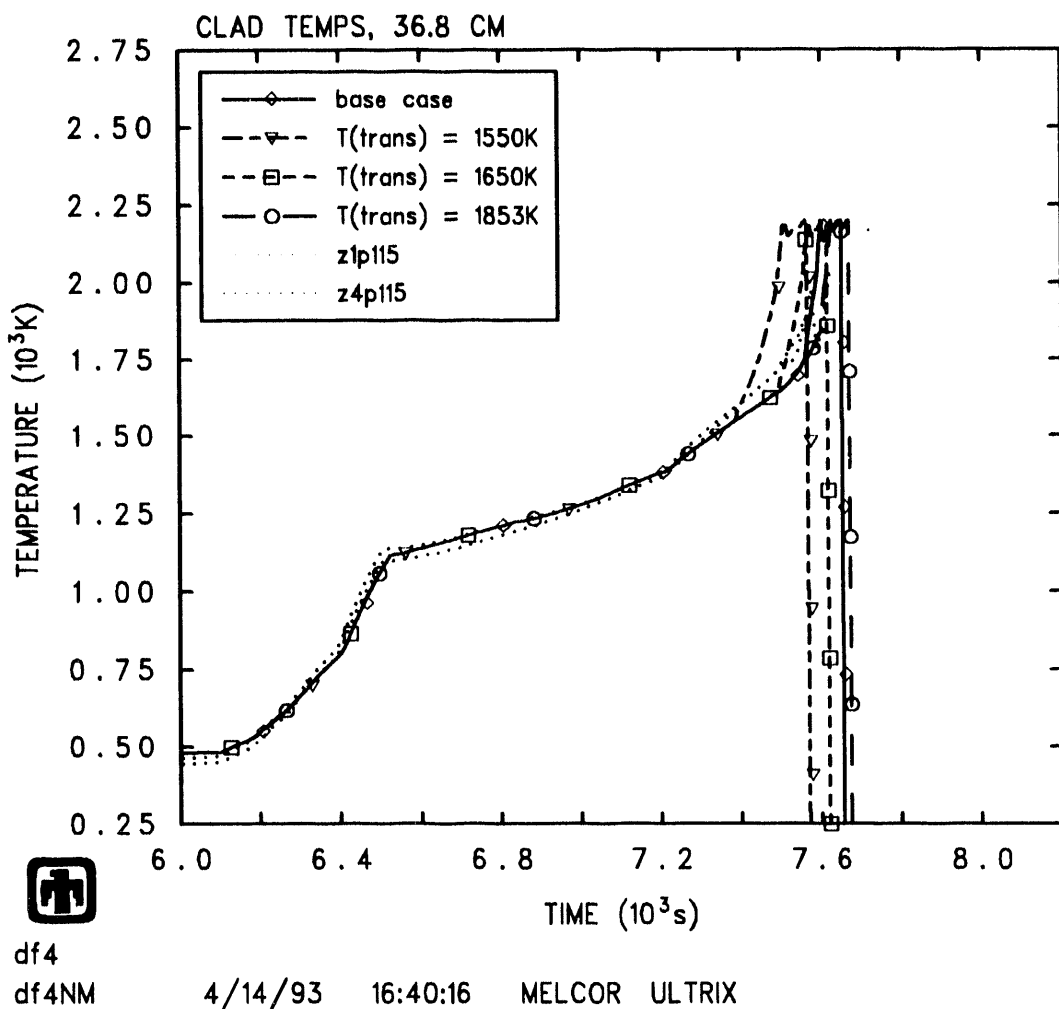
Figure 5.3.1. Cladding temperature response at the 36.8 cm plane for the
oxidation reaction rate transition temperature sensitivity study,
compared to base case and measured values.
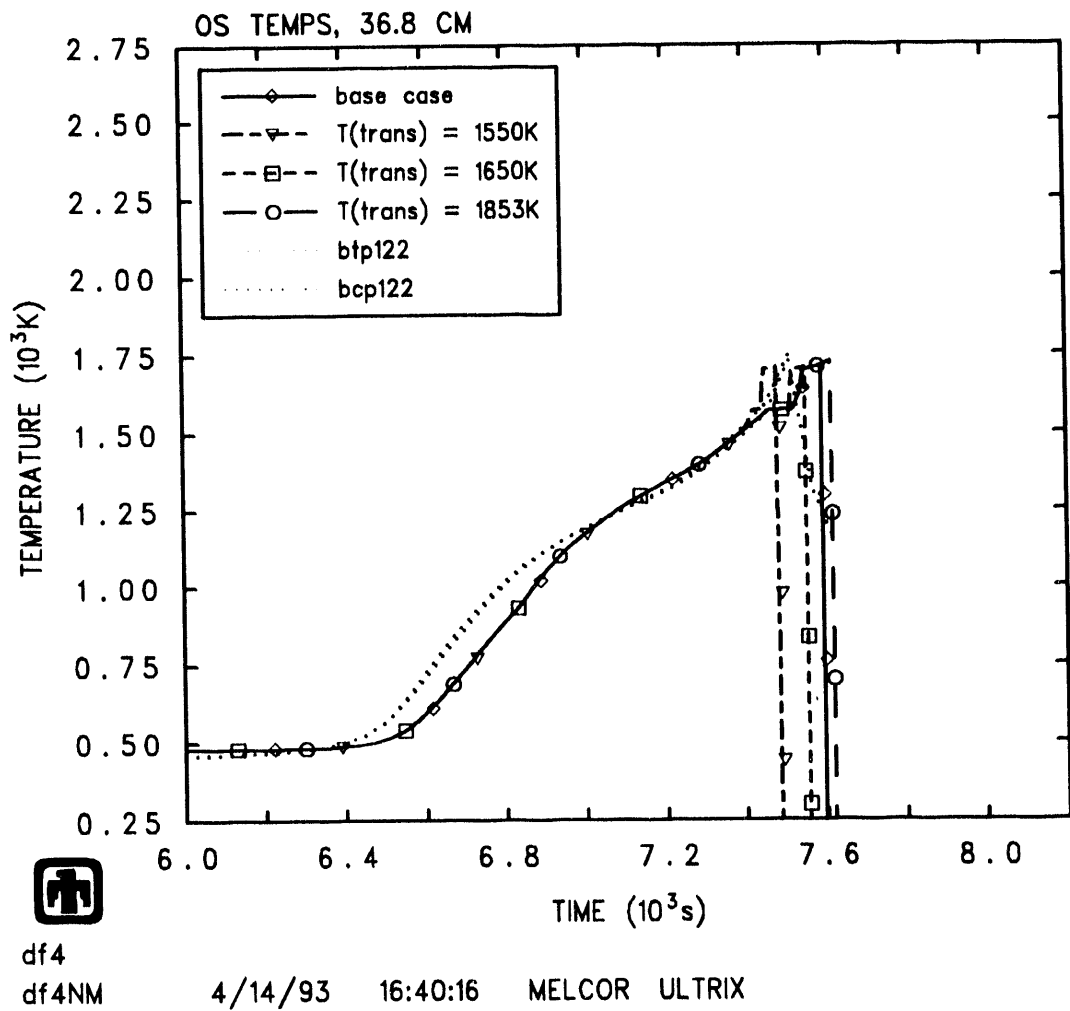
Figure 5.3.2. Control blade temperature response at the 36.8 cm plane for the oxidation reaction rate transition temperature sensitivity study, compared to base case and measured values.

HYDROGEN MASS PRODUCTION
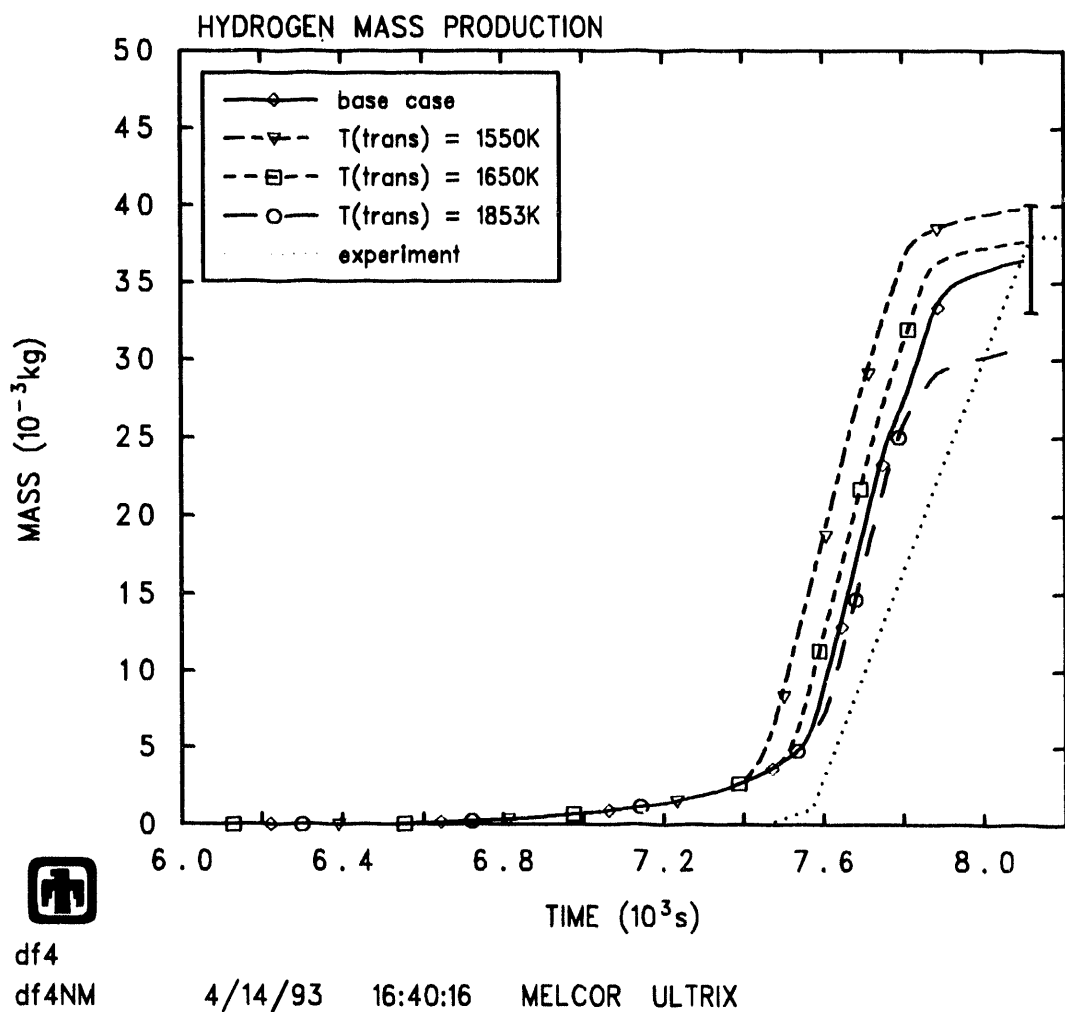
Figure 5.3.3. Hydrogen production for the oxidation reaction rate transition temperature sensitivity study, compared to base case and measured values.

components by debris materials already residing at those levels. Eutectic dissolution of the fuel and cladding component moves material from that component to the particulate debris component. Moving zircaloy to the particulate debris component made it available for oxidation, whereas in the fuel and cladding component the zircaloy had been covered by an oxide layer. Thus, deactivating the new eutectics model left more material in the fuel and cladding component, making it unavailable for oxidation and reducing the total amount of hydrogen produced. Figure 5.4.4, the hydrogen production for the no eutectics interaction case, shows that this was indeed the case.

The control blade temperature with the eutectic model inactive at the 36.8 cm plane is compared with the base case and measured results in Figure 5.4.5. The results without eutectic modeling were the same until the control blade reached the eutectic temperature of 1570K (this was the value used in the base case model). The eutectic model held the control blade at this temperature to model the B_4C-stainless steel interaction, while with no eutectic modeling the control blade temperature rose to the stainless steel melting temperature of 1700K.

The cladding temperatures at the 36.8 cm and 25.4 cm planes are compared with base case and measured results in Figures 5.4.6 and 5.4.7, respectively. At the 25.4 cm plane, deactivating the eutectic model resulted in earlier failure of the cladding. This is because there was less material refrozen onto the control blade at that level, providing less of a heat sink for the fuel rod. The change in failure time was less than 50 seconds, though, so this was a small effect. The effect on temperature and failure timing of the control blade at the 36.8 cm level was even more slight.

This study clearly shows that the eutectic model should be used in future MELCOR BWR models. The temperature results were not very sensitive to the use of this model, but the relocation behavior of control blade materials was strongly affected by the eutectic model. Eutectic dissolution reactions were also important in determining the final debris state.

5.4.2 Stainless Steel-B_4C Eutectic Interaction Temperature

One of the most important models affecting control blade temperature and relocation behavior in DF-4 was the new materials interactions model in MELCOR [7]. This model accounts for the liquifaction of B_4C and stainless steel at a temperature well below the melting temperature of either constituent, as well as interactions between other materials. In this sensitivity study, the eutectic temperature of the B_4C-stainless steel mixture was varied by $\pm 50K$ from its base case model value of 1570K. This parameter is located in sensitivity coefficient array 1011 in MELCOR.

The control blade temperature response at the 36.8 cm plane was expected to show the effects of varying the eutectic temperature, because this was the first plane to show signs of eutectic interaction. The temperatures at this plane are compared with base case and measured results in Figure 5.4.8. As expected, lowering the eutectic interaction temperature caused the control blade to begin forming eutectic earlier. No matter what the eutectic temperature, the amount of energy required by the eutectic reaction between B_4C and stainless steel is the same. Since the energy deposited in
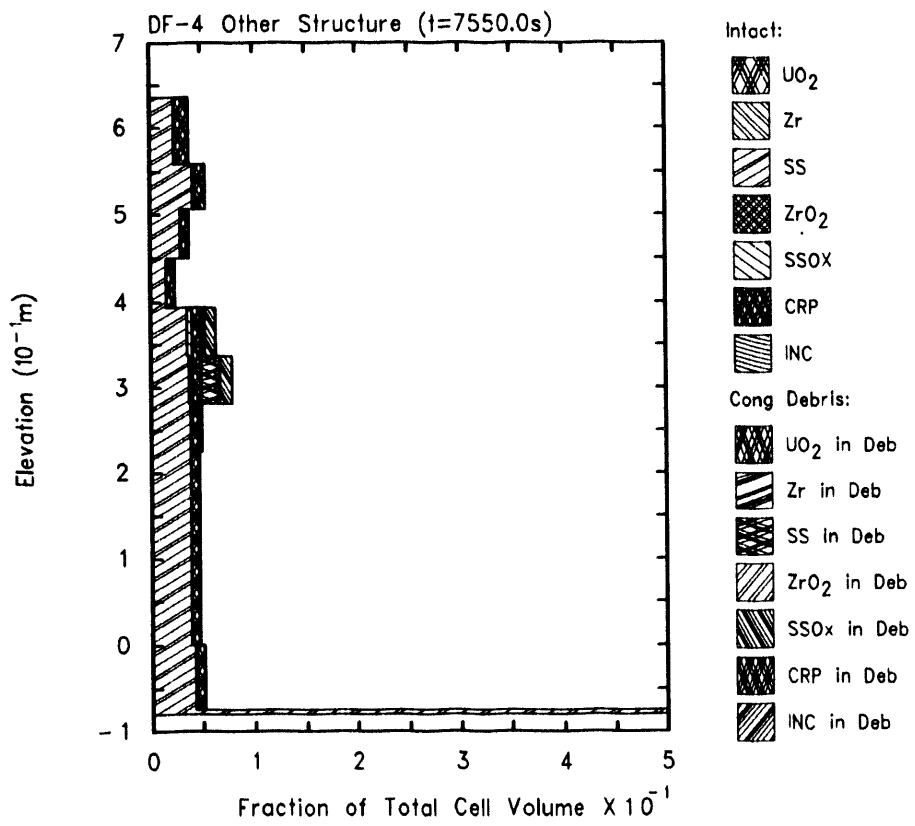
Figure 5.4.1. Other Structure component material locations at 7550 seconds for the eutectic model deactivation sensitivity study.
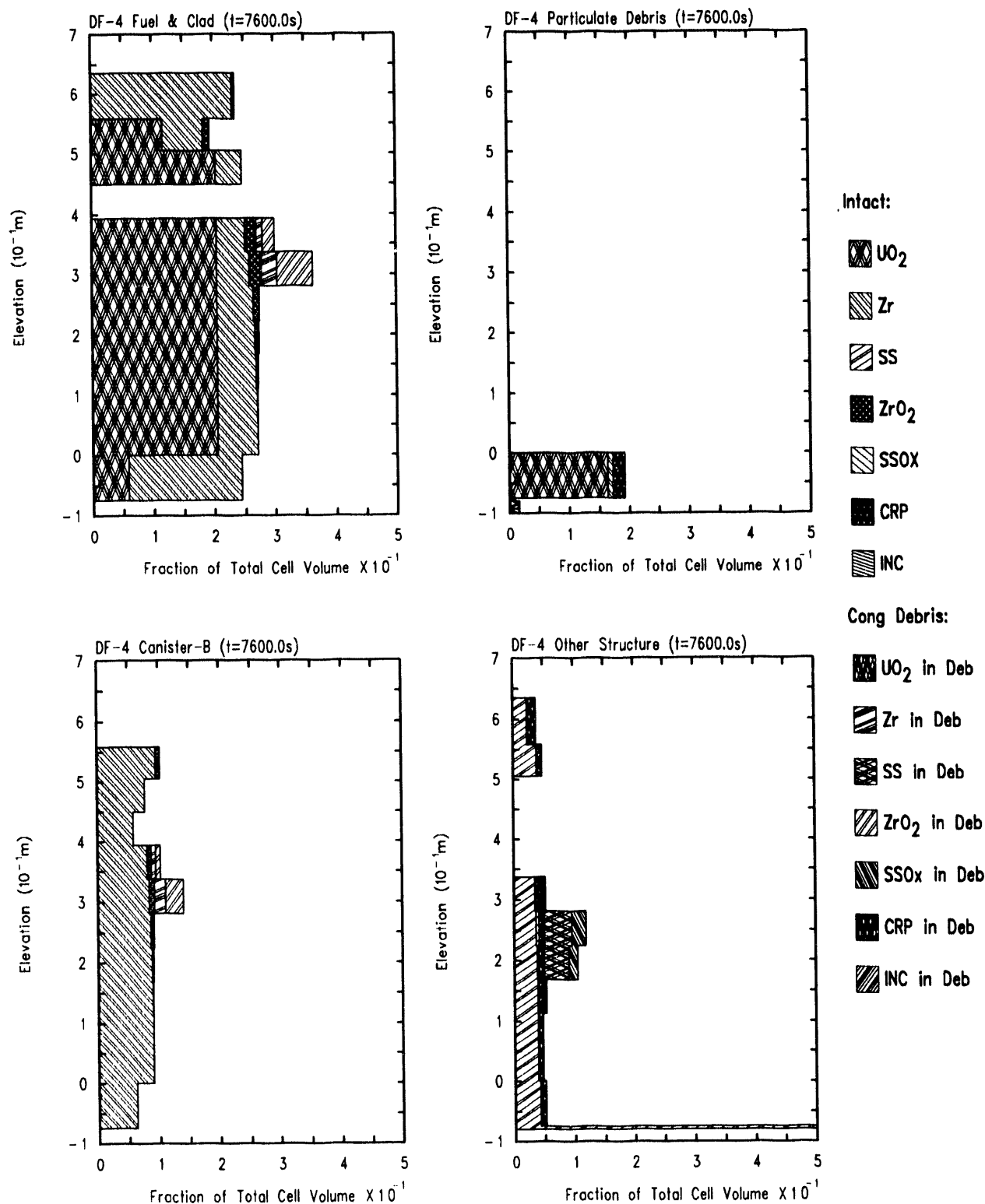
Figure 5.4.2. Locations of fuel and clad (upper left), particulate debris (upper right), canister-b (lower left) and other structure (lower right) component materials at 7600 seconds for the eutectic model deactivation sensitivity study.

DF-4 Fuel & Clad (t=8100.0s)

Elevation $(10^{-1}m)$

Fraction of Total Cell Volume

DF-4 Particulate Debris (t=8100.0s)

Elevation $(10^{-1}m)$

Fraction of Total Cell Volume

Intact:

UO_2

Zr

SS

ZrO_2

SSOX

CRP

INC

Cong Debris:

UO_2 in Deb

Zr in Deb

SS in Deb

ZrO_2 in Deb

SSOx in Deb

CRP in Deb

INC in Deb

DF-4 Canister-B (t=8100.0s)

Elevation $(10^{-1}m)$

Fraction of Total Cell Volume

DF-4 Other Structure (t=8100.0s)

Elevation $(10^{-1}m)$

Fraction of Total Cell Volume
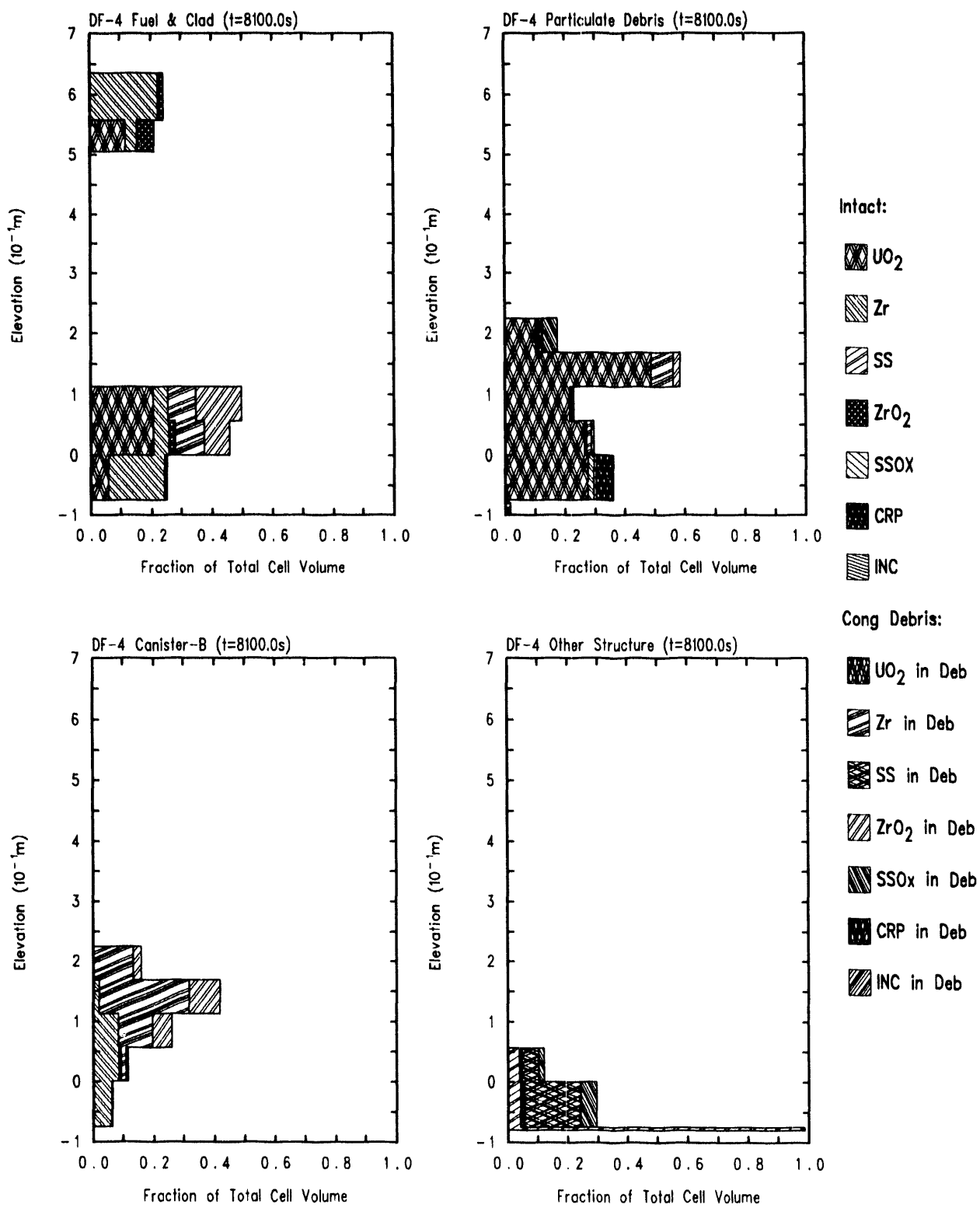
Figure 5.4.3. Material locations for the fuel and clad (upper left), particulate debris (upper right), canister-b (lower left) and other structure (lower right) components at 8100 seconds for the eutectic model deactivation sensitivity study.

117
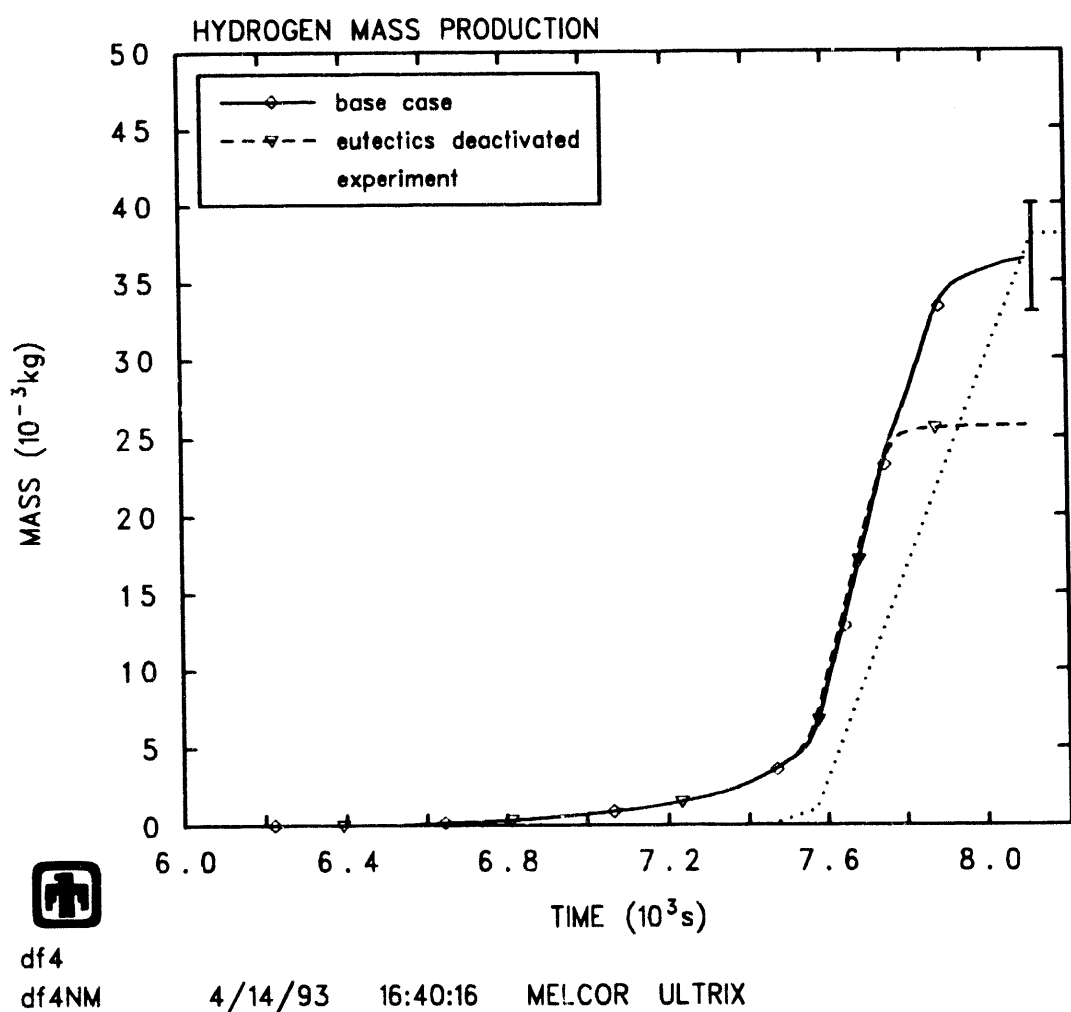
Figure 5.4.4. Hydrogen production for the eutectic model deactivation sensitivity study, compared to base case and measured values.
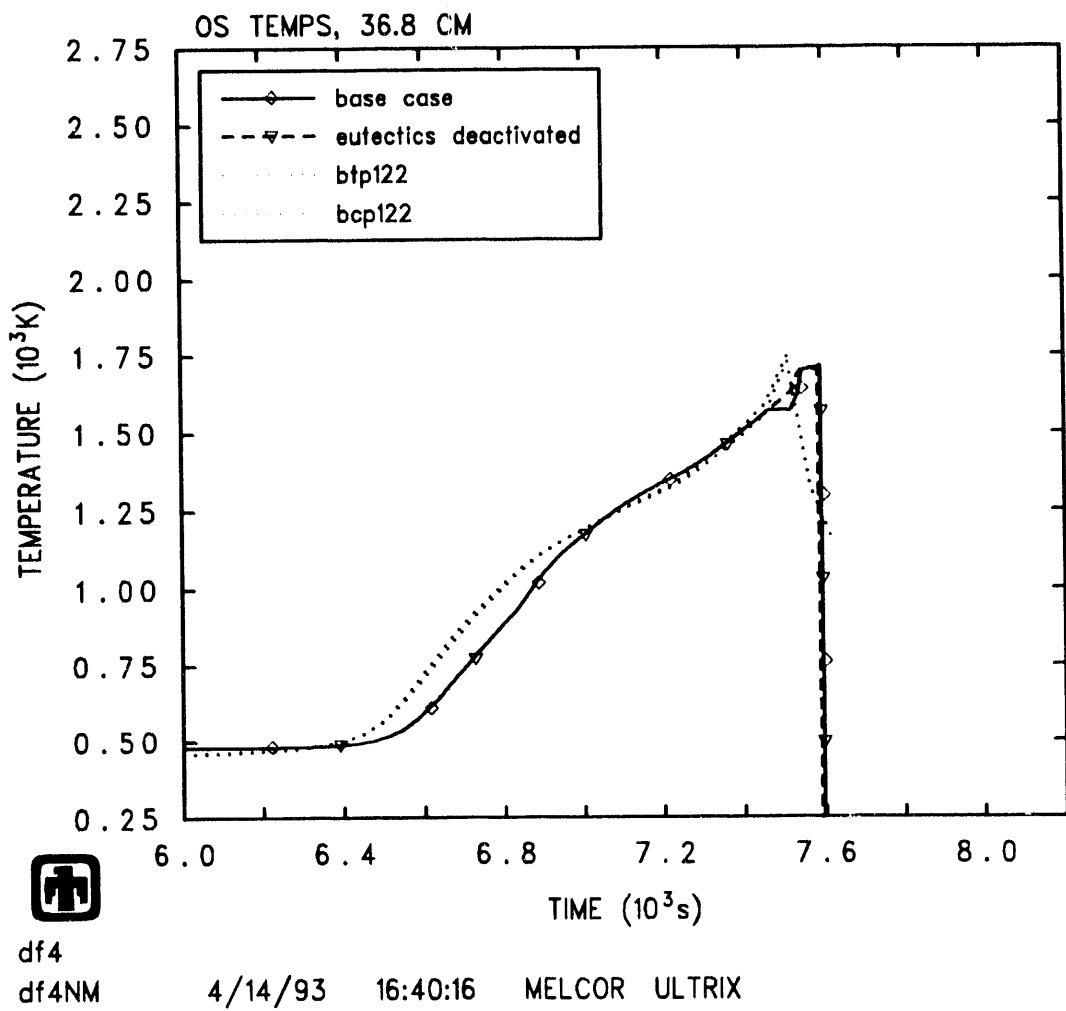
Figure 5.4.5. Control blade temperature response at the 36.8 cm plane for the eutectic model deactivation sensitivity study, compared to base case and measured values.

119
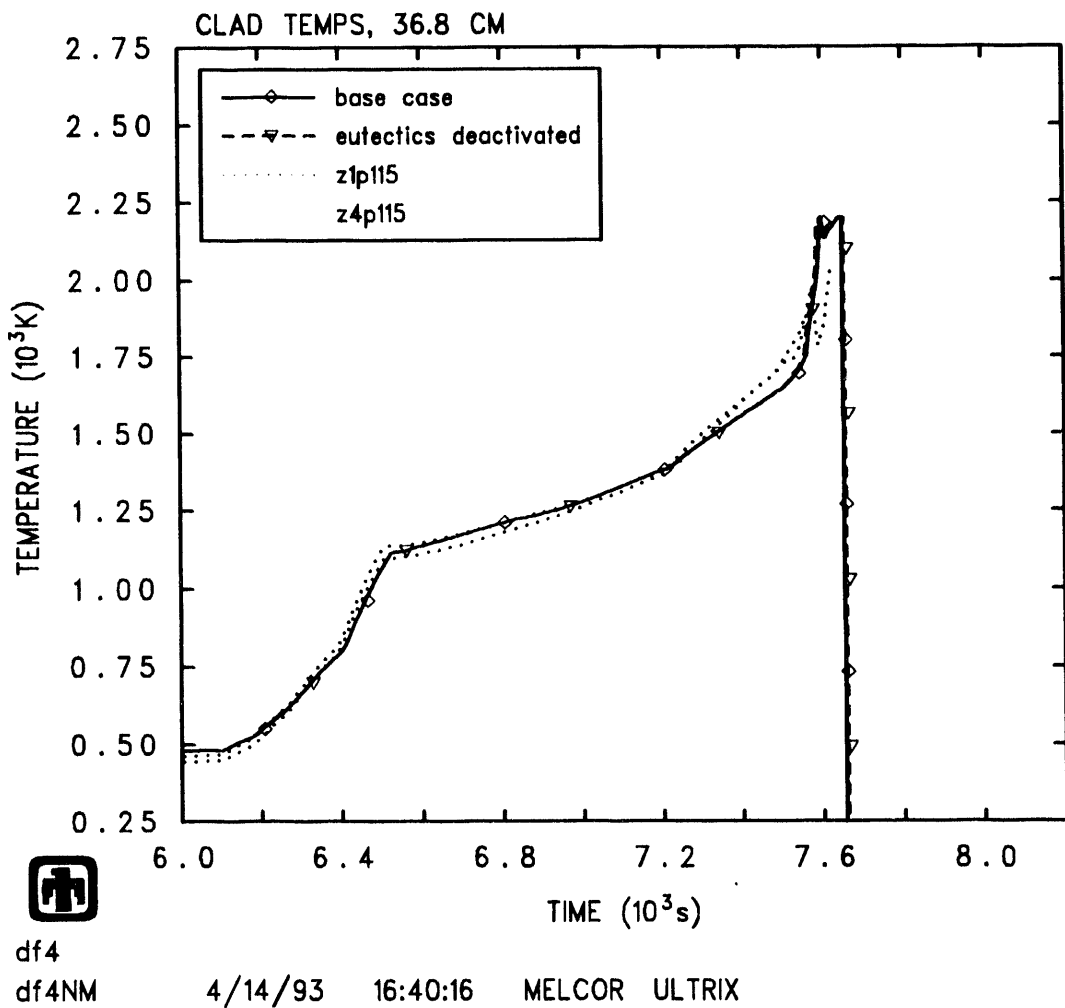
Figure 5.4.6. Cladding temperature response at the 36.8 cm plane for the eutectic model deactivation sensitivity study, compared to base case and measured values.
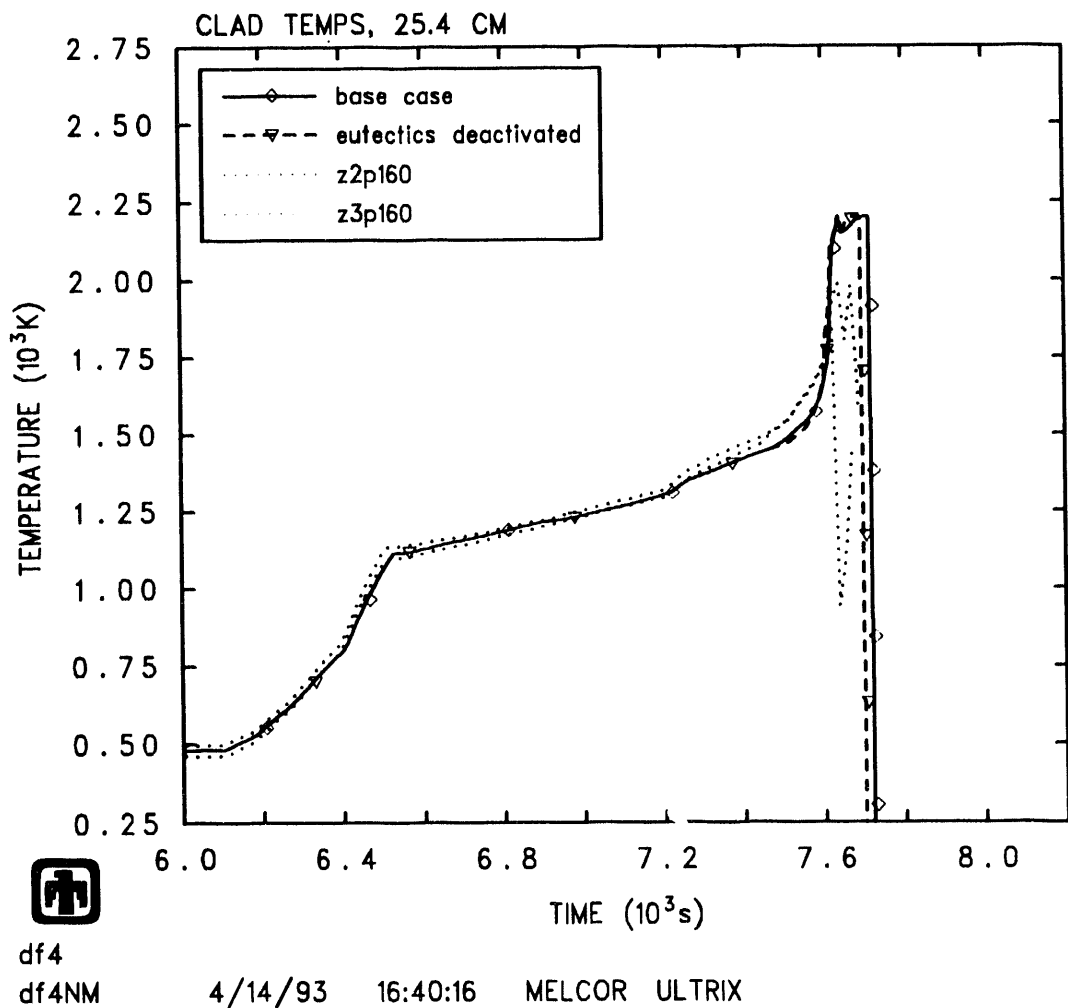
Figure 5.4.7. Cladding temperature response at the 25.4 cm plane for the eutectic model deactivation sensitivity study, compared to base case and measured values.

the control blade during this time is the same for all cases, it follows that the failure timing for the control blade should not change significantly. This assumes a negligible difference in sensible heat addition below the eutectic interaction temperature for all cases.

The control blade temperature at the 25.4 cm plane showed the effects of earlier eutectic interaction at higher planes. Figure 5.4.9 shows that relocating material arrived about 50 seconds earlier for the 1520K case, and about the same amount of time later for the 1620K case. Again, failure timing at this level was not affected.

The hydrogen production response, shown in Figure 5.4.10, was not affected by the variation in the eutectic temperature of the B_4C-stainless steel mixture.

The control blade material distributions in the other structure component for the 1520K case at 7450 seconds are shown in Figure 5.4.11, to be compared with the base case control blade material distributions in Figure 4.2.2. Figure 5.4.11 shows earlier relocation of control blade materials as a result of decreasing the B_4C-stainless steel eutectic temperature. The control blade material relocations for the 1620K case were delayed in time for the 1620K case, in the same way that the relocations were moved forward in time for the 1520K case.

5.5 Thermal/Hydraulic Initial and Boundary Conditions

Five sensitivity studies were done in the area of thermal/hydraulic initial and boundary conditions. Most of the studies were performed to investigate the effects of uncertainties or assumptions about the experimental initial and boundary conditions.

5.5.1 Steam Mass Flow Rate

The steam mass flow rate in the experiment was measured using a flow meter and data from this instrument was provided on one of the data channels. This data was used in the MELCOR base case model. For this sensitivity study, the mass flow rate was varied by ±10%. This was done by scaling the control function which calculated flow into the channel and bypass control volumes in the MELCOR DF-4 model.

The cladding temperature at the 36.8 cm plane for this study is compared with the base case and measured results in Figure 5.5.1. Increasing and decreasing the flow had the expected results of causing later and earlier failure, respectively. This was obviously the result of cooling proportional to the steam mass flow rate.

The hydrogen production behaved as expected during the early part of the experiment, as shown in Figure 5.5.2. However, the final amount of hydrogen produced for the 110% flow case was slightly less than the base case result. This suggests that the hydrogen production later in the experiment was not limited by flow. Rather, the oxidation reaction may have been limited by the characteristics of the debris.
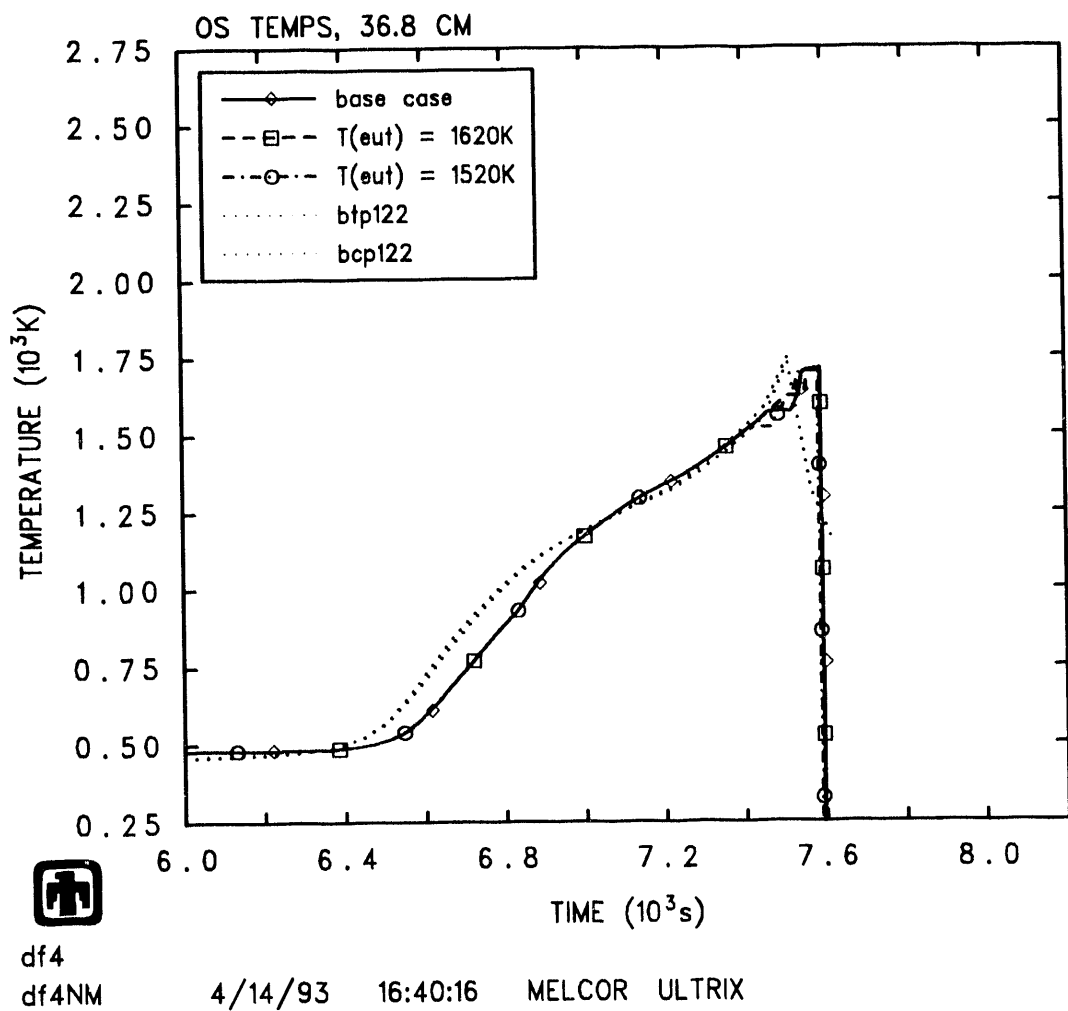
Figure 5.4.8. Control blade temperature response at the 36.8 cm plane for the B$_4$C-stainless steel eutectic temperature sensitivity study, compared to base case and measured values.
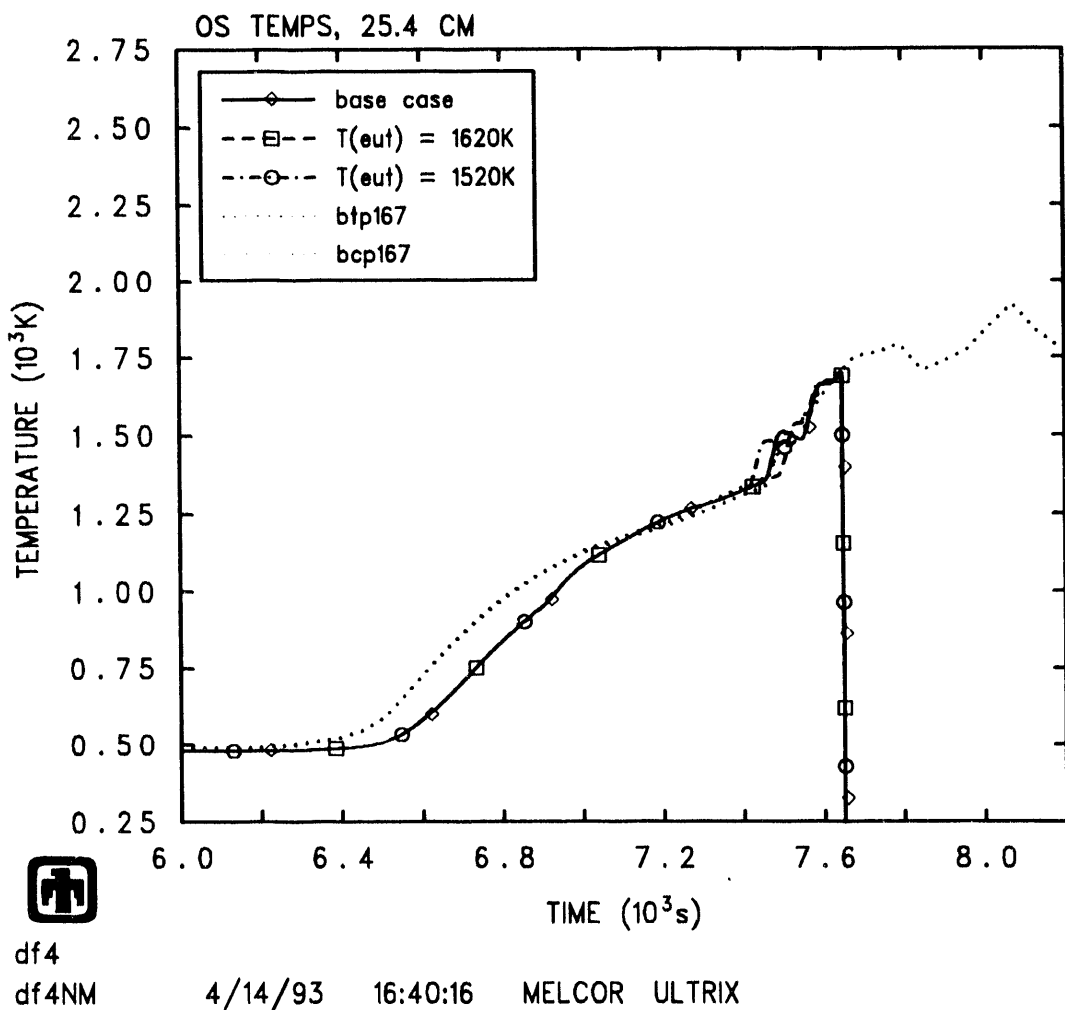
Figure 5.4.9. Control blade temperature response at the 25.4 cm plane for the B₄C-stainless steel eutectic temperature sensitivity study, compared to base case and measured values.

HYDROGEN MASS PRODUCTION
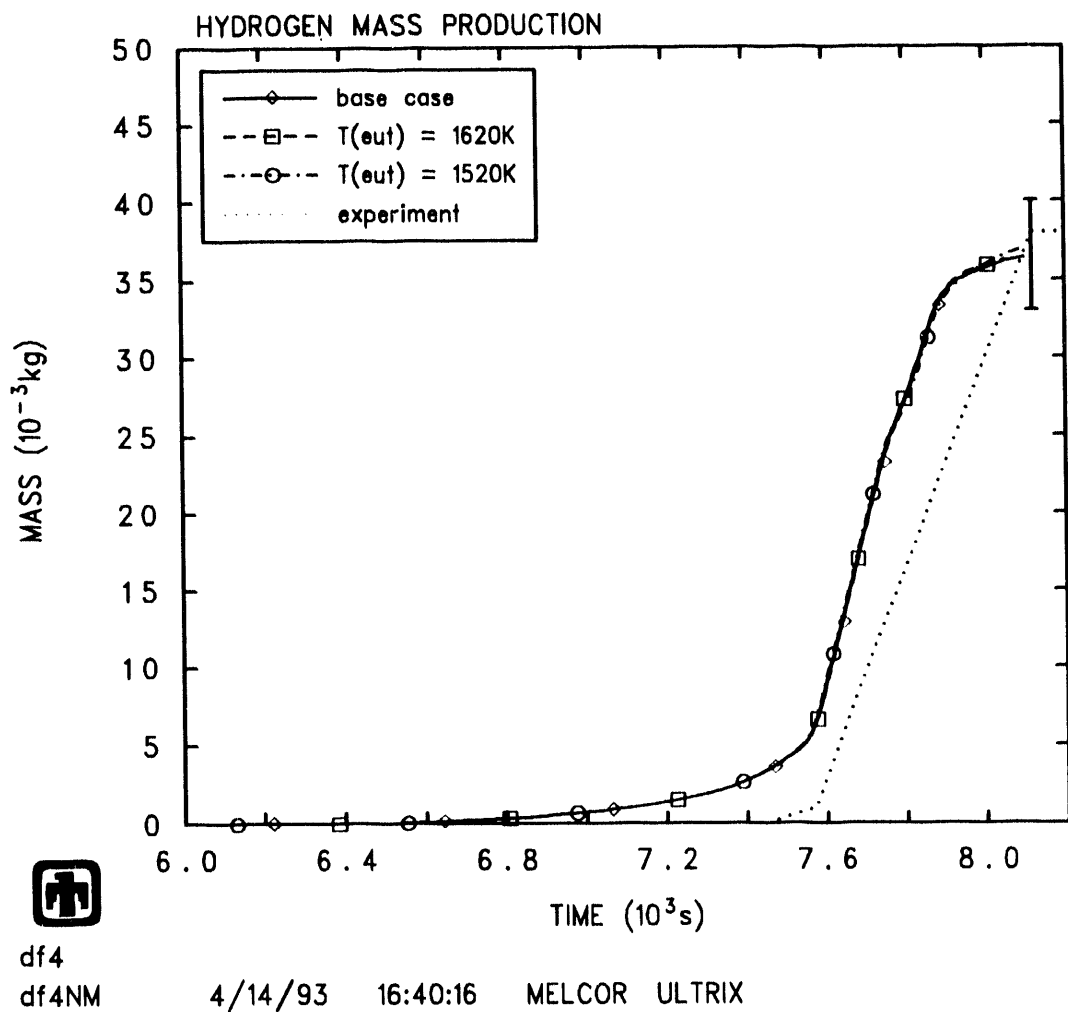
Figure 5.4.10. Hydrogen production for the B$_4$C-stainless steel eutectic temperature sensitivity study, compared to base case and measured values.

125
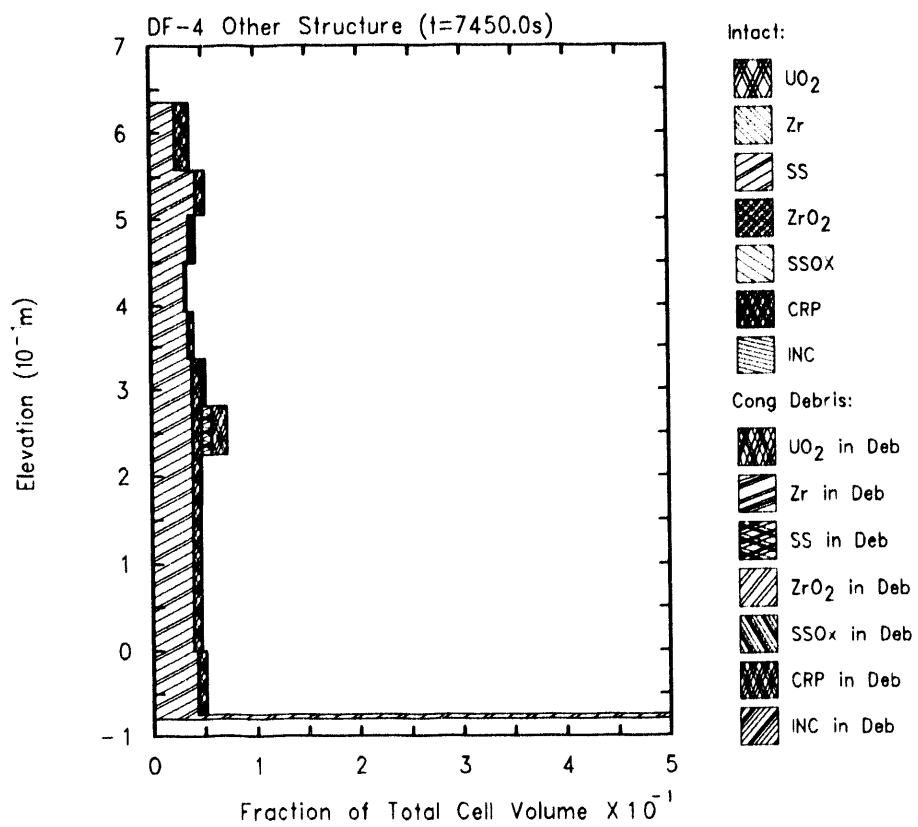
Figure 5.4.11. Other Structure component material locations at 7450 seconds for the 1520K case of the eutectic temperature sensitivity study.
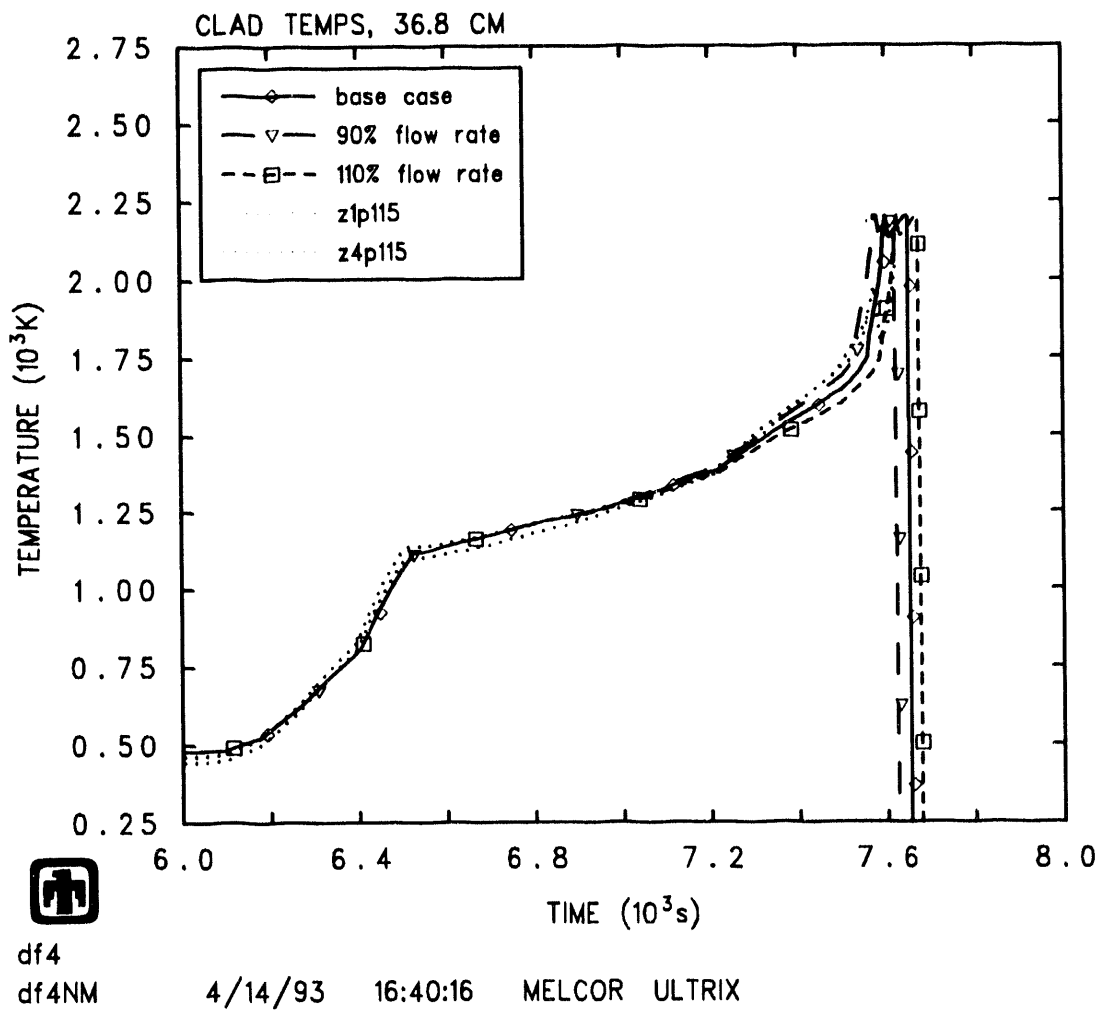
Figure 5.5.1. Cladding temperature response at the 36.8 cm plane for the steam mass flow rate sensitivity study, compared to base case and measured values.

HYDROGEN MASS PRODUCTION

base case
90% flow rate
110% flow rate
experiment
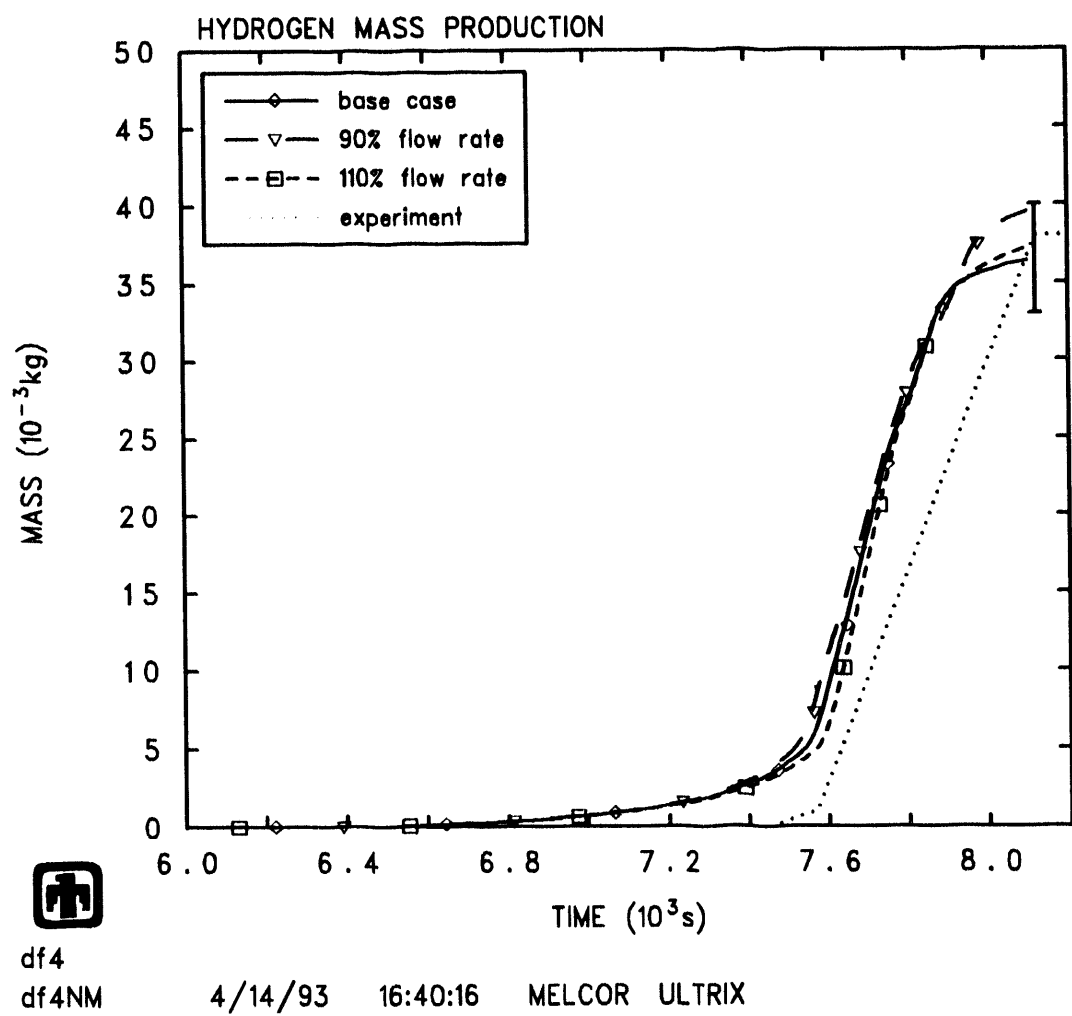
Figure 5.5.2. Hydrogen production for the steam mass flow rate sensitivity study, compared to base case and measured values.

128

5.5.2 Steam Inlet Temperature

The steam inlet temperature in the experiment was measured using a thermocouple in the inlet plenum below the DF-4 test bundle. This data was provided on a data channel and was used in the MELCOR base case model. For this sensitivity study, the inlet temperature was varied by ±10%. This was done by scaling the control function which specified the temperature in the time-dependent volume below the test bundle in the MELCOR DF-4 model.

The cladding temperature at the 25.4 cm plane for this study is compared with the base case and measured results in Figure 5.5.3. Increasing and decreasing the steam inlet temperature had the expected results of increasing and decreasing cladding temperatures and causing earlier and later failure, respectively. The variations from the base case were very slight; this was not surprising, considering the overall temperature increase as the steam traveled up the test bundle. The temperature response of the control blade was very similar.

The hydrogen production is shown in Figure 5.5.4. Increasing the inlet temperature resulted in slightly increased hydrogen production early on, but resulted in less overall hydrogen production. This was the result of more zircaloy ending up in debris, which was then covered by a layer of ZrO_2 which prevented further oxidation. Decreasing the inlet temperature resulted in the same amount of hydrogen produced as the base case.

In conclusion, the MELCOR results for this experiment were not very sensitive to the steam inlet temperature, due to the large temperature rise in the steam as it traveled up the test bundle.

5.5.3 Porous Zirconia Thermal Conductivity

Part of the test bundle insulation consisted of a porous zirconia material whose density was approximately 23% that of fully dense ZrO_2. A correlation for the thermal conductivity was given in [5] which accounted for the enhanced conductivity due to steam absorbed in this material. This correlation is given in Equation (3.1). For this study, the thermal conductivity was varied by ±25% by scaling the control function used to input this correlation.

The cladding temperatures at the 36.8 cm plane for this study are compared with base case and experimental results in Figure 5.5.5. The results changed only at higher temperatures, when radiation heat transfer to the boundary heat structure and heat conduction through that structure were significant. Increasing and decreasing the conductivity through the heat structure resulted in decreasing and increasing the energy absorbed in the test bundle components, respectively. The more energy absorbed in the core components, the earlier component failure occurred. Temperature behaviors at other levels and in the control blade were very similar.

The hydrogen produced for this case is compared to the base case and measured results in Figure 5.5.6. The timing of hydrogen production was affected by changes to the heat structure conductivity, but the total amount of hydrogen produced was changed only for the case which increased the heat structure conductivity. The de-

129
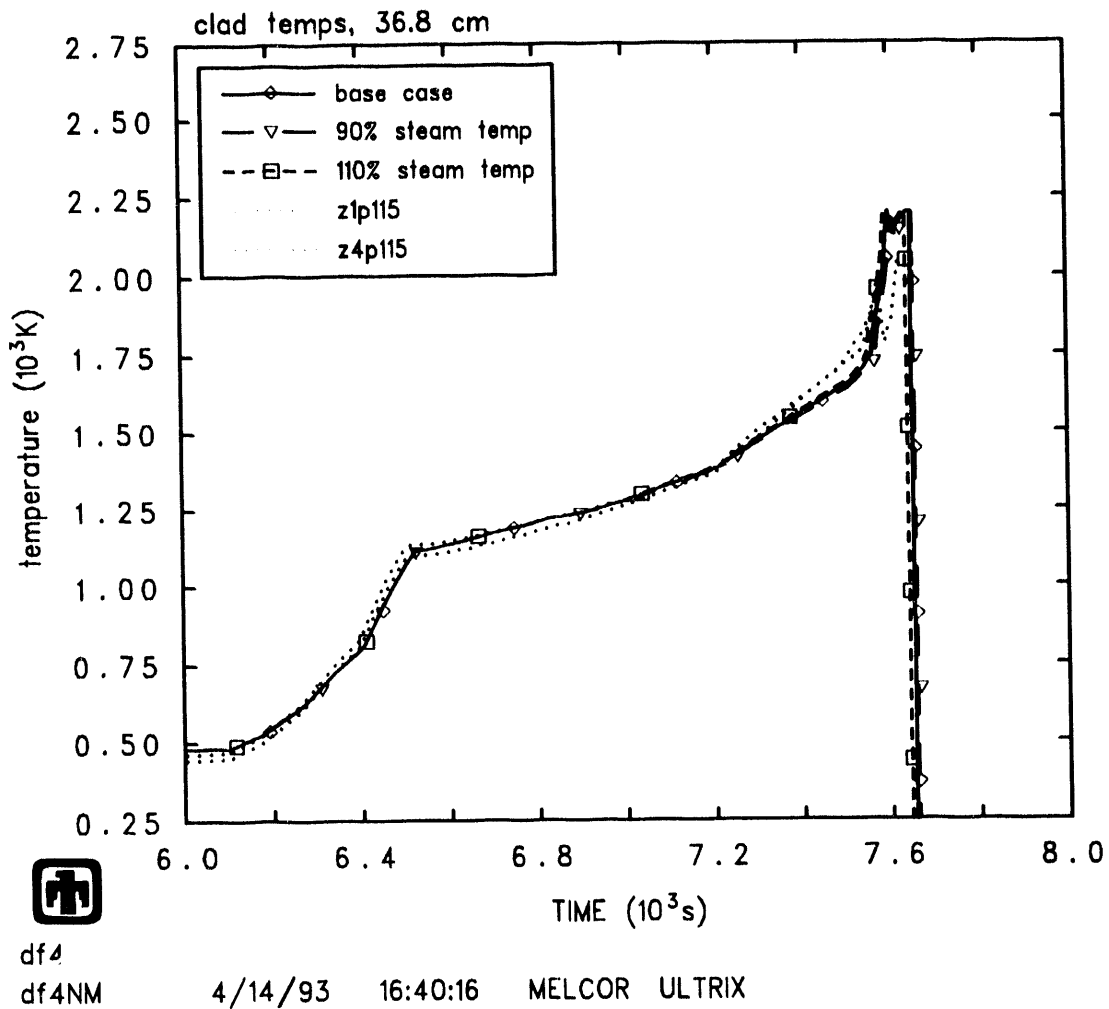
Figure 5.5.3. Cladding temperature response at the 36.8 cm plane for the steam inlet temperature sensitivity study, compared to base case and measured values.
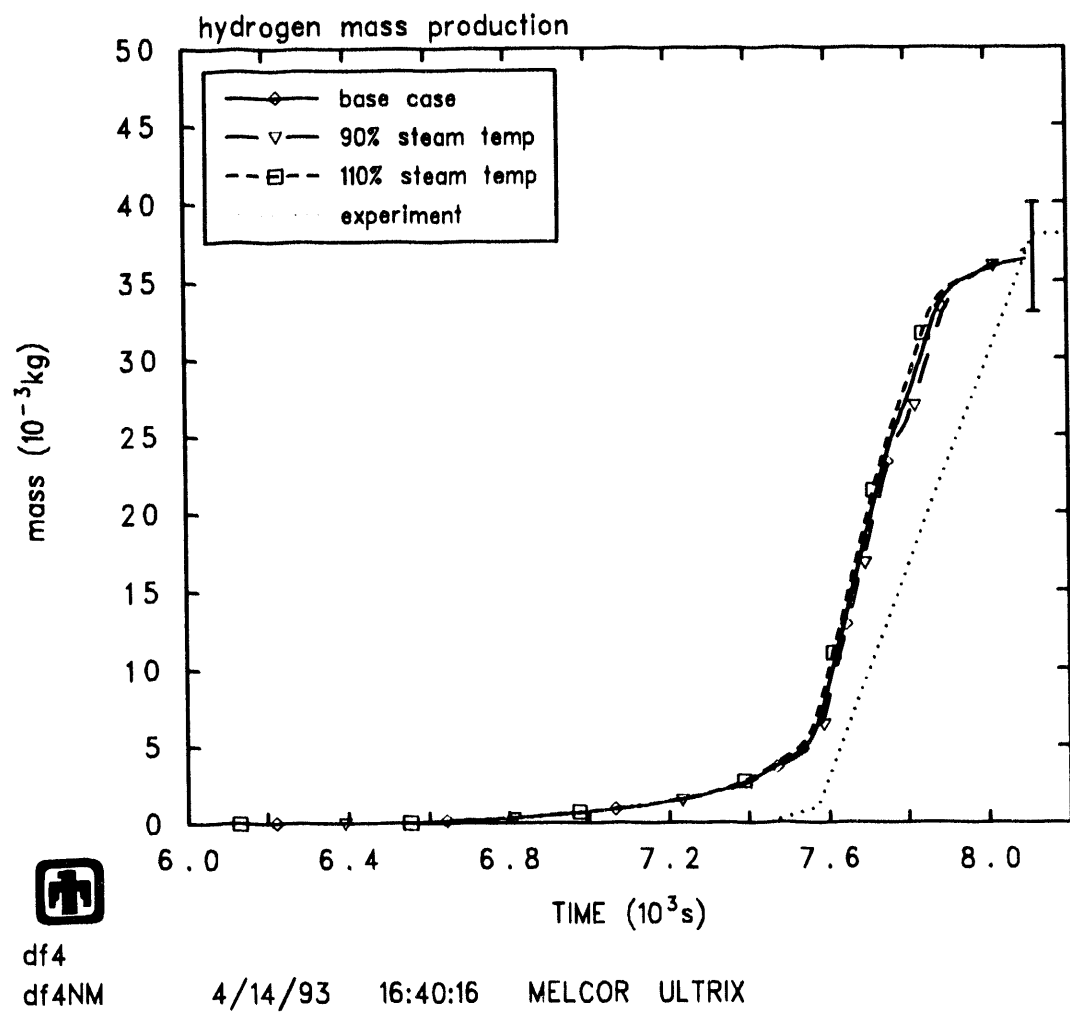
Figure 5.5.4. Hydrogen production for the steam inlet temperature sensitivity study, compared to base case and measured values.

crease in hydrogen production was probably due to the increased heat loss through the heat structure.

The MELCOR results were sensitive to the boundary heat structure conductivity. This was not surprising, given the high exposure of the fuel rods to the insulating boundary.

5.5.4 Radial Heat Structures Outer Boundary Temperature

The outer surface of the boundary heat structure in the MELCOR base case model corresponded to the pressure boundary shown in Figure 2.1.1. In the experiment, this boundary was heated to 473K to prevent condensation on the inside surface of the test bundle insulation. The outer surface of the boundary heat structure was held at this temperature in the MELCOR base case model. During the experiment, this surface was actually heated to higher temperatures because of heat transfer from the test bundle region. In this study, the temperature of this surface was raised and lowered by 10% (about 50K). In addition, a temperature ramp case was performed, where the temperature was raised from 460K to 600K on an even ramp from 6000 to 8500 seconds. This was accomplished using a control function to specify the outer boundary temperature for all radial heat structures in the MELCOR base case model.

The temperature and hydrogen production results for this study are compared to base case and measured results in Figures 5.5.7 and 5.5.8. These figures show that the MELCOR base case calculation for DF-4 was not very sensitive to changes in the outer boundary temperature of the radial heat structures.

5.5.5 Bundle Fission Power

The fission power experienced by the test bundle components was input to the MELCOR base case model using a power coupling correlation from [5]. This correlation was derived from ACRR power increases and measured cladding temperature response during the initial nuclear heating subphase of the experiment. Figure 3.2.2 shows that there were large uncertainties (between 10% and 40%) in the coupling between the ACRR and the test bundle fission powers. In this study, the total amount of test bundle power was adjusted by ±10%, using the same peaking factors derived from Equation (3.2). This was accomplished by scaling the control function used to input total fission power.

Figures 5.5.9 and 5.5.10 show that the MELCOR base case calculation for DF-4 was quite sensitive to the amount of fission power deposited in the test bundle. The deviations in temperature, failure timing and total hydrogen production were all nearly proportional to bundle power changes. Temperatures in other axial levels and components were very similar.
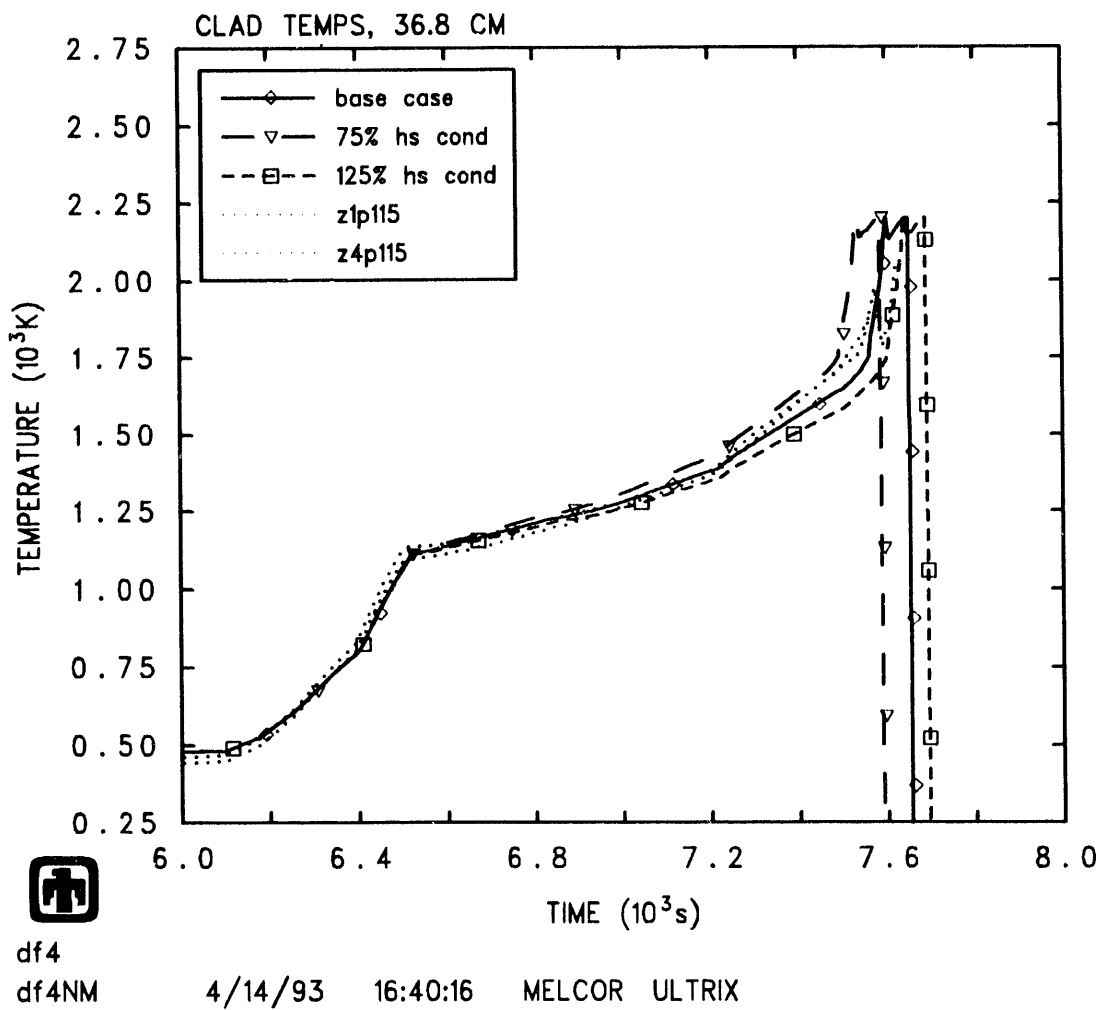
Figure 5.5.5. Cladding temperature response at the 36.8 cm plane for the boundary heat structure conductivity sensitivity study, compared to base case and measured values.

HYDROGEN MASS PRODUCTION

Legend:
- base case
- 75% hs cond
- 125% hs cond
- experiment

df4
df4NM   4/14/93   16:40:16   MELCOR   ULTRIX
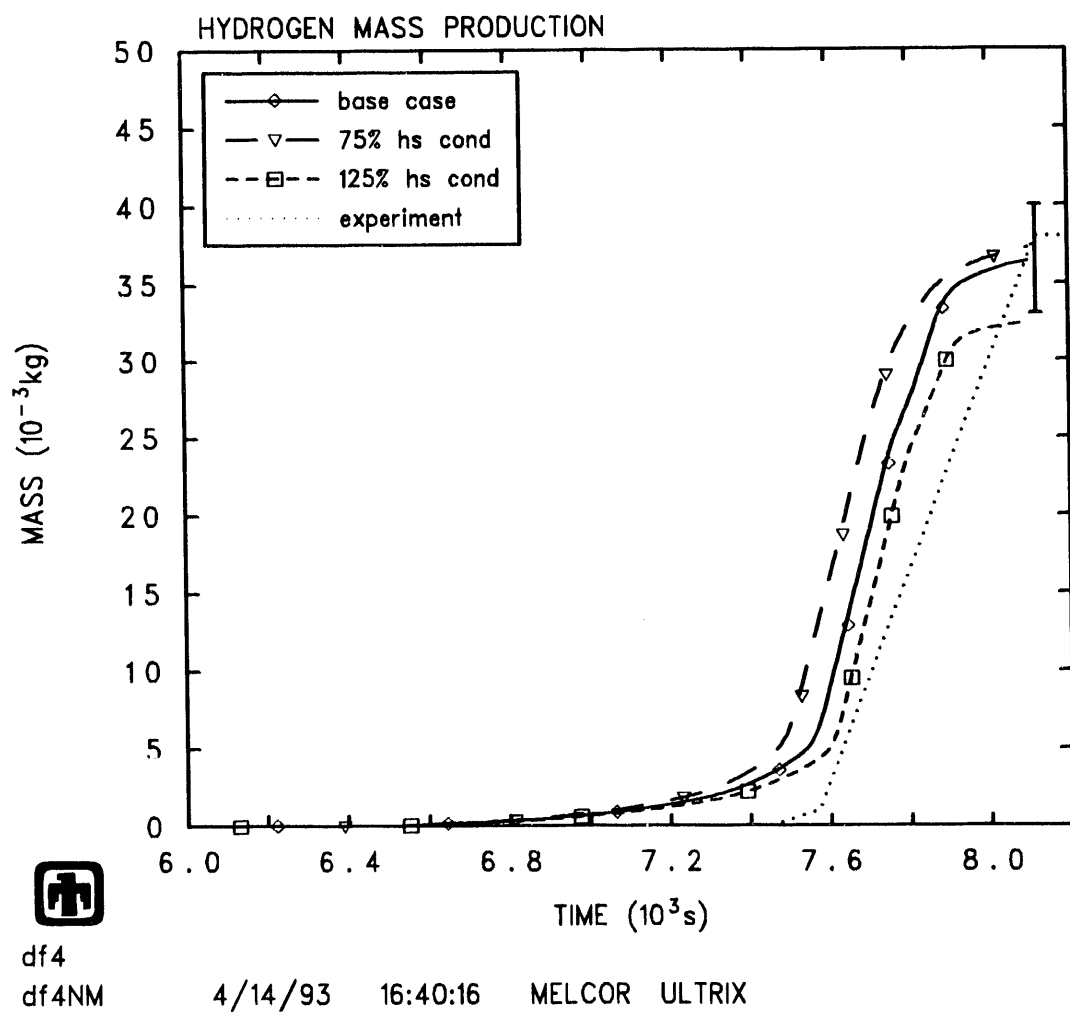
Figure 5.5.6. Hydrogen production for the boundary heat structure conductivity sensitivity study, compared to base case and measured values.
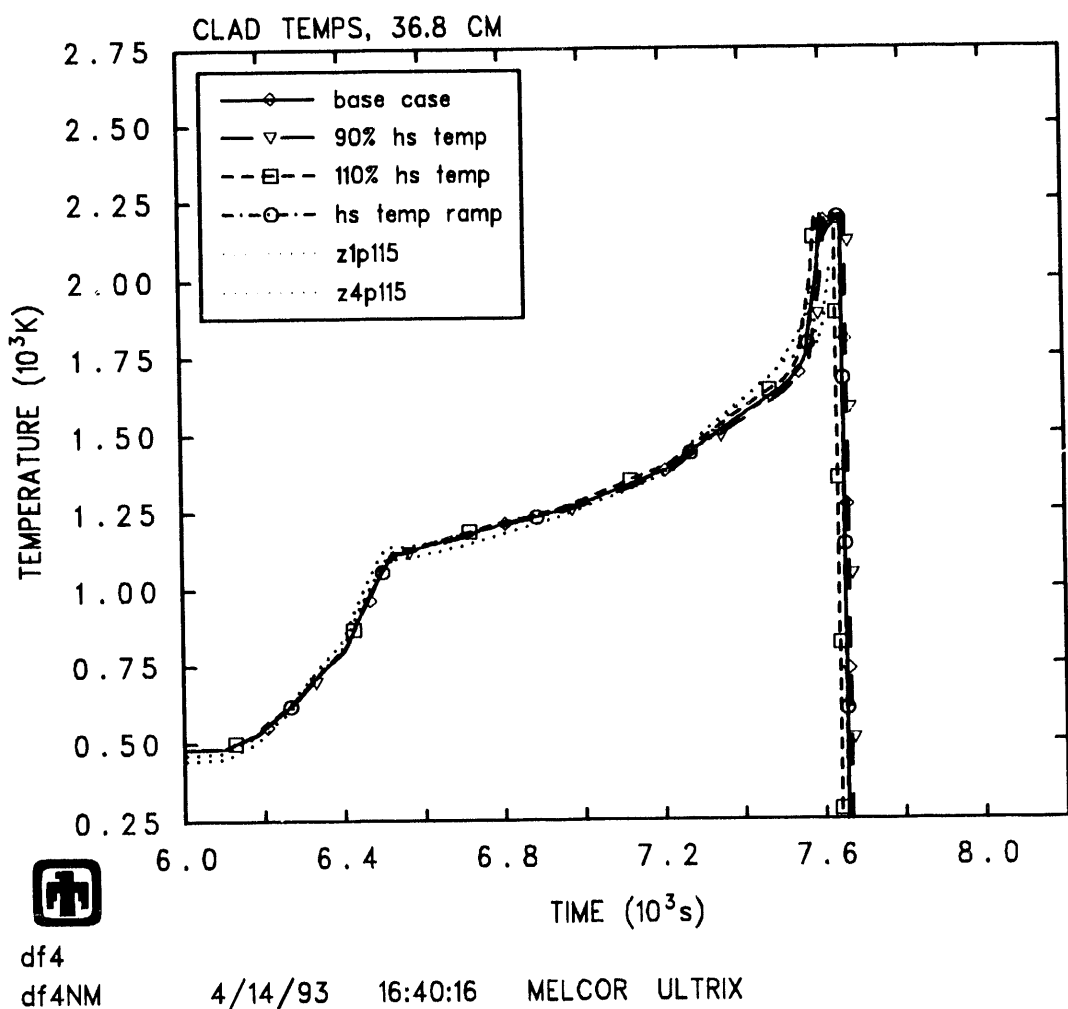
Figure 5.5.7. Cladding temperature response at the 36.8 cm plane for the boundary heat structure temperature sensitivity study, compared to base case and measured values.

HYDROGEN MASS PRODUCTION
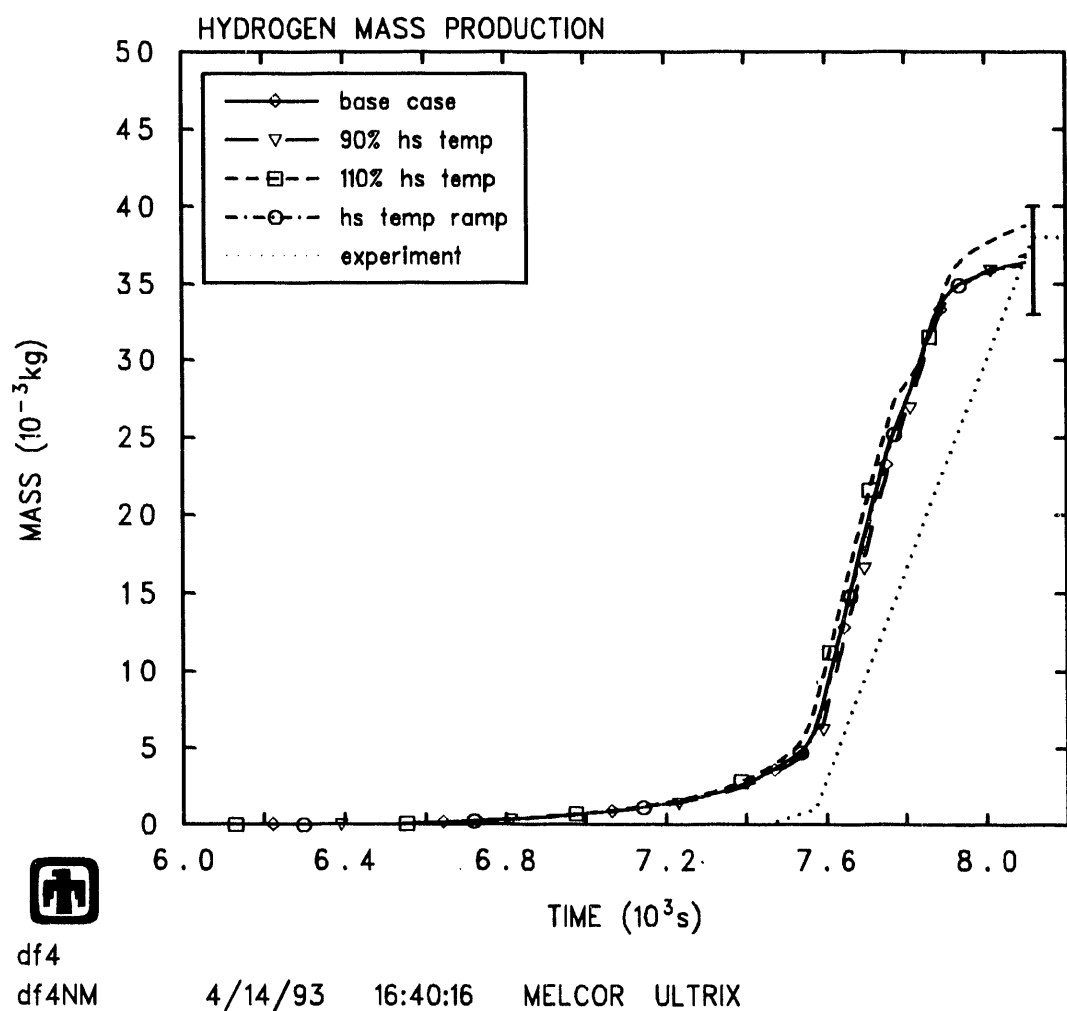
Figure 5.5.8. Hydrogen production for the boundary heat structure temperature sensitivity study, compared to base case and measured values.
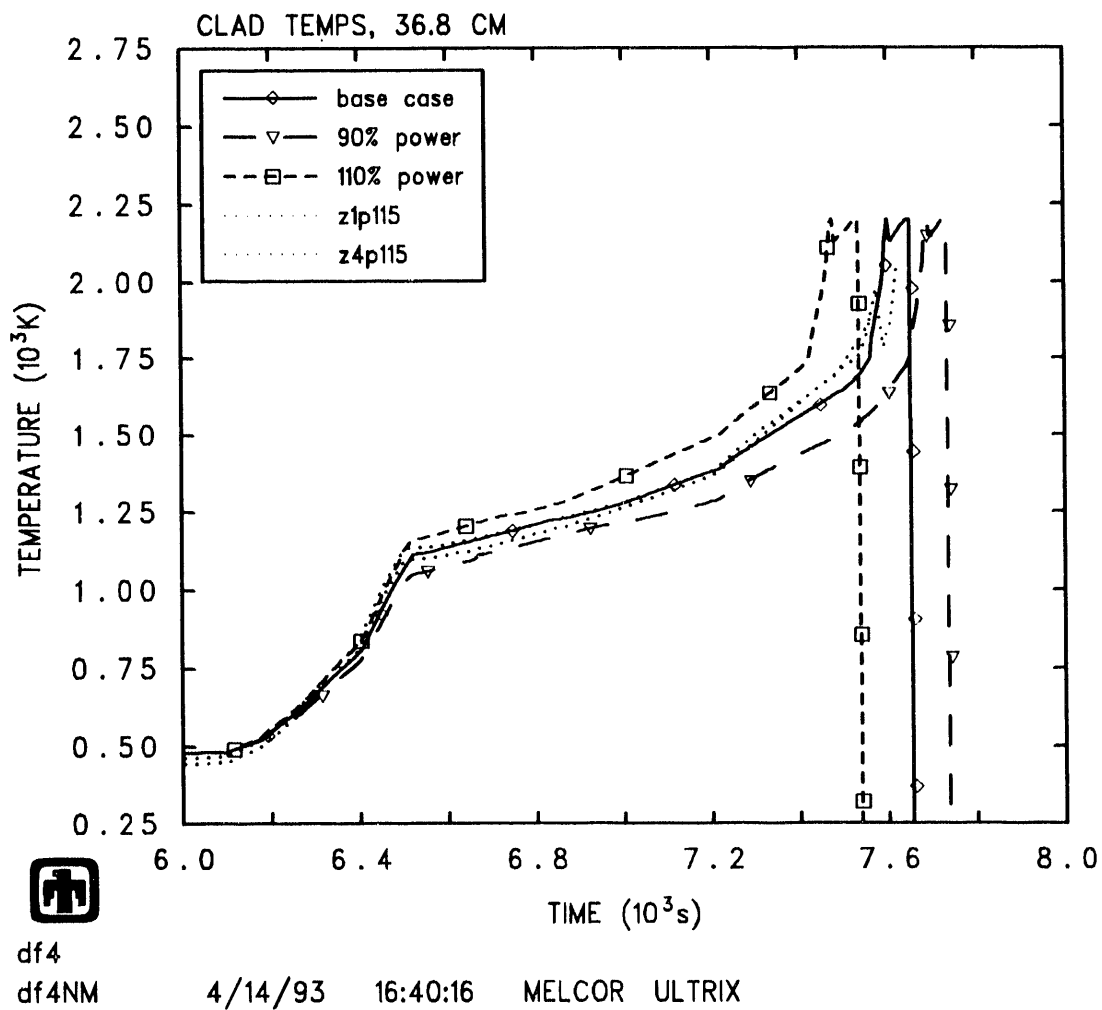
Figure 5.5.9. Cladding temperature response at the 36.8 cm plane for the bundle power sensitivity study, compared to base case and measured values.
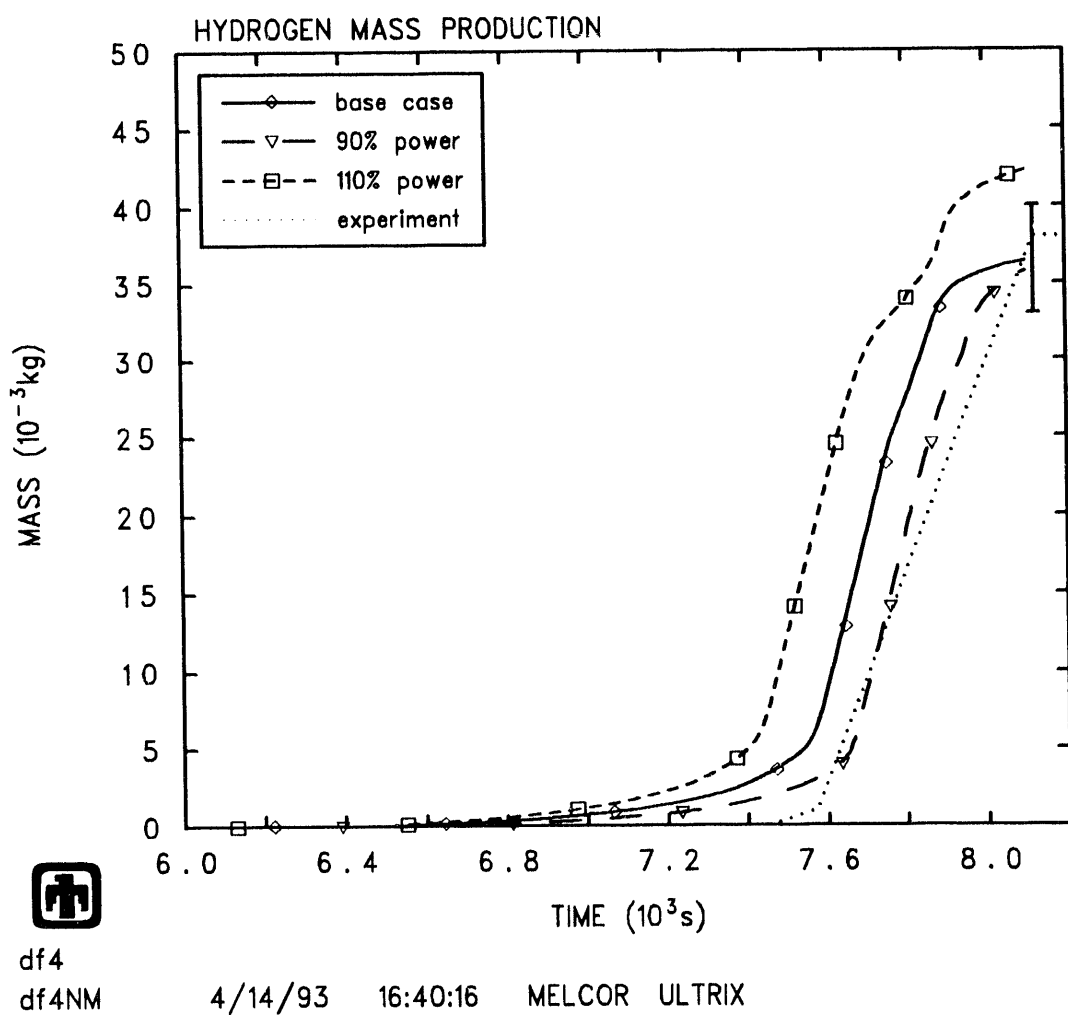
Figure 5.5.10. Hydrogen production for the bundle power sensitivity study, compared to base case and measured values.

5.6 General Heat Structures Package Studies

Two sensitivity studies were done on HS package parameters. The first was on the radiation model used for all heat structures, and the second was on the emissivities used for all heat structures.

5.6.1 HS Radiation Model Option

The heat structures package has two options for calculating radiation heat transfer from the steam environment to the heat structures. The base case model used the default option, the equivalent band ("equiv-band") model. In this study, the model was changed to use the "gray-gas-a" option.

The temperature and hydrogen production results from this study were almost identical to the base case results. The radiation model employed in the heat structures package had no effect on the final calculated results for this problem.

5.6.2 Heat Structures Emissivities

The emissivities for all heat structures surfaces in the MELCOR base case models were chosen arbitrarily to be 0.7. A sensitivity study was done to investigate the effects of varying this emissivity. Two cases were done for this study, setting the emissivities for all heat structures surfaces to 0.5 and 0.9.

The temperature and hydrogen production results for both cases of this study were almost identical to those of the MELCOR base case. Thus, there was very little sensitivity to the emissivity used for heat structures surfaces.

5.7 COR and CVH Nodalization

In the MELCOR base case model, there were nine core cells in the active fuel region and two control volumes in the core (one each for the channel and bypass regions). Four variations on the nodalization in the DF-4 model were performed for this study. For the first three cases, the number of core cells in the active fuel region was changed to 5, 18 and 27 core cells. For the last case, the 18 cell problem was used with six CVH control volumes instead of two, where the active fuel region was split equally among three axial control volumes in the channel and bypass regions.

The cladding and control blade temperatures at the 36.8 cm plane are shown in Figures 5.7.1 and 5.7.2, respectively. For the first 500 seconds of the problem, the temperature response was very close in all cases. The temperatures diverge after that, and generally the cases with the finer nodalizations calculated higher cladding temperatures and early failure times. Note that the temperatures monotonically increase with the number of core cells used, with the base case results closer to the finer nodalization cases.

The hydrogen production for all cases is compared to base case and measured results in Figure 5.7.3. Like the temperature response, the hydrogen response is

sensitive to nodalization, with the two finest nodalization problems producing less hydrogen and the other problems producing about as much hydrogen as the base case calculation. Note that only the 27-cell problem hydrogen production is outside the uncertainty band of the PIE data.

The reason for higher temperatures and lower hydrogen production with finer nodalizations can possibly be linked to the competition between advection and oxidation for steam flowing through the test bundle. The increased temperatures could be caused by the same effect, where smaller core cells have less steam cooling (this is only a suggestion; it could also be argued that smaller core cells produce less heat and therefore require less cooling). This study shows the need for better time step control during periods of rapid zircaloy oxidation.

5.8   Time Step and Machine Dependency Studies

The MELCOR code contains both global time step control and package-specific time step subcycling. However, the effectiveness of that time step control is sometimes suspect, and it is always a good idea to investigate a range of time steps for any particular input model. Also, MELCOR is considered a very portable code and does in fact run on many different computer platforms of both 32-bit and 64-bit architectures. Comparing code results across these platforms can reveal both machine dependencies and general coding problems [10]. In this section, studies that were performed to investigate the time step control in MELCOR and the dependency of DF-4 results on computer platform are discussed.

5.8.1   Time Step Study

The time step in the DF-4 base case model was restricted to a maximum of 0.25 seconds between 7200 and 8000 seconds. This was the period of time when core degradation took place. During the rest of the calculation, the maximum time step was set to 1.0 seconds. For this sensitivity study, cases were run with the maximum time step set at 0.1 seconds, 0.5 seconds, 1.0 second and a time step much larger than the MELCOR-default time step between 7200 and 8000 seconds (the maximum time step for the final case was chosen such that the code always used the MELCOR-chosen time step).

The overall MELCOR time step used by the four cases is compared with that used by the base case model in Figure 5.8.1. The overall code was using the specified maximum time step, except for the case that used the MELCOR-default time step. The COR package time step used by the four cases is compared with that used by the base case model in Figure 5.8.2. For time steps of 0.1 and 0.25 seconds, the COR package time step is the same as the system time step. However, using a time step above 0.25 seconds caused the COR package to choose smaller time steps. This caused difficulties when core components began to oxidize. The cladding temperature at the 49.5 cm plane in Figure 5.8.3 shows the problem encountered in DF-4 runs using timesteps that were too large. At approximately 7400 seconds, the "Δt = default"

110
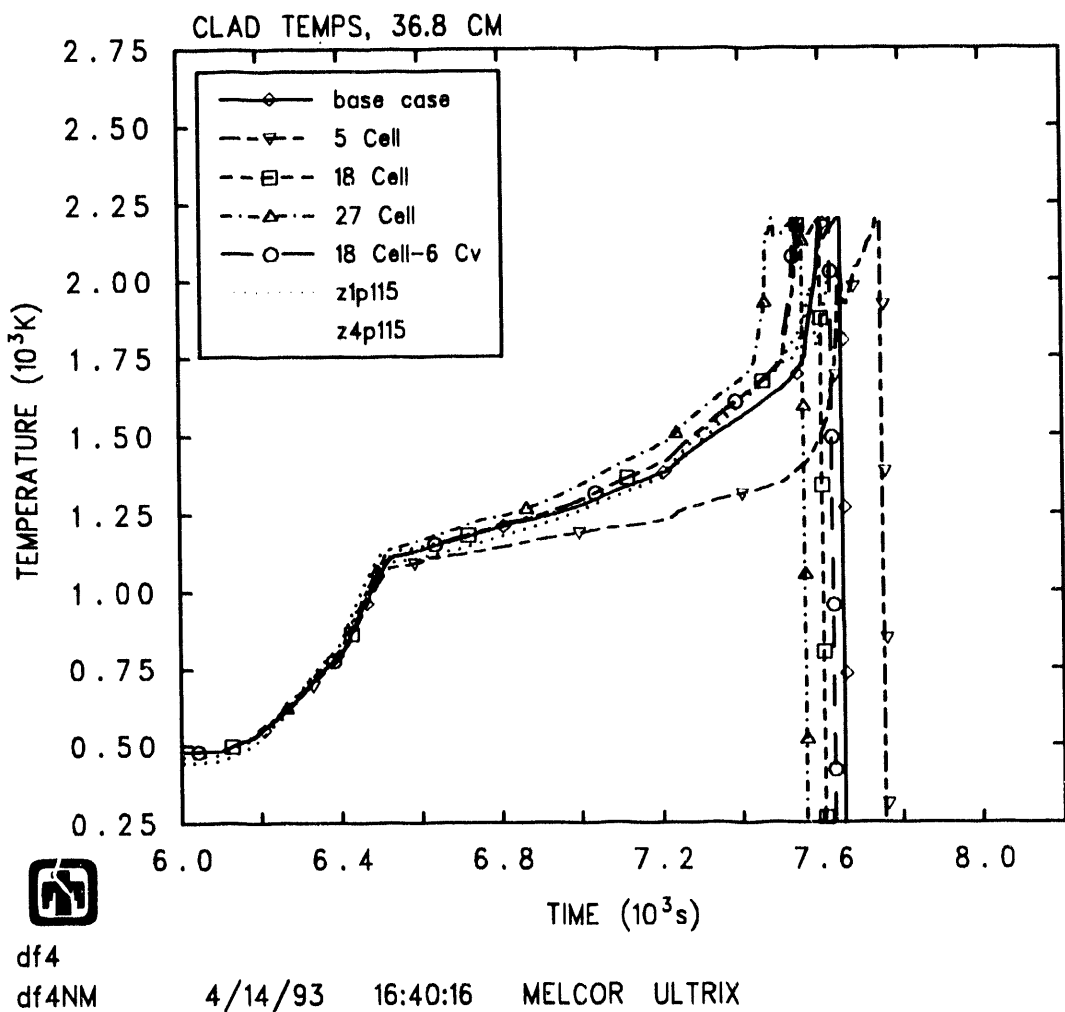
Figure 5.7.1. Cladding temperature response at the 36.8 cm plane for the COR and CVH nodalization sensitivity study, compared to base case and measured values.

OS TEMPS, 36.8 CM
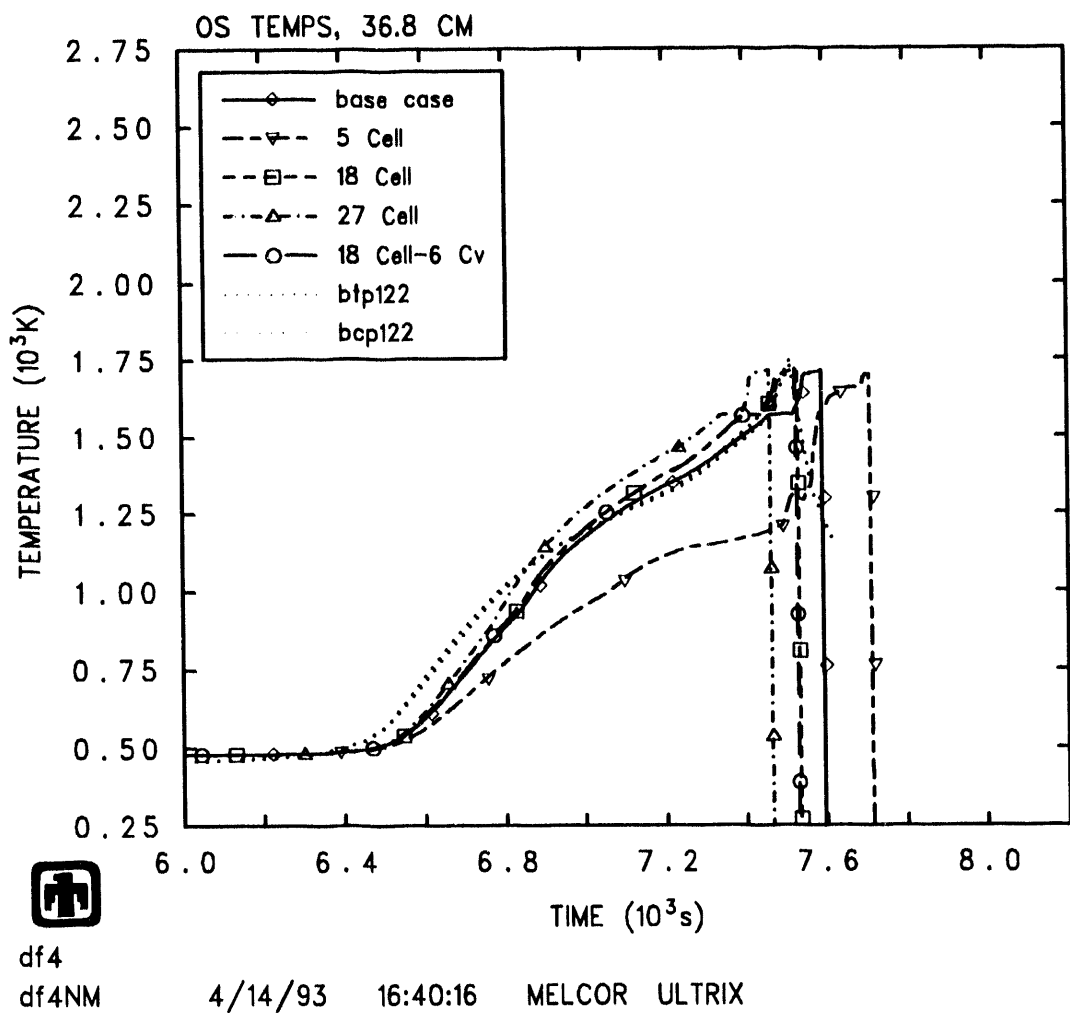
**Figure 5.7.2.** Control blade temperature response at the 36.8 cm plane for the COR and CVH nodalization sensitivity study, compared to base case and measured values.

HYDROGEN MASS PRODUCTION

Legend:
- ◇ base case
- ▽ 5 Cell
- ⊟ 18 Cell
- △ 27 Cell
- ○ 18 Cell-6 Cv
- ⋯⋯ experiment

Y-axis: MASS (10^{-3} kg)

X-axis: TIME (10^3 s)

df4
df4NM   4/14/93   16:40:16   MELCOR   ULTRIX
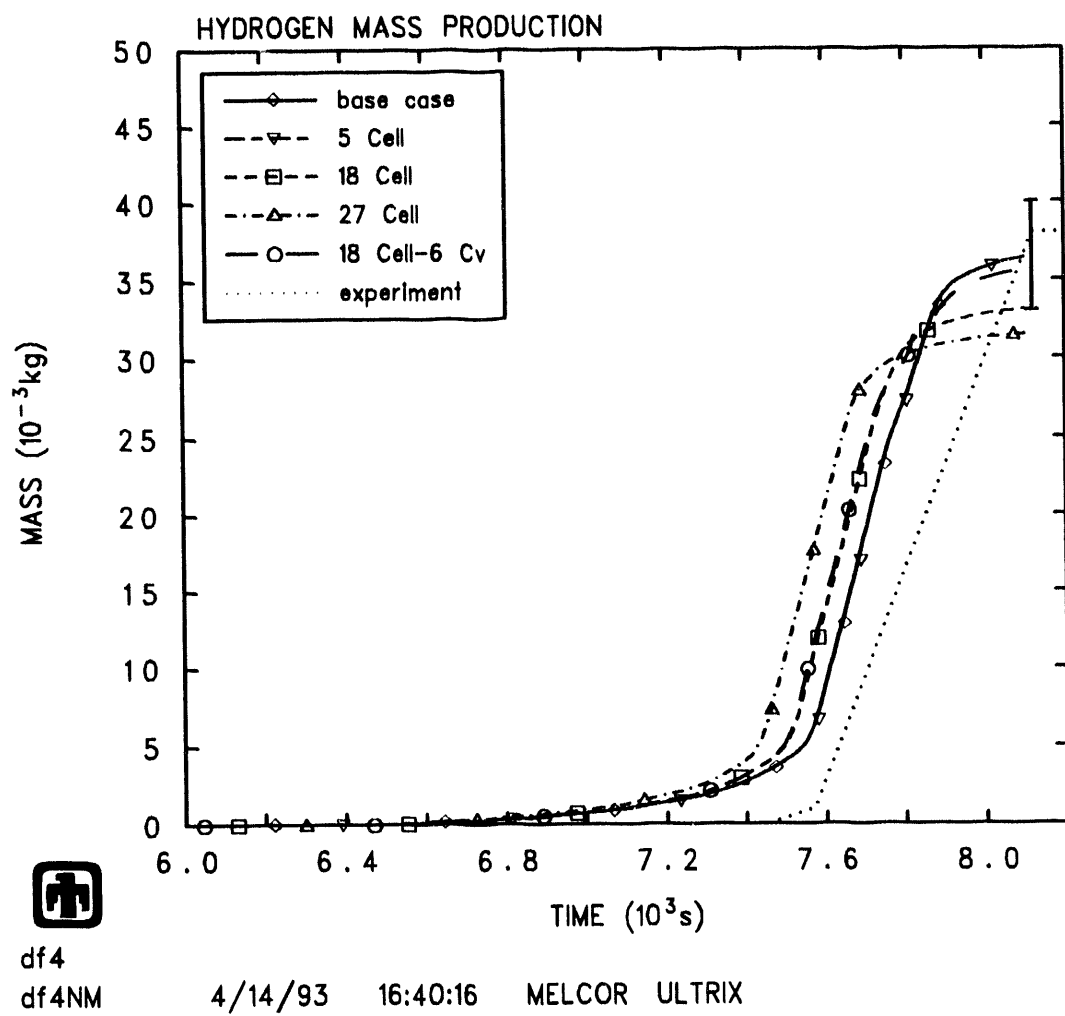
Figure 5.7.3. Hydrogen production for the bundle power sensitivity study, compared to base case and measured values.

case showed a spike in temperature. The cause of this was apparently the beginning of oxidation at that axial level, which stopped soon afterward due to steam starvation. This phenomenon went away when a smaller time step was used. This was the reason for limiting the time step to 0.25 seconds between 7200 and 8000 seconds for the base case calculation.

The cladding and control blade temperatures at the 36.8 cm and 25.4 cm planes are shown in Figures 5.8.4 and 5.8.5, respectively. Temperature behavior before 7200 seconds was identical because the same time step was being used in all cases. After 7200 seonds, results were also relatively close, until the beginning of rapid oxidation. There was a spread of approximately 100 seconds around all cases for the start of rapid oxidation in the cladding at the 36.8 cm plane. Also, for this plane the base case temperature data was bounded by other cases. The spread in failure time of the cladding at this plane was less than 100 seconds. The temperatures in the control blade were also very close for all cases, until the beginning of the B_4C-stainless steel eutectic interaction. After this point, the temperatures drifted apart, but were still relatively close. The spread of failure times was approximately 100 seconds, similar to the spread in cladding failure times at the 36.8 cm plane.

The hydrogen production for the time step study cases is shown in Figure 5.8.6, compared to base case and measured results. The hydrogen production in the base case model was bounded by that of the cases run for this study. It is difficult to find the reason for variations in hydrogen production with differing time steps, because of competing time step-dependent phenomena affecting hydrogen production (e.g., core material relocation and steam starvation effects). In any event, a sensitivity study should always be done on time steps used in MELCOR, at least for the portions of a calculation when core materials are degrading or oxidizing rapidly.

In conclusion, this study showed that core component temperatures calculated by MELCOR for this problem were slightly sensitive to the choice of time step, and that hydrogen production was somewhat sensitive to time step. The proper time step for this problem was in the neighborhood of 0.1–0.5 seconds, and was limited by relocation and oxidation phenomena in the COR package. Time steps for other problems will be different since they depend on flow velocity and other accident progression phenomena.

5.8.2   Machine Dependency Study

MELCOR 1.8.2 was installed on six different computer platforms, where the DF-4 base case input model was run. These computer platforms were: DECstation 5000/240, Hewlett Packard 755, IBM RS/6000 Model 550, SUN Sparcstation 2, Cray X/MP-24, and Gateway 486/DX2-50. The first four machines are 32-bit UNIX workstations, the fifth a 64-bit supercomputer, and the sixth an IBM PC compatible. The base case results for each of these machines were translated to one machine and cross-plotted to compare results. Note that the base case and other sensitivity study calculations were performed on the DECstation 5000/240.

The cladding and control blade temperatures at the 36.8 cm plane for all machines are compared to measured results in Figures 5.8.7 and 5.8.8, respectively. The

144
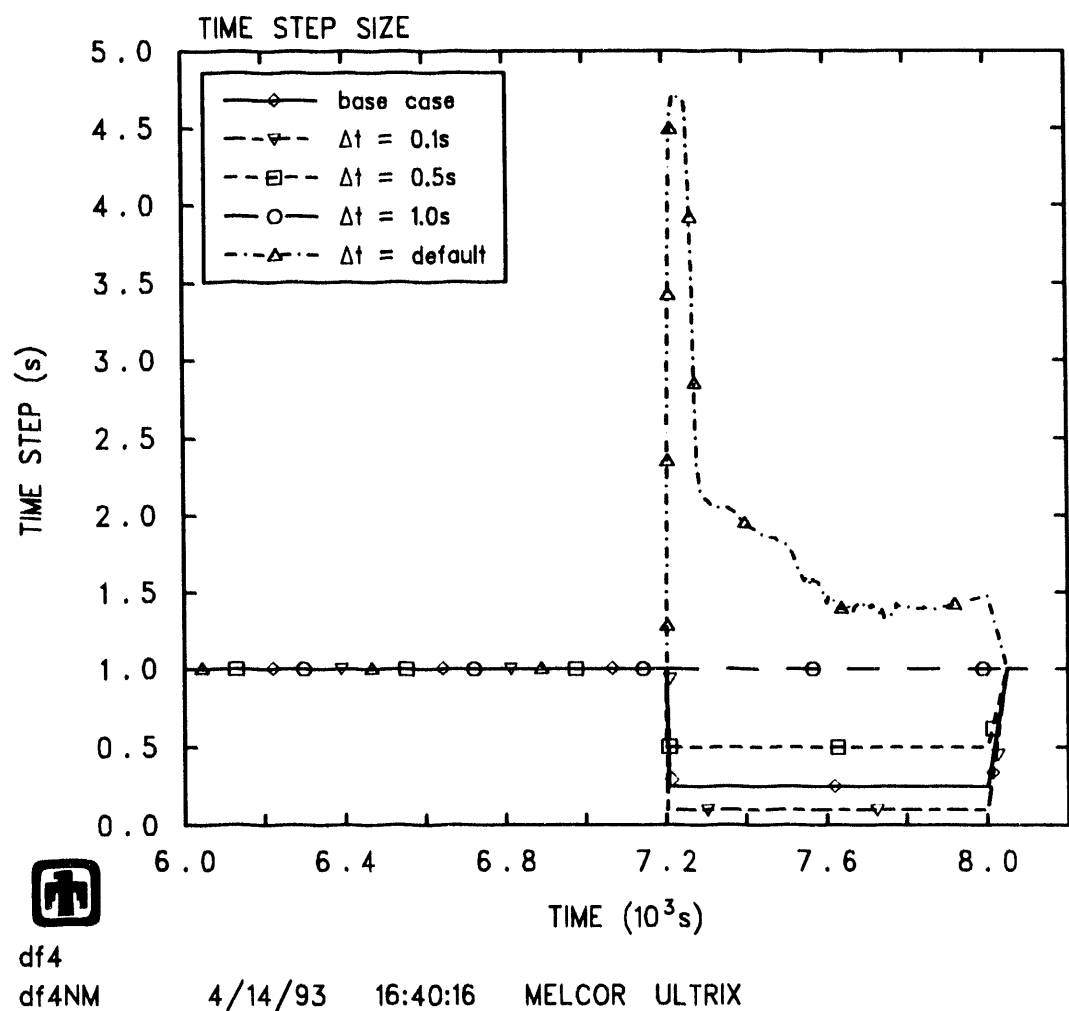
Figure 5.8.1. Time steps used for the time step sensitivity study, compared to base case and measured values.

COR PACKAGE TIME STEP SIZE
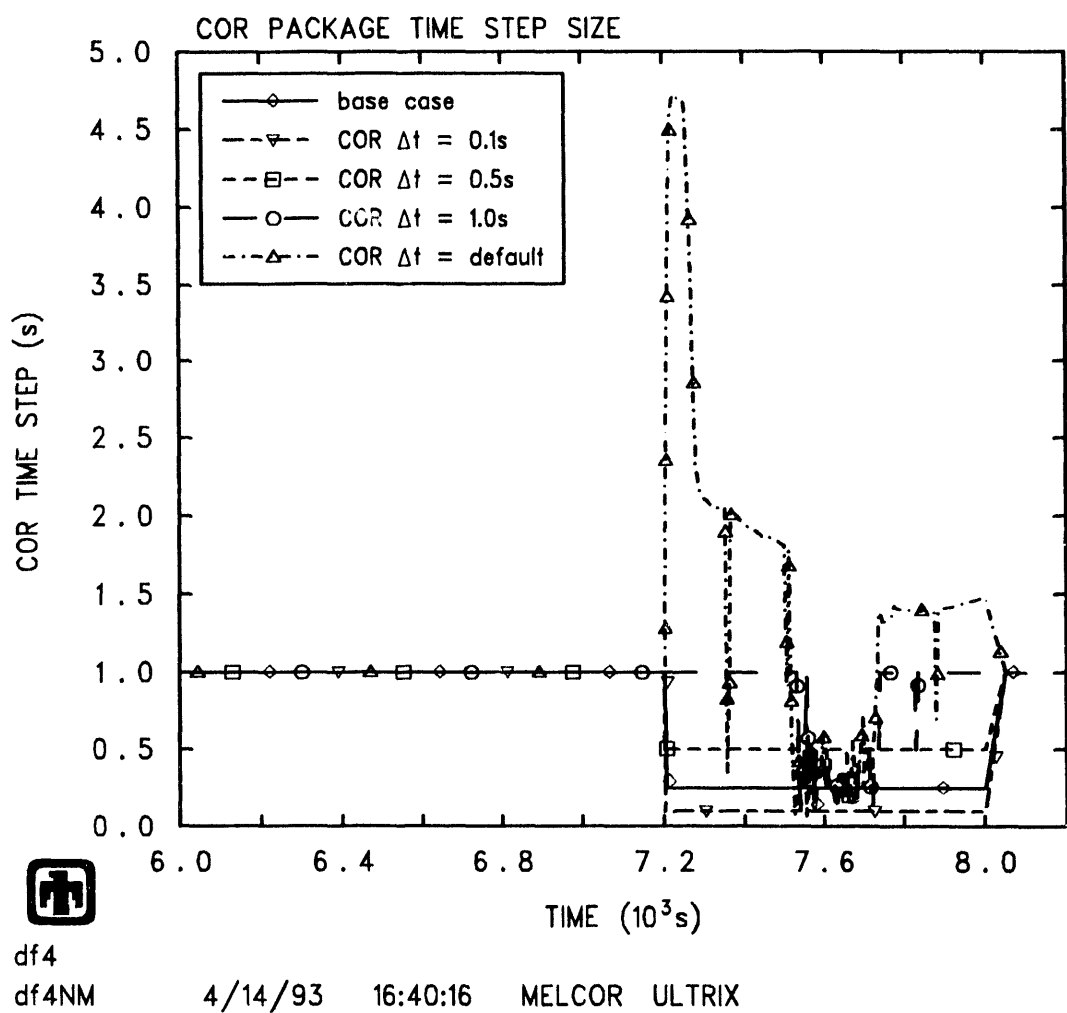
Figure 5.8.2. COR package time steps used for the time step sensitivity study, compared to base case and measured values.
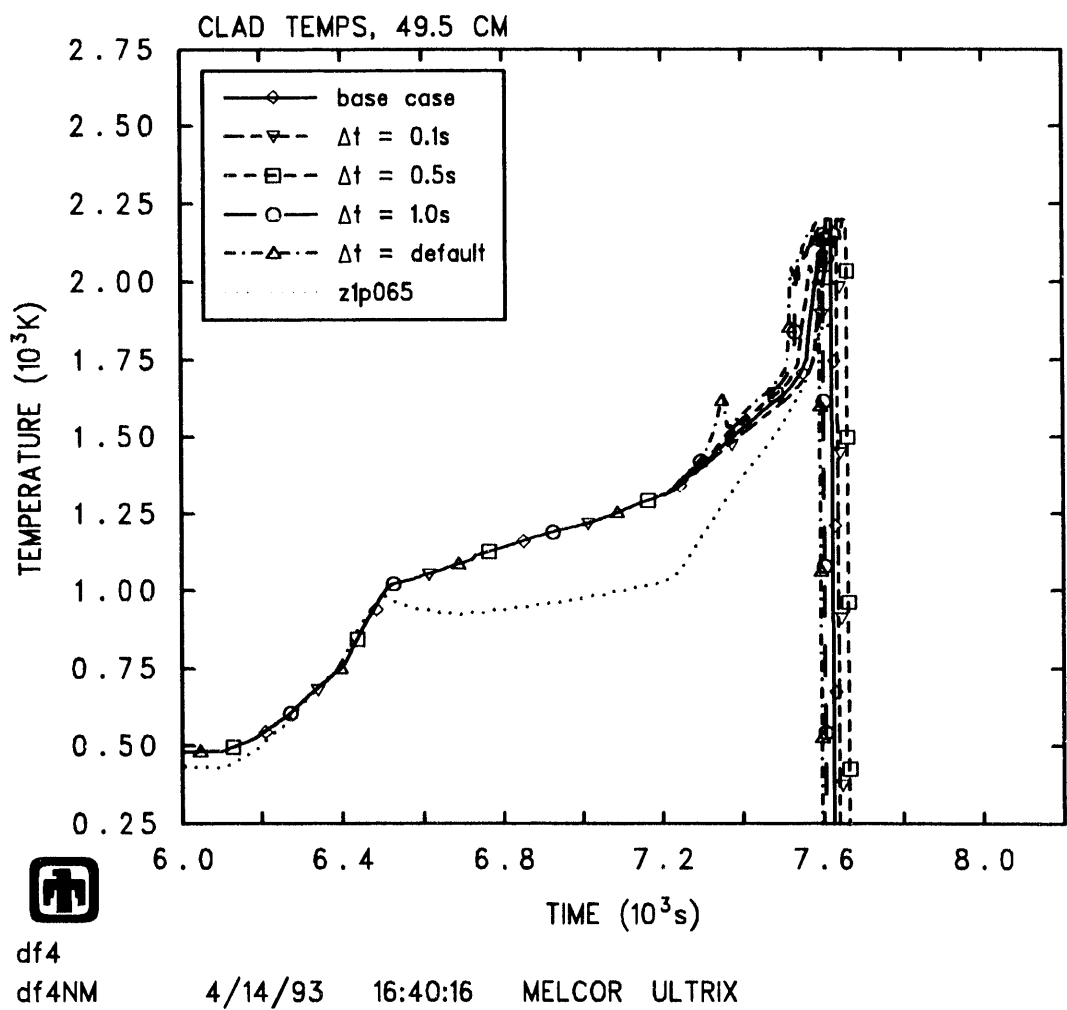
Figure 5.8.3. Cladding temperature response at the 49.5 cm plane for the time step sensitivity study, compared to base case and measured values.
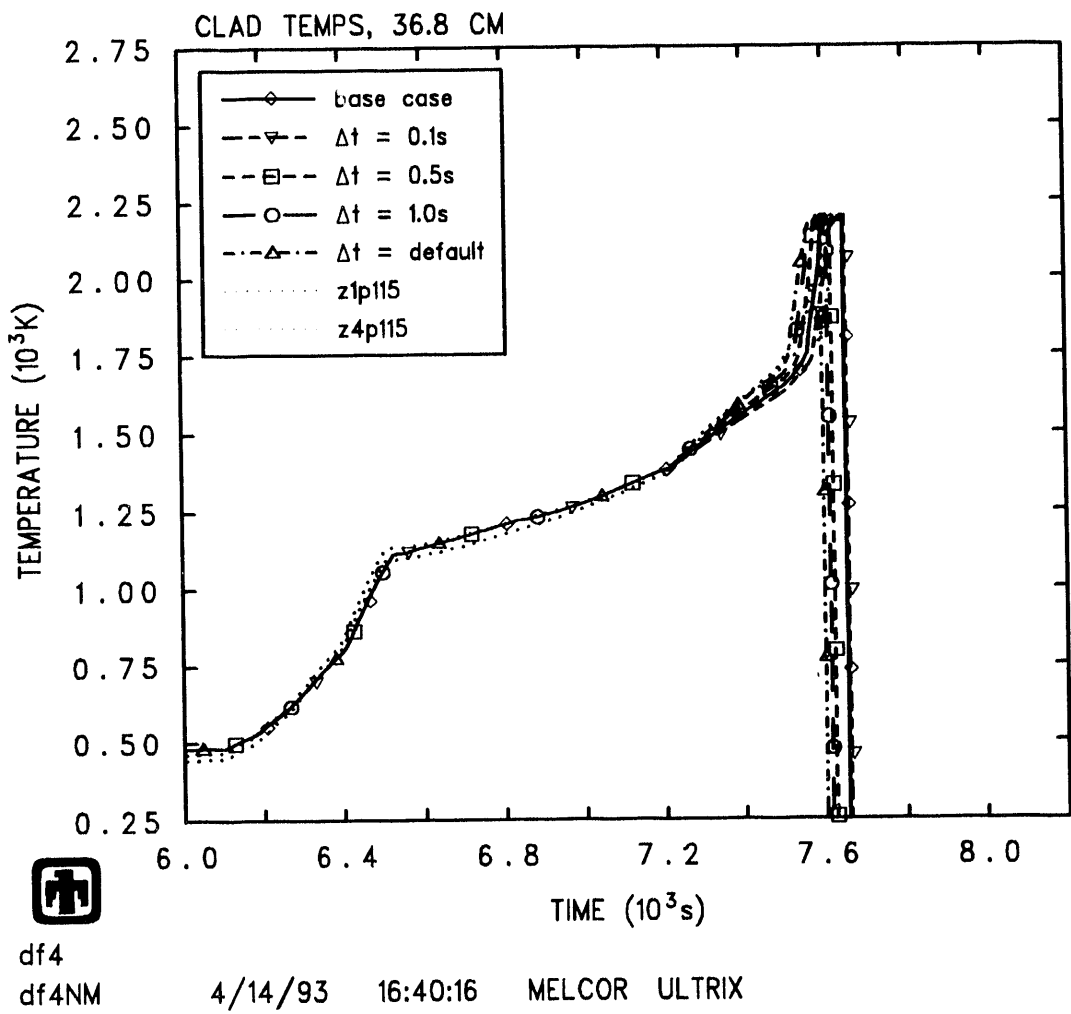
Figure 5.8.4. Cladding temperature response at the 36.8 cm plane for the time step sensitivity study, compared to base case and measured values.
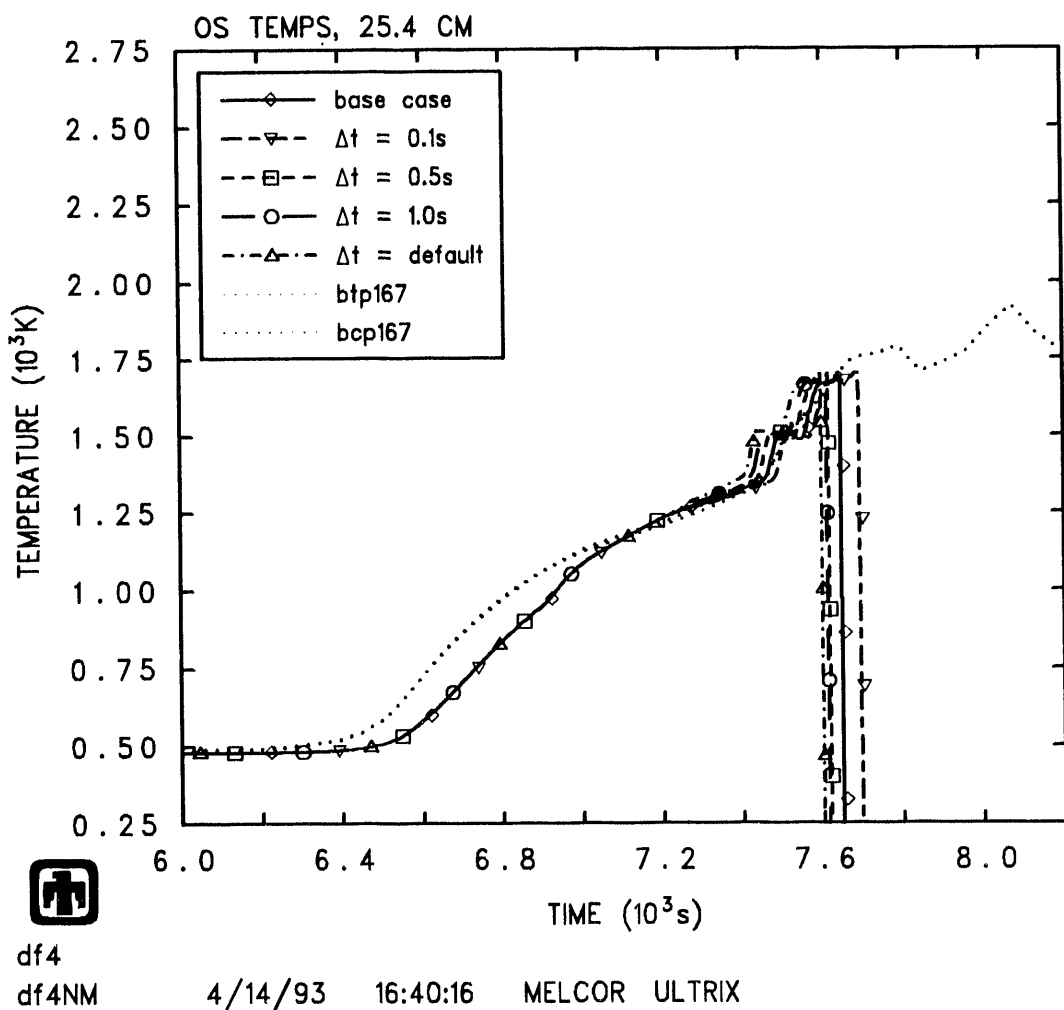
Figure 5.8.5. Control blade temperature response at the 25.4 cm plane for the time step sensitivity study, compared to base case and measured values.

HYDROGEN MASS PRODUCTION
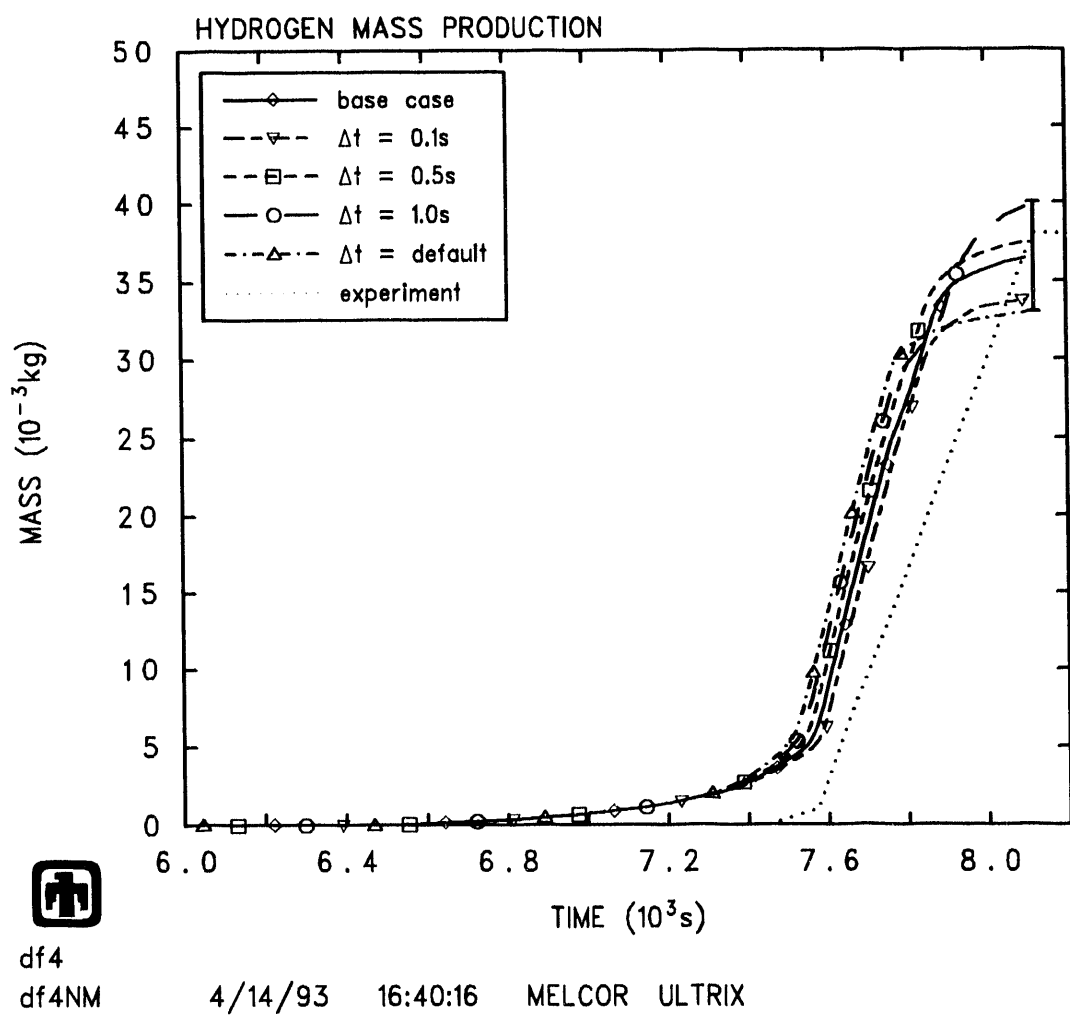
Figure 5.8.6. Hydrogen production for the time step sensitivity study, compared to base case and measured values.

hydrogen production is shown in Figure 5.8.9. These figures show that there were no machine dependencies when running the DF-4 base case problem.

The final component states at 8100 seconds for all machines are shown in Figures 5.8.10— 5.8.15. The final material locations were nearly identical across the machines, with the Cray and the SUN versions showing only slight variations and the bottom of the test bundle.

The overall system time steps and the COR package time steps taken by the various machines are shown in Figures 5.8.16 and 5.8.17, respectively. The system time steps were identical for all machines. The COR package time steps were identical and equal to the system time steps for most of the problem, but started to subcycle around 7550 seconds. At this time, a great deal of core component relocation was taking place (see Figures 4.2.4— 4.2.9), which would cause some COR package subcycling to occur. Since there were no significant differences in temperature and relocation results, the differences in COR package subcycling time step results were not significant.

The ending cycle number, the number of fallbacks, and the subcycle ratios for the CVH and COR packages are listed for each machine in Table 5.8.1. The only difference between the results are in the number of COR package subcycles per timestep on the Cray and the SUN compared with those on the other machines. Again, since the temperature and hydrogen production results agreed so well across the machines, these differences were insignificant.

The overall execution time for all the machines is shown in Figure 5.8.18. The execution time ratios, normalized to that of the fastest machine (the Hewlett Packard), are also listed in Table 5.8.1. Some features of the cpu time data to note are:

- The Hewlett Packard 755 was the fastest machine for running MELCOR on the DF-4 problem.

- The Hewlett Packard 755 was over twice the speed of the Cray X/MP-24.

- The slowest machine was the Gateway 486/DX2-50 PC, but not by much.

These execution time data also show the rapid evolution of workstation-class computers in terms of speed. The HP 755, a relatively new workstation, was somewhat faster than the IBM RS/6000 Model 550, which was in turn faster than the Cray X/MP-24. The 486 PC had almost caught up to the slowest UNIX workstation on the list (in other assessment calculations, the 486 PC is sometimes faster than the SUN Sparc2, and sometimes slower [11],[19]).

The MELCOR code runs on 386 PC's and VAX computer systems, but these systems were not treated in this assessment. In past assessments, the 386 PC and VAX 8650/8700 computers have been about half the speed of a 486 PC.

The execution times of the CVH, COR and HS packages are compared with the overall execution time for the base case model in Figure 5.8.19. These data are for the run made on the DECStation 5000/240; data for other machines were quite similar. This figure reflects the emphasis placed on COR package calculations and the relatively simple CVH model in the base case input model.
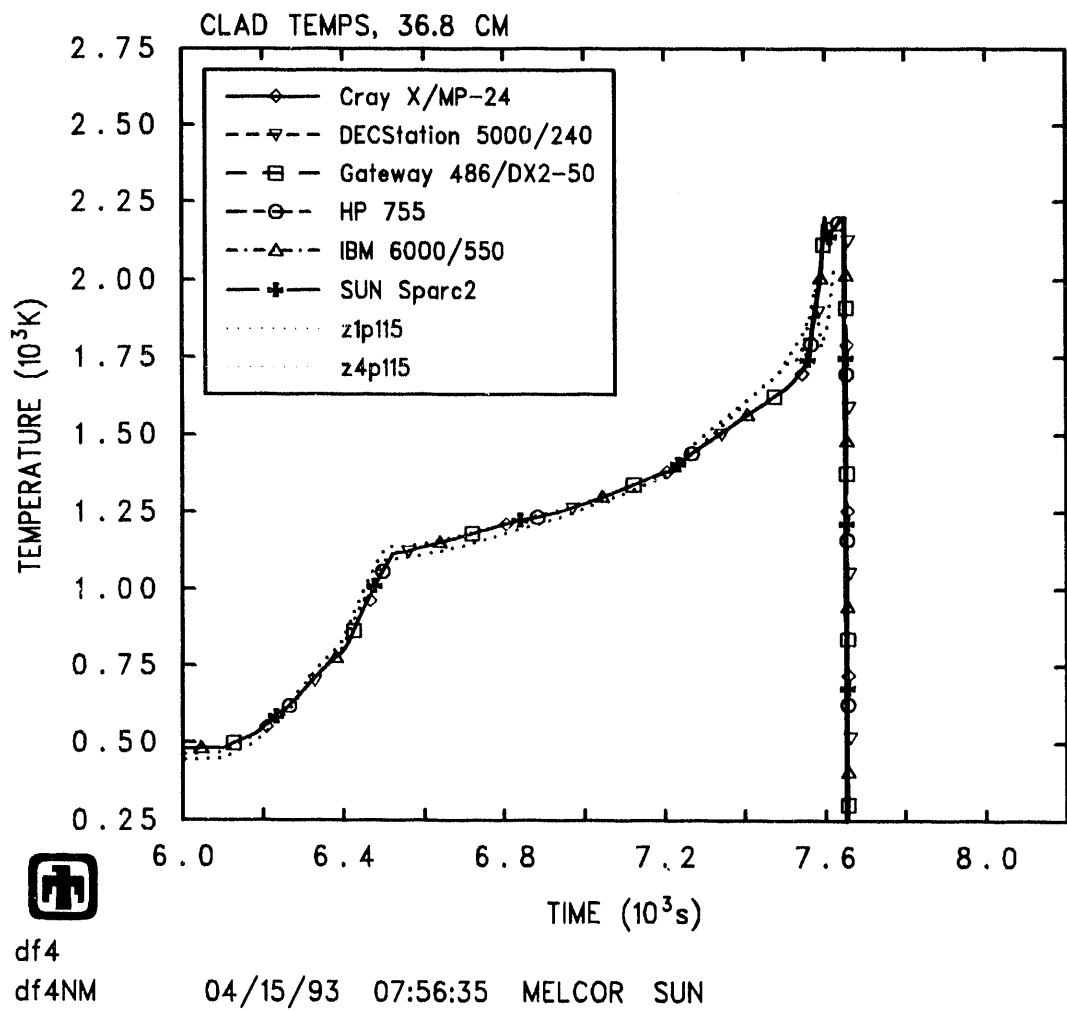
Figure 5.8.7. Cladding temperatures at the 36.8 cm plane for the six computers in the machine dependency sensitivity study, compared to measured values.

OS TEMPS, 36.8 CM
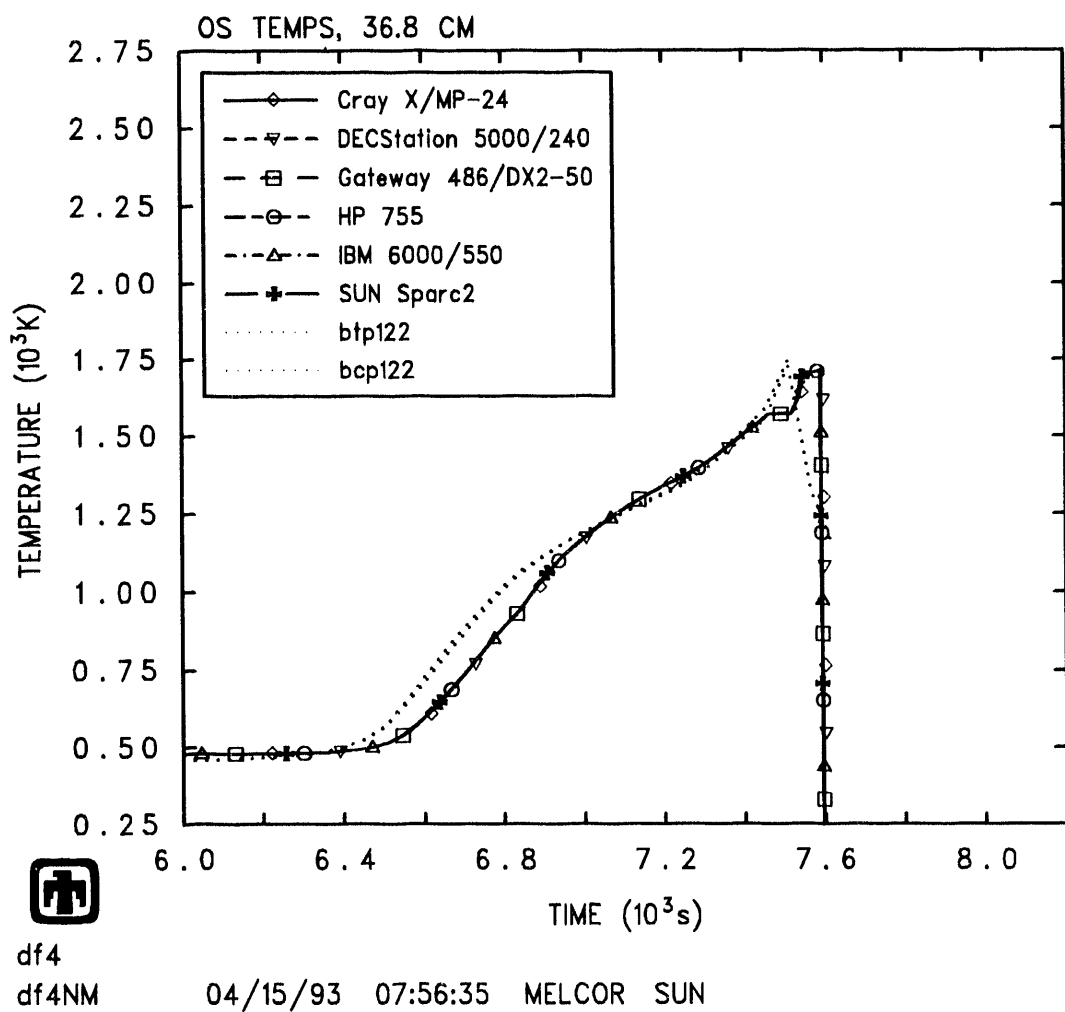
Figure 5.8.8. Control blade temperatures at the 36.8 cm plane for six computers in the machine dependency sensitivity study, compared to measured values.

HYDROGEN MASS PRODUCTION

Legend:
- Cray X/MP-24
- DECStation 5000/240
- Gateway 486/DX2-50
- HP 755
- IBM 6000/550
- SUN Sparc2
- experiment

Y-axis: MASS (10^{-3}kg)

X-axis: TIME (10^3s)

df4
df4NM   04/15/93 07:56:35   MELCOR SUN
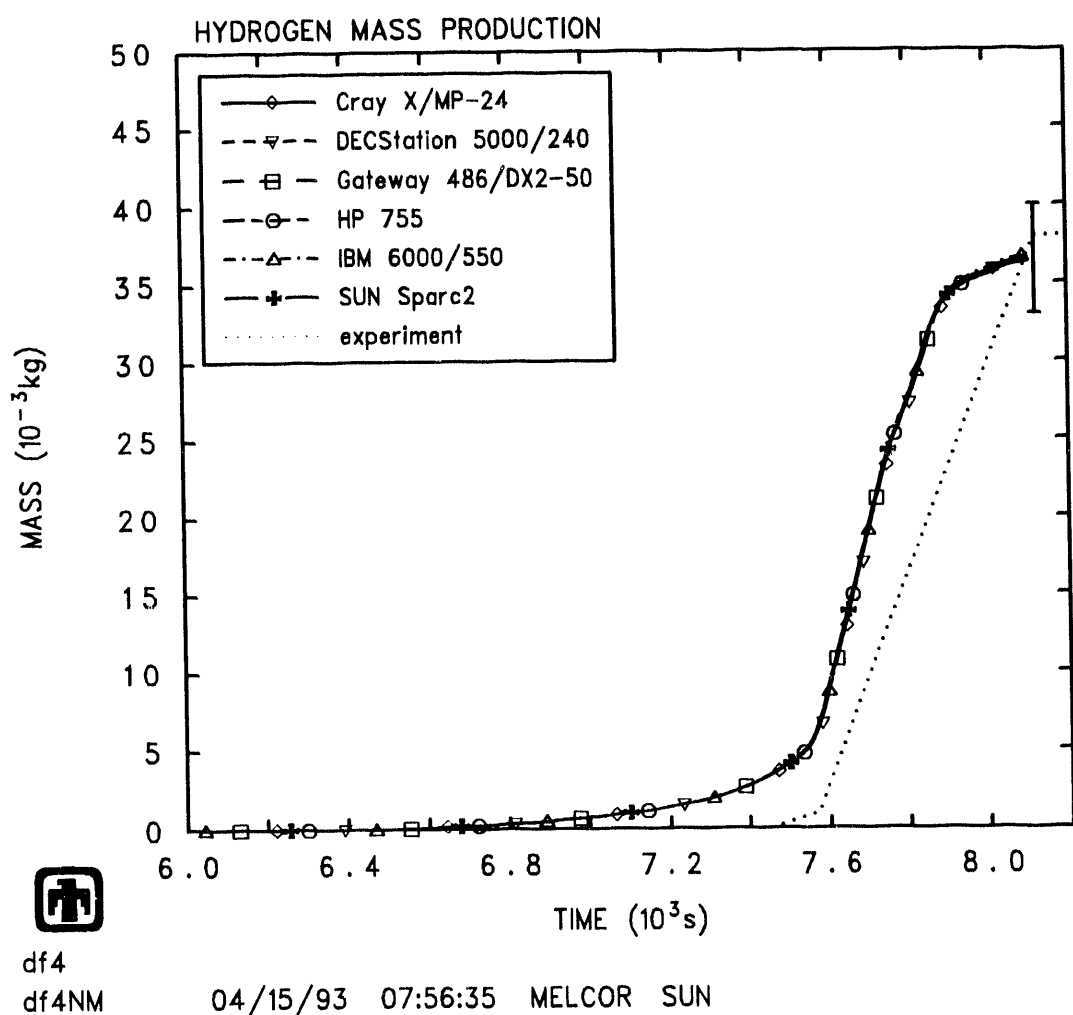
Figure 5.8.9. Hydrogen production for six computers in the machine dependency sensitivity study, compared to measured values.
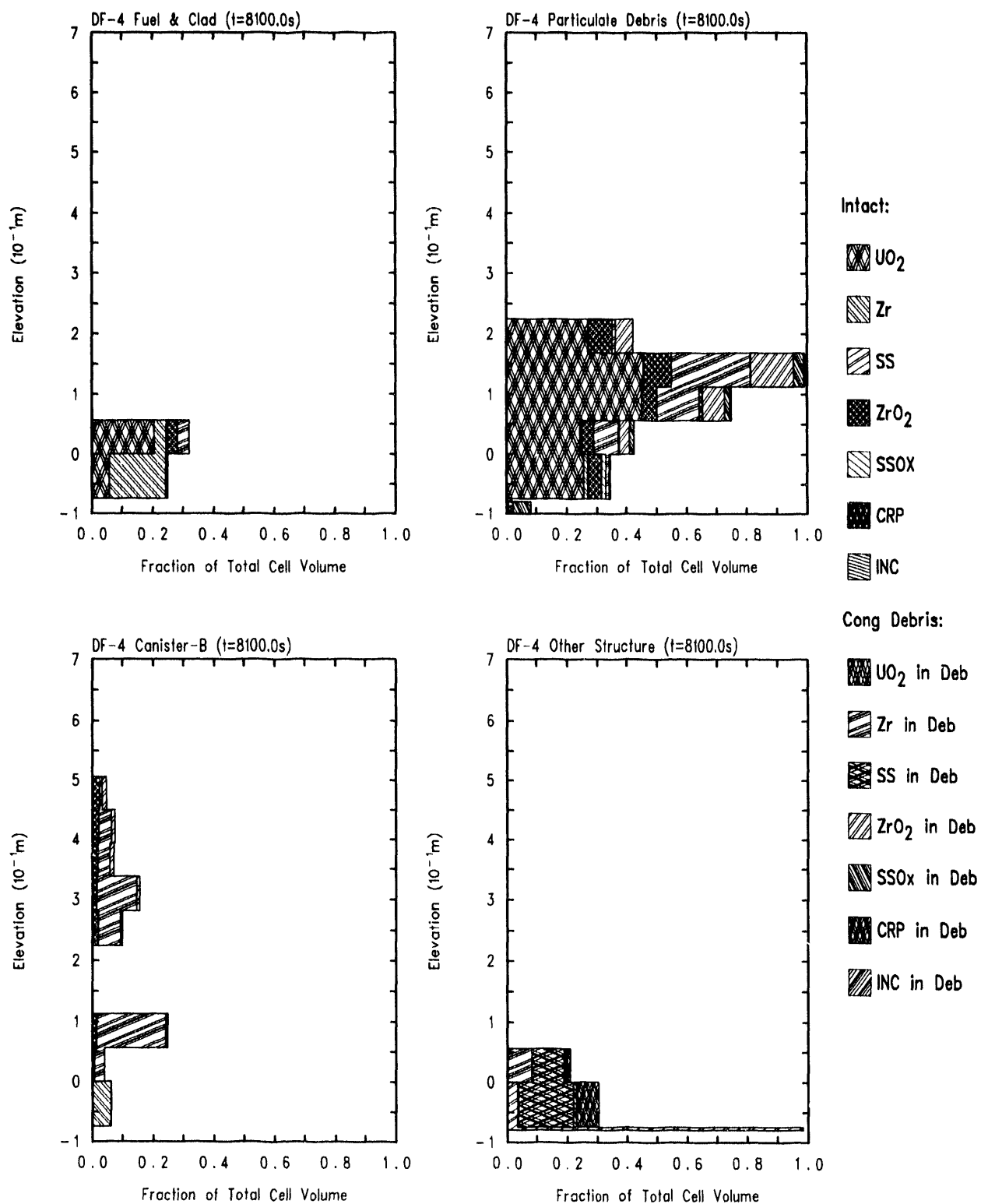
Figure 5.8.10. Component material locations at 8100 seconds for the Cray X/MP-24 case of the machine dependency sensitivity study. For an explanation of the format of this figure, see Section 4.2.1.
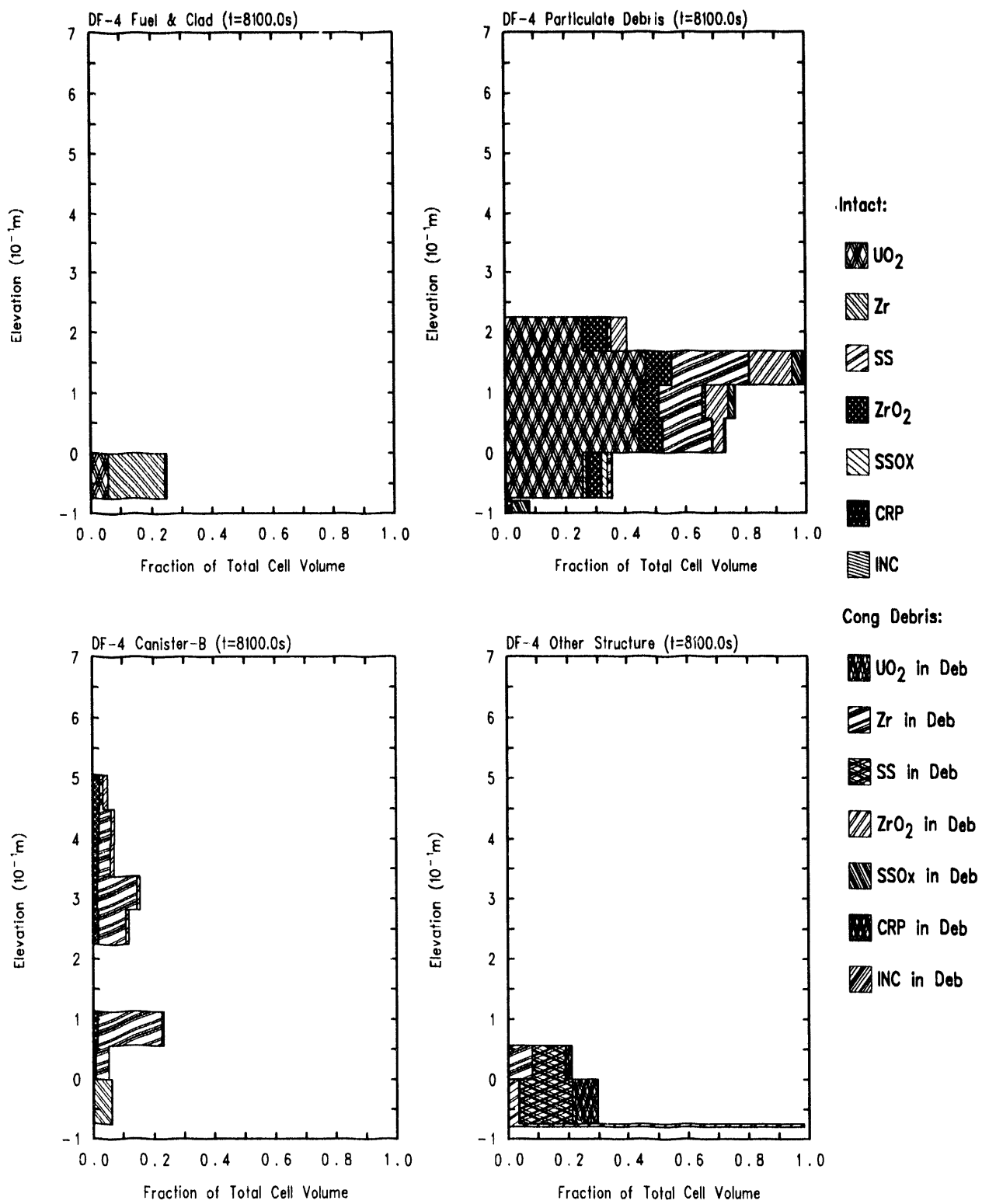
Figure 5.8.11. Component material locations at 8100 seconds for the DECstation 5000/240 case of the machine dependency sensitivity study. For an explanation of the format of this figure, see Section 4.2.1.
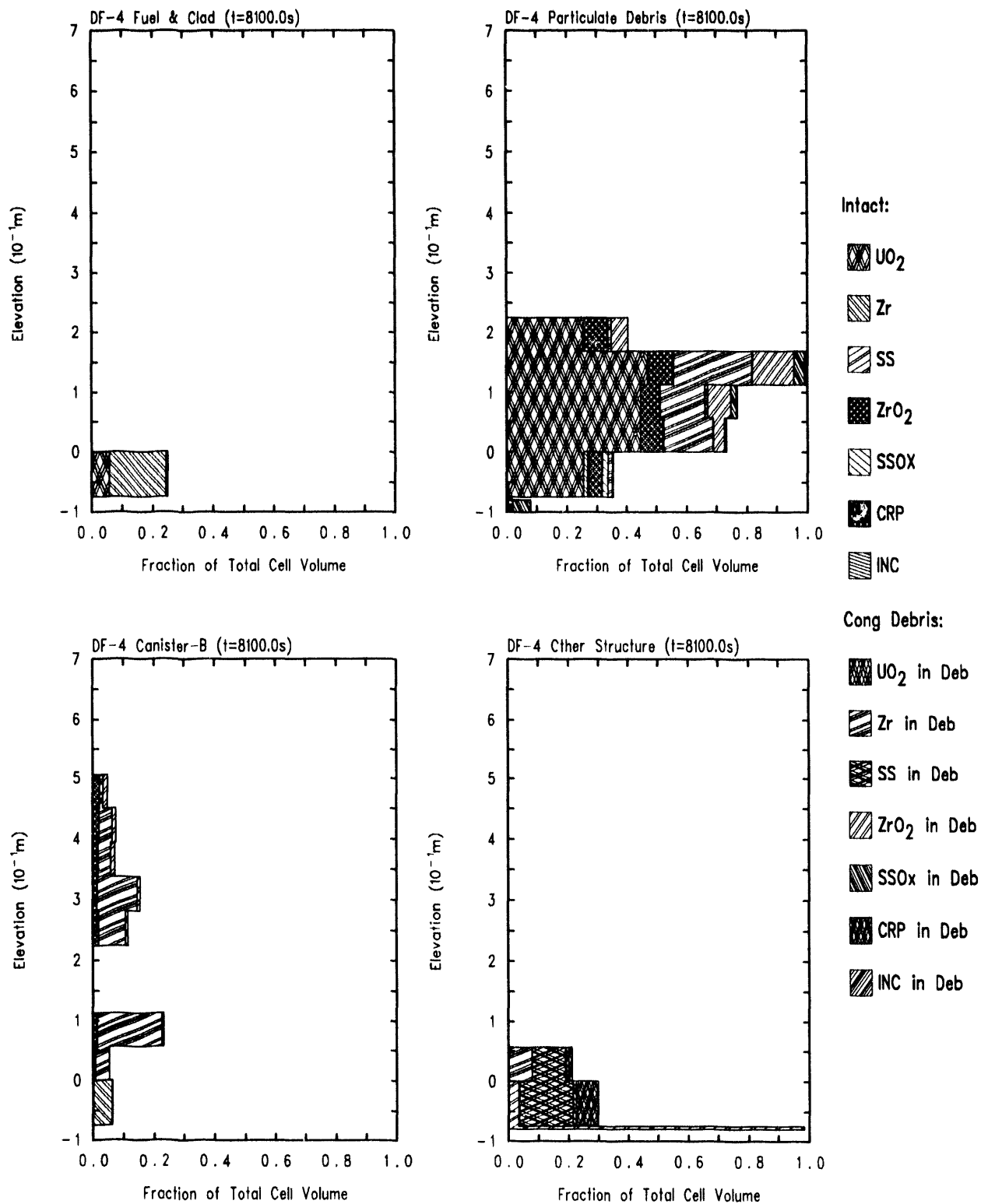
Figure 5.8.12. Component material locations at 8100 seconds for the Gateway 486/DX2-50 case of the machine dependency sensitivity study. For an explanation of the format of this figure, see Section 4.2.1.

157
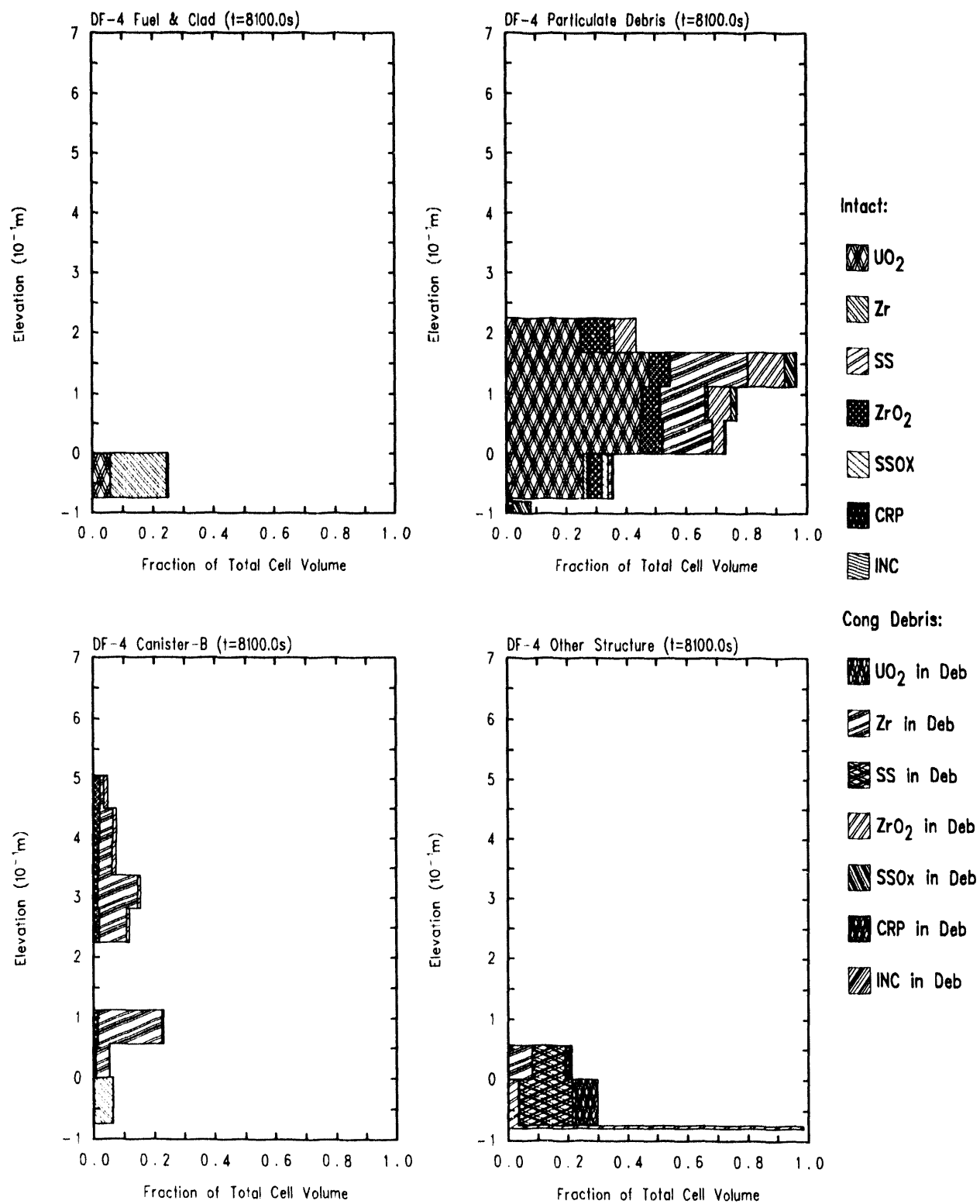
Figure 5.8.13. Component material locations at 8100 seconds for the Hewlett Packard 755 case of the machine dependency sensitivity study. For an explanation of the format of this figure, see Section 4.2.1.
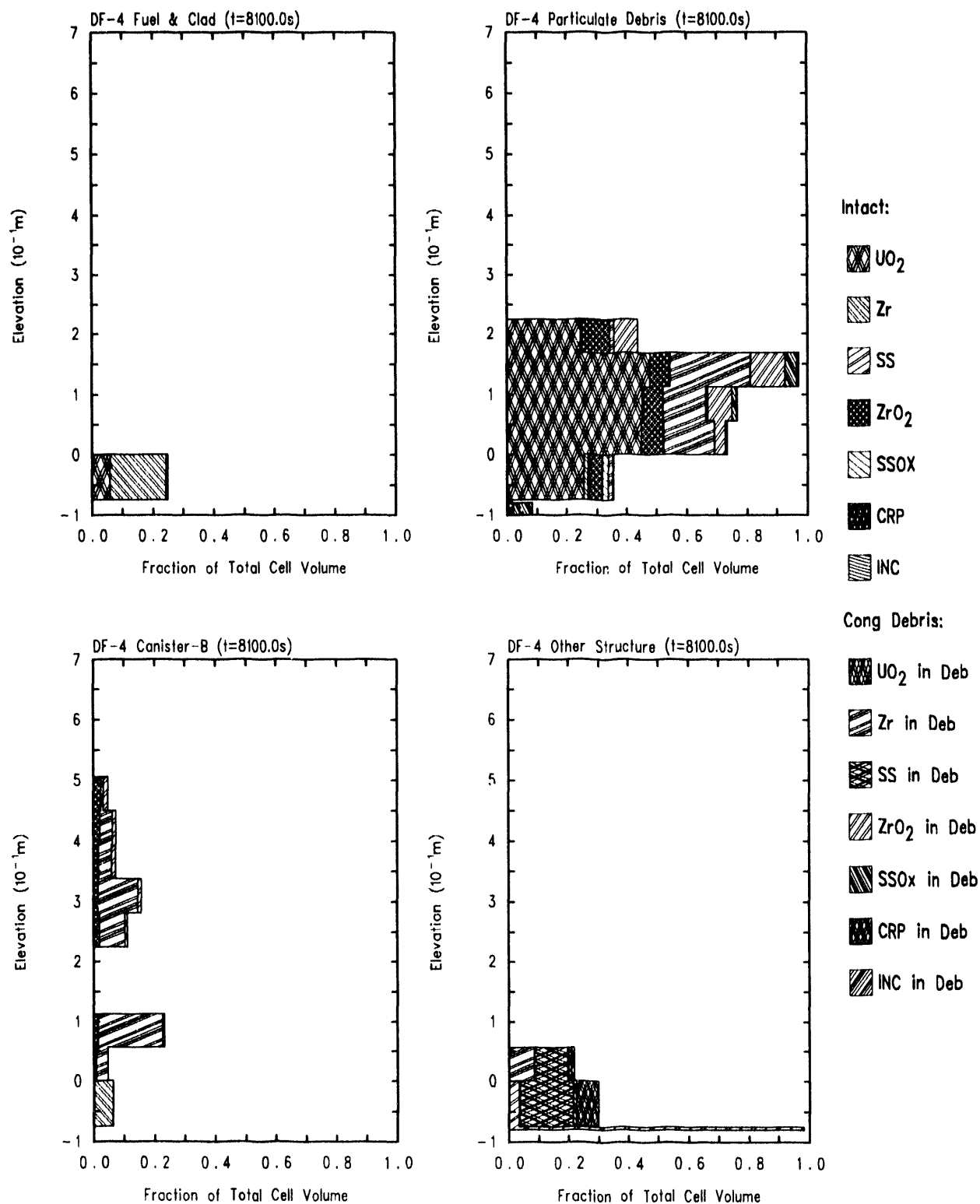
Figure 5.8.14. Component material locations at 8100 seconds for the IBM RS/6000 Model 550 case of the machine dependency sensitivity study. For an explanation of the format of this figure, see Section 4.2.1.

159
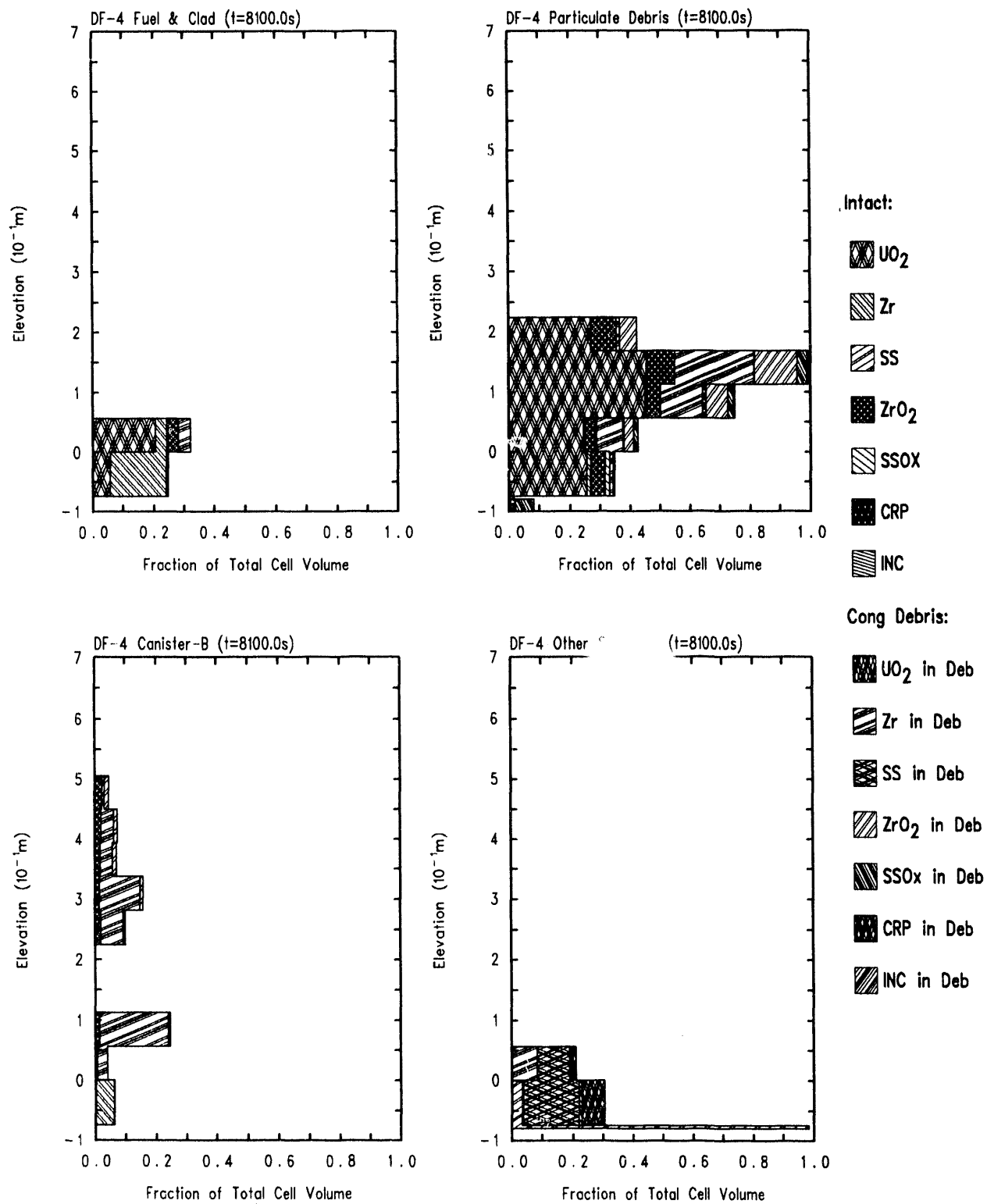
Figure 5.8.15. Component material locations at 8100 seconds for the SUN Sparcstation 2 case of the machine dependency sensitivity study. For an explanation of the format of this figure, see Section 4.2.1.
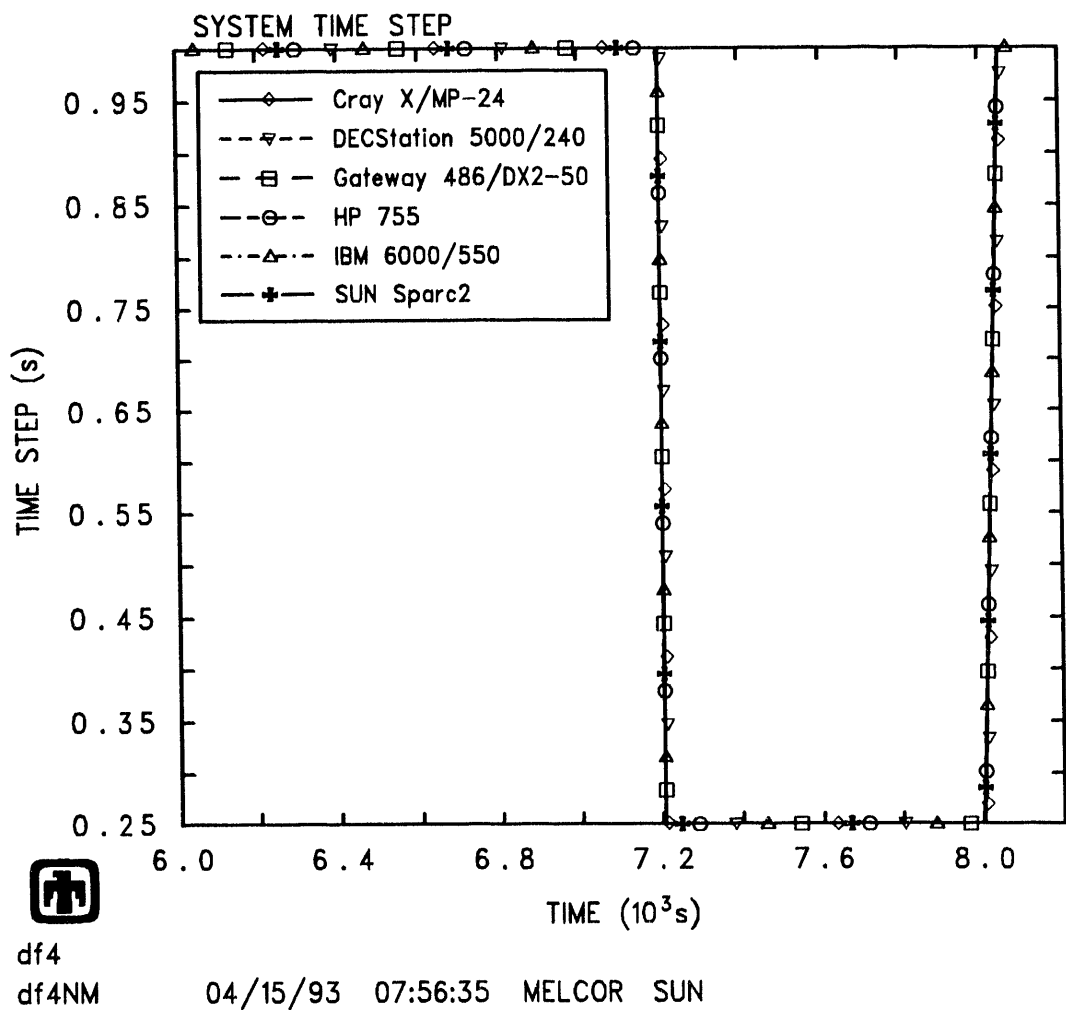
Figure 5.8.16. System time steps used by the six computers in the machine dependency sensitivity study.
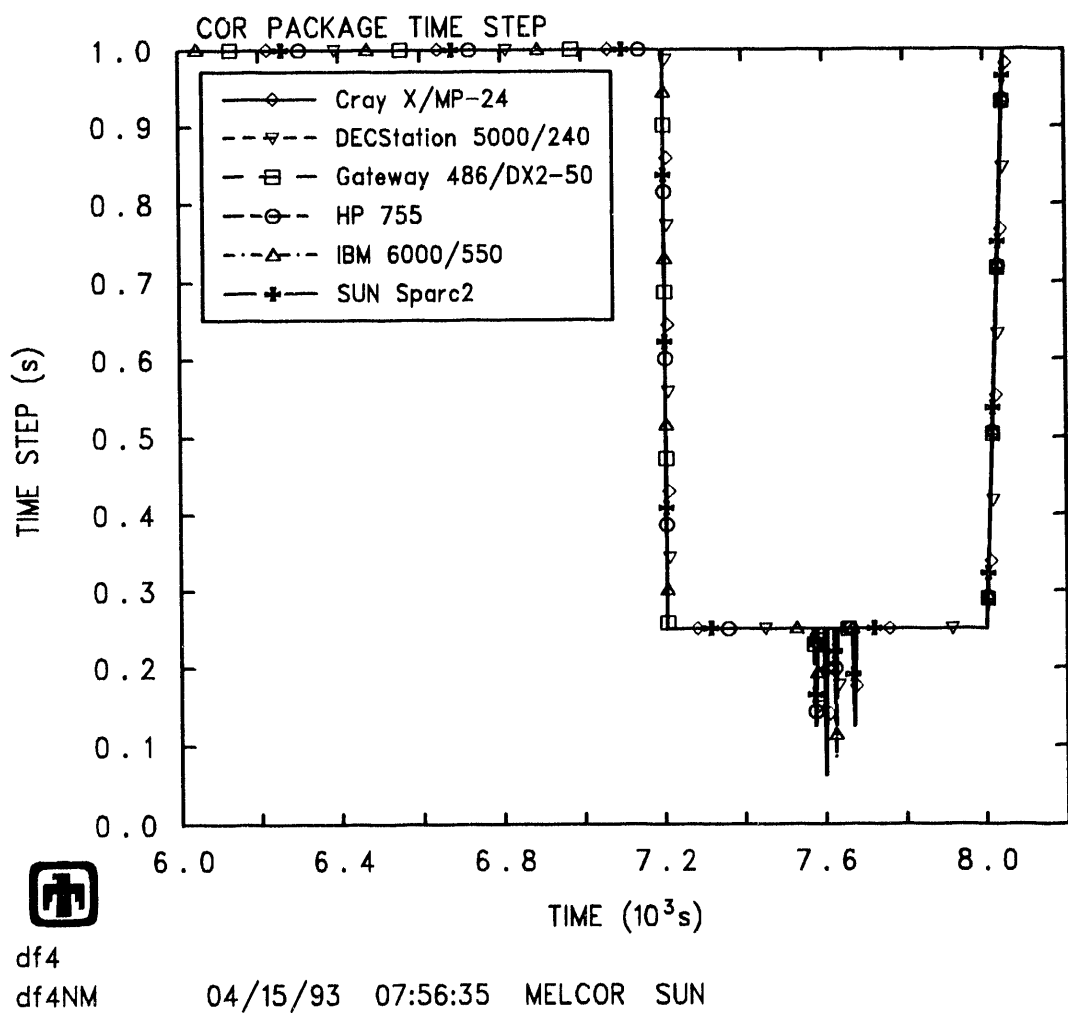
Figure 5.8.17. COR package time steps used by the six computers in the machine dependency sensitivity study.
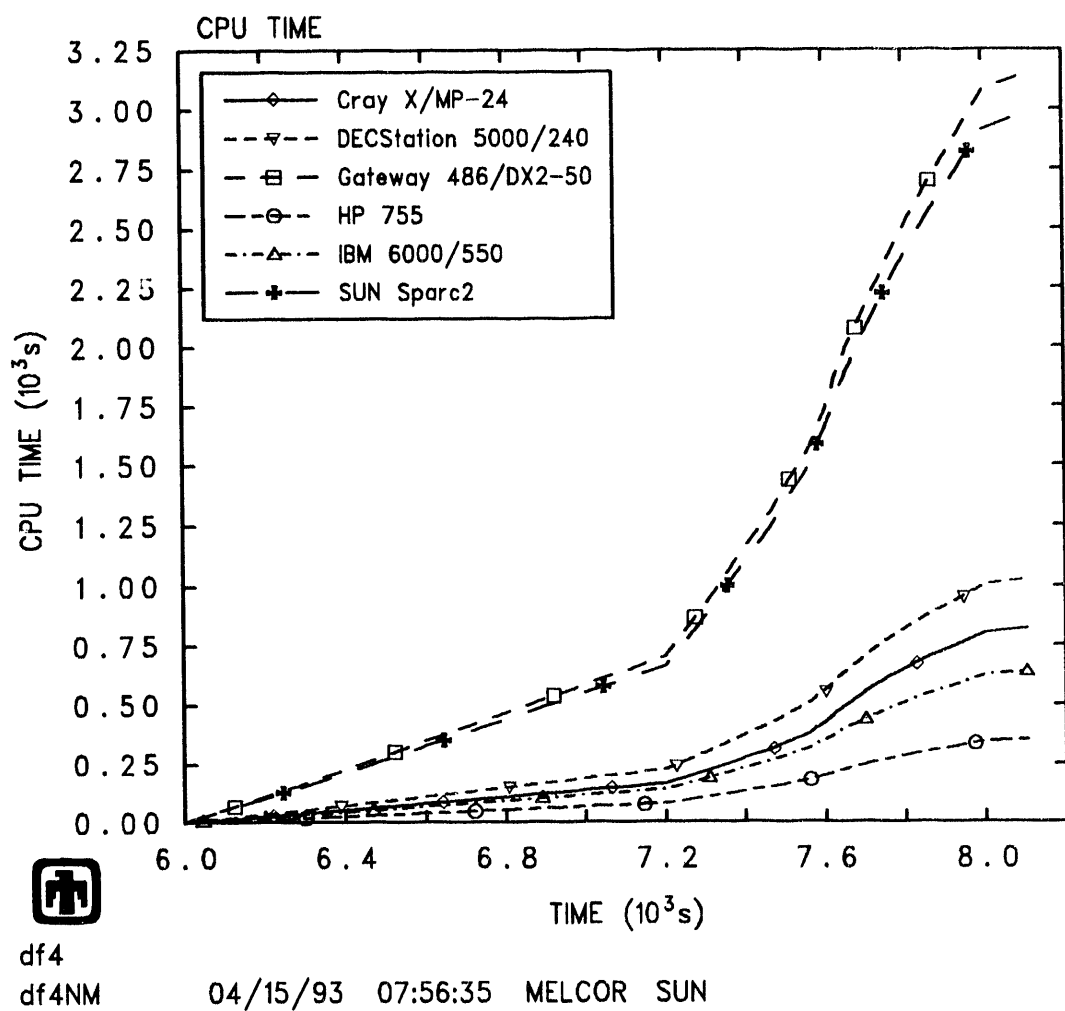
Figure 5.8.18. Overall execution time used by the six computers in the machine dependency sensitivity study.
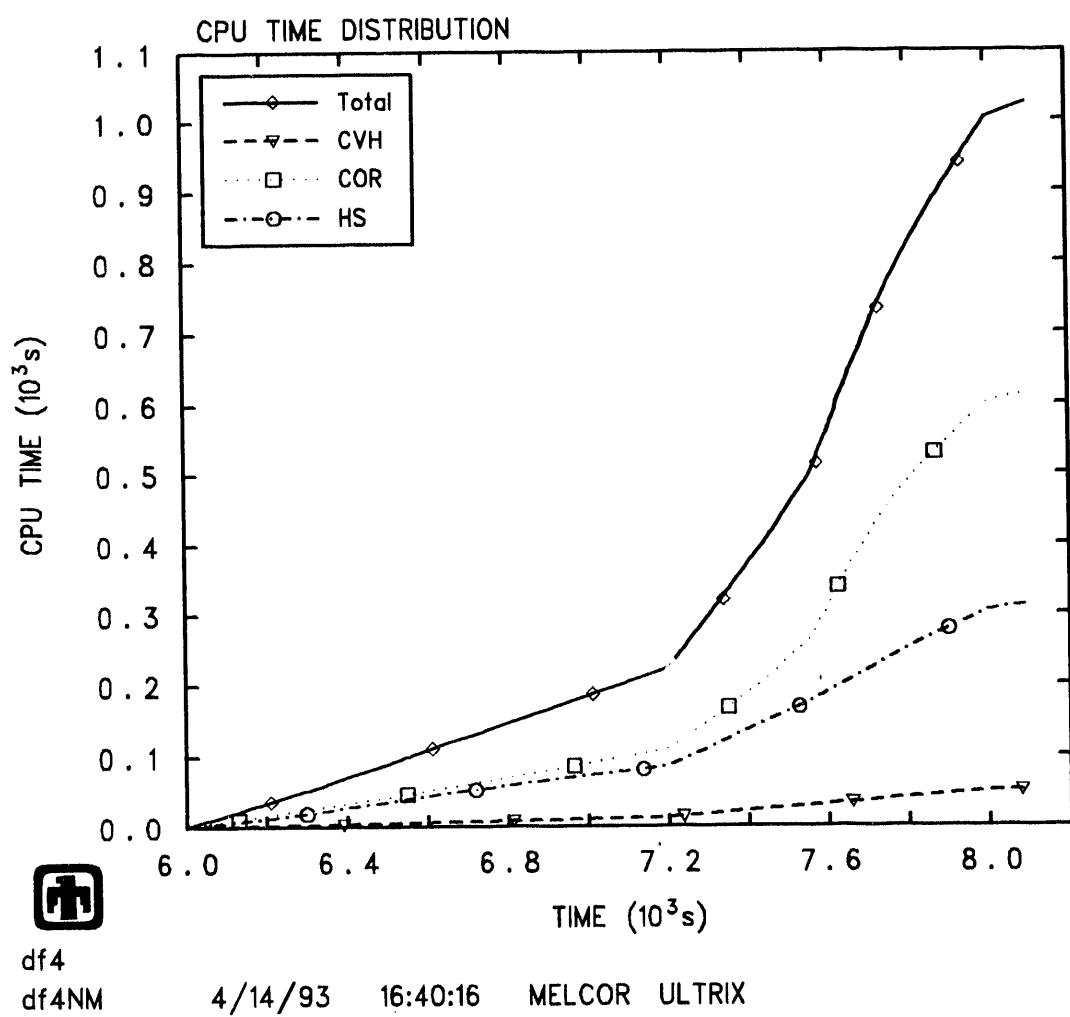
Figure 5.8.19. Package execution times for the DF-4 base case model executed on a DECStation 5000/240.

Table 5.8.1. CVH and COR subcycle ratios used by the six computers in the machine dependency sensitivity study. Also shown are the total execution times and the total execution times normalized to that of the Hewlett Packard 755.

Machine	Avg. No. of CVH Subcycles per Cycle	Avg. No. of COR Subcycles per Cycle	Total Execution Time (s)	Normalized Execution Time
Cray X/MP-24	1.00	1.021	819.3	2.35
DECStation 5000/240	1.00	1.018	1024.3	2.94
Gateway 486/DX2-50	1.00	1.018	3144.3	9.04
HP 755	1.00	1.018	348.0	1.00
IBM RS/6000 Model 550	1.00	1.018	635.7	1.83
SUN Sparc 2	1.00	1.021	2976.7	8.55

Chapter 6

Comparison With Other Codes

Several other codes have been used to model the DF-4 experiment. It is instructive to compare the results of the MELCOR DF-4 model to those of other codes, to evaluate the success of the parametric modeling approach taken by MELCOR. Results are discussed for the following codes: APRIL.MOD3 [20], BWRSAR/DF4 [21], MELPROG-PWR/MOD1 [15], and SCDAP/RELAP5/MOD2 [16].

The APRIL.MOD3 model [22] used twenty axial nodes and three radial rings for a total of sixty nodes to model the core region; 18 of 20 axial nodes were in the active fuel region. The BWRSAR/DF4 code model [23] used a total of 27 axial nodes in one radial ring, twenty of which were in the active fuel region. The MELPROG-PWR/MOD1 DF-4 code model [8] used ten axial nodes and three radial rings for a total of thirty nodes to model the core region; seven of the ten axial nodes were in the active fuel region. The SCDAP/RELAP5 code model [24] used nine axial nodes, five in the active fuel region. These are comparable to the MELCOR model, which had a total of 14 axial levels, 9 of which are in the active fuel region.

The BWRSAR/DF4 and SCDAP/RELAP5 codes were each modified to improve the results of the DF-4 analyses [23],[24]. BWRSAR/DF4 required modifications to model the DF-4 geometry as well as the B_4C-stainless steel eutectic interaction. SCDAP/RELAP5 required modifications in order to model the radiation heat transfer between the channel box and the stainless steel control blade. The MELPROG and APRIL computer codes required no major modifications to model the DF-4 experiment, according to the published reports [8], [22]. The MELCOR code required some modifications as described in Chapter 7, but these changes were relatively minor and were included in the release version of MELCOR. However, this work was performed shortly after the addition of a new materials interactions (eutectics) model into the core package of MELCOR; this model greatly enhanced the ability of MELCOR to model the DF-4 experiment. Note also that the MELCOR model input was the result of some optimization using some of the sensitivity studies described in Chapter 5.

6.1   Temperature Response

The control blade temperatures calculated by MELCOR at the 36.8 cm and 25.4 cm planes are compared to experimental values and temperatures calculated by APRIL.MOD3, BWRSAR/DF4, MELPROG and SCDAP/RELAP5 in Figures 6.1.1 and 6.1.2, respectively. APRIL results were not available for the 25.4 cm plane. At 36.8 cm, MELCOR temperatures were within the envelope of other codes everywhere except during the initial bundle heatup. Note that only MELCOR and BWRSAR/DF4 predicted some sort of melting behavior below 1700K, the melting point of stainless steel (melting behavior is indicated by a constant temperature over some period of time). BWRSAR/DF4 held the temperature at 1520K, which was the MELCOR default temperature for the stainless steel-B_4C eutectic reaction. MELCOR held the control blade temperature at 1570K because this reaction temperature was increased by user input for the base case model.

MELCOR was farther from the measured temperatures during the early parts of the experiment at the 25.4 cm plane as well. However, MELCOR predicted the arrival of candling material and the subsequent heatup and failure better than MELPROG, BWRSAR/DF4 and SCDAP/RELAP5 at this level. BWRSAR/DF4 again modeled a small amount of control blade melting at this plane before 1700K was reached. Note that MELCOR predicted earlier melt arrival and heatup, which was the result of its eutectic modeling.

The cladding temperatures calculated by MELCOR at the 36.8 cm and 25.4 cm planes are compared to experimental values and temperatures calculated by APRIL.MOD3, BWRSAR/DF4, MELPROG and SCDAP/RELAP5 in Figures 6.1.3 and 6.1.4, respectively. APRIL results were not available for the 25.4 cm plane. At the 36.8 cm plane, MELCOR-calculated temperatures were well within the envelope of the other codes; MELCOR also predicted the onset of rapid oxidation more accurately than all codes except APRIL.

At the 25.4 cm plane, MELCOR was within the envelope until midway through rapid oxidation, when the cladding heated up slightly faster than the other codes. Note that at both levels, MELCOR predicted cladding failure (indicated by the temperature dropping to zero) while the other codes show the cladding heating up to the zircaloy melting temperature of 2200K and beyond. This could be because the other codes did not transfer cladding material to another component once it had melted, as did MELCOR.

The cladding temperature response at the 49.5 cm plane is shown in Figure 6.1.5. This figure shows that, indeed, the temperatures predicted at this plane by all codes were higher than the measured temperatures. This indicates that the power coupling relationship may have been in error at the upper-most plane.
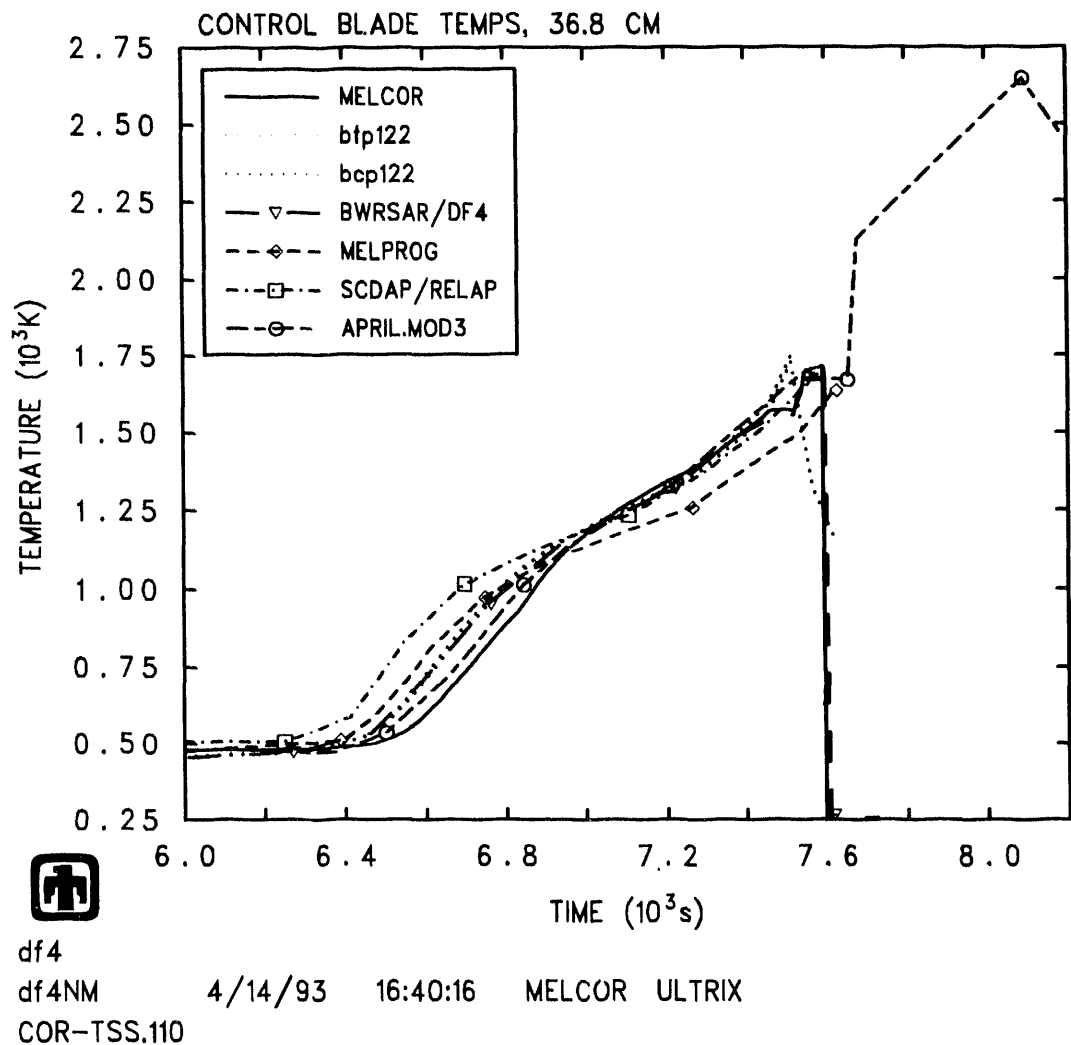
Figure 6.1.1. Comparison of control blade temperatures at the 36.8 cm plane calculated by APRIL, BWRSAR/DF4, MELPROG, SCDAP/RELAP, and MELCOR against experimental results.
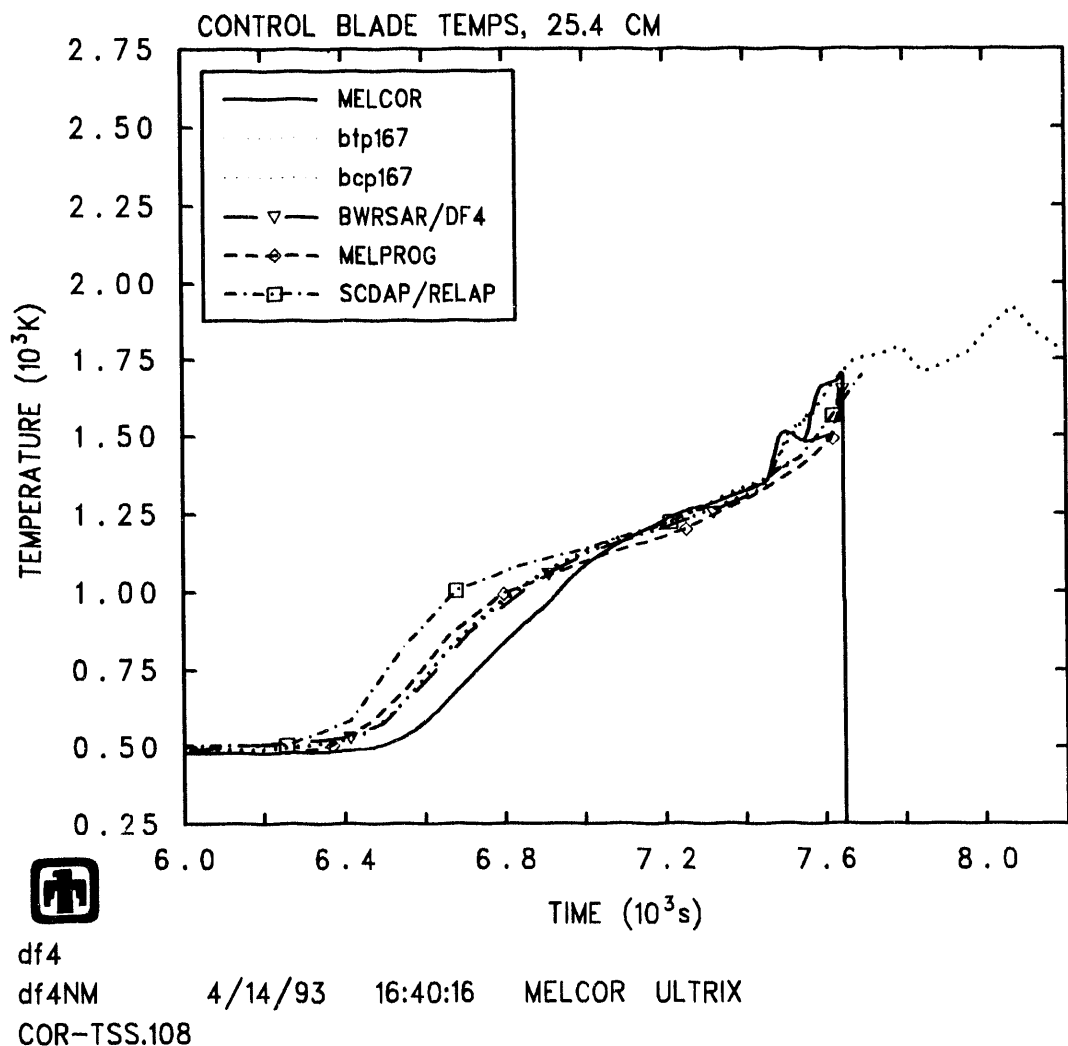
Figure 6.1.2. Comparison of control blade temperatures at the 25.4 cm plane calculated by APRIL, BWRSAR/DF4, MELPROG, SCDAP/RELAP, and MELCOR against experimental results.
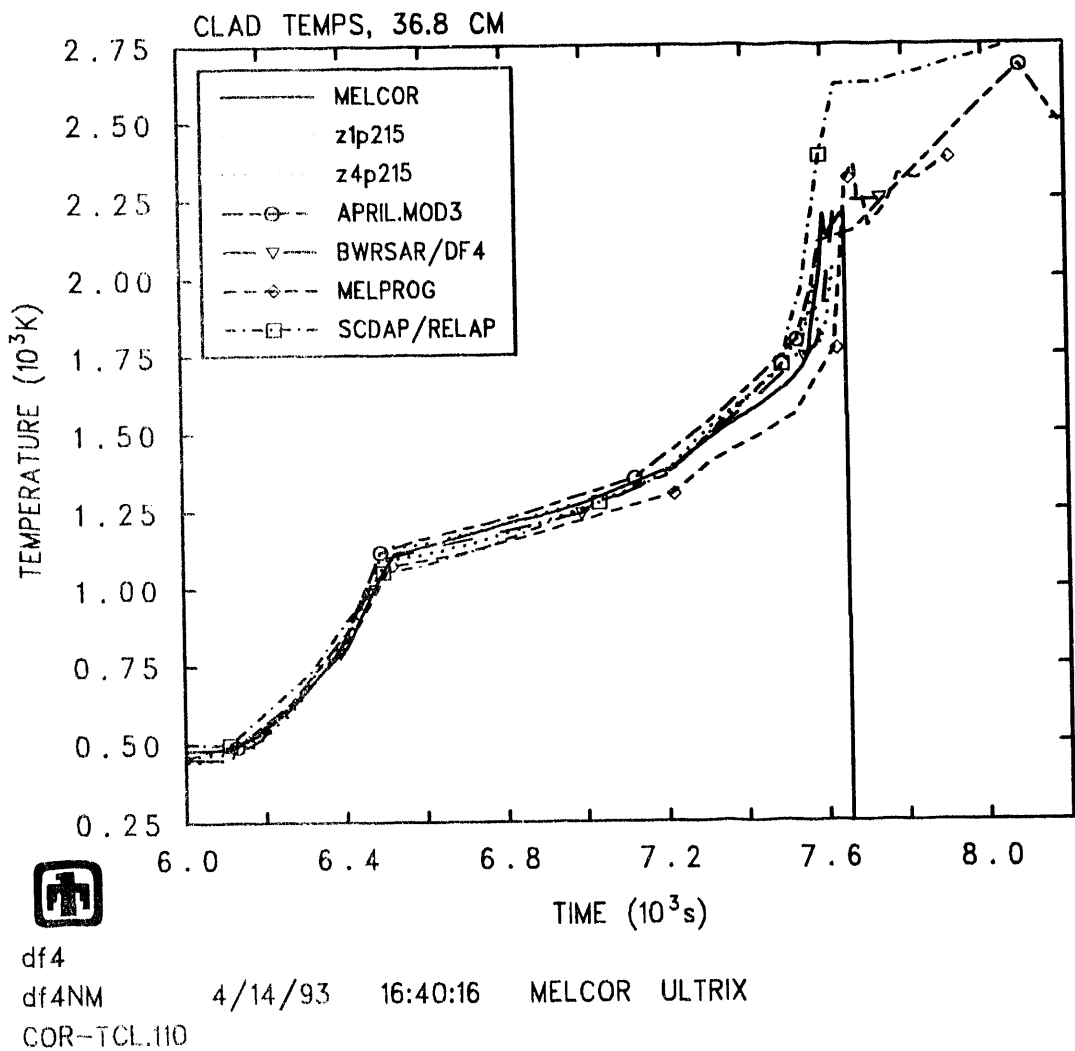
Figure 6.1.3. Comparison of cladding temperatures at the 36.8 cm plane calculated by APRIL, BWRSAR/DF4, MELPROG, SCDAP/RELAP, and MELCOR against experimental results.
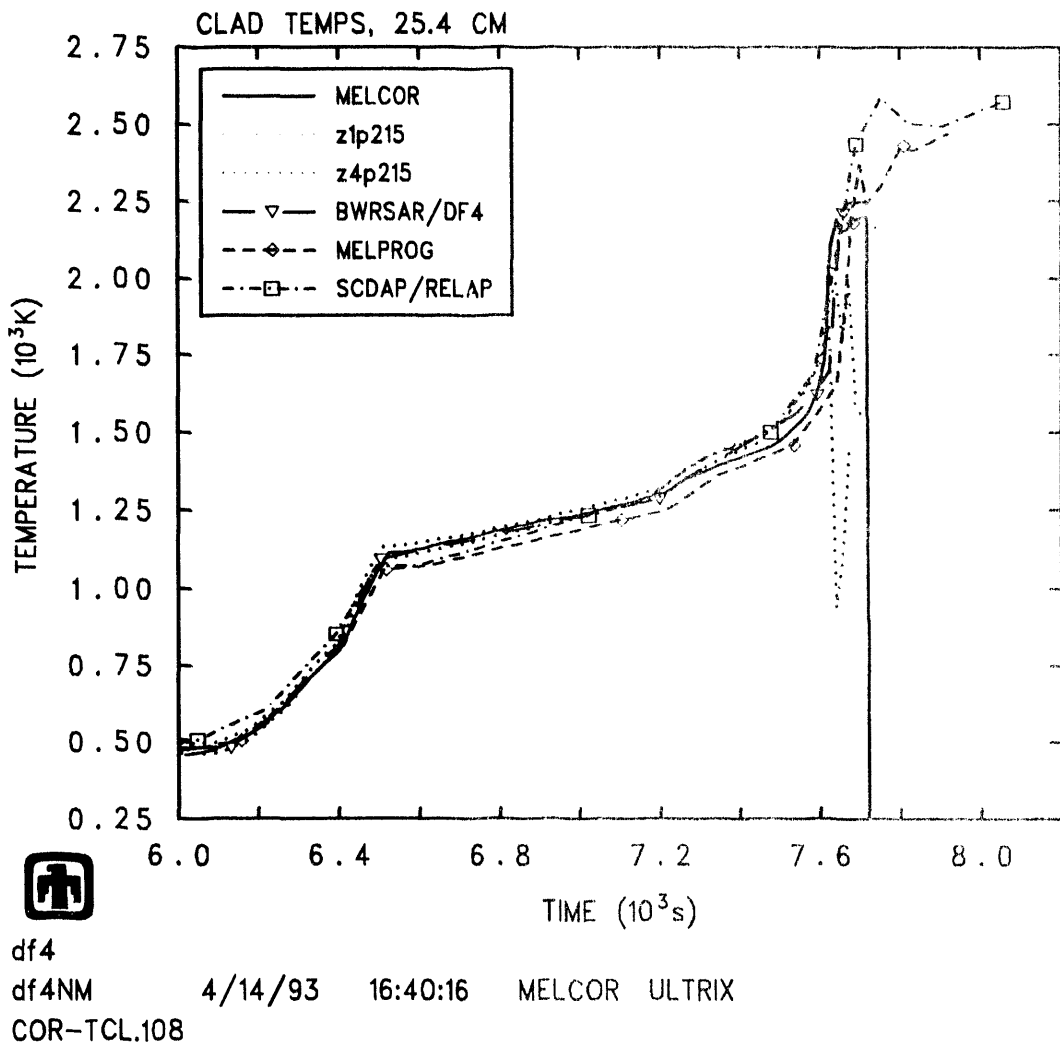
Figure 6.1.4. Comparison of cladding temperatures at the 25.4 cm plane calculated by APRIL, BWRSAR/DF4, MELPROG, SCDAP/RELAP, and MELCOR against experimental results.
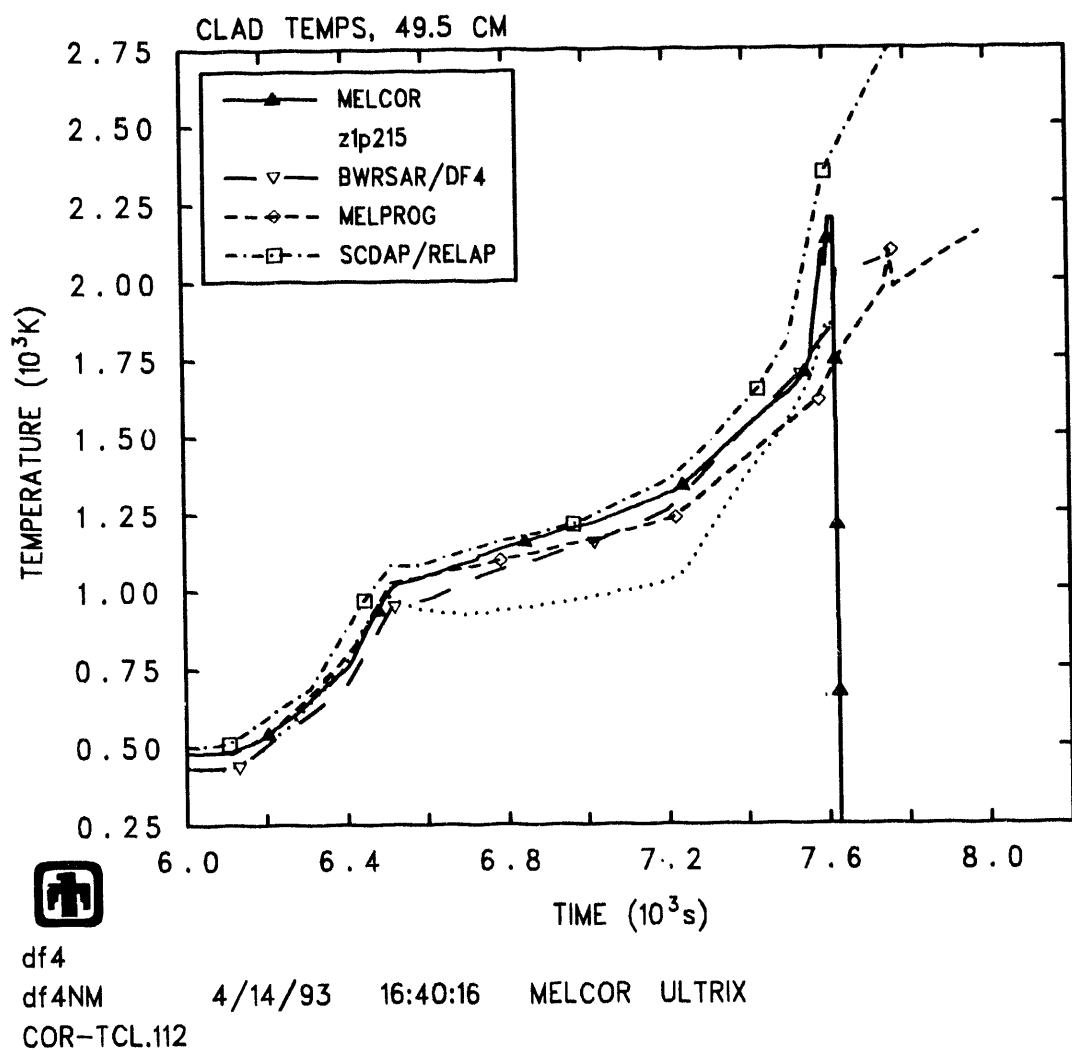
Figure 6.1.5. Comparison of cladding temperatures at the 49.5 cm plane calculated by APRIL, BWRSAR/DF4, MELPROG, SCDAP/RELAP, and MELCOR against experimental results.

6.2 Hydrogen Production

The hydrogen production rates calculated by APRIL.MOD3, BWRSAR/DF4, MELPROG, SCDAP/RELAP5, and MELCOR are compared to experimental measurements in Figure 6.2.1. Again MELCOR was within the calculational envelope during most of the experiment. All codes except SCDAP/RELAP5 predicted steam-starved conditions during the most vigorous oxidation. Note also that all codes predicted substantial hydrogen production before 7500 seconds, suggesting that the recombiner system used to measure hydrogen production was not sensitive enough to register a low hydrogen production rate. The increase in hydrogen production after 7800 seconds calculated by MELCOR was also calculated by the APRIL.MOD3 code, as shown in Figure 6.2.1. This effect was seen later on in the experiment, when the recombiner tubes were somewhat depleted and were not measuring the true hydrogen production (see Figure 4.3.1). As explained in Section 4.3, this effect was probably real, and so the only codes predicting the correct amount of hydrogen production after 7800 seconds were APRIL and MELCOR.

The total integrated hydrogen production is shown in Table 6.2.1 for all codes except BWRSAR/DF4 (for which no data were available). Again, MELCOR was well within the envelope of other code results as well as the experimental uncertainty.

Table 6.2.1. Comparison of the total hydrogen generation calculated by MELCOR, APRIL, MELPROG and SCDAP/RELAP5 to experimental data. Experimental data is from the PIE [5], which gave a range of possible values.

Code	Total Hydrogen Produced
Experiment	38.0 ± 4.0 grams
MELCOR	36.4 grams
APRIL	37.5 grams
MELPROG	51.0 grams
SCDAP/RELAP5	43.0 grams

HYDROGEN MASS PRODUCTION RATE

df4
df4NM   4/14/93   16:40:16   MELCOR   ULTRIX
CFVALU.801
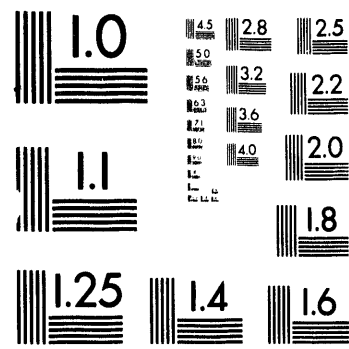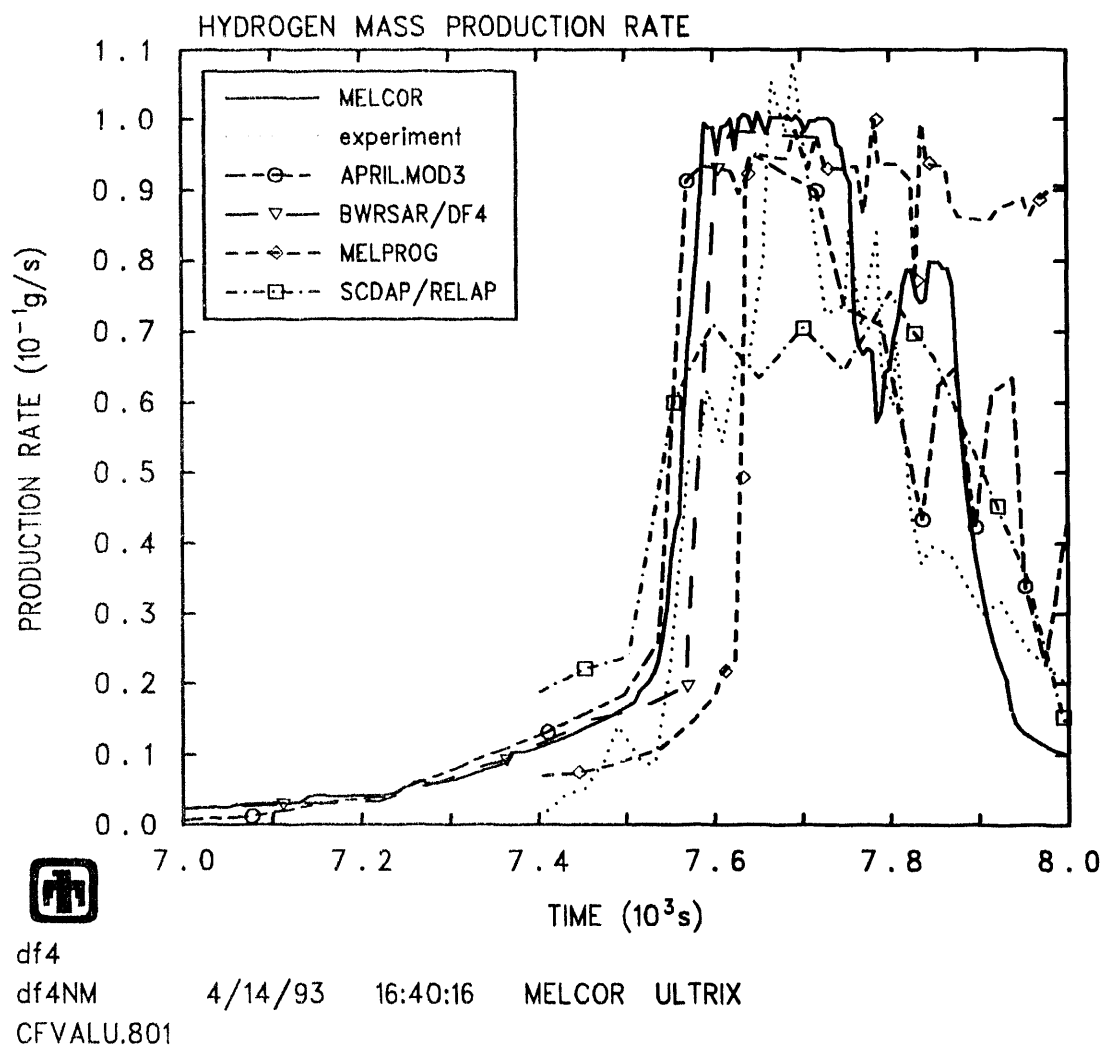
Figure 6.2.1. Comparison of the hydrogen generation rates calculated by APRIL, BWRSAR/DF4, MELPROG, SCDAP/RELAP, and MELCOR against experimental results.

6.3 Final State

The final states of the test bundle predicted by MELPROG and MELCOR differed in the locations of fuel material, zircaloy and other core materials. The other codes gave no information on the predicted final state of the test bundle.

At 8100 seconds, MELPROG predicted some of the fuel material to be left standing, while MELCOR predicted the relocation of all fuel to the bottom of the test bundle (see Figure 4.2.10). This was because MELCOR relocated fuel as soon as the intact cladding thickness fell below the minimum required to hold up fuel. MELPROG also predicted the existence of a ZrO_2 crust all the way up the bundle, while MELCOR relocated the oxidized cladding as well. The upper surface of debris relocated to the bottom of the test bundle predicted by MELPROG was at approximately 35 cm, while MELCOR predicted the elevation of this surface to be approximately 22 cm. Figures 4.2.11- 4.2.14 suggest that the upper surface of the debris pile was somewhere in between these two levels, depending on the interpretation of what materials in the calculations correspond to the materials shown in the photographs. The existence of fuel material all the way up the test bundle, which was predicted by MELPROG, was closer to the final experimental state than that predicted by MELCOR.

Chapter 7

Code Problems Identified

Several code problems were identified during the course of this assessment project. These problems resulted in the submission of seven MELCOR Defect Investigation Reports (DIR's).

7.1 Heat Transfer From Heat Structures to Channel Volume

The COR package requires a radial boundary heat structure to be input for every axial level. This heat structure was assumed by the dT/dz model to communicate with the bypass volume for heat transfer purposes. This represented the situation in a normal BWR core, where the radial boundary heat structures represent the core shroud, whose inside surface is cooled by the bypass region. In the DF-4 experiment, however, the channel region was adjacent to the radial boundary heat structures. The dT/dz model was modified to use either the channel or bypass control volume to calculate heat transfer with the boundary heat structures, depending on which control volume was specified as the inside boundary volume for each heat structure. This change was implemented in version 1.8ME of MELCOR, as a result of DIR 1078.

7.2 Divide By Zero in CVHBVT

A time-specified volume was used to provide inlet steam to the MELCOR calculation. The conditions in this volume were specified to CVH on input records CV100Aj, and consisted of entries for PVOL, TATM, PH2O and MLFR.4. The entry for a noncondensible gas (MLFR.4) is required when TATM is used. However, in the case of DF-4, where there was no non-condensible gas flowing into the test bundle, the number input for this field had to be zero. In the routine CVHBVT, a normalization was done over all the non-condensible gasses, which divided by the total NCG mole fraction, which was zero in this case. A modification was made to set the total NCG mole fraction to one if it was calculated as zero. This still resulted in normalized

176

mole fractions equal to zero, without the floating point exception. This change was implemented in version 1.8MN as a result of DIR 1095.

7.3 Internal File Length in MPDFVL

In MPDFVL, a character variable CHERRS is used to build an error message, using an internal write statement. When the code attempted this operation, a fatal error was issued because the string being written into this variable was longer than the dimension of that variable. The dimension of this variable was increased to accommodate this error message. This change was implemented in version 1.8MQ as a result of DIR 1104.

7.4 Boundary Fluid Temperature Option in dT/dz

The COR package dT/dz model takes into account heat transfer with the radial boundary heat structures when calculating the temperature increase of steam flowing through the core control volumes. The temperature used to calculate heat transfer with the heat structures was the CVH bulk atmosphere temperature. In some cases, this bulk atmosphere temperature was very different from the local dT/dz temperature calculated by the core package. This was particularly true when there was a large temperature gradient across the core. This problem manifested itself in the heat transfer to the boundary heat structures in the lower two cells. There, the heat structures were in the neighborhood of 500K, while the bulk atmosphere temperature was over 1500K (this temperature is normally close to the dT/dz temperature in the uppermost core cell). As a result, the atmosphere was being cooled below the freezing point due to the artificially high heat transfer to the boundary heat structures.

A new option was added to the Heat Structures package to solve this problem. Each heat structure was allowed the option of using either the bulk atmosphere temperature or the local COR dT/dz temperature for calculating heat transfer to a core radial boundary heat structure's atmosphere. This change solved the problem of freezing in the core, and also resulted in better agreement with experimental data, since it improved the calculation of heat transfer with the radial boundary heat structures (see Section 5.1.9). This change was implemented in version 1.8MY as a result of DIR's 1105 and 1120.

7.5 Radiation Heat Transfer in dT/dz

In the calculation of heat transfer with radial boundary heat structures in the dT/dz model, only convective heat transfer was considered. In problems for which the radiation heat transfer dominated the overall heat transfer, as in some stages of DF-4, this resulted in a disagreement between the COR and HS packages on how much heat was transferred to the boundary heat structures. This resulted in the HS package removing too much energy from the core control volume as a result of

177

COR calculating dT/dz temperatures that were too high. A change accounting for radiation heat transfer with boundary heat structures in dT/dz was requested in DIR 1139 and was implemented in MELCOR in version 1.8 NT.

7.6 COR Energy Error Due to Fission Power

The DF-4 experiment was driven by fission power from the ACRR. This fission power was represented by a tabular function in the MELCOR DF-4 input deck. The total fission power was specified along with peaking factors for each axial level, and these parameters were used to distribute fission power amongst the core cells. The fission power deposited in the fuel in each cell also depends on the amount of fuel material (UO_2) in the cell. After major relocation started taking place in the DF-4 calculation, the actual amount of fission power deposited in the core was much less than the power specified in the tabular function. This resulted in a large COR package energy error, since the fission power specified in the tabular function was the value used for fission power accounting in the core package. This problem was reported in DIR 1140 and was implemented in MELCOR version 1.8NX.

Chapter 8

Conclusions

MELCOR is a fully integrated, engineering-level computer code being developed at Sandia National Laboratories for the USNRC, that models the entire spectrum of severe accident phenomena in a unified framework for both BWRs and PWRs. As a part of an ongoing assessment program, MELCOR has been used to model the DF-4 Damaged Fuel experiment. DF-4 provided data for early phase melt progression in BWR fuel assemblies, particularly for phenomena associated with eutectic interactions in the BWR control blade and zircaloy oxidation in the canister and cladding.

The MELCOR base case input model for the DF-4 experiment consisted of 4 control volumes, 4 flow paths, and 15 heat structures. Fourteen core cells were modeled in 1 ring, with 9 cells in the active fuel region. The base case input model was based on the sensitivity studies performed as part of this assessment, and represented the best approximation of the experimental conditions and physical phenomena. Of the non-default MELCOR input parameters used in the base case model, the most important were the activation of the new eutectics model in MELCOR, those that changed the zircaloy melting temperature and the transition temperature for zircaloy oxidation rate, and the input enabling a new option for calculating heat transfer between core radial boundary heat structures and the core control volume atmosphere.

The base case model under-predicted control blade temperatures in the early parts of the experiment by almost 200K, but in later stages of the experiment, when all the core damage was taking place, calculated control blade temperatures corresponded almost exactly to measured values. Control blade failure times in most of the test bundle were predicted almost exactly compared to experimental data.

Cladding temperatures were predicted almost exactly compared to experimental data at all times and at all levels except for the upper-most axial level. MELCOR, and other codes, over-predicted temperatures in the upper-most axial level by close to the same amount (250K) during the middle of the experiment, leading us to believe that the power coupling relationship did not predict power coupling well in this part of the core. Fuel failure times calculated by MELCOR corresponded almost exactly to experimental data.

Calculated canister temperatures were also very close to experimental data, after correcting this data for the time and temperature lags associated with the slow-response thermocouples used for the canister.

Material distribution plots for the melting and relocation portions of the experiment very clearly showed the effect of the B_4C-stainless steel eutectic interaction in the control blade. This reaction resulted in the first control blade failure around 7450 seconds, which was within 10 seconds of the first observed failure in the experiment. Eutectic dissolution of the canister wall was also evident and was responsible for the calculated failure of lower portions of the canister. Evidence of canister failure was seen in the post irradiation examination of the DF-4 test bundle.

The material distribution plots also showed clearly that in the DF-4 calculation, core materials relocated by axial level and not by component. That is, all components at a single axial level (fuel, clad, canister and control blade) melted and relocated before significant component relocation at other levels. This behavior could be strongly affected by code input parameters. For example, the default candling heat transfer coefficients resulted in the control material refreezing quite close to the axial location from which it melted. Behavior would be much different if the control blade materials were allowed to candle to the bottom of the test bundle, as they did during the DF-4 test. These results are important when considering the possibility of reactivity excursions due to control poison relocation without accompanying relocation of fuel material.

The amount of hydrogen production calculated by MELCOR was 36.4 grams, which was close to the amount derived from the PIE, which was 38.0 ± 4.0 grams. MELCOR calculated the autocatalytic oxidation reaction to begin sooner than was measured, and predicted 5 grams of hydrogen produced before the autocatalytic stage, compared to no hydrogen production measured in the experiment during that time. Other codes predicted early hydrogen production and early transition to the autocatalytic stage as well.

A large number of sensitivity studies were performed on MELCOR parameters, most of which were in the COR package, but also some in the HS and CVH packages. A study which deactivated the eutectics model showed clearly the benefits of using this model, as it predicted much different behavior of the B_4C and did not show any canister dissolution. Hydrogen production without the eutectics model was well below the measured and MELCOR base case values. A sensitivity study which varied the eutectic temperature of the B_4C-stainless steel reaction by $\pm 50K$ showed little variation of results. A study which used the default heat structure boundary fluid temperature option (which uses bulk atmosphere temperature instead of local dT/dz temperatures for calculating heat transfer to the heat structures) resulted in much earlier component failure and poorer temperature agreement with experimental data. This study showed the usefulness of the new HS boundary fluid temperature option. Finally, a study on minimum oxide shell thickness and two other core relocation parameters in the COR package showed no variation in results until the critical minimum thicknesses for intact zircaloy and stainless steel were set to zero. After these parameters were changed, the final core material configuration showed the fuel pellet stacking observed in the PIE, but did not relocate any of the ZrO_2 that resulted from cladding oxidation. Other sensitivity studies showed sensitivities to zircaloy properties, COR component view factors, allocation of canister mass to either the canister or canister-b component, candling heat transfer coefficient, COR

and CVH nodalization, and slight sensitivity to COR and overall time steps. No sensitivities were found to minimum component mass, B_4C oxidation modeling, and HS outer boundary temperature, and only slight variations in final material locations were found in the machine sensitivity study.

The results of the base case calculation were compared to those from four mechanistic codes: APRIL.MOD3, BWRSAR/DF4, MELPROG-PWR/MOD1, and SC-DAP/RELAP5/MOD2. Early control blade temperatures predicted by MELCOR were lower than those predicted by other codes, but otherwise data calculated by MELCOR compared well with both the experimental data and those from the other codes.

This task resulted in improvements to the COR dT/dz model, in particular with the addition of the HS boundary fluid temperature option. Several other code errors were uncovered and corrected during this analysis.

In conclusion, the MELCOR code achieved good agreement with experimental data. Temperatures, hydrogen production and control blade eutectic behavior compared well with data measured during the experiment and revealed from the PIE. The final configuration of debris calculated by MELCOR did not show the fuel pellet stacking observed in DF-4, but it was not clear that this configuration represented the behavior in full scale reactor cores during postulated severe accidents. This assessment task served to validate the part of the new MELCOR eutectics model that models BWR materials, in particular the B_4C-stainless steel reaction.

Bibliography

[1] R. M. Summers, R. K. Cole Jr., E. A. Boucheron, M. K. Carmel, S. E. Dingman, and J. E. Kelly. MELCOR 1.8.0: A computer code for nuclear reactor severe accident source term and risk assessment analyses. Technical Report SAND90-0364, NUREG/CR-5531, Sandia National Laboratories, January 1991.

[2] R. D. Gasser, C. P. Fryer, R. O. Gauntt, A. C. Marshall, K. O. Reil, and K. T. Stalker. Damaged fuel experiment DF-1: Results and analysis. Technical Report SAND86-1030, NUREG/CR-4668, Sandia National Laboratories, January 1990.

[3] R. D. Gasser, C. P. Fryer, R. O. Gauntt, A. C. Marshall, K. O. Reil, and K. T. Stalker. Damaged fuel experiment DF-2: Results and analysis. Technical Report SAND86-1441, NUREG/CR-4669, Sandia National Laboratories, September 1992.

[4] C. P. Fryer, R. O. Gauntt, and A. W. Cronenberg. Damaged fuel experiment DF-3: Test results. Technical Report SAND87-1212, NUREG/CR-6006, Sandia National Laboratories, December 1992.

[5] Randall O. Gauntt, August W. Cronenberg, Carol P. Fryer, Susan C. Bourcier, Ronald D. Gasser, Kenneth O. Reil, and Jay J. Weingardt. Damaged fuel experiment DF-4: Test results. Sandia National Laboratories. to be published.

[6] R. O. Gauntt, R. D. Gasser, and L. J. Ott. The DF-4 BWR fuel damage experiment in ACRR with a BWR control blade and channel box. Technical Report SAND86-1443, NUREG/CR-4671, Sandia National Laboratories, November 1989.

[7] R. C. Smith. The core package eutectic model. Sandia National Laboratories. Letter report to R. B. Foulds, NRC, November 11 1992.

[8] Rodney C. Schmidt. MELPROG-PWR/MOD1 analysis of the DF-4 experiment. SAND90-1098, NUREG/CR-5578, Sandia National Laboratories. to be published.

[9] D. L. Hagrman, G. A. Reymann, and R. E. Mason. MATPRO version 11 (revision 1): A handbook of materials properties for use in the analysis of light water reactor fuel rod behavior. Technical Report TREE-1280 Rev. 1, NUREG/CR-0497, EG&G Idaho, February 1980.

[10] L. N. Kmetyk. MELCOR 1.8.1 assessment: ACRR source term experiments ST-1/ST-2. Technical Report SAND91-2833, Sandia National Laboratories, April 1992.

[11] L. N. Kmetyk. MELCOR 1.8.1 assessment: LOFT integral experiment LP-FP-2. Technical Report SAND92-1373, Sandia National Laboratories, December 1992.

[12] S. Hagen et al. Results of SFD experiment CORA-13 (OECD international standard problem 31). Technical Report KfK 5054, Kernforschungszentrum Karlsruhe, February 1993.

[13] Robert J. Gross, Samuel L. Thompson, and Gail M. Martinez. MELCOR 1.8.1 calculations of ISP31: The CORA13 experiment. Technical Report SAND92-2863, Sandia National Laboratories, June 1993.

[14] K. E. Washington et al. Reference manual for the CONTAIN 1.1 code for containment severe accident analysis. Technical Report SAND91-0835, NUREG/CR-5715, Sandia National Laboratories, July 1991.

[15] S. S. Dosanjh and et al. MELPROG-PWR/MOD1: A two-dimensional mechanistic code for analysis of reactor core melt progression and vessel attack under severe accident conditions. Technical Report SAND88-1824, NUREG/CR-4909, Sandia National Laboratories, 1987.

[16] C. M. Allison and E. C. Johnson. SCDAP/RELAP5/MOD2 code manual: Volume 1: SCDAP code structure, systems models, and solutions methods. Technical Report EGG-2555, NUREG/CR-5273, EG&G Idaho, Inc., July 1989.

[17] R. M. Summers and R. C. Smith. Core (COR) package reference manual, version 1.8.2. Sandia National Laboratories, January 1993.

[18] V. F. Urbanic and T. R. Heidrick. High-temperature oxidation of zircaloy-2 and zircaloy-4 in steam. J. Nuc. Matls., 75:251–261, 1978.

[19] L. N. Kmetyk. MELCOR 1.8.1 assessment: Marviken-V aerosol transport tests ATT-2b/ATT-4. Technical Report SAND92-2243, Sandia National Laboratories, January 1993.

[20] R. T. Lahey Jr. and M. Z. Podowski. Degraded core modeling APRIL.MOD3 severe accident code. Technical Report ESEERCO PROJECT EP84-4, 1990. Final Report.

[21] S. A. Hodge and L. J. Ott. Boiling water reactor severe accident response (BWR-SAR) code description and assessment. Technical Report NUREG/CR-5318, Oak Ridge National Laboratory. to be published.

[22] S. W. Kim, M. Z. Podowski, and R. T. Lahey, Jr. Numerical simulation of DF-4 and CORA-16/17 severe fuel damage experiments using APRIL.MOD3. In *Proceedings of the 5th International Topical Meeting on Reactor Thermal/Hydralics (NURETH-5)*, pages 1497–1506, September 1992.

183

[23] L. J. Ott. Post-test analyses of the DF-4 BWR experiment using the BWR-SAR/DF4 code. Oak Ridge National Laboratory letter report, August 1989.

[24] Judith K. Hohorst and Chris M. Allison. DF-4 analysis using SCDAP/RELAP5. *Nuclear Technology*, 98:149–159, May 1992.

Appendix A

Base Case Input Deck

```
*eor* melgen
*
* MELCOR DF4 input deck
*
*  Model layout:
*
*
*
*
*         |---> up (vertical)
*
*                            --------------------
*              FL101   |                    | FL201
*                    ----|        CV 101      |----
*                    |---| (channel volume)  |---|
*  --------------------   |   |                    |   |   --------------------
*  |                  |   |   |  --------------------   |   |                  |
*  |      CV 100      |----!                        |----|      CV 200      |
*  |  (lower plenum)  |----|                        |----| (out plenum)    |
*  |                  |   |   |  --------------------   |   |                  |
*  --------------------   |   |                    |   |   --------------------
*                    |---|        CV 102      |---|
*                    ----| (bypass volume) |----
*              FL102   |                    | FL202
*                            --------------------
*
*
*
**********************
* exec package input  *
**********************
*
title      'df4'
restartf  'df4.rst'
outputf   'df4.gout'
```

```
diagf     'df4.gdia'
*
tstart  6000.0    * initial problem time is 6000 sec.
*
*********************
* cor package input *
*********************
*
*-----------------------
* general core input
*-----------------------
*       nrad naxl ntlp ncvol nlh npntot
cor00000 1  14   1    2    3   1  *
*          rfuel    rclad     drgap   pitch   dxcan   dxss     dzlh
cor00001 4.51e-3  4.815e-3  7.6e-4  1.27e-2 2.5e-3  1.42e-3  3.05e-3
cor00002 bwr  b4c                   * bwr type, b4c poison
* view factors: can-clad, sheath-can, cell-cell(rad), cell-cell(axial),
*               pool-struc   (from MELPROG DF-4 report)
cor00003       0.550  0.9999  0.10  0.50  0.25
*
cor00004  0  -10  0  * no TP, cf #10 for fission power, no extra gap cond
*
cor00006  1  * activate eutectic modeling
*
* increase failure temperature for lower head and penetrations
*
cor00009  1000.0  1000.0  1700.0  1.0  * htc's for pen, lh, lh failure temp
*
*---------------------
* axial segment input
*---------------------
*
* axial geometry
corz0101  -0.1085  0.03200  0.0  0.50  * bottom elev, height, intact &
                                       * debris porosities
corz0201  -0.0765  0.00150  0.0  0.50  *
corz0301  -0.0750  0.07500  0.0  0.50  *
corz0401   0.0     0.05611  0.0  0.50  *
corz0501   0.05611 0.05611  0.0  0.50  *
corz0601   0.11222 0.05611  0.0  0.50  *
corz0701   0.16833 0.05611  0.0  0.50  *
corz0801   0.22444 0.05611  0.0  0.50  *
corz0901   0.28055 0.05611  0.0  0.50  *
corz1001   0.33666 0.05611  0.0  0.50  *
corz1101   0.39277 0.05611  0.0  0.50  *
corz1201   0.44888 0.05611  0.0  0.50  *
corz1301   0.50500 0.05240  0.0  0.50  *
corz1401   0.55740 0.07740  0.0  0.50  *
```

186

```
* boundary heat structures, isup
corz0102  10101  01  *
corz0202  10102  11  *
corz0302  10103  01  *
corz0402  10104  01  *
corz0502  10105  01  *
corz0602  10106  01  *
corz0702  10107  01  *
corz0802  10108  01  *
corz0902  10109  01  *
corz1002  10110  01  *
corz1102  10111  01  *
corz1202  10112  01  *
corz1302  10113  01  *
corz1402  10114  01  *
* axial power profile: use Equation 10 from MELPROG DF-4 report:
*   f = 1.3 + 0.4 * sin(pi*(x/50.5 - .2))
* integrated over each axial cell and normalized
*
corz0103  0.0
corz0203  0.0
corz0303  0.0
corz0403  0.8324015
corz0503  0.9206076
corz0603  0.9989634
corz0703  1.058018
corz0803  1.090649
corz0903  1.092921
corz1003  1.064558
corz1103  1.008983
corz1203  0.9328981
corz1303  0.0
corz1403  0.0
*
* structure failure temp for core plate and lower head
*
corz0204  10000.0
*
* radial input:
corr0101  3.729e-3  * ring cross-sectional area
corr0102  10115  * upper boundary heat structure
* cell-specific input:
cor10101  -1  101  102  * no ref cell, channel, bypass cvh volumes
cor10102  0.0  0.0  0.0  0.0  0.0  0.0  * no core component masses in lp
cor10103  480.0  480.0  480.0  480.0  * initial temps of fuel, clad, struc, can
* Dhyd:    clad       sheath    part deb  can in    can out
cor10104  9.630e-3  1.156e-2  8.260e-3  2.524e-2  3.090e-2
cor10105  6.928e-3  1.632e-3  5.211e-4  * radial bound area, channel, byp area
```

187

```
* surf area: fuel, clad, os, can in
cor10106  0.0  0.0  0.0  0.0  0.0
*
cor10201  101  101  102  * ref cell 101, channel, bypass cvh volumes
cor10202  0.0  0.0  2.218e-1  0.0  0.0  0.0  * comp masses
cor10205  3.248e-3  3.683e-4  9.208e-5  * bound area, channel, byp area
cor10206  0.0  0.0  2.828e-2  0.0  0.0  * os area = (clad + os area) from cell 104
*
cor10301  101  101  102  * ref cell 101, channel, bypass cvh volumes
* masses: fuel        clad        os          poison      can         ht-elem
cor10302  1.601e-1  3.046e-1  8.436e-2  5.891e-3  1.028e-1  0.0
cor10305  1.624e-2  1.632e-3  5.211e-4  * bound area, channel, byp area
* surf areas: fuel   clad        os          can-inside
cor10306  2.724e-2  3.178e-2  6.025e-3  8.955e-3
*
cor10401  -1  101  102  * no ref cell, channel, bypass cvh volumes
* masses: fuel        clad        os          poison      can         ht-elem
cor10402  4.588e-1  8.826e-2  6.310e-2  4.407e-3  1.199e-1  0.0
cor10403  480.0  480.0  480.0  480.0  * initial temps of fuel, clad, struc, can
* Dhyd:    clad        sheath      part deb    can in      can out
cor10404  9.630e-3  1.156e-2  8.260e-3  2.524e-2  3.090e-2
cor10405  1.215e-2  1.632e-3  5.211e-4  * bound area, channel, byp area
* surf areas: fuel   clad        os          can-inside
cor10406  2.038e-2  2.377e-2  4.508e-3  6.700e-3
*
cor10501  104  * ref cell 104
cor10601  104  * ref cell 104
cor10701  104  * ref cell 104
cor10801  104  * ref cell 104
cor10901  104  * ref cell 104
cor11001  104  * ref cell 104
cor11101  104  * ref cell 104
cor11201  104  * ref cell 104
*
cor11301  103  * ref cell 103
* masses: fuel        clad        os          poison      can         ht-elem
cor11302  2.201e-1  8.243e-2  5.892e-2  4.115e-3  1.120e-1  0.0
cor11305  1.134e-2  -1.1  -1.1  * bound area, channel, byp area
* surf areas: fuel   clad        os          can-inside
cor11306  1.904e-2  2.220e-2  4.210e-3  6.256e-3
*
cor11401  101  101  102  * ref cell 101, channel, byp volumes
* masses: fuel clad        os          poison      can  heat-elem
cor11402  0.0  3.507e-1  4.303e-2  8.191e-3  0.0  0.0
cor11405  1.676e-2  -1.1  -1.1  * bound area, channel, byp area
* surf areas: fuel clad  os          can-inside
cor11406  0.0  3.278e-2  6.218e-3  0.0
*
```

```
* lower head input
corlhd01  1  1  4.587e-1  480.0  1.897e-2  101  100  * beginning, ending ring no's
                                                    * mass, init temp, surf area,
                                                    * inner cv, cav cv
* penetration input
corpen01  -1  1  1.0e-5  480.0  1.0e-5  1.0e-5  1.0e-5  * try for no penetration
* core inlet temp
cortin01  101 100  * for cv 101 (channel), use time-dep volume for inlet temp
cortin02  102 100  * for cv 102 (bypass), use time-dep volume for inlet temp
*
*------------------------
* cf010 and edf010 for fission power
*------------------------
*
cf01000  'fission power cf'  equals  1  6334.947  0.0  * name, type, args, scale f
*
* multiplier comes from integration of coupling factor equation
*
cf01010  1.0  0.0  edf.10.1  * first argument
*
edf01000  reapow  1  read  * reactor power, 1 channels, read edf
edf01001  '/user/tjtautg/df4/data/exp/reapow.dat'  * data file name
edf01002  2e15.6    * format for data fields
*
*
sc15021  1502  1.0e-5  1  * minimum mass
sc15022  1502  1.0e-4  2  * minimum mass for temperature control
*
**********************
* cvh package input  *
**********************
*
*------------------------
* cv #100 - inlet plenum
*------------------------
*
cv10000  'inlet plenum'  2  2  1    * non-eq thermo, vertical flow, rcs volume
cv10001  0  -2        * properties specified as a fcn of time
cv100a0  3            * option 3 for specifying properties
cv100a1  pvol edf.1.1 * time-dependent properties for this volume are in
cv100a2  tatm cf.104 * edf file #1
cv100a3  ph2o edf.1.1 *
cv100a4  mlfr.4 edf.1.3 *
cv100b1  -0.2000      0.0        * altitude-volume table
cv100b2  -0.1085      5.00e-4
*
*------------------------
* edf.1 (for cv 100)
```

189

```
*------------------------
*
* edf.1.1 = time-dependent pressure in cv 100
* edf.1.2 = time-dependent temperature in cv 100
*
edf00100  inlet-vol  3  read  * inlet mass flow, 3 channels, read edf
edf00101  '/user/tjtautg/df4/data/inlet-vol.dat'  * data file name
edf00102  4e12.5    * format for data fields, time, pressure and temp
*
*------------------------
* cf 104 (for cv100)
*------------------------
*
cf10400  inlet-temp  equals  1  1.0  0.0  * name, type, 2 args, mult & add factors
cf10401  506.7  * initial value
cf10410  1.0  0.0  edf.4.1  * first argument
*
*------------------------
* edf.4 (for cv 100)
*------------------------
*
* edf.4.1 = time-dependent temperature in cv 100
*
edf00400  inlet-temp  2  read  * inlet temp, 2 channels, read edf
edf00401  '/user/tjtautg/df4/data/exp/inlettemp.dat'  * data file name
edf00402  2e16.6    * format for data fields, time, pressure and temp
*
*------------------------
* cv #200 - outlet volume
*------------------------
*
cv20000  'outlet plenum'  2  2  1    * non-eq thermo, vertical flow, rcs volume
cv20001  0  -2        * properties specified as a fcn of time
cv200a0  3            * option 3 for specifying properties
cv200a1  pvol edf.2.1 * time-dependent properties for this volume are in
cv200a2  tatm edf.2.2 * edf file #1
cv200a3  ph2o edf.2.1 * ph2o is the total volume pressure, so use pvol data
cv200a4  mlfr.4 edf.2.3 *
cv200b1  6.617e-1  0.0        * altitude-volume table
cv200b2  7.117e-1  1.865e-4
*
*------------------------
* edf.2 (for cv 200)
*------------------------
*
* edf.2.1 = time-dependent pressure in cv 200
* edf.2.2 = time-dependent temperature in cv 200
*
```

```
edf00200  outlet-vol  3  read  * inlet mass flow, 2 channels, read edf
edf00201  '/user/tjtautg/df4/data/outlet-vol.dat'  * data file name
edf00202  3e12.5    * format for data fields, time, pressure and temp
*
*------------------------
* cv #101 - channel volume
*------------------------
*
cv10100  'channel volume'  2  2  1    * non-eq thermo, vertical flow, rcs volume
cv10102  3.6592e-1  0.0  * initial atmosphere and pool velocities
cv10103  1.632e-3   * area for velocity calc's
cv101a0  2          * option 2 for specifying properties
cv101a1  pvol 7.1573e5  * volume initial conditions
cv101a2  tatm 506.7
cv101a3  ph2o 6.8946e5     * water vapor partial press equal to total volume pres
cv101a4  mfrc.3  1.0    * atmosphere is all water vapor
cv101b1  -0.1085   0.0        * altitude-volume table
cv101b2  -0.0765   4.600e-4
cv101b3  6.617e-1  1.665e-3
*
*
*------------------------
* cv #102 - bypass volume
*------------------------
*
cv10200  'bypass volume'  2  2  1    * non-eq thermo, vertical flow, rcs volume
cv10202  2.8650e-1  0.0  * initial atmosphere and pool velocities
cv10203  5.211e-4   * area for velocity calc's
cv102a0  2          * option 2 for specifying properties
cv102a1  pvol 7.1573e5  * volume initial conditions
cv102a2  tatm 506.7
cv102a3  ph2o 6.8946e5     * water vapor partial press equal to total volume pres
cv102a4  mfrc.3  1.0    * atmosphere is all water vapor
cv102b1  -0.1085   0.0        * altitude-volume table
cv102b2  -0.0765   1.469e-4
cv102b3  6.617e-1  5.316e-4
*
*
********************
* fl package input  *
********************
*
*------------------
* fl path 101
*------------------
*
fl10100 inlet->channel  100  101  -0.1085  -0.1085 * from, to, inlet and outlet a
fl10101 1.632e-3  0.3888  1.0 * area, length, fraction open
```

```
fl101s1  1.632e-3  0.3888  8.197e-3  * area, length, hyd diam
fl101t1  2  101  * use control function input, number 101, for time-specified velo
*
*--------------------
* fl path 102
*--------------------
*
fl110200  inlet->bypass  100  102  -0.1085  -0.1085  * from, to, inlet and outlet al
fl110201  5.211e-4  0.3888  1.0  * area, length, fraction open
*fl110203  2.0  1.0  * forward & reverse loss coeff's
fl102s1  5.211e-4  0.3888  2.609e-3  * area, length, hyd diam
fl102t1  2  102  * use control function input, number 102, for time-specified velo
*
*--------------------
* cf 101 (for fl 101) - inlet flow in channel
*--------------------
*
*   cf101 = velocity in junction fl 101
*         = 0.80 * Mdot(edf.3.1) / (Rho(cv100) * A(fl101))
*         = 490.20 * Mdot(edf.3.1) / Rho(cv100)
*
cf10100  inlet-vel-chan  divide  2  490.20  0.0  * name, type, 2 args, multiplier
cf10101  7.318e-2  * initial value; used Mdot = 0.44e-3kg/s, Rho = 2.9472kg/m**3
cf10110  1.0  0.0  cvh-rho.100  * first argument: divisor
cf10111  1.0  0.0  cfvalu.103   * second argument: dividend
*
*--------------------
* cf 102 (for fl 102) - inlet flow in bypass
*-------------- -------
*
*   cf102 = velocity in junction fl 102
*         = 0.20 * Mdot(edf.3.1) / (Rho(cv100) * A(fl102))
*         = 383.80 * Mdot(edf.3.1) / Rho(cv100)
*
cf10200  inlet-vel-chan  divide  2  383.80  0.0  * name, type, 2 args, multiplier
cf10201  5.730e-2  * initial value; used Mdot = 0.44e-3kg/s, Rho = 2.9472kg/m**3
cf10210  1.0  0.0  cvh-rho.100  * first argument: divisor
cf10211  1.0  0.0  cfvalu.103   * second argument: dividend
*
*-------------------------
* cf 103 (for cf101, cf102) (inlet mass flow rate)
*-------------------------
*
* cf103 = inlet mass flow rate (kg/s) - evaluated from integrated
*         flow input on edf.3.1
*
cf10300  inlet-flow  equals  1  1.0e-3  0.0  * name, type, 2 args, mult & add fact
cf10301  0.44e-3  * initial value; use 0.44e-3kg/s
```

```
cf10310  1.0  0.0  edf.3.1  * first argument
*
*------------------------
* edf.3 (for cf 103) (steam mass flow rate)
*------------------------
*
* edf.3.1 = inlet mass flow rate (g/s)
*
edf00300  inlet-flow  1  read  * inlet mass flow, 1 channel, read edf
edf00301  '/user/tjtautg/df4/data/exp/inletflow.dat'  * data file name
edf00302  2e16.6   * format for data fields, time and flow rate
*
*--------------------
* fl path 201
*--------------------
*
f120100 channel->outlet  101  200  0.6617  0.6617  * from, to, inlet and outlet al
f120101  1.632e-3  0.3728  1.0  * area, length, fraction open
f1201s1  1.632e-3  0.3728  8.197e-3  * area, length, hyd diam
*
*--------------------
* fl path 202
*--------------------
*
f120200 bypass->outlet  102  200  0.6617  0.6617  * from, to, inlet and outlet alt
f120201  5.211e-4  0.3728  1.0  * area, length, fraction open
f1202s1  5.211e-4  0.3728  2.609e-3  * area, length, hyd diam
*
*********************
* ncg package input  *
*********************
*
ncg001  h2  4
ncg002  o2  5
ncg003  co  6
ncg004  co2  7
ncg005  ch4  8
*
*********************
* hs package input  *
*********************
*
*--------------------
* hs 10101
*--------------------
*
hs10101000  36  2  1  * 36 nodes, cylindrical geom, ss initialization performed
hs10101001  'lp wall'  * hs name
```

```
hs10101002  -0.1085  1.0 * bottom elevation, vertical surface
hs10101004  101  0  * use core cell 101 for hs bound fluid temp
* location data:
hs10101100  -1  1  3.445e-2  * node locations follow, ifrmt=1, inner radius
hs10101101  5.874e-2  11  * outer radius of layer 1: ZrO2 (porous)
hs10101102  6.350e-2  21  * outer radius of layer 2: ZrO2 (dense)
hs10101103  8.255e-2  31  * outer radius of layer 3: ZrO2 (porous)
hs10101104  8.890e-2  36  * outer radius of layer 4: Stainless Steel
* composition data:
hs10101200  -1  * composition data follows
hs10101201  'zirconium oxide (porous)'  10 * layer 1: ZrO2 (porous)
hs10101202  'zirconium oxide'  20         * layer 2: ZrO2 (dense)
hs10101203  'zirconium oxide (porous)'  30 * layer 3: ZrO2 (porous)
hs10101204  'stainless steel'  35         * layer 4: Stainless Steel
* internal heat source (none):
hs10101300  0  * no internal source
* inside boundary data:
hs10101400  1  101  int  1.0  1.0  * convective b.c., bound volume 101, int bounda
                                   * crit. pool & atms fractions
hs10101401  0.7  equiv-band  9.63e-3  * emissivity of ZrO2 (guess!), radiation mod
                                      * radiation path length (diameter of a fuel
hs10101500  6.927e-3  8.197e-3  0.032  * area, char length (hyd diam used), axial
* outside boundary data:
hs10101600  2101  -1  'ext'  1.0  1.0  * const-temp b.c. specified by tf101, no bo
                                       * exterior surface, etc
*
*---------------------
* hs 10102
*---------------------
*
hs10102000  36  2  1  * 36 nodes, cylindrical geom, ss initialization performed
hs10102001  'core plate wall'  * hs name
hs10102002  -0.0765  1.0 * bottom elevation, vertical surface
hs10102004  102  0  * use core cell 101 for hs bound fluid temp
* location data:
hs10102100  10101  1  3.445e-2  * node locations follow, ifrmt=1, inner radius
* composition data:
hs10102200  10101  * composition data from hs10101
* internal heat source (none):
hs10102300  0  * no internal source
* inside boundary data:
hs10102400  1  101  int  1.0  1.0  * convective b.c., bound volume 101, int bounda
                                   * crit. pool & atms fractions
hs10102401  0.7  equiv-band  9.63e-3  * emissivity of ZrO2 (guess!), radiation mod
                                      * radiation path length (diameter of a fuel
hs10102500  3.247e-4  8.197e-3  0.0015  * area, char length (hyd diam used), axial
* outside boundary data:
hs10102600  2101  -1  'ext'  1.0  1.0  * const-temp b.c. specified by tf101, no bo
```

194

```
                                   * exterior surface, etc
*
*---------------------
* hs 10103
*---------------------
*
hs10103000  36  2  1  * 36 nodes, cylindrical geom, ss initialization performed
hs10103001  'bot spacer wall'  * hs name
hs10103002  -0.0750  1.0 * bottom elevation, vertical surface
hs10103004  103  0  * use core cell 103 for hs bound fluid temp
* location data:
hs10103100  -1  1  3.445e-2  * node locations follow, ifrmt=1, inner radius
hs10103101  5.874e-2  11  * outer radius of layer 1: ZrO2 (porous)
hs10103102  6.350e-2  21  * outer radius of layer 2: ZrO2 (dense)
hs10103103  8.255e-2  31  * outer radius of layer 3: ZrO2 (porous)
hs10103104  8.890e-2  36  * outer radius of layer 4: Stainless Steel
* composition data:
hs10103200  -1  * composition data follows
hs10103201  'zirconium oxide (porous)'  10 * layer 1: ZrO2 (porous)
hs10103202  'zirconium oxide'  20         * layer 2: ZrO2 (dense)
hs10103203  'zirconium oxide (porous)'  30 * layer 3: ZrO2 (porous)
hs10103204  'stainless steel'  35          * layer 4: Stainless Steel
* internal heat source (none):
hs10103300  0  * no internal source
* inside boundary data:
hs10103400  1  101  int  1.0  1.0  * convective b.c., bound volume 100, int bounda
                                   * crit. pool & atms fractions
hs10103401  0.7  equiv-band  9.63e-3  * emissivity of ZrO2 (guess!), radiation mod
                                      * radiation path length (diameter of a fuel
hs10103500  1.623e-3  8.197e-3  0.0750  * area, char length (hyd diam used), axial
* outside boundary data:
hs10103600  2101  -1  'ext'  1.0  1.0  * const-temp b.c. specified by tf101, no bo
                                       * exterior surface, etc
*
*---------------------
* hs 10104
*---------------------
*
hs10104000  36  2  1  * 36 nodes, cylindrical geom, ss initialization performed
hs10104001  'fu cell 104 wall'  * hs name
hs10104002  0.0  1.0 * bottom elevation, vertical surface
* location data:
hs10104100  10103  1  3.445e-2  * node locations from hs10103
* composition data:
hs10104200  10103  * composition data from hs10103
* internal heat source (none):
hs10104300  0  * no internal source
* inside boundary data:
```

```
hs10104400  1  101  int  1.0  1.0  * convective b.c., bound volume 101, int bounda
                                    * crit. pool & atms fractions
hs10104401  0.7  equiv-band  9.63e-3  * emissivity of ZrO2 (guess!), radiation mod
                                      * radiation path length (diameter of a fuel
hs10104500  1.215e-2  8.197e-3  0.05611  * area, char length (hyd diam used), axia
* outside boundary data:
hs10104600  2101  -1  'ext'  1.0  1.0  * const-temp b.c. specified by tf101, no bo
                                       * exterior surface, etc
*
*--------------------
* hs's 10105-10112
*--------------------
* hsmmmmm000:
hs10105000  36  2  1  * 36 nodes, cylindrical geom, ss initialization performed
hs10106000  36  2  1  * 36 nodes, cylindrical geom, ss initialization performed
hs10107000  36  2  1  * 36 nodes, cylindrical geom, ss initialization performed
hs10108000  36  2  1  * 36 nodes, cylindrical geom, ss initialization performed
hs10109000  36  2  1  * 36 nodes, cylindrical geom, ss initialization performed
hs10110000  36  2  1  * 36 nodes, cylindrical geom, ss initialization performed
hs10111000  36  2  1  * 36 nodes, cylindrical geom, ss initialization performed
hs10112000  36  2  1  * 36 nodes, cylindrical geom, ss initialization performed
* hsmmmmm001:
hs10105001  'fu cell 105 wall'  * hs name
hs10106001  'fu cell 106 wall'  * hs name
hs10107001  'fu cell 107 wall'  * hs name
hs10108001  'fu cell 108 wall'  * hs name
hs10109001  'fu cell 109 wall'  * hs name
hs10110001  'fu cell 110 wall'  * hs name
hs10111001  'fu cell 111 wall'  * hs name
hs10112001  'fu cell 112 wall'  * hs name
* hsmmmmm002:
hs10105002  0.05611  1.0 * bottom elevation, vertical surface
hs10106002  0.11222  1.0 * bottom elevation, vertical surface
hs10107002  0.16833  1.0 * bottom elevation, vertical surface
hs10108002  0.22444  1.0 * bottom elevation, vertical surface
hs10109002  0.28055  1.0 * bottom elevation, vertical surface
hs10110002  0.33666  1.0 * bottom elevation, vertical surface
hs10111002  0.39277  1.0 * bottom elevation, vertical surface
hs10112002  0.44888  1.0 * bottom elevation, vertical surface
* hsmmmmm100:
hs10105100  10103  1  3.445e-2  * get node location data from hs 10103
hs10106100  10103  1  3.445e-2  * get node location data from hs 10103
hs10107100  10103  1  3.445e-2  * get node location data from hs 10103
hs10108100  10103  1  3.445e-2  * get node location data from hs 10103
hs10109100  10103  1  3.445e-2  * get node location data from hs 10103
hs10110100  10103  1  3.445e-2  * get node location data from hs 10103
hs10111100  10103  1  3.445e-2  * get node location data from hs 10103
hs10112100  10103  1  3.445e-2  * get node location data from hs 10103
```

```
* hsmmmmm200:
hs10105200   10103   * get mesh composition data from hs 10103
hs10106200   10103   * get mesh composition data from hs 10103
hs10107200   10103   * get mesh composition data from hs 10103
hs10108200   10103   * get mesh composition data from hs 10103
hs10109200   10103   * get mesh composition data from hs 10103
hs10110200   10103   * get mesh composition data from hs 10103
hs10111200   10103   * get mesh composition data from hs 10103
hs10112200   10103   * get mesh composition data from hs 10103
* hsmmmmm300:
hs10105300   0   * no internal heat source
hs10106300   0   * no internal heat source
hs10107300   0   * no internal heat source
hs10108300   0   * no internal heat source
hs10109300   0   * no internal heat source
hs10110300   0   * no internal heat source
hs10111300   0   * no internal heat source
hs10112300   0   * no internal heat source
* inside boundary data:
hs10105400   1   101   int   1.0   1.0   * convective b.c., bound volume 101, int bounda
                                          * crit. pool & atms fractions
hs10106400   1   101   int   1.0   1.0   *
hs10107400   1   101   int   1.0   1.0   *
hs10108400   1   101   int   1.0   1.0   *
hs10109400   1   101   int   1.0   1.0   *
hs10110400   1   101   int   1.0   1.0   *
hs10111400   1   101   int   1.0   1.0   *
hs10112400   1   101   int   1.0   1.0   *
*
hs10105401   0.7   equiv-band   9.63e-3   * emissivity of ZrO2 (guess!), radiation mod
                                          * radiation path length (diameter of a fuel
hs10106401   0.7   equiv-band   9.63e-3   *
hs10107401   0.7   equiv-band   9.63e-3   *
hs10108401   0.7   equiv-band   9.63e-3   *
hs10109401   0.7   equiv-band   9.63e-3   *
hs10110401   0.7   equiv-band   9.63e-3   *
hs10111401   0.7   equiv-band   9.63e-3   *
hs10112401   0.7   equiv-band   9.63e-3   *
*
hs10105500   1.215e-2   8.197e-3   0.05611   * area, char length (hyd diam used), axia
hs10106500   1.215e-2   8.197e-3   0.05611   *
hs10107500   1.215e-2   8.197e-3   0.05611   *
hs10108500   1.215e-2   8.197e-3   0.05611   *
hs10109500   1.215e-2   8.197e-3   0.05611   *
hs10110500   1.215e-2   8.197e-3   0.05611   *
hs10111500   1.215e-2   8.197e-3   0.05611   *
hs10112500   1.215e-2   8.197e-3   0.05611   *
* outside boundary data:
```

```
hs10105600  2101  -1  'ext'  1.0  1.0  * const-temp b.c. specified by tf101, no bo
                                        * exterior surface, etc
hs10106600  2101  -1  'ext'  1.0  1.0  *
hs10107600  2101  -1  'ext'  1.0  1.0  *
hs10108600  2101  -1  'ext'  1.0  1.0  *
hs10109600  2101  -1  'ext'  1.0  1.0  *
hs10110600  2101  -1  'ext'  1.0  1.0  *
hs10111600  2101  -1  'ext'  1.0  1.0  *
hs10112600  2101  -1  'ext'  1.0  1.0  *
*
*--------------------
* hs 10113
*--------------------
*
hs10113000  36  2  1  * 36 nodes, cylindrical geom, ss initialization performed
hs10113001  'top spacer wall'  * hs name
hs10113002  0.5050  1.0 * bottom elevation, vertical surface
* location data:
hs10113100  10103  1  3.445e-2  * node locations from hs10103
* composition data:
hs10113200  10103  * composition data from hs10103
* internal heat source (none):
hs10113300  0  * no internal source
* inside boundary data:
hs10113400  1  101  int  1.0  1.0  * convective b.c., bound volume 100, int bounda
                                   * crit. pool & atms fractions
hs10113401  0.7  equiv-band  9.63e-3  * emissivity of ZrO2 (guess!), radiation mod
                                      * radiation path length (diameter of a fuel
hs10113500  1.134e-2  8.197e-3  0.0524  * area, char length (hyd diam used), axial
* outside boundary data:
hs10113600  2101  -1  'ext'  1.0  1.0  * const-temp b.c. specified by tf101, no bo
                                       * exterior surface, etc
*
*--------------------
* hs 10114
*--------------------
*
hs10114000  36  2  1  * 36 nodes, cylindrical geom, ss initialization performed
hs10114001  'inc spring wall'  * hs name
hs10114002  0.5574  1.0 * bottom elevation, vertical surface
* location data:
hs10114100  10103  1  3.445e-2  * node locations from hs10103
* composition data:
hs10114200  10103  * composition data from hs10103
* internal heat source (none):
hs10114300  0  * no internal source
* inside boundary data:
hs10114400  1  101  int  1.0  1.0  * convective b.c., bound volume 100, int bounda
```

198

```
                                          * crit. pool & atms fractions
hs10114401  0.7  equiv-band  9.63e-3  * emissivity of Zr02 (guess!), radiation mod
                                      * radiation path length (diameter  ! a fuel
hs10114500  1.675e-2  8.197e-3  0.0774  * area, char length (hyd diam used), axial
* outside boundary data:
hs10114600  2101  -1  'ext'  1.0  1.0  * const-temp b.c. specified by tf101, no bo
                                       * exterior surface, etc

*
*--------------------
* hs 10115
*--------------------
*
hs10115000  11  1  1  * 11 nodes, cylindrical geom, ss initialization performed
hs10115001  'upper bound hs'  * hs name
hs10115002  0.6617  0.0 * bottom elevation, vertical surface
* location data:
hs10115100  -1  1  0.0  * node locations follow
hs10115101  0.0232  11  *
* composition data:
hs10115200  -1  * composition data follows
hs10115201  'stainless steel'  10  * all stainless steel
* internal heat source (none):
hs10115300  0  * no internal source
* inside boundary data:
hs10115400  1  101  int  1.0  1.0  * convective b.c., bound volume 101, int bounda
                                   * crit. pool & atms fractions
hs10115401  0.7  equiv-band  9.63e-3  * emissivity of Zr02 (guess!), radiation mod
                                      * radiation path length (diameter of a fuel
hs10115500  3.728e-3  8.197e-3  0.03724  * area, char length (hyd diam used), axia
* outside boundary data:
hs10115600  0  -1  'ext'  1.0  1.0  * const-temp b.c. specified by tf101, no bound
                                    * exterior surface, etc
*
* add boundary fluid temperature option to make hs's see core cell
* atm temperatures
*
hs10101004  101  0
hs10102004  102  0
hs10103004  103  0
hs10104004  104  0
hs10105004  105  0
hs10106004  106  0
hs10107004  107  0
hs10108004  108  0
hs10109004  109  0
hs10110004  110  0
hs10111004  111  0
hs10112004  112  0
```

```
hs10113004  113  0
hs10114004  114  0
*
*
*----------------------
* tf 101 (for hs 10104-10112)
*----------------------
*
tf10100  'hs outer boundry'  2  1.0  0.0  * name, # data pairs, scale factors
* data pairs:
*        (time)  (Tboundary)
tf10110  0.0      473.0
tf10111  10000.0 473.0
*
**********************
* mp package input  *
**********************
*
***           material 5 is zircaloy
*
*   change default values for zircaloy to raise melting
*   temperature 102 k to be consistent with melprog and matpro
***
mpmat00500  zircaloy
mpmat00501  enh  220
mpmat00502  cps  221
mpmat00503  tmp  222
mpmat00550  mlt  2200.    *change melt temp to 2200 k, default=2098. k
*
tf22000  'ezirc'  16  1.0
tf22011    300.0        0.0
tf22012    400.0    21915.0
tf22013    640.0   105110.0
tf22014   1090.0   263960.0
tf22015   1093.0   265275.5
tf22016   1113.0   276195.5
tf22017   1133.0   288245.5
tf22018   1153.0   301585.5
tf22019   1173.0   316935.5
tf22020   1193.0   332795.5
tf22021   1213.0   346685.5
tf22022   1233.0   357565.5
tf22023   1248.0   363753.0
tf22024   2200.0   702665.0
tf22025   2200.01 927665.0
tf22026   3598.0  1425353.0
*
tf22100  'cpzirc'  15  1.0
```

```
tf22111   273.15   275.0
tf22112    400.0   302.0
tf22113    640.0   331.0
tf22114   1090.0   375.0
tf22115   1093.0   502.0
tf22116   1113.0   590.0
tf22117   1133.0   615.0
tf22118   1153.0   719.0
tf22119   1173.0   816.0
tf22120   1193.0   770.0
tf22121   1213.0   619.0
tf22122   1233.0   469.0
tf22123   1248.0   356.0
tf22124   2098.0   356.0
tf22125   5000.0   356.0
*
tf22200   'tzirc'   16   1.0
tf22211   0.0         300.0
tf22212   21915.0     400.0
tf22213   105110.0    640.0
tf22214   263960.0    1090.0
tf22215   265275.5    1093.0
tf22216   276195.5    1113.0
tf22217   288245.5    1133.0
tf22218   301585.5    1153.0
tf22219   316935.5    1173.0
tf22220   332795.5    1193.0
tf22221   346685.5    1213.0
tf22222   357565.5    1233.0
tf22223   363753.0    1248.0
tf22224   702665.0    2200.0
tf22225   927665.0    2200.01
tf22226   1425353.0   3598.0
*
*
*-------------------------
* zirconium oxide (porous)
*-------------------------
*
* define a new material, porous zirconium oxide, which has properties
* determined by the df-4 experimenters to give proper heat transfer
* characteristics
*
* tabular functions 201-204:
* tf201: enthalpy vs temp, use standard MELCOR values
* tf202: temp vs enthalpy, use standard MELCOR values
* tf203: spec heat cap vs temp, use standard MELCOR values
* tf204: therm conductivity vs temp, use correlation from
```

```
*          MELPROG DF-4 report
* tf205: density vs temp, use 0.21 * Rho(ZrO2-dense)
*
mpmat10100   'zirconium oxide (porous)'
*
mpmat10101    enh  201
mpmat10102    tmp  202
mpmat10103    cps  203
mpmat10104    thc  204
mpmat10105    rho  205
*
mpmat10151  den  1288.0  *  0.21 x rho(ZrO2-dense)
mpmat10152  mlt  2990.0
mpmat10153  lhf  7.07e5
*
*-------------------------------------------
* tf 201: enthalpy vs. temp for porous ZrO2
*-------------------------------------------
*
tf20100 'ZrO2(por) e vs t'  4  1.0  0.0  * name, # data pairs, scale facts
tf20110  300.00  0.0
tf20111  2990.00  1464167.0
tf20112  2990.01  2171167.0
tf20113  3500.00  2448760.0
*
*-------------------------------------------
* tf 202: temp vs. enthalpy for porous ZrO2
*-------------------------------------------
*
tf20200 'ZrO2(por) t vs e'  4  1.0  0.0  * name, # data pairs, scale facts
tf20210  0.0         300.00
tf20211  1464167.0  2990.00
tf20212  2171167.0  2990.01
tf20213  2448760.0  3500.00
*
*-------------------------------------------
* tf 203: cp vs. temp for porous ZrO2
*-------------------------------------------
*
tf20300 'Z02(por) cp vs t'  2  1.0  0.0  * name, # data pairs, scale facts
tf20310  273.15  544.3
tf20311  5000.0  544.3
*
*-------------------------------------------
* tf 204: thermal cond vs. temp for porous ZrO2
*-------------------------------------------
*
tf20400 'ZrO2(por) k vs t'  8  1.0  0.0  * name, # data pairs, scale facts
```

```
tf20410    273.15 1.4834e-1
tf20411    500.0  1.9374e-1
tf20412    750.0  2.6237e-1
tf20413   1000.0  3.5049e-1
tf20414   1250.0  4.5811e-1
tf20415   1500.0  5.8523e-1
tf20416   2000.0  8.9796e-1
tf20417   5000.0  4.4121e0
*
*--------------------------------------------
* tf 205: density vs. temp for porous ZrO2
*--------------------------------------------
*
tf20500 'ZrO2(por) d vs t'  2  1.0  0.0  * name, # data pairs, scale facts
tf20510    273.15 1288.0
tf20511   5000.0  1288.0
*
*----------------------
* boron carbide density
*----------------------
*
mpmat30100  boron-carbide
mpmat30101  rho  301
mpmat30151  den  1700.0
*
*----------------------------------------------
* tf 301: density vs. temp for boron carbide
*----------------------------------------------
*
tf30100  'b4c den vs t'  2  1.0  0.0
tf30111  273.15  1700.0
tf30112  5000.0  1700.0
*
*
************************
* misc cf package input *
************************
*
* cf's to define special functions
*
cf80100 h2rate  add  2  1.0  0.0
cf80111  1.0  0.0  fl-mflow.4.201
cf80112  1.0  0.0  fl-mflow.4.202
*
********************
* sc package input  *
********************
*
```

```
* change sensitivity coeff's to ensure 100% canister-b mass (SC 1501)
*
sc15011  1501  1.0  1  * mass
sc15012  1501  1.0  2  * surf area, channel, blade
sc15013  1501  1.0  3  *  "     "   , bypass, blade
sc15014  1501  0.0  4  * surf area, channel, non-blade
sc15015  1501  0.0  5  *  "     "   , bypass, non-blade
*
* molten material holdup parameters (SC 1131)
*
sc11311  1131  6.1e-5  1  * minumum Zr oxide thickness to hold up melt
sc11312  1131  1.42e-4 2  * minumum steel thickness to hold up melt
*
* change eutectic temperature of b4c-steel on SC 1011
*
sc10111  1011  1570.0 3  * b4c-steel eutectic temperature
*
* decrease autocatalytic oxidation switchover temperature
*
sc10011  1001  1750.0  5  1 * low to high range oxidation temp boundary
*
**********************
* edf package input  *
**********************
*
* specify temperature and melt fraction variables to be written to separate
* edf's
*
*-------------------------------
* edf 11: clad temp vs. position
*-------------------------------
*
*edf01100  clad-temp-vs-pos  9  write  * name, no of channels, direction
*edf01101  'clad-temp-pos.out'  * external file name
*edf01102  '10(1pe12.5)'  * format of data
*edf01111  7600.0  20.0  * time increment for data writes
*edf01112  7700.0  100000.0  * time increment for data writes
*edf011a0  cor-tcl.104 cor-tcl.105 cor-tcl.106 cor-tcl.107 cor-tcl.108  * dep var'
*edf011a1  cor-tcl.109 cor-tcl.110 cor-tcl.111 cor-tcl.112  *
*
*----------------------------------
* edf 12: fuel intact mass vs. position
*----------------------------------
*
*edf01200  fuel-mfr-vs-pos  9  write  * name, no of channels, direction
*edf01201  'fuel-mfr-pos.out'  * external file name
*edf01202  '10(1pe12.5)'  * format of data
*edf01211  7600.0  50.0  * time increment for data writes
```

```
*edf01212  7900.0  100000.0  * time increment for data writes
*edf012a0 cor-mltfr.104.1.1 cor-mltfr.105.1.1 cor-mltfr.106.1.1 * dep var's
*edf012a1 cor-mltfr.107.1.1 cor-mltfr.108.1.1 cor-mltfr.109.1.1
*edf012a2 cor-mltfr.110.1.1 cor-mltfr.111.1.1 cor-mltfr.112.1.1  *
*
*----------------------------------
* edf 13: clad intact mass vs. position
*----------------------------------
*
*edf01300  clad-mfr-vs-pos  9  write  * name, no of channels, direction
*edf01301  'clad-mfr-pos.out'  * external file name
*edf01302  '10(1pe12.5)'  * format of data
*edf01311  7600.0  50.0  * time increment for data writes
*edf01312  7900.0  100000.0  * time increment for data writes
*edf013a0 cor-mltfr.104.2.2 cor-mltfr.105.2.2 cor-mltfr.106.2.2 * dep var's
*edf013a1 cor-mltfr.107.2.2 cor-mltfr.108.2.2 cor-mltfr.109.2.2
*edf013a2 cor-mltfr.110.2.2 cor-mltfr.111.2.2 cor-mltfr.112.2.2  *
*
*----------------------------------
* edf 14: canister intact mass vs. position
*----------------------------------
*
*edf01400  can-mfr-vs-pos  9  write  * name, no of channels, direction
*edf01401  'can-mfr-pos.out'  * external file name
*edf01402  '10(1pe12.5)'  * format of data
*edf01411  7600.0  50.0  * time increment for data writes
*edf01412  7900.0  100000.0  * time increment for data writes
*edf014a0 cor-mltfr.104.2.4 cor-mltfr.105.2.4 cor-mltfr.106.2.4 * dep var's
*edf014a1 cor-mltfr.107.2.4 cor-mltfr.108.2.4 cor-mltfr.109.2.4
*edf014a2 cor-mltfr.110.2.4 cor-mltfr.111.2.4 cor-mltfr.112.2.4  *
*
*----------------------------------
* edf 15: os intact mass vs. position
*----------------------------------
*
*edf01500  os-mfr-vs-pos  9  write  * name, no of channels, direction
*edf01501  'os-mfr-pos.out'  * external file name
*edf01502  '10(1pe12.5)'  * format of data
*edf01511  7600.0  50.0  * time increment for data writes
*edf01512  7900.0  100000.0  * time increment for data writes
*edf015a0 cor-mltfr.104.3.5 cor-mltfr.105.3.5 cor-mltfr.106.3.5 * dep var's
*edf015a1 cor-mltfr.107.3.5 cor-mltfr.108.3.5 cor-mltfr.109.3.5
*edf015a2 cor-mltfr.110.3.5 cor-mltfr.111.3.5 cor-mltfr.112.3.5  *
*
*****************************************
* allowreplace record, to allow insertion of any
* sensitivity study input
*****************************************
```

```
*
allowreplace
r*i*f 'sens.dat'
.
*
*eor* melcor
*
*
* MELCOR DF4 input deck
*
*********************
* exec package input  *
********************
*
title     'df4'
jobid     'df4'
*
diagf     'df4.dia'
outputf   'df4.out'
plotf     'df4.ptf'
messagef  'df4.mes'
restartf  'df4.rst'
statusf   'df4.mai'
crtout
*
*
restart  0
cpuleft  10.
cpulim   1.e6
*
*tend
tend      8100.0
*
*****************************************************************
*           time  dtmax  dtmin  dtedt  dtplt  dtrst  dcrest
*
time1    6000.0  1.0   0.0001   500.0    10.0    500.0
*
time2    7200.0  0.25  0.0001   500.0     5.0    500.0
*
time3    8000.0  1.0   0.001    500.0    50.0   500.0
*
*****************************************************************
*
* enable additional cor output
*
coredv01  1  1  1  1  1  1 * turn on volume fraction plot output
*
```

206

```
allowreplace
r*i*f 'sens2.dat'
*
.
*
*eor* hisplt
file1  'df4.ptf'
title,df4 experiment base case
nologo,wide
*
*
title,hydrogen mass production
vlabel,mass (()kg)
limits 0,0,0.0,50.0e-3
plot,time,cor-dmh2-tot, line = 'solid',  sym=',',le='base case',file=1
data,le='experiment',line = dot
*readfile,'/user/tjtautg/df4/data/exp/h2mass.dat'
lege,ul
*
title,bundle power
vlabel,power (()w)
limits 6000.0,8000.0,0,0
 plot,time, cor-efpd-rat,line = 'solid', sym=',',le='base case',file=1
lege,ul
*
title,ACRR Reactor Power
vlabel,Reactor Power (()Mw)
ulabel,Time (()s)
limits 6000.0,8200.0,0,0
uplot,line = 'solid', sym=','
*readfile,'/user/tjtautg/df4/data/exp/reapow.dat'
lege,ul
*
title,core package energy error
vlabel,error (()j)
limits 6000.0,8000.0,0,0
 plot,time, cor-energyerr,line = 'solid', sym=',',le='base case',file=1
lege,ul
*
title,clad temps,9.6 cm
vlabel,temperature (()K)
limits 6000.0,8000.0,400.0,2600.0
 plot,time, cor-tcl.105,line = 'solid', sym=',',le='base case',file=1
data,le='z1p215',line = dot
*readfile,'/user/tjtautg/df4/data/exp/cladtemp.dat','z1p215'
data,le='z4p215',line = dot
*readfile,'/user/tjtautg/df4/data/exp/cladtemp.dat','z4p215'
lege,ul
```

```
*
title,clad temps,25.4 cm
vlabel,temperature (()K)
limits 6000.0,8000.0,400.0,2600.0
 plot,time, cor-tcl.108,line = 'solid', sym=',',le='base case',file=1
data,le='z2p160',line = dot
*readfile,'/user/tjtautg/df4/data/exp/cladtemp.dat','z2p160'
data,le='z3p160',line = dot
*readfile,'/user/tjtautg/df4/data/exp/cladtemp.dat','z3p160'
lege,ul
*
title,clad temps,36.8 cm
vlabel,temperature (()K)
limits 6000.0,8000.0,400.0,2600.0
 plot,time, cor-tcl.110,line = 'solid', sym=',',le='base case',file=1
data,le='z1p115',line = dot
*readfile,'/user/tjtautg/df4/data/exp/cladtemp.dat','z1p115'
data,le='z4p115',line = dot
*readfile,'/user/tjtautg/df4/data/exp/cladtemp.dat','z4p115'
lege,ul
*
title,clad temps,49.5 cm
vlabel,temperature (()K)
limits 6000.0,8000.0,400.0,2600.0
 plot,time, cor-tcl.112,line = 'solid', sym=',',le='base case',file=1
data,le='z1p065',line = dot
*readfile,'/user/tjtautg/df4/data/exp/cladtemp.dat','z1p065'
lege,ul
*
title,clad temperatures
vlabel,temperature (()K)
limits 7400.0,8000.0,400.0,2600.0
 plot,time, cor-tcl.107,line = 'mdash', sym='^',le='base case,c107',file=1
cplot,time, cor-tcl.108,line = 'solid', sym=',',le='base case,c108',file=1
cplot,time, cor-tcl.109,line = dashdash, sym='"',le='base case,c109',file=1
cplot,time, cor-tcl.110,line = 'sdash', sym='&',le='base case,c110',file=1
cplot,time, cor-tcl.111,line = 'ldash', sym='<',le='base case,c111',file=1
cplot,time, cor-tcl.112,line = 'dotdash', sym='@',le='base case,c112',file=1
lege,ur
*
title,canister temps,9.6 cm
vlabel,temperature (()K)
limits 6000.0,8000.0,400.0,2600.0
 plot,time, cor-tcb.105,line = 'solid', sym=',',le='base case',file=1
data,le='ctw217',line = dot
*readfile,'/user/tjtautg/df4/data/exp/cantemp.dat','ctw217'
lege,ul
*
```

```
title,canister temps,25.4 cm
vlabel,temperature (()K)
limits 6000.0,8000.0,400.0,2600.0
 plot,time, cor-tcb.108,line = 'solid', sym=',',le='base case',file=1
data,le='ctw162',line = dot
*readfile,'/user/tjtautg/df4/data/exp/cantemp.dat','ctw162'
data,le='cbw162',line = dot
*readfile,'/user/tjtautg/df4/data/exp/cantemp.dat','cbw162'
lege,ul
*
title,canister temps,36.8 cm
vlabel,temperature (()K)
limits 6000.0,8000.0,400.0,2600.0
 plot,time, cor-tcb.110,line = 'solid', sym=',',le='base case',file=1
data,le='ctw117',line = dot
*readfile,'/user/tjtautg/df4/data/exp/cantemp.dat','ctw117'
data,le='cbw117',line = dot
*readfile,'/user/tjtautg/df4/data/exp/cantemp.dat','cbw117'
lege,ul
*
title,canister temps,49.5 cm
vlabel,temperature (()K)
limits 6000.0,8000.0,400.0,2600.0
 plot,time, cor-tcb.112,line = 'solid', sym=',',le='base case',file=1
data,le='ctw067',line = dot
*readfile,'/user/tjtautg/df4/data/exp/cantemp.dat','ctw067'
lege,ul
*
title,canister temperatures (high)
vlabel,temperature (()K)
limits 7400.0,8000.0,400.0,2600.0
plot,time, cor-tcb.108,line = 'solid', sym=',',le='base case,c108',file=1
cplot,time, cor-tcb.109,line = dashdash, sym='"',le='base case,c109',file=1
cplot,time, cor-tcb.110,line = 'sdash', sym='&',le='base case,c110',file=1
cplot,time, cor-tcb.111,line = 'ldash', sym='<',le='base case,c111',file=1
cplot,time, cor-tcb.112,line = 'dotdash', sym='@',le='base case,c112',file=1
lege,lr
*
title,canister temperatures (low)
vlabel,temperature (()K)
limits 7400.0,8000.0,400.0,2600.0
 plot,time, cor-tcb.104,line = 'mdash', sym='^',le='base case,c107',file=1
cplot,time, cor-tcb.105,line = 'solid', sym=',',le='base case,c108',file=1
cplot,time, cor-tcb.106,line = dashdash, sym='"',le='base case,c109',file=1
cplot,time, cor-tcb.107,line = 'sdash', sym='&',le='base case,c110',file=1
lege,lr
*
title,intact zr mass in clad
```

```
vlabel,mass (()kg)
limits 7400.0,8000.0,0,0
 plot,time, cfvalu.904,line = 'dotdash', sym='^',le='base case,c107',file=1
cplot,time, cfvalu.905,line = 'mdash', sym='@',le='base case,c108',file=1
cplot,time, cfvalu.906,line = 'solid', sym=',',le='base case,c109',file=1
cplot,time, cfvalu.907,line = dashdash,  sym='"',le='base case,c110',file=1
cplot,time, cfvalu.908,line = 'sdash', sym='&',le='base case,c111',file=1
cplot,time, cfvalu.909,line = 'ldash', sym='<',le='base case,c112',file=1
lege,ur
*
title,intact zr mass in canister
vlabel,mass (()kg)
limits 7400.0,8000.0,0,0
 plot,time, cfvalu.914,line = 'dotdash', sym='^',le='base case,c107',file=1
cplot,time, cfvalu.915,line = 'mdash', sym='@',le='base case,c108',file=1
cplot,time, cfvalu.916,line = 'solid', sym=',',le='base case,c109',file=1
cplot,time, cfvalu.917,line = dashdash,  sym='"',le='base case,c110',file=1
cplot,time, cfvalu.918,line = 'sdash', sym='&',le='base case,c111',file=1
cplot,time, cfvalu.919,line = 'ldash', sym='<',le='base case,c112',file=1
lege,lr
*
title,total zr mass in cell
vlabel,mass (()kg)
limits 7400.0,8000.0,0,0
 plot,time, cor-mzr.107,line = 'dotdash', sym='^',le='base case,c107',file=1
cplot,time, cor-mzr.108,line = 'mdash', sym='@',le='base case,c108',file=1
cplot,time, cor-mzr.109,line = 'solid', sym=',',le='base case,c109',file=1
cplot,time, cor-mzr.110,line = dashdash, sym='"',le='base case,c110',file=1
cplot,time, cor-mzr.111,line = 'sdash', sym='&',le='base case,c111',file=1
cplot,time, cor-mzr.112,line = 'ldash', sym='<',le='base case,c112',file=1
lege,ur
*
title,intact uo2 mass in fuel
vlabel,mass (()kg)
limits 7400.0,8000.0,0,0
 plot,time, cfvalu.924,line = 'dotdash', sym='^',le='base case,c107',file=1
cplot,time, cfvalu.925,line = 'mdash', sym='@',le='base case,c108',file=1
cplot,time, cfvalu.926,line = 'solid', sym=',',le='base case,c109',file=1
cplot,time, cfvalu.927,line = dashdash,  sym='"',le='base case,c110',file=1
cplot,time, cfvalu.928,line = 'sdash', sym='&',le='base case,c111',file=1
cplot,time, cfvalu.929,line = 'ldash', sym='<',le='base case,c112',file=1
lege,ur
*
title,total uo2 mass in cell
vlabel,mass (()kg)
limits 7400.0,8000.0,0,0
 plot,time, cor-muo2.107,line = 'dotdash', sym='^',le='base case,c107',file=1
cplot,time, cor-muo2.108,line = 'mdash', sym='@',le='base case,c108',file=1
```

```
cplot,time, cor-muo2.109,line = 'solid', sym=',',le='base case,c109',file=1
cplot,time, cor-muo2.110,line = dashdash, sym='"',le='base case,c110',file=1
cplot,time, cor-muo2.111,line = 'sdash', sym='&',le='base case,c111',file=1
cplot,time, cor-muo2.112,line = 'ldash', sym='<',le='base case,c112',file=1
lege,lr
*
title,other struc temps,9.6 cm
vlabel,temperature (()K)
limits 6000.0,8000.0,400.0,2600.0
 plot,time, cor-tss.105,line = 'solid', sym=',',le='base case',file=1
data,le='btp222',line = dot
*readfile,'/user/tjtautg/df4/data/exp/ostemp.dat','btp222'
data,le='bcp222',line = dot
*readfile,'/user/tjtautg/df4/data/exp/ostemp.dat','bcp222'
lege,ul
*
title,other struc temps,25.4 cm
vlabel,temperature (()K)
limits 6000.0,8000.0,400.0,2600.0
 plot,time, cor-tss.108,line = 'solid', sym=',',le='base case',file=1
data,le='btp167',line = dot
*readfile,'/user/tjtautg/df4/data/exp/ostemp.dat','btp167'
data,le='bcp167',line = dot
*readfile,'/user/tjtautg/df4/data/exp/ostemp.dat','bcp167'
lege,ul
*
title,other struc temps,36.8 cm
vlabel,temperature (()K)
limits 6000.0,8000.0,400.0,2600.0
 plot,time, cor-tss.110,line = 'solid', sym=',',le='base case',file=1
data,le='btp122',line = dot
*readfile,'/user/tjtautg/df4/data/exp/ostemp.dat','btp122'
data,le='bcp122',line = dot
*readfile,'/user/tjtautg/df4/data/exp/ostemp.dat','bcp122'
lege,ul
*
title,other struc temps,49.5 cm
vlabel,temperature (()K)
limits 6000.0,8000.0,400.0,2600.0
 plot,time, cor-tss.112,line = 'solid', sym=',',le='base case',file=1
data,le='btp072',line = dot
*readfile,'/user/tjtautg/df4/data/exp/ostemp.dat','btp072'
lege,ul
*
title,other struc temps
vlabel,temperature (()K)
limits 7300.0,7700.0,400.0,2600.0
 plot,time, cor-tss.107,line = 'mdash', sym='^',le='base case,c107',file=1
```

```
cplot,time, cor-tss.108,line = 'solid', sym=',',le='base case,c108',file=1
cplot,time, cor-tss.109,line = dashdash, sym='"',le='base case,c109',file=1
cplot,time, cor-tss.110,line = 'sdash', sym='&',le='base case,c110',file=1
cplot,time, cor-tss.111,line = 'ldash', sym='<',le='base case,c111',file=1
cplot,time, cor-tss.112,line = 'dotdash', sym='@',le='base case,c112',file=1
data,le='btp167',line = dot
*readfile,'/user/tjtautg/df4/data/exp/ostemp.dat','btp167'
data,le='bcp167',line = dot
*readfile,'/user/tjtautg/df4/data/exp/ostemp.dat','bcp167'
data,le='btp122',line = dot
*readfile,'/user/tjtautg/df4/data/exp/ostemp.dat','btp122'
data,le='bcp122',line = dot
*readfile,'/user/tjtautg/df4/data/exp/ostemp.dat','bcp122'
data,le='btp072',line = dot
*readfile,'/user/tjtautg/df4/data/exp/ostemp.dat','btp072'
lege,next
*
title,intact steel mass in os
vlabel,mass (()kg)
limits 7300.0,7700.0,0,0
 plot,time, cfvalu.934,line = 'dotdash', sym='^',le='base case,c107',file=1
cplot,time, cfvalu.935,line = 'mdash', sym='@',le='base case,c108',file=1
cplot,time, cfvalu.936,line = 'solid', sym=',',le='base case,c109',file=1
cplot,time, cfvalu.937,line = dashdash,   sym='"',le='base case,c110',file=1
cplot,time, cfvalu.938,line = 'sdash', sym='&',le='base case,c111',file=1
cplot,time, cfvalu.939,line = 'ldash', sym='<',le='base case,c112',file=1
lege,ll
*
title,total steel mass in cell
vlabel,mass (()kg)
limits 7300.0,7700.0,0,0
 plot,time, cor-mss.107,line = 'dotdash', sym='^',le='base case,c107',file=1
cplot,time, cor-mss.108,line = 'mdash', sym='@',le='base case,c108',file=1
cplot,time, cor-mss.109,line = 'solid', sym=';',le='base case,c109',file=1
cplot,time, cor-mss.110,line = dashdash, sym='"',le='base case,c110',file=1
cplot,time, cor-mss.111,line = 'sdash', sym='&',le='base case,c111',file=1
cplot,time, cor-mss.112,line = 'ldash', sym='<',le='base case,c112',file=1
lege,ul
*
title,intact b4c mass in os
vlabel,mass (()kg)
limits 7300.0,7700.0,0,0
 plot,time, cfvalu.944,line = 'dotdash', sym='^',le='base case,c107',file=1
cplot,time, cfvalu.945,line = 'mdash', sym='@',le='base case,c108',file=1
cplot,time, cfvalu.946,line = 'solid', sym=',',le='base case,c109',file=1
cplot,time, cfvalu.947,line = dashdash, sym='"',le='base case,c110',file=1
cplot,time, cfvalu.948,line = 'sdash', sym='&',le='base case,c111',file=1
cplot,time, cfvalu.949,line = 'ldash', sym='<',le='base case,c112',file=1
```

```
lege,ll
*
title,total b4c mass in cell
vlabel,mass (()kg)
limits 7300.0,7700.0,0,0
 plot,time, cor-mcrp.107,line = 'dotdash', sym='^',le='base case,c107',file=1
cplot,time, cor-mcrp.108,line = 'mdash', sym='@',le='base case,c108',file=1
cplot,time, cor-mcrp.109,line = 'solid', sym=',',le='base case,c109',file=1
cplot,time, cor-mcrp.110,line = dashdash, sym='"',le='base case,c110',file=1
cplot,time, cor-mcrp.111,line = 'sdash', sym='&',le='base case,c111',file=1
cplot,time, cor-mcrp.112,line = 'ldash', sym='<',le='base case,c112',file=1
lege,ul
*
title,fluid volume fractions
vlabel,volume fraction
limits 7300.0,7700.0,0.0,1.0
 plot,time, cor-volf-fl.107,line = 'dotdash', sym='^',le='base case,c107',file=1
cplot,time, cor-volf-fl.108,line = 'mdash', sym='@',le='base case,c108',file=1
cplot,time, cor-volf-fl.109,line = 'solid', sym=',',le='base case,c109',file=1
cplot,time, cor-volf-fl.110,line = dashdash, sym='"',le='base case,c110',file=1
cplot,time, cor-volf-fl.111,line = 'sdash', sym='&',le='base case,c111',file=1
cplot,time, cor-volf-fl.112,line = 'ldash', sym='<',le='base case,c112',file=1
lege,ll
*
title,debris volume fractions
vlabel,volume fractions
limits 7500.0,8200.0,0.0,1.0
 plot,time, cor-volf-dp.102,line = 'dotdash', sym='^',le='base case,c102',file=1
cplot,time, cor-volf-dp.103,line = 'mdash', sym='@',le='base case,c103',file=1
cplot,time, cor-volf-dp.104,line = 'solid', sym=',',le='base case,c104',file=1
cplot,time, cor-volf-dp.105,line = dashdash, sym='"',le='base case,c105',file=1
cplot,time, cor-volf-dp.106,line = 'sdash', sym='&',le='base case,c106',file=1
cplot,time, cor-volf-dp.107,line = 'ldash', sym='<',le='base case,c107',file=1
lege,ul
*
title,debris temperatures
vlabel,temperature (()K)
limits 7500.0,8200.0,0,0
 plot,time, cor-tdp.102,line = 'dotdash', sym='^',le='base case,c102',file=1
cplot,time, cor-tdp.103,line = 'mdash', sym='@',le='base case,c103',file=1
cplot,time, cor-tdp.104,line = 'solid', sym=',',le='base case,c104',file=1
cplot,time, cor-tdp.105,line = dashdash, sym='"',le='base case,c105',file=1
cplot,time, cor-tdp.106,line = 'sdash', sym='&',le='base case,c106',file=1
cplot,time, cor-tdp.107,line = 'ldash', sym='<',le='base case,c107',file=1
lege,lr
*
```

External Distribution:

Idaho National Engineering Laboratory (5)
Attn: A. Brown
       R. J. Dallman
       D. W. Golden
       S. E. Reed
       G. W. Johnsen
EG&G Idaho
P. O. Box 1625
Idaho Falls, ID 83404

D. Jones
EI International
P. O. Box 50736
Idaho Falls, ID 83405

Electric Power Research Institute (3)
Attn: E. Fuller
       R. N. Oehlberg
       B. R. Sehgal
P. O. Box 10412
Palo Alto, CA 94303

Los Alamos National Laboratory
Attn: B. E. Boyack, K-551
P. O. Box 1663
Los Alamos, NM 87545

Oak Ridge National Laboratory (11)
P. O. Box 2009
Oak Ridge, TN 37831-8057
Attn: S. R. Greene, MS-8057
       R. H. Morris, MS-8057
       S. E. Fisher, MS-8057
       R. Sanders, MS-8057
       T. L. Heatherly, MS-8057
       S. A. Hodge, MS-8057
       C. R. Hyman, MS-8057
       B. W. Patton, MS-8057
       D. B. Simpson, MS-8057
       R. P. Taleyarkhan, MS-8057
       M. L. Tobias, MS-8088
P. O. Box 2009
Oak Ridge, TN 37831-8057

Andrzej Drozd
Nuclear Regulatory Commission
OWFN, MS 8E1
11555 Rockville Pike
Rockville, MD 20852

W. P. Barthold
Barthold & Associates
132 Seven Oaks Drive
Knoxville, TN 37922

K. C. Wagner
Science Applications Intl. Corp.
2109 Air Park Rd. SE
Albuquerque, NM 87106

Savannah River Laboratory (2)
Attn: B. DeWald
        D. Allison
Westinghouse Savannah River Co.
Bldg. 773-41A
Aiken, SC 29808-0001

Westinghouse Hanford Co. (2)
Attn: D. Ogden
        O. Wang
P. O. Box 1970
Richland, WA 99352

General Electric Company (4)
Knolls Atomic Pwer Laboratory
Attn: D. F. McMullan
        G. H. Epstein
        E. Menard
        Joe Alfeo
Bldg. F3, Room 8
P. O. Box 1072
Schenectady, NY 12301-1072

Bettis Atomic Power Laboratory (4)
Attn: Mark Riley
        Vincent Baiamonte
        Joe Semancik
P. O. Box 79
West Mifflin, PA 15122

Mohsen Khatib-Rahbar
Energy Research Inc.
P. O. Box 2034
Rockville, MD 20852

V. K. Dhir
2445 22nd Street
Santa Monica, CA 90403

R. Viskanta
Purdue University
Heat Transfer Laboratory
School of Mechanical Engineering
West Lafayette, IN 47907

Dr. Jim Gieseke
Battelle Memorial Institute
505 King Ave.
Columbus, Ohio 43201

M. A. Kenton
Gabor, Kenton & Associates
770 Pasquinelli Drive
Suite 426
Westmont, IL 60559

University of California (2)
Attn: W. H. Amarasooriya
      T. Theofanous
ERC-CRSS
Santa Barbara, CA 93106

F. E. Haskin
University of New Mexico
Department of Chemical and Nuclear Engineering
Albuquerque, NM 87131

J. C. Lee
University of Michigan
Dept. of Nuclear Engineering
Cooley Building, North Campus
College of Engineering
Ann Arbor, MI 48109-2104

University of Wisconsin (2)
Dept. of Nuclear Engineering
Attn: M. L. Corradini
      G. A. Moses
Engineering Research Building
1500 Johnson Drive
Madison, WI 53706

Ramu K. Sundaram
Manager, LOCA Analysis Group
Nuclear Engineering
Yankee Atomic Electric Company
580 Main Street
Bolton, MA 01740

CEGA
Attn: John Bolin
P. O. Box 85608
San Diego, CA 92186-9784

M. Plys
Fauske & Associates
16W070 West 83rd Street
Burr Ridge, IL 60521

Nick Trikouros
GPU Nuclear Corporation
One Upper Pond Road
Parsippany, NJ 07054

B. Raychaudhuri
Nebraska Public Power District
PRA & Engineering Review Group
P. O. Box 499
Columbus, NE 68601

Frank Elia
Stone & Webster Engineering Corp.
245 Summer Street
Boston, MA 02210

Samir S. Girgis
Atomic Energy of Canada Limited
CANDU Operations
Sheridan Park Research Community
Mississagua, Ontario
CANADA L5K1B2

Paul J. Fehrenbach
Chalk River Nuclear Laboratories
Fuel Engineering Branch, RSR Division
Chalk River, Ontario
CANADA KOJ1J0

Dr. Bohumír Kujal
Department of Reactor Technology
Nuclear Research Institute Ře־z plc
250 68 Řež
CZECH REPUBLIC

Andrej Mitro
Institute of Radioecology and Applied Nuclear Techniques
Garbiarska 2
P. O. Box A-41
040 61 Košice
CHECHOSLOVAKIA

Shih-Kuei Cheng
Atomic Energy Council, Nuclear Safety
67, Lane 144, Keelung Rd. Sec. 4
Taipei, Taiwan
REPUBLIC OF CHINA

Lainsu Kao, Associate Scientist
Atomic Energy Council
Institute of Nuclear Energy Research
P. O. Box 303
Lung-Tan, 32500
Taiwan
REPUBLIC OF CHINA

Technical Research Centre of Finland (3)
Nuclear Engineering Laboratory
Attn: Lasse Mattila
      Ilona Lindholm
      Esko Pekkarinen
P. O. Box 208 (Tekniikantie 4)
SF-002151 Espoo
FINLAND

Jorma V. Sandberg
Finnish Center Radiation & Nucl. Safety,
Dept. of Nuclear Safety
P. O. Box 268
SF-00101 Helsinki
FINLAND

Akihide Hidaka
Safety Research Department
Reactor Accident Studies and Modelling Branch
DRS/SEMAR
Cadarache Nuclear Center
13108 Saint-Paul-Lez-Durance Cedex
FRANCE

Dr. Lothar Wolf
Battelle Institute EV
AM Romerhof 35
D-6000
Frankfurt/Main90
GERMANY

Gesellschaft fur Anlagen- und Reaktorsicherheit (3)
Attn: Ulrich Erven
      Walter Erdmann
      Manfred Firnhaber
Schwertnergasse 1
D-5000 Koln 1
GERMANY

Kernforschungzentrum, Karlsruhe (3)
Attn: P. Hofmann
       Werner Scholtyssek
       Philipp Schmuck
P. O. Box 3640
D-7500 Karlsruhe 1
GERMANY

Udo Brockmeier
University of Bochum
Energietechnik
IB-4-128
D-4630 Bochum
GERMANY

György Gyenes
Central Research Institute for Physics
Institute for Atomic Energy Research
H-1525 Budapest, P. O. Box 49
HUNGARY

Joint Research Center
Commission of the European Communities
Attn: Alan Jones
       Iain Shepherd
Safety Technology Institute
21020 Ispra (Va)
ITALY

Giovanni Saponaro
ENEA
Natl. Comm. for R&D of Nuclear Energy
Via Vitaliano Brancati, 48
00144 Rome
ITALY

Japan Atomic Energy Research Institute (2)
Attn: Kunihisa Soda
       Jun Sugimoto
       Norihiro Yamano
Tokai-mura, Naka-gun, Ibaraki-ken
319-11, JAPAN

Dr. Masayoshi Shiba, Director General
Institute of Nuclear Safety
Nuclear Power Engineering Corporation
Fujita Kankou Toranoman Bldg. 7F
3-17-1, Toranoman
Minato-Ku, Tokyo, 105
JAPAN

Masao Ogino
Mitsubishi Atomic Power Industries
4-1 Shibakoen 2-Chome
Minatoku Tokyo
JAPAN

Hidetoshi Okada
Nuclear Power Engineering Corporation
3-17-1, Toranomon Bldg. 5F
Minato-ku, Tokyo 105
JAPAN

Hirohide Oikawa
Toshiba Corporation
8, Shin-Sugita, Isogo-ku
Yokohama
JAPAN

Korea Atomic Energy Research Inst. (3)
Attn: Kun-Joong Yoo
      Song-Won Cho
      Dong-Ha Kim
P. O. Box 7, Daeduk Danji
Taejon
SOUTH KOREA 305-353

Jae Hong Park
Safety Assessment Department
Korea Atomic Energy Research Institute
P. O. Box 16, Daeduk-Danji
Taejon
SOUTH KOREA 305-353

Netherlands Energy Research Foundation (2)
Attn: Karel J. Brinkmann
        E. J. Velema
P. O. Box 1
1755 ZG Petten
THE NETHERLANDS

Dr. Valery F. Strizhov
Russian Academy of Science
Institute of Nuclear Safety
Moscow, G. Tulsky, 52
113191, RUSSIA

Universidad Politecnica de Madrid (2)
Attn: Augustin Alonzo Santos
        Francisco Martin
E.T.S. Ingenieros Industriales
Jose Gutierrez Abascal, 2
28006 Madrid
SPAIN

Juan Bagues
Consejo de Seguridad Nuclear
Justo Dorado, 11
28040, Madrid
SPAIN

Oddbjörn Sandervåg
Statens Kärnkraftinspektion
Swedish Nuclear Power Inspectorate
Box 27106 102 52 Stockholm
SWEDEN

L. Hammar, Director
Division of Research
Swedish Nuclear Power Inspectorate
Statens Karnkraftinspektion
Sehlstedtsgatan 11
Box 27106
S-102-50 Stockholm
SWEDEN

Swiss Federal Nuclear Safety Inspectorate (4)
Attn: S. Chakraborty
      Sang Lung Chan
      U. Schmocker
      H. P. Isaak
CH-5232 Villigen-HSK
SWITZERLAND

United Kingdom Atomic Energy Agency (3)
Winfrith Technology Center
Attn: T. Haste
      S. R. Kinnersley
      D. W. Sweet
Winfrith, Dorchester, Dorset
UNITED KINGDOM, DTS 8DH

United Kingdom Atomic Energy Authority (2)
Safety & Reliability Directorate
Attn: M. I. Robertson
      C. Wheatley
Wigshaw Lane, Culcheth, Warrington
Cheshire, WA3 4NE
UNITED KINGDOM

Geoffrey A. Brown
AEA Technology
Consultancy Services
Thomson House, Risley, Warrington
Cheshire, WA3 6AT
UNITED KINGDOM

Internal Distribution:

6400 N. R. Ortiz
6403 W. A. von Riesemann
6404 D. A. Powers
6412 A. L. Camp
6412 S. E. Dingman
6413 F. T. Harper
6414 J. E. Kelly
6418 S. L. Thompson (10)
6418 R. K. Cole
6418 A. A. Elsbernd
6418 L. N. Kmetyk
6418 R. C. Smith
6418 D. S. Stuart
6418 R. M. Summers
6418 T. J. Tautges (10)
6422 M. D Allen
6423 K. O. Reil
6423 R. O. Gauntt
6423 R. C. Schmidt
6429 K. E. Washington
7141 Technical Library (5)
7151 Technical Publications
7613-2 Document Processing for DOE/OSTI (10)
8523-2 Central Technical Files

END

DATE FILMED
2 / 10 / 94